Dissertation zur Erlangung des Doktorgrades
der Fakultät für Chemie und Pharmazie
der Ludwig-Maximilians-Universität München

Structural and mechanistic insights into the bacterial Mre11-Rad50 DNA repair complex

Fabian Gut

aus

Albstadt, Deutschland

2023

Erklärung

Diese Dissertation wurde im Sinne von § 7 der Promotionsordnung vom 28. November 2011 von Herrn Prof. Dr. Karl-Peter Hopfner betreut.

Eidesstattliche Versicherung

Diese Dissertation wurde eigenständig und ohne unerlaubte Hilfe erarbeitet.

München, 03.04.2023

_____

Fabian Gut

Dissertation eingereicht am:	03.04.2023
1. Gutachter:	Prof. Dr. Karl-Peter Hopfner
2. Gutachter:	Prof. Dr. Roland Beckmann
Mündliche Prüfung am:	21.06.2023

This thesis has been prepared from April 2019 to April 2023 in the laboratory of Prof. Dr. Karl-Peter Hopfner at the Gene Center of the Ludwig-Maximilians-Universität München, Germany.

This is a cumulative thesis based on the following publications:

Lisa Käshammer*, Jan-Hinnerk Saathoff*, Katja Lammens, Fabian Gut, Joseph Bartho, Aaron Alt, Brigitte Kessler, Karl-Peter Hopfner, Mechanism of DNA End Sensing and Processing by the Mre11-Rad50 Complex, *Molecular Cell*, Volume 76, 07 November 2019, Pages 382-394
https://doi.org/10.1016/j.molcel.2019.07.035

Fabian Gut*, Lisa Käshammer*, Katja Lammens, Joseph D. Bartho, Anna-Maria Boggusch, Erik van de Logt, Brigitte Kessler, Karl-Peter Hopfner, Structural mechanism of endonucleolytic processing of blocked DNA ends and hairpins by Mre11-Rad50, *Molecular Cell*, Volume 82, 19 August 2022, Pages 3513-3522
https://doi.org/10.1016/j.molcel.2022.07.019

* These authors contributed equally

Table of Contents

Abstract ..... **III**

1 Introduction **1**

1.1 DNA damage and its role in aging and disease 1

1.1.1 DNA damage by exogenous sources 3

1.1.2 DNA damage by endogenous sources 4

1.1.3 DNA double-strand breaks promoted by exo- and endogenous factors 5

1.1.4 Programmed endogenous DNA double-strand breaks 7

1.1.4.1 V(D)J recombination and immunoglobulin class switching 7

1.1.4.2 Spo11-dependent DSBs in meiotic recombination 8

1.2 DNA repair 9

1.2.1 NHEJ – Non-homologous end joining 11

1.2.2 HR – Homologous recombination 14

1.2.3 NHEJ or HR - Regulation and pathway choice in DSB repair 18

1.3 The MRN complex 20

1.3.1 Mre11 21

1.3.2 Rad50 23

1.3.3 Nbs1 28

1.3.4 CtIP 29

1.3.5 The MRN complex in health and disease 31

1.3.5.1 MRN as a cell cycle checkpoint mediator in DNA damage signaling 31

1.3.5.2 MRN in telomere maintenance and dysfunction 32

1.3.5.3 MRNs functional role in innate immunity 33

1.4 The bacterial Mre11-Rad50 complex 34

1.5 Objectives 36

2 Publications 37

2.1 Mechanism of DNA End Sensing and Processing by the Mre11-Rad50 Complex .. 37

2.2 Structural mechanism of endonucleolytic processing of blocked DNA ends and hairpins by Mre11-Rad50 74

3 Discussion 103

3.1 From resting to cutting state – a unified nuclease mechanism for different DNA substrates 104

3.2 Reversed polarity of MR on free versus blocked DNA ends 111

3.3 Towards a structural model for the full MR reaction cycle 113

3.4 A model for the 3' endonucleolytic cleavage activity based on the existing 5' endonuclease structure 116

3.5 *Ec*MR as a model system for MRN - transferring the unified nuclease mechanism to eukaryotes 118

4 References 121

5 Acknowledgements 138

Abstract

In all living organisms, various types of DNA damage pose a constant risk to genomic DNA. Among these DNA damages, DNA double-strand breaks (DSBs) are one of the biggest threats to genomic integrity, as they can cause gross chromosomal aberrations and rearrangements, if left unrepaired. Two major DSB repair pathways exist: Non-homologous end joining (NHEJ) and homologous recombination (HR). NHEJ repairs DSBs in a template-free mechanism by direct ligation of two DNA ends. While this enables NHEJ to act throughout the cell cycle, it may also lead to insertions or deletions. HR on the other hand, is a more complex repair pathway, using sister chromatids as a template to allow error free DSB repair, but is restricted to S and G2 phases of the cell cycle.

A key player in the initial steps of DSB repair is the Mre11-Rad50-Nbs1 (MRN) complex. The heterotetrameric Mre11-Rad50 core complex (MR) is conserved throughout all domains of life and is formed by the Mre11 nuclease and the ATP-binding cassette (ABC)-type ATPase Rad50 with its long protruding coiled coils (CCs). Complemented by Nbs1 in eukaryotes, the MR(N) complex forms a versatile ATP-dependent nuclease complex able to sense and process DSB ends. Aside of its physiologically critical nuclease functions, the MRN complex acts in DSB end tethering, DNA damage response signaling and telomere maintenance.
After 25 years of research on MR(N), several key questions about the complex's functionality remain unanswered. Lacking a structural basis for MR(N)'s conserved exo- and endonuclease activities, it is not clear how the DNA can access the Mre11 nuclease active site to enable cleavage. Although it was shown that Rad50's CCs are essential for MR(N) functionality, the mechanistic role of the coiled coils is still not understood. Here, the recent resolution revolution in cryo-EM enabled us to structurally investigate the full-length *E. coli* MR (*Ec*MR) complex.

The first part of this thesis describes two structures of the *Ec*MR head complex: an ATPγS bound resting and an ADP (ATP post-hydrolysis) and DNA bound exonuclease active state. In the resting state, *Ec*MR matches former MR crystal structures, where the ATP-bound Rad50 NBDs block the Mre11 nuclease active sites, forming an autoinhibitory state. Moreover, the CCs point outwards from the globular head domain, suggesting a ring-shaped conformation. Upon DNA binding and ATP hydrolysis, the exonuclease state reveals large conformational rearrangements. The CCs move inwards to clamp around the DNA, transitioning from a ring- to rod-shape conformation that could be resolved up to 200 Å in distance. In addition, the Mre11 dimer relocates to the side of the Rad50 NBD, forming a DNA cutting channel. This positions

the free DNA end close to the nuclease active site of one Mre11 monomer to enable exonucleolytic cleavage.

The second part of this thesis presents the structures of *Ec*MR bound to a protein-blocked DNA end, as well as a DNA hairpin. These ATP-regulated endonuclease states of *Ec*MR match the previously described exonuclease state. Our data reveals that the formed DNA cutting channel can accommodate and process free DNA ends, hairpins and internal sites of DNA in a unified nuclease mechanism. The endonuclease state further shows that *Ec*MR bends internal DNA for endonucleolytic cleavage and is loaded onto blocked ends with Mre11 pointing away from the block. Taken together, this not only explains the distinct biochemistries of the exo- and endonuclease activities through the way Mre11-Rad50 interacts with diverse DNA ends, but also unifies MR's enigmatic nuclease diversity in a single structural framework.

1 Introduction

1.1 DNA damage and its role in aging and disease

DNA damage is a naturally occurring event in all living organisms, steadily threatening genomic integrity. Unlike most macro-molecules in the cell, being degraded and replaced when damaged, the genome acts as a persistent blueprint for all cellular functions. Thus, upon harmful events, it is dependent on rapid and precise DNA repair mechanisms[1,2].
Underlying causes for DNA damage include numerous endogenous and exogenous factors[1,2]. These share common chemical events and mechanisms such as hydrolysis, exposure to reactive oxygen species (ROS) or other reactive metabolites[3]. Spontaneous occurring DNA damage adds up to the order of 10^4-10^5 events per cell and day, leaving the maintenance of genomic stability as a continuous challenge. While endogenous sources of DNA damage, e.g. metabolic ROS, are known to appear continuously, exogenous factors such as chemicals or ionizing radiation can be more potent[2-4]. Examples of DNA damage include for instance ultraviolet light (UV)-induced photo-products, inter- and intrastrand crosslinks, bulky chemical adducts, abasic sites, base pairing mismatches or ROS-driven oxidative damage products such as 8-oxoguanine (8-oxoG) (Figure 1)[5]. Among these DNA threats, abasic sites formed by hydrolysis of the glycosidic bond between the DNA base and the sugar moiety is known to be the most abundant one[3,4]. Less frequent but potentially more toxic are single- or double-stranded breaks (SSBs and DSBs) in the phosphate deoxyribose backbone of the DNA. These DNA strand breaks can either arise as a consequence of exogenous influences, e.g. ionizing radiation, or intrinsic DNA metabolism, such as replication or decatenation of closed, circular chromosomes[2,3]. If left unrepaired, DSBs may lead to large chromosomal rearrangements or aneuploidy, threatening chromosomal stability and overall genomic integrity[5].

Accumulation of damage in cells, tissue and organs over time is associated with gradual functional decline and aging. However, the influence of DNA alterations on aging and the underlying molecular basis is still not fully understood[5,6]. The central role of intact genomic DNA is exemplified by a rapidly expanding family of rare inherited disorders called segmental progeroid syndromes. In these syndromes, genome maintenance is compromised with the phenotypic outcome of many accelerated features of aging[5,7]. Intriguingly, this also indicates functional genome maintenance as a potential anti-aging mechanism[5,7].

While DNA damage is the driving force behind both, cancer and aging, the consequences of the accumulated damage are essentially twofold. First, misrepair or replication of damaged DNA templates will lead to the consolidation of mutations. This will further result in permanent changes of the genetic code as well as chromosomal aberrations, ultimately increasing the risk of cancer formation. Second, DNA damage might dysregulate the process of DNA transcription or lead to replication arrest, resulting in cell death or cellular senescence, which is linked to aging[5].

To protect the cell from the effects of DNA damage, all organisms developed a series of robust repair mechanisms and signaling cascades. These help to sense the various types of DNA damage, halt the cell-cycle to prevent mutagenic consolidation and repair the genomic lesions that occur[2,5].

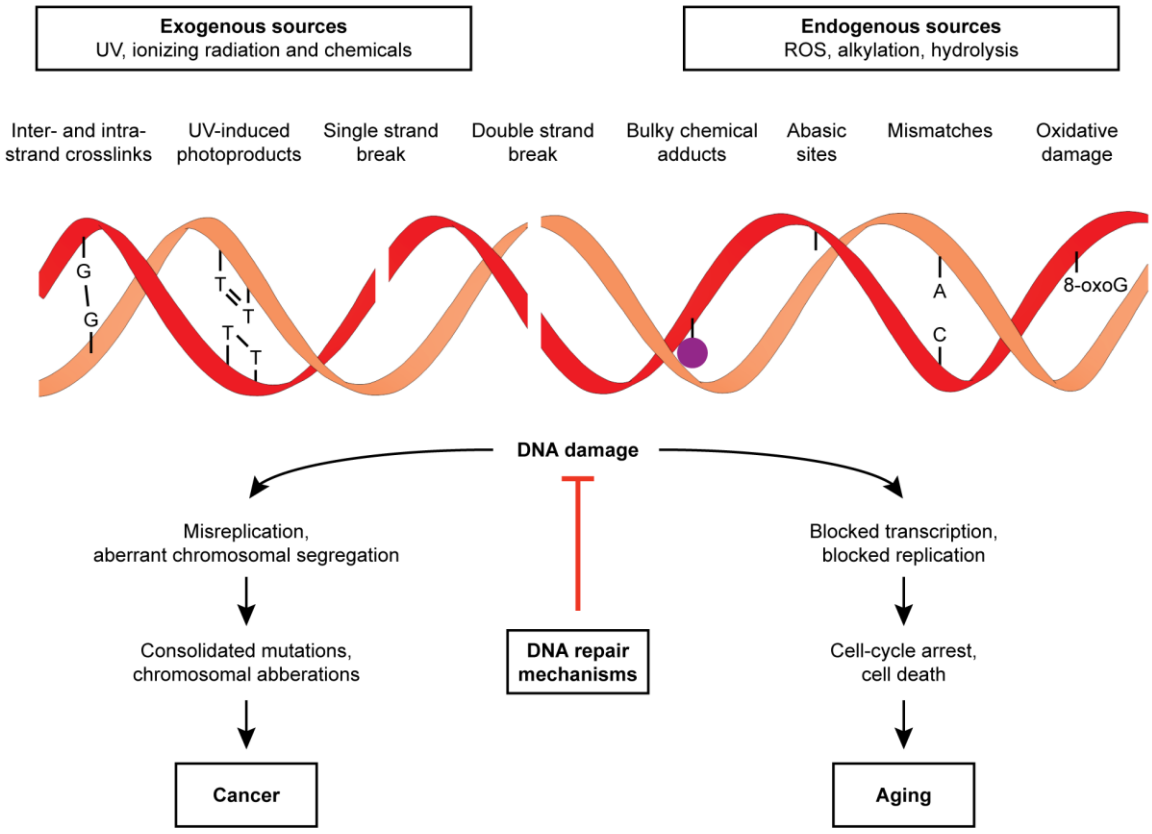

Figure 1: Examples of DNA damage sources, types and their impact on cancer and aging. The upper part shows different DNA damaging agents accounted to the two main groups of exo- and endogenous sources and the kinds of damage that can be inflicted on DNA. The lower section illustrates the twofold consequences of those various damage types on cancer development contrary to the process of aging, as well as the antagonistic effect of DNA repair mechanisms. Figure based on Hoeijmakers, 2009[5].

1.1.1 DNA damage by exogenous sources

Exogenous sources of DNA damage, also known as environmental DNA damaging factors, include ionizing radiation (IR), UV light, and a variety of chemical agents (Figure 1)[5]. Epidemiologic studies showed that exogenous factors are the pivotal cause in the development of about 75-80% of sporadic cancers[3,8,9]. These numbers are probably even underrated, considering the numerous currently unidentified exogenous DNA damaging factors likely playing a role in many cases of cancer[3].

One of the most prominent examples of exogenous sources of DNA damage is the exposure to high energy radiation, such as X-rays or γ radiation[10]. Those ionizing radiations damage the DNA in a twofold manner, either by direct or indirect effects, leading to single- or double-strand breaks and ROS formation. Direct DNA damage by IR results from absorption of the radiation energy by the DNA. This leads to ionization and thus alterations in nucleobases and sugar molecules[11]. Indirect damage on the other hand, manifests in cleavage of water molecules, generating highly reactive hydroxyl radicals[10,11]. Due to the water dominated nature of biological systems, ROS formed by water radiolysis are a major source for high energy radiation-induced indirect DNA damage[11]. The produced hydroxyl radicals have been found to induce the formation of e.g. DNA-protein crosslinks (DPCs). These DPCs are formed through a covalent linkage of nuclear proteins to the DNA. Furthermore, formation of DPCs is preferentially induced in actively transcribing or replicating regions of the genome[12-14].

Another example of an exogenous source of DNA damage is UV light. Upon exposure to UV radiation, e.g. from sunlight, cyclobutane pyrimidine dimers (CPDs) and 6-4 photoproducts are frequently formed DNA lesions. They are further classified among the UV-induced photo-products, covalently linking two adjacent pyrimidines[11].

A ubiquitous group of DNA damaging chemicals frequently found in the environment, although generally in low concentrations, are alkylating agents[15]. Alkylating agents are electrophilic compounds able to react with many sites in DNA, based on their affinity for nucleophilic centers as found in DNA bases[11]. In principle, alkylating reagents react with the extra-cyclic oxygen and ring nitrogen atoms of the nucleobase, generating a large variety of covalent alkyl-adducts with varying complexity[15,16]. Following up on those primary alkylation products, the damaged sites are also highly susceptible for consecutive damage by generation of abasic sites, strand breaks or inter-strand cross-links. In human, N-nitroso compounds (e.g. N-nitrosodimethyl-amine), e.g. found and formed in tobacco smoke, are known to be the major exogenous source of alkylation DNA damage[15,17].

Aside from direct DNA interaction and damage, some exogenous agents also promote genomic instability by direct interference with a specific repair pathway, rather than DNA itself. For example, it was shown that chronic exposure to environmental levels of cadmium inactivates the mismatch repair (MMR) pathway in yeast, both, *in vivo* and *in vitro*[18,19]. As MMR takes a

pivotal role in the maintenance of genome stability, interference with the latter is a great risk factor for the development of cancer. Hence, even moderate inhibition of the MMR pathway by Cadmium or other exogenous agents might harbor drastic implications for human health[19].

1.1.2 DNA damage by endogenous sources

Based on their concentrations and mutagenic potentials, exogenous factors of DNA damage are not sufficient to explain the full incidence of sporadic cancer cases, to date[3,20]. Hence, a comprehensive knowledge of endogenous DNA damage types and their prevalence, also in combination with exogenous factors, appears to be crucial to understand the process of carcinogenesis[3].
Endogenous DNA damage includes a variety of different factors, e.g. oxidative damage via ROS, alkylation, hydrolysis or hydrolytic deamination. Even though those types of DNA damage are produced by ordinary cellular processes, they are chemically very similar to the damages caused by some exogenous agents and their metabolites[3,10].

A major source of endogenous DNA damage occurs on the basis of ROS. ROS are generated as a natural byproduct of cellular processes such as cellular respiration. Here, the cytochrome oxidase of the respiratory chain metabolizes some oxygen only by a sequence of one electron reductions resulting in ROS molecules. Metabolism of approximately 10^{12} molecules of oxygen per human cell and day, results in 1% ROS production of this total metabolic turnover – a vast source of endogenous DNA damage[10,21]. In addition, cell injury, inflammation, phagocytosis or hydroxylation of steroids and drugs are further examples for sources of ROS generation[10,22,23]. The generated ROS species include not only hydroxyl radicals, which are assumed to be the predominant species, but also hydrogen peroxide, superoxide, as well as singlet oxygen. The damaging effects of the latter are numerous, ranging from SSBs and DSBs, to abasic sites after oxidative attack on the sugar moiety, or direct nucleotide modifications, such as 5-hydroxycytidine[10,24,25].
Another source of endogenous DNA damage are various classes of naturally occurring enzymes, e.g. topoisomerases. Topoisomerases are a class of enzymes, which release superhelical stress from DNA during replication and transcription. Furthermore, they aid recombinatorial processes such as meiotic recombination through generation of single- and double-strand breaks[26]. TOP1, for example, introduces single-strand nicks to initiate DNA relaxation. During this DNA cleavage event, a covalent phosphodiester bond is formed between the conserved catalytic tyrosine and the 3'-phosphate DNA residue at the break site[27-29]. Stabilization of this cleavage complex, by e.g. topoisomerase poisoning, is detrimental to cells due to disrupted DNA uncoiling, increased strand breaks, incomplete DNA replication and

unstable RNA transcripts. This knowledge is nowadays also exploited for cancer treatment using novel TOP1 inhibitors based on the initially discovered agent camptothecin[29-31].

Aside of topoisomerases, polymerases are another class of enzymes, which may contribute to endogenous DNA damage. Polymerases may introduce insertions or deletions, when the replication machinery encounters repetitive DNA sequences, causing polymerase slippage[32]. Several of the 15 known mammalian DNA polymerases adopt important roles in base excision repair (BER) and nucleotide excision repair (NER). Here, they fill in the gaps left by the removal of damaged bases and nucleotides[33]. In case of unrepaired DNA lesions, some of those polymerases are specialized on a process called translesion DNA synthesis (TLS). Thereby, the polymerases are able to insert a nucleotide opposite to a DNA lesion and bypass the damaged site as part of a DNA damage tolerance mechanism[33]. However, this process also leads to the accumulation of point mutations and hence carries a high mutagenic risk[33,34], particularly in cancer tissue exhibiting elevated DNA lesion rates compared to normal tissues[35]. On the other hand, a deficiency of one of those TLS polymerases, e.g. Pol η in xeroderma pigmentosum variant XP-V, predisposes humans to cancer[33,36]. Pol η normally bypasses TT-cyclobutane pyrimidine dimers (CPDs) and correctly inserts Adenosine deoxynucleotides, upon DNA damage by UV radiation[37]. However, in XP-V patients, mutations in the *POLH* gene leave the enzyme dysfunctional[38,39]. This results in DSBs due to replication fork stalling and collapse at sites of UV-induced DNA damage and ultimately in a greatly increased risk of sunlight-induced carcinomas[40].

1.1.3 DNA double-strand breaks promoted by exo- and endogenous factors

DSBs are one of the least occurring but most toxic DNA lesions, requiring repair to ensure chromosomal integrity[41]. Studies estimated breakage rates of ~50 break sites per cell and cell cycle for vertebrate cells, derived from experiments in chicken DT40 cells[42,43]. In comparison, spontaneously occurring DNA damage by exo- and endogenous factors, such as oxidative damage to DNA bases, adds up to the order of 10^4-10^5 events per cell and day[5]. This illustrates the low abundance of DSB events in comparison to other DNA lesions[5,41]. High doses of IR, for example, normally create DNA SSBs but can also give rise to DSBs, if two nicks are present within one turn of the DNA double helix. Moreover, usage of topoisomerase inhibitors, such as camptothecin or etoposide in cancer treatment, will lead to the formation of DNA single- and double-strand breaks, respectively[41,44]. But even without exogenous stress factors, the cell cycle and in particular the process of genome replication, leaves DNA vulnerable to damage, promoting genomic instability if unrepaired[41]. Many of those endogenous hazards are prone to lead to replication fork stalling, e.g. due to altered DNA or chromatin structures. This may then give rise to DSBs due to replication fork regression and formation of a Holliday junction (HJ)

"chicken foot" intermediate, which is cleaved by HJ resolvases, leading to a fork collapse. The collapsed replication fork reflects a one-ended DNA double-strand break, able to initiate homologous recombination by strand invasion and bypass potential DNA lesions to restart replication[41,45] (Figure 2).

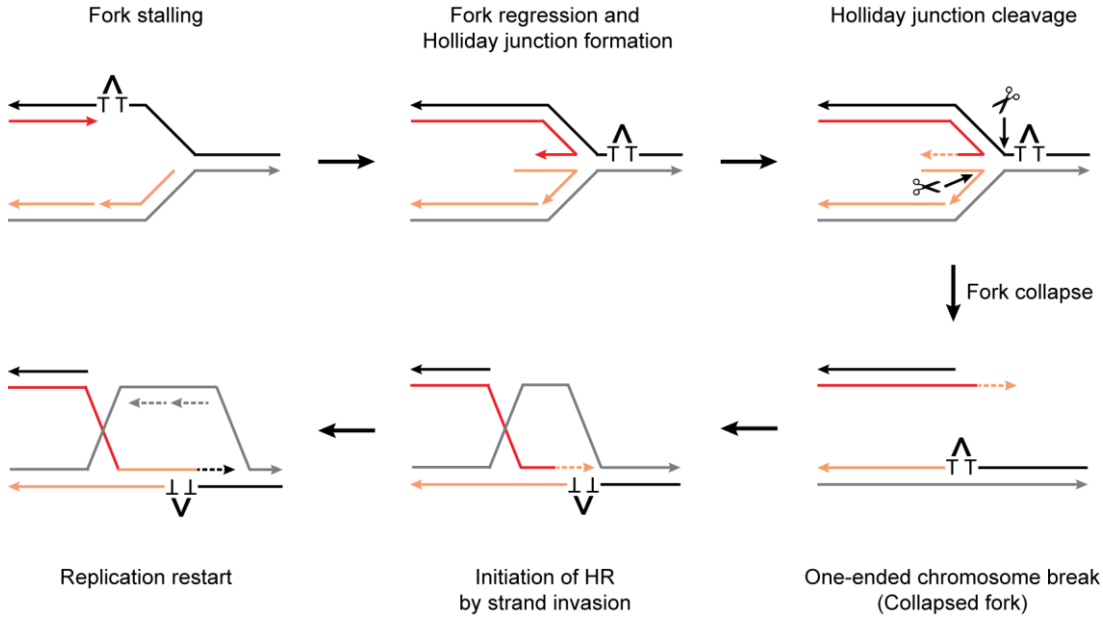

Figure 2: Example of replication fork stalling and restart due to a DNA lesion. In this schematic illustration, DNA replication stalled at an UV-induced thymidine dimer (TT). The stalled replication fork may now undergo regression, initially forming a holiday junction (HJ) "chicken foot" intermediate by pairing of the newly synthesized strands. HJ resolvases, which are endonucleases, are now cleaving this HJ generating a collapsed fork. This collapsed fork is effectively a one-ended chromosome or double-strand break, able to subsequently initiate homologous recombination (HR) by strand-invasion to bypass the DNA lesion and restart replication. Dashed lines illustrate newly synthesized DNA in the same color as the parental strand. Arrowheads indicate the 3' ends of the DNA strand. Figure based on Mehta and Haber, 2014[41].

Despite their threatening nature and the resulting gross chromosomal aberrations, if left unrepaired, DSBs are central to a couple of cellular processes. These processes, involved in immunity and meiosis, utilize DSBs as a recombinatorial force in a controlled and regulated framework[46].

1.1.4 Programmed endogenous DNA double-strand breaks

Even though, DSBs are the most toxic DNA lesions given their oncogenic potential, programmed DSBs (prDSBs) are essential to a number of biological processes. Such prDSBs are e.g. generated during V(D)J recombination, immunoglobulin class switching or meiotic recombination. As defects in these processes may lead to sterility, aneuploidy or severe immune deficiency, efficient control mechanisms co-evolved to avoid the deleterious consequences of uncontrolled or misrepaired prDSBs[46].

1.1.4.1 V(D)J recombination and immunoglobulin class switching

In V(D)J recombination, exons encoding for the variable domains of T cell receptors and B cell immunoglobulins are varied and assembled prior to expression. A “cut and paste” transposition mechanism physically links previously shuffled variable (V), diversity (D), and joining (J) segments in a combinatorial somatic rearrangement process[46,47]. The initiating prDSBs for this mechanism are generated by the lymphoid-specific enzymes RAG1 and RAG2 (recombination-activating genes 1 and 2) forming the RAG endonuclease[47]. To ensure site-specificity, RAG1 and 2 are only acting on V(D)J segment flanking recombination signal sequences (RSSs). Here, endonucleolytic DNA cleavage by RAG occurs by a nick-hairpin mechanism. Using 3'-OH ends exposed by initial single-strand nicking, the reaction yields a pair of blunt, 5'-phosphorylated signal ends and a pair of covalently sealed hairpin-terminated coding ends[48,49]. Due to the limitation of V(D)J recombination to the G0/G1 phase of the cell cycle, resulting prDSBs are predominantly repaired by NHEJ (see also 1.2.1 NHEJ – Non-homologous end joining)[46,50]. The NHEJ mediated repair results in two types of joined products. First, a due to the blunt-ends precisely formed signal joint. Second, a coding joint often accompanied by small nucleotide insertions or deletions. The latter is due to the required hairpin-rescission prior to ligation, but may even increase the gained sequence variability[49]. Overall, this guarantees a mere infinite bandwidth of antigenic recognition specificities by the adaptive immune systems B and T lymphocytes[46]. Yet, the inability to perform V(D)J recombination, either by non-functional prDSB introduction or insufficient repair, leads to B- and T cell maturation arrest and finally to severe combined immune deficiency (SCID) syndromes in human and mice[51].

Another mechanism related to the B lymphocyte mediated immune response is the immunoglobulin (Ig) class switch recombination (CSR). B lymphocytes use this gene rearrangement process to change the isotype of the Ig heavy chain constant region from IgM (μ), to IgG (γ), IgA (α) or IgE (ε). Roughly speaking, class switching from IgM to a different Ig class occurs as an intrachromosomal DNA deletion between preceding repetitive switch regions (S-region). This then results in replacement of the IgM constant region with a downstream one (γ, α or ε)[52,53]. At the molecular level, activation-induced deaminase (AID), a

B cell and ssDNA specific enzyme[54], catalyzes the conversion of cytosine nucleobases to uracil by a deamination reaction at transcribed regions[55]. This deamination can either be recognized as a base damage or as a U:G mismatch, which generally would be processed by BER or MMR pathways, respectively. However, repair of AID-generated uracils was shown to be highly mutagenic in B lymphocytes leading to DSBs during CSR, even though the exact mechanism for this error-prone outcome still remains elusive[52,56]. Once the DSBs are formed between the S-regions, the generated ends will be processed and ligated by the NHEJ repair pathway[57].

1.1.4.2 Spo11-dependent DSBs in meiotic recombination

Meiosis is the fundamental process for sexual reproduction, due to its ability to generate haploid cells containing a single copy of each chromosome. During meiotic prophase of sexually reproducing organisms, hundreds of prDSBs are generated along the chromosomes which need to be repaired in the subsequent process. DSB formation and repair is pivotal for meiotic recombination of DNA segments between homologous chromatids, generating genetic diversity. However, due to the numerous prDSBs, meiotic recombination may also harbor a serious threat for the genomic integrity and stability, if malfunctions occur[46,58].

The mechanism of meiosis, and meiotic recombination in particular, is evolutionary conserved. Initiation of this process was early on found to be connected to DSB formation by the dimeric topoisomerase-like protein Spo11, which cleaves both DNA strands creating a DSB site [59]. Extrapolation of the structure of the closely related Topoisomerase VIA enzyme helped to understand this cleavage mechanism in greater detail[60]. The dimeric Spo11 contains two metal binding sites which are positioned in close proximity to the scissile bonds on either strand of the DNA duplex. A catalytic tyrosine residue in the active site of each monomer can now interact with the pre-positioned metal binding pocket of the mutual monomer[61]. Thereby, two hybrid active sites are formed on both DNA strands of the duplex, enabling DSB formation by a transesterification reaction[59,61]. The newly created 5' DNA ends remain covalently bound to the catalytic tyrosine residues in each of the active sites of the Spo11 monomers. Due to the dimeric nature of Spo11, this cleavage mechanism further results in a spatial tethering of the newly generated DSB ends[62]. To enable DSB repair by HR, the covalent Spo11 adducts need to be removed, but to date the underlying mechanism is not fully understood. Different studies, mainly performed in yeast, suggest that Spo11 is removed by asymmetric endonucleolytic incisions of the attached 5' ended DNA strand by the Meiotic recombination 11 homolog A (Mre11) nuclease[63,64].

1.2 DNA repair

To cope with the constant challenge of environmental and metabolic sources of DNA damage, several DNA repair pathways have evolved. Upon accumulation of DNA damage, deficiencies in these repair mechanisms may lead to genomic instability, apoptosis or senescence on a cellular level. These cellular effects in turn are the basis for drastic functional consequences including embryonic lethality, rapid aging, a variety of medical syndromes or the development of cancer. Hence, efficient recognition and repair of DNA damage through coordinated checkpoints and repair pathways is crucial for cells and organisms[65]. Figure 3 summarizes the main DNA repair pathways and examples for their corresponding types of DNA damage.

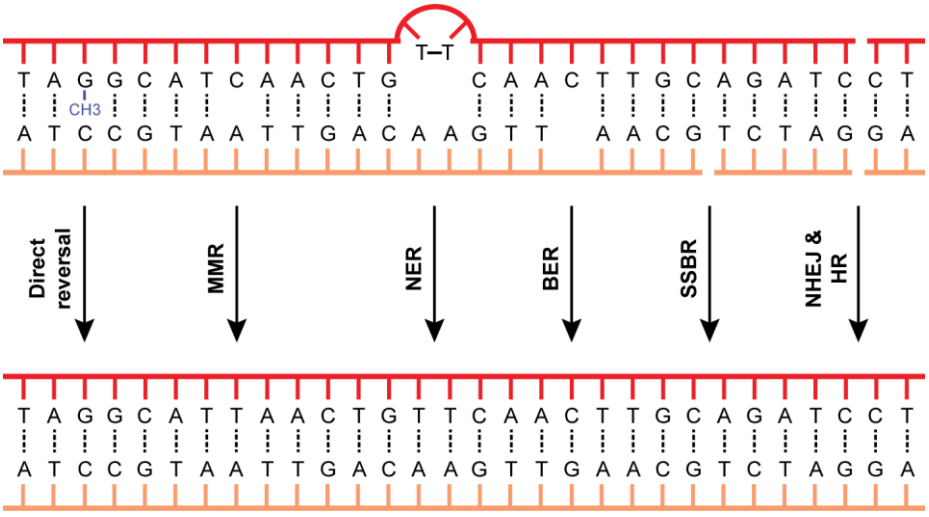

Figure 3: DNA damage repair pathways. Several DNA repair pathways exist to deal with a vast number of different DNA lesions from which some are illustrated here. The existing DNA repair pathways include: direct reversal of DNA lesions, mismatch repair (MMR), nucleotide excision repair (NER), base excision repair (BER), single-strand break repair (SSBR), non-homologous end joining (NHEJ) and homologous recombination (HR). Figure based on Hakem, 2008[65].

Comparably small DNA lesions, such as alkylations of nucleobases, can be repaired by a single step direct reversal pathway. One example would be the reversal of O^6-methylguanine, e.g. generated upon exposure to N-nitroso compounds such as N-nitroso-N-methylurea. In mammals, the enzyme O^6-methylguanine-DNA methyltransferase (MGMT) executes single-step repair by transfer of the methyl group to an inherent, specific cysteine residue[65,66].

Base-base mismatches can be caused by DNA polymerase errors, defective proof-reading functions or extrahelical insertion/deletion loops (IDLs) due to slippery microsatellite repeats (e.g. $[A]_n$ or $[CA]_n$). If present, they are main targets of the mismatch repair system (MMR). As MMR is a complex, but evolutionary conserved pathway, large parts of our understanding of the mammalian mechanism come from studies of the *E. coli* MMR proteins MutS, MutL and

MutH. In brief, post-replicative MMR recognizes and degrades the mismatched section of the newly synthesized DNA strand and corrects them with the help of DNA polymerases[67]. Intriguingly, it is essential for successful mismatch repair to only recognize and target the newly synthesized strand, which contains the error – a requirement not met in alternative repair pathways such as BER or NER[68].

The majority of endogenously derived and nucleobase-focused DNA damage, e.g. alkylations, oxidations or deaminations and depurinations, are the target of BER. DNA glycosylases take over the initial step of damaged DNA base recognition. Here, they share the mechanistic feature of turning the damaged base out of the DNA helix into a substrate-specific binding pocket. By cleavage of the N-glycosyl bond an abasic site is generated, that is subsequently excised[69]. In short patch BER, Pol β removes the remaining sugar by its lyase activity, further enabling it to fill the gap, which is then sealed by ligase 1 or ligase IIIα/XRCC1. If, however, the sugar removal is impaired, a long patch alternative is initiated. Here, the damage containing strand is displaced and removed by flap structure-specific endonuclease 1 (FEN1), enabling re-synthesis by different replicative polymerases such as Pol λ[69,70].

Nucleotide excision repair (NER) acts on the clearance of bulky DNA lesions, such as UV-induced CPDs (see also 1.1.1 DNA damage by Exogenous Sources) using a multifaceted "cut and patch" reaction[11,71]. In the early NER stages, there are two main sub-pathways: Global genome NER (GG-NER) and transcription-coupled NER (TC-NER) – both involved in lesion detection and initiation of latter uniform steps of NER. GG-NER examines the genome for nucleotide alterations which are associated with DNA helical distortions, while TC-NER focuses on selective repair of transcription-blocking lesions due to RNA Pol II stalling. Upon damage detection, the latter is verified in a mechanism dependent on the transcription factor IIH (TFIIH) complex. TFIIH's intrinsic helicase activity extends the ssDNA region around the lesion until a point of no return is reached. At this point, a 22-30 nucleotide ssDNA stretch containing the DNA lesion is bilaterally excised and correctly reconstituted with the help of DNA polymerases and ligases[71].

The vast majority of SSBs are repaired by a global single-strand break repair (SSBR) pathway, including the main four steps of SSB detection, end processing, gap filling re-synthesis and ligation. Poly-(ADP-ribose) polymerase (PARP) superfamily proteins, e.g. PARP1, take a central position in the recognition and signalling phases of SSBR via their poly-(ADP-ribose) modifications on themselves and many other factors. As most DNA SSB termini are chemically altered, they need to be cleared by processing of various nuclease active enzymes, e.g. AP endonuclease 1 (APE1) which is also involved in BER. The restored termini can then be subject to the finalizing steps of gap filling and ligation, mediated by DNA polymerases and ligases[72].

For the repair of the less abundant but in comparison to other DNA lesions more toxic DSBs, two main repair pathways – NHEJ and HR – have evolved, which are further described below.

1.2.1 NHEJ – Non-homologous end joining

In non-dividing haploid or diploid organisms in G0/G1-phase, NHEJ is the predominant DSB repair pathway, due to the lack of a homology donor for homology-directed repair. By definition, NHEJ repairs DSBs by direct re-ligation of the DNA ends – an error-prone mechanism. First identified and mainly studied in eukaryotic systems, NHEJ consists of the following three main steps: limited nucleolytic resection to clear damaged and altered DNA ends, refilling DNA synthesis to create blunt ends and joint ligation to restore genomic integrity[50].

In canonical NHEJ (c-NHEJ), the double-ring shaped, heterodimeric complex Ku70/80 is one of the first proteins to arrive at the DSB site. Here, Ku70/80 binds to the DNA ends with high affinity, protecting them from uncontrolled nuclease attacks[50,73]. The Ku:DNA complex formed on both DNA ends of the break site can be seen as a central docking node for other NHEJ core proteins, e.g. nucleases, polymerases and ligases[50]. After formation of the Ku:DNA complex, the PIKK-kinase family member DNA-dependent protein kinase catalytic subunit (DNA-PKcs) is recruited to form the DNA-PK holoenzyme[74]. Recent structural studies used cryo-electron microscopy (cryo-EM) to reveal a structural model for the NHEJ supercomplex. The latter is formed by assembly of the additional NHEJ core proteins X-ray repair cross-complementing protein 4 (XRCC4), XRCC4-like factor (XLF) and ligase IV around the central DNA-PK holoenzyme[75,76] (Figure 4). This also provides a structural basis for DNA end tethering and formation of a DNA-PK dimer, either mediated via a conserved C-terminal helix of Ku80 or a bridging element formed by XLF, XRCC4 and ligase IV[74-77]. Initiation of further conformational changes in the NHEJ supercomplex leads to the transition from a long-range (LR) to a short-range (SR) synaptic complex, where DNA-PKcs gets removed after autophosphorylation. The short-range synaptic complex, bringing the broken DNA ends into closer proximity, ultimately provides the structural and mechanistical basis for sequential DNA end ligation by both ligase IV subunits (Figure 4)[76].

The discussed c-NHEJ pathway may be relatively straight forward for free DNA ends, but DSBs bear many structural difficulties. For example, non-complementary and different length overhangs or chemical modifications can arise, that require additional excision and resynthesis[78]. Although limited in capacity, NHEJ includes several other factors to clean these ends and modify minor alterations. The nuclease Artemis is one of the most prominent examples of NHEJ co-factors, combining DNA-PKcs autophosphorylation regulated endo- and exonuclease activities to clean altered DNA ends[78,79]. Another example would be polymerases of the Pol X family, e.g. mammalian Pol μ, which is able to catalyze template-independent synthesis to restore a nucleotide gap of a broken strand, despite a disrupted template strand[78,80].

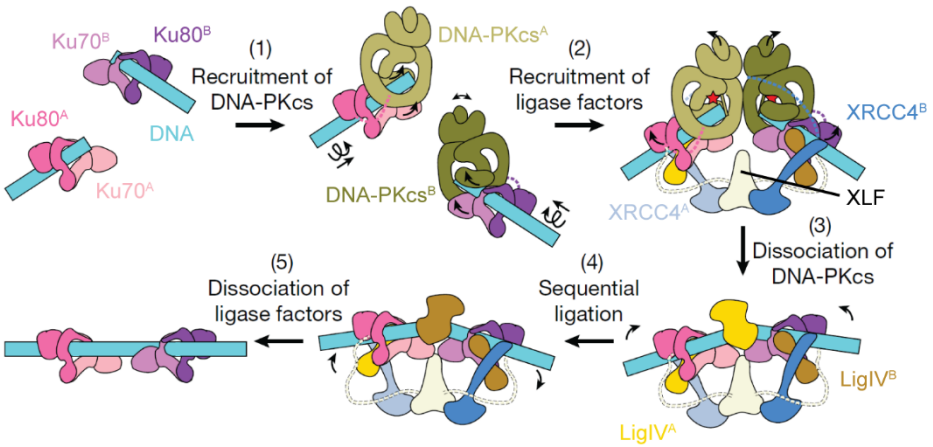

Figure 4: Schematic structure and transition of the DNA repair NHEJ supercomplex. The DNA DSB ends are detected by Ku70/80 and DNA-PKcs is recruited to form the DNA-PK holoenzyme (1). LigIV, XRCC4 and XLF act as a scaffold in a 2:2:1 ratio to arrange the two DNA-PK holoenzymes in a LR complex (2). Autophosphorylation leads to the dissociation of DNA-PKcs (3), enabling sequential sealing of one DNA nick after another, coupled to conformational transition from a LR to a SR complex (4). Dissociation of the ligase factors after successful DNA repair by joint ligation (5). Figure modified from Chen, 2021[76].

Aside from c-NHEJ, alternative NHEJ (alt-NHEJ), also known as microhomology-mediated end joining (MMEJ) serves as an optional substitute pathway, if c-NHEJ or HR fail (Figure 5)[78]. The MRN-CtIP (see also 1.3 The MRN complex) complex gets recruited and activated by PARP1 to resect the DNA ends and expose short homology domains (2-20 nucleotides) to bridge the DNA ends and guide repair[81,82]. Furthermore, more recent studies suggested PARP1 to recognize and compete with Ku70/80 for DNA ends[83,84]. Potential, non-homologous 3' tails are cleaved by the ERCC1/XPF (ERCC1, Excision repair cross-complementing 1; XPF, Xeroderma Pigmentosum type F) heterodimeric nuclease. The resulting single-stranded gaps are then filled by PARP1-mediated recruitment of DNA Polymerase θ[82], before DNA end ligation by the ligase III/XRCC1 complex[81,82].
In prDSB repair during immunoglobulin CSR, alt-NHEJ was also shown to act as a less efficient c-NHEJ substitute, e.g. in the rare case where Ku70 and DNA ligase IV are absent[85]. Moreover, beyond the role of acting as a backup pathway, alt-NHEJ may also adopt a physiological role in mitochondrial DNA maintenance since DNA ligase III is the main mitochondrial DNA ligase[81].

With the discovery of bacterial Ku-like proteins and several ATP-dependent ligases in 2001, it first became apparent that NHEJ may also be present in bacteria[86,87]. Studies on bacterial NHEJ have shown that a reduced two-component pathway exists, based on a homodimeric Ku homolog and an ATP-dependent Ligase called LigD, substituted by LigC in case of absence[86,88]. Intriguingly, LigD adopts a multifunctional role, occurring as a multidomain protein with an N-terminal polymerase, a central 3' to 5' exonuclease and a C-terminal ligase domain[86,89]. Hence,

LigD not only mediates DSB ligation in bacterial NHEJ, but also DNA end processing and resynthesis, which enables independent end joining of a wide range of DNA breaks[86].

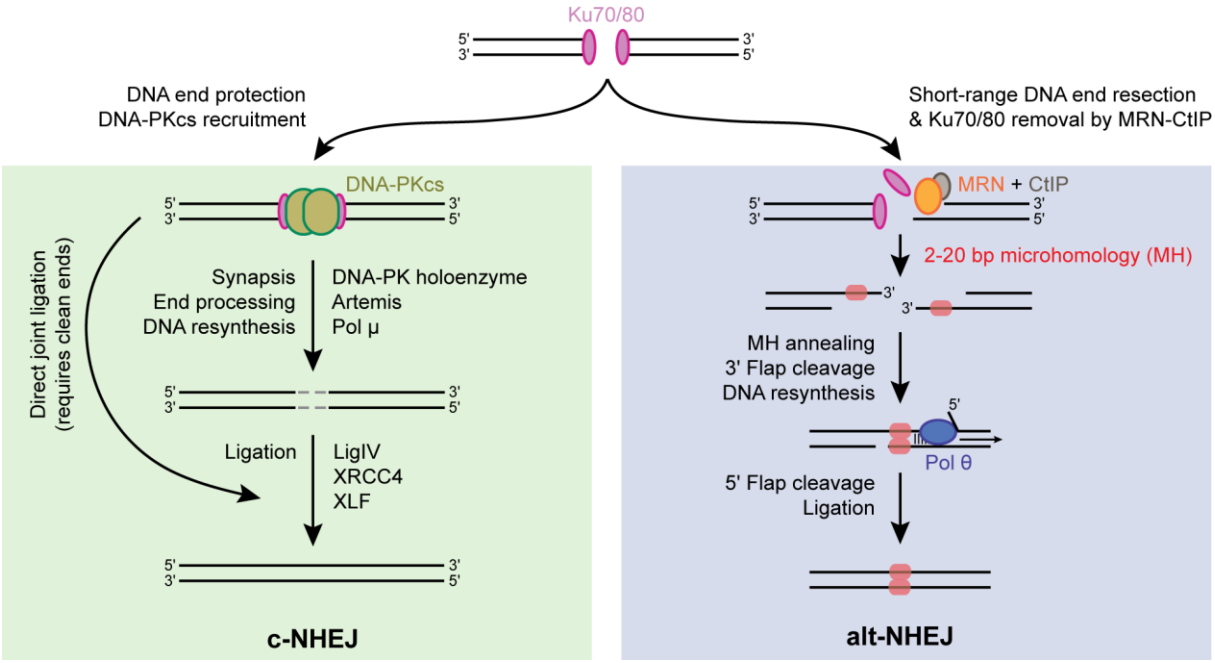

Figure 5: Non-homologous end joining (NHEJ) DSB repair pathways in mammalian cells. Both, canonical and alternative NHEJ pathways start with DSB end detection and protection by Ku70/80. In c-NHEJ this is followed by recruitment of DNA-PKcs, to form the end-tethering DNA-PK holoenzyme, and different other cofactors, e.g. the nuclease Artemis to process chemically altered DNA ends. XLF, XRCC4 and DNA ligase IV are recruited to form the NHEJ supercomplex and mediate the final ligation step (see also Figure 4). In alt-NHEJ the MRN-CtIP complex gets recruited and activated by PARP1 to resect the DNA ends and expose short homology domains to bridge the DNA ends. Eventually, non-homologous 3' tails are cleaved by ERCC1/XPF nucleases. The resulting single-stranded gaps are then filled by PARP1-mediated recruitment of DNA Polymerase θ, before DNA end ligation by the ligase III/XRCC1 complex. Eventual 5' flaps generated by the Pol θ activity can be cleaved by the nuclease FEN1, prior to ligation[81,82]. Figure based on Trenner and Sartori, 2019[82].

1.2.2 HR – Homologous recombination

Homologous recombination (HR) plays a pivotal role as template-based DSB repair pathway in somatic cells and during meiosis of germline cells[90]. HR's need for a DNA template or a sister chromatid restricts it to the S and G2 phases of the mitotic cell cycle. However, this also offers the advantage of complete and accurate restoration of genetic information lost during DSB formation or initial DNA end processing. In general, canonical HR combines steps of initial DSB recognition and end processing with long-range resection to generate 3' ssDNA overhangs that can invade the template DNA for homology search, enabling subsequent DNA resynthesis and repair[82,90,91].

In eukaryotic HR, DSB recognition, initial end processing and downstream repair pathway signalling are initiated by binding of the MRN (Mre11; Rad50; Nijmegen breakage syndrome protein 1 (Nbs1), Xrs2 in yeast – denoted MRX) complex to the DSB ends[91,92]. Upon DNA binding, MRN generates short 3' overhangs by ATP-dependent 5' single-strand endonucleolytic cleavage. This is strictly dependent on the additional eukaryotic cofactor CtBP-interacting protein (CtIP; Ctp1 in fission yeast; Sae2 in budding yeast)[93] and further followed by 3' to 5' exonuclease resection from the nick towards the DSB end[92,94]. Several biochemical and single-molecule studies have demonstrated that human MRN-CtIP and its yeast homologs can actively remove Ku70/80 from DSB ends (Figure 6)[95-99]. Thus, while mainly counteracting c-NHEJ repair initiation and promoting HR[92], MRN mediated short-range resection may also give rise to microhomology domains, which can lead to DNA end tethering and initiate alt-NHEJ repair (see also 1.2.1 NHEJ – Non-Homologous End Joining; Figure 5)[81,82].
In canonical HR the nicks introduced by MRN, as well as the following clean, short 3' overhangs, serve as an entry point for the downstream long-range resection. The latter attenuates additional nicking by MRN-CtIP and is mediated by either Exonuclease 1 (Exo1)[100] or the nuclease DNA2 (DNA replication helicase/nuclease 2) in complex with the Bloom's syndrome helicase (BLM; Sgs1 in yeast)[92,94,101]. Extensive long-range resection and generation of 3' ssDNA tails by Exo1 or BLM/DNA2 is accompanied by replication protein A (RPA) single-strand coating (Figure 6). The ubiquitous, heterotrimeric RPA is a key player in both, coordination of long-range resection and high affinity binding to ssDNA to prevent degradation[82,91]. Furthermore, RPA activates the Ataxia Telangiectasia and Rad3 related (ATR) central signalling kinase to promote replication checkpoint arrest and stabilize replication forks[102,103]. Using the protected 3' ssDNA overhang, the central steps of HR can be initiated – strand exchange and homology search. Main catalyst of the DNA strand exchange reaction is the ATP-dependent recombinase Rad51 that needs to replace RPA on ssDNA, forming helical nucleoprotein filaments[91]. While RPA was found to prevent and negatively regulate Rad51 loading and filament formation on DNA[104], it stimulates the Rad51 strand exchange reaction[105]. Yet, RPA is not the sole interacting protein involved in the process of Rad51 filament formation

and strand exchange. Breast cancer 2 (BRCA2), for example, forms a complex with BRCA1/BARD1 (BRCA1-associated RING domain protein 1) and PALB2 (Partner and localizer of BRCA2), which mediates delivery of Rad51 monomers to RPA coated ssDNA to enable strand invasion and homology search (Figure 6)[82,91]. BRCA2 not only enhances Rad51 binding to ssDNA but also stabilizes the filament. This is mainly based on direct interaction of the BRCA2 C-terminal BRC repeats with Rad51, resulting in inhibition of Rad51's ATPase activity and thus promoting filament stabilization[91,106]. The Rad51 filament probes the template DNA by destabilization and opening of the dsDNA helix. In a resulting base-flipping mechanism, the DNA is sampled for sequence homology and once found, a meta-stable synaptic complex is formed[90,107,108]. The synaptic complex generates a 3' end primer-template junction - an intermediate known as displacement loop (D-loop) - building the basis for DNA synthesis. The D-loop can now be extended by DNA synthesis executed by an interplay of Replication factor C subunit 1-5 (RFC1-5), Proliferating-cell nuclear antigen (PCNA) and DNA Pol δ (Figure 6)[90].

This template-dependent extension of the invading strand is then either followed by "synthesis-dependent strand annealing" (SDSA), resulting in a non-crossover repair product or a second end annealing event where a double Holliday Junction (HJ) is formed (Figure 6)[82,90]. The latter annealing event has been shown to be catalysed by Rad52 in yeast[109,110]. SDSA has the advantage that the extended D-loop can be unwound, followed by annealing of the newly synthesized homology regions between the two ends to achieve DSB repair. This, in combination with the favoured use of sister over homologous chromosomes for HR in somatic cells[111], further limits the risk of a potential loss of heterozygosity due to crossover events[82,90]. Double HJ's on the other hand, are migrated in both directions during DNA synthesis. They can be resolved by decatenation, forming non-crossover repair products or by nucleolytic resolution, resulting in either a non-crossover or a crossover product between the repaired and the template DNA (Figure 6)[82,90,109]. Dissolution by decatenation is catalysed by the BLM-TopIIIα-RMI 1/2 (BTR) complex in humans[112]. Nucleolytic resolution leads to non-crossover products, if it occurs asymmetrically by MUS81-EME1 or SLX1-SLX4[113,114]. On the other hand, symmetrical GEN1 mediated resolution results in formation of crossover products[115,116].

Aside from this canonical HR pathway, long-range resection tracts may also promote another non-canonical pathway called single-strand annealing (SSA). This happens particularly in the absence of important downstream HR components, e.g. Rad51. Here, in contrast to alt-NHEJ, more extensive DNA resection is needed to enable Rad52 mediated annealing of >20 bp homologous tandem repeat sequences and downstream repair of the broken ends. As the annealing sequences only flank the DSB site, the SSA repair pathway causes loss of genetic information between the repeats. Due to the previous extensive end resection the deletions are also expanded compared to the alt-NHEJ repair pathway[82,117].

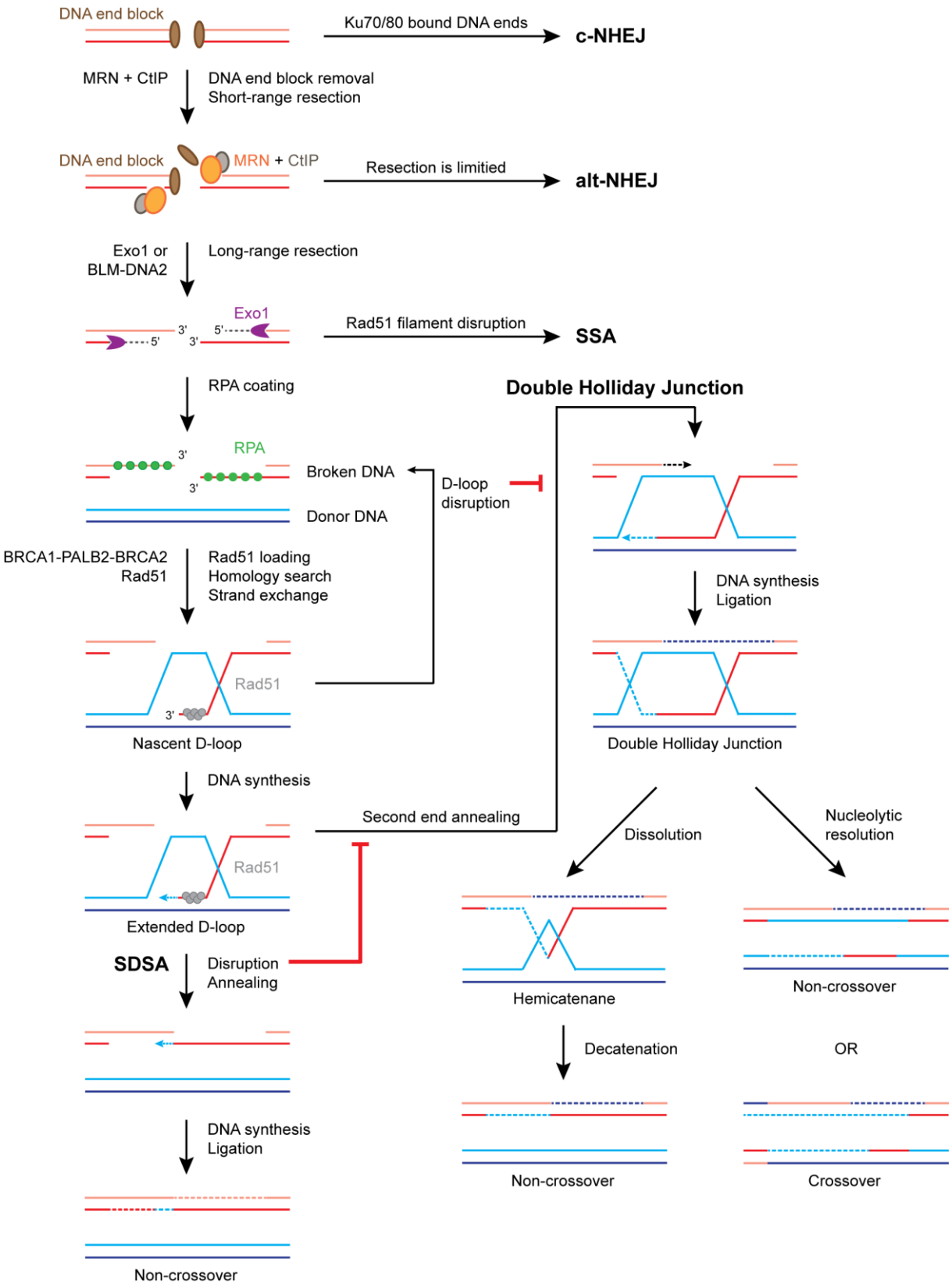

Figure 6: Eukaryotic Homologous recombination (HR) DSB repair pathways. HR repair is initiated via DSB detection by MRN. MRN in complex with CtIP cleans DSB ends from protein blocks and other obstructions and generates the essential long 3' ssDNA overhang, counteracting c-NHEJ. The 3' overhangs

are protected by RPA binding and serve for Rad51 mediated homology search to form a D-loop, which allows template-dependent DNA synthesis and repair. If end resection is limited or the Rad51 filament gets disrupted, alternative repair pathways as alt-NHEJ or SSA can take over. In the SDSA pathway, the D-loop gets disrupted after a short DNA replication cycle, enabling re-annealing to the homologous original strand followed by DNA resynthesis and ligation. This leads to a non-crossover repair product. Alternatively, via second end annealing, a double Holliday Junction can be formed. This structure either needs to be resolved by dissolution or nucleolytic resolution, leading to non-crossover or crossover repair products. Figure based on Wright et al., 2018, and Trenner and Sartori, 2019[82,90].

As homologous recombination is a mechanistically conserved pathway throughout all domains of life, it is also found in prokaryotes. Intriguingly, aside of acting as a classical DNA repair and maintenance pathway, bacterial HR was also found to be central to DNA integration following horizontal gene transfer[86]. In most bacteria, recombinatorial repair is divided into two tightly connected pathways, the RecBCD and RecF pathways. Studies in *E. coli* showed that the RecBCD pathway is crucial for the repair of DSBs, while the RecF pathway focuses on the repair of single-stranded DNA gaps (SSGs)[118]. The bacterial heterotrimeric and dsDNA end specific complex RecBCD combines DNA helicase and recombination hotspot χ regulated ssDNA nuclease activities to ensure the initial DSB end processing and resection. RecBCD further reveals the specialty of a bidirectional helicase motor activity, mediated by the ATP-driven subunits RecB (3' to 5' helicase and nuclease activity) and RecD (5' to 3' helicase). At first, RecBCD unwinds and rapidly degrades both DNA strands. Upon encounter with a χ hotspot, RecBCD's nuclease activity is shifted towards the 5' and away from the 3' strand, creating and preserving the recombinatorial important 3' overhang – a process initiated by binding of the χ sequence to RecC, followed by a cascade of structural rearrangements[118]. Furthermore, the χ -activated RecBCD mediates RecA (bacterial homolog of eukaryotic Rad51) loading and thus displacement of the protective RPA homolog single-strand binding protein (SSB). In the RecF pathway, this process is substituted by the joint 3' to 5' helicase RecQ and the 5' to 3' ssDNA nuclease RecJ[118]. Moreover, there are several members of the SMC-family (structural maintenance of chromosomes) playing important roles, not only in the bacterial world of homologous recombination repair. One complex is formed by the Mre11-Rad50 bacterial homologs SbcD and SbcC, which were found to be essential for the processing and repair of hairpin-capped DSB ends (see also 1.4 The bacterial Mre11-Rad50 complex)[118-120].
The formed RecA filaments mediate sequence homology search and DNA strand exchange. They share the main features described for the eukaryotic Rad51 and rather differ in details. Similar to eukaryotic BRCA1/BARD1-PALB2-BRCA2, the so-called RecFOR complex acts as an additional mediator, catalysing RecA filament formation on SSB-coated ssDNA[118,121]. More recent single-molecule data on *E. coli* RecA revealed new mechanistic insights into the RecA-mediated homology search. Depending on the dsDNA coiled structure and the RecA filament length, homologous DNA is sampled via weak contact formation of the RecA filament DNA - a mechanism described as the intersegmental contact sampling model. Upon encounter of homologous DNA stable contacts are formed, which will trigger binding of additional parts

of the filament to find a homologous sequence[109,122]. Finally, as described for eukaryotes, the strand-invasion process will lead to formation of a heteroduplex, the so-called D-loop[90,118].
In case of a double HJ formation, prokaryotic branch migration is catalysed by RuvAB, where RuvA recognizes and RuvB pushes the HJ forward via its motor activity[123-125]. Dissolution of dHJ in bacteria is mediated by the RecQ helicase and the type IA topoisomerase Topo III, resulting in strictly non-crossover repair products as in eukaryotes[126]. Alternatively, nucleolytic resolution is mediated by the endonuclease RuvC, either forming non-crossover or crossover repair products[118,127].

1.2.3 NHEJ or HR - Regulation and pathway choice in DSB repair

The choice between the main DSB repair pathways NHEJ and HR, as well as their regulation, is very versatile and complex. Primary influences on the choice between NHEJ and HR are the cell-cycle phase and the complexity of the break site. The cell-cycle influences pathway choice as NHEJ is active throughout the cell-cycle, but favored in G1 phase, while HR is restricted to S/G2 phases due to the requirement of an intact sister chromatid. Another major regulatory mechanism is again coupled to the cell cycle stage and associated protein phosphorylation patterns due to changing cyclin-dependent kinase (CDK) activities[128]. Phosphorylation of human CtIP at Thr847 or the *Saccharomyces cerevisiae* homolog Sae2 at Ser267 are important examples for CDK-mediated regulation, and hence cell cycle dependent signal transduction. In this case, phosphorylation triggers activation of the MRN-CtIP short-range resection machinery and thus drives DSB repair pathway choice towards HR[93,129]. This also further explains HR's restriction to only function in S and G2 phases of the cell cycle, where suitable CDK levels are available[128].
Varying complexity of DNA ends in form of chemical modifications or protein blocks might further influence pathway choice as NHEJ's ability to clean those ends is rather limited compared to HR[130]. During the last decades, a competitive model was drawn for pathway choice, mainly based on the initial NHEJ and HR factors – Ku70/80 and MRN-CtIP. Both factors are sensors of DSB ends and among the first ones to arrive at a break site. Hence, a first decisive crossroad would be the initiation of MRN-CtIP mediated (endo-)nucleolytic processing of DNA ends, as a first HR initiating and NHEJ counteracting step[131]. Consistent with biochemical observations made *in vitro*, this competition model suggests a race between Ku70/80 and MRN for DNA end binding to dictate the pathway choice[131-133]. Even though, MRN-CtIP end resection is also able to initiate template-free repair pathways, such as alt-NHEJ or SSA, it still promotes long-range resection dependent canonical HR in the majority of cases[131]. However, there were also several observations made in yeast and mammals opposing this competitive model, while favoring a sequential model as basis for DSB repair decisions. Contradicting the idea of a competition between NHEJ and HR factors, this new model suggests

that nearly all DSB ends are initially bound by generally faster associating NHEJ-promoting factors[83,131,134]. If however, NHEJ is unsuccessful, this will lead to association of MRN-CtIP, which resects and removes the DNA-PK holoenzyme from the DNA end to enable DSB repair by HR[96,131,135].

Furthermore, chromatin and associated histone post-translational modifications have an impact on DSB repair pathway choice and regulation. This is not least due to DSB-induced extensive changes on chromatin. On one hand, the central DNA damage response kinases Ataxia Telangiectasia Mutated (ATM), ATR and DNA-PKcs phosphorylate Ser139 of the DNA damage associated histone variant H2AX. Thereby, γ-H2AX chromatin domains are formed, able to recruit the adaptor protein MDC1 (Mediator of DNA damage checkpoint 1). MDC1 in turn, helps to drive different processes, e.g. HR between sister chromatids, also mediated by BRCA-1 recruitment, and ATM signal amplification. On the other hand, p53-binding protein 1 (53BP1), a key regulator of c-NHEJ, gets recruited to and binds monomethylated histones H2A and H4. There, it antagonizes the DNA resection functions of BRCA1 and thus shifts the poise towards c-NHEJ. As a consequence of this, chromatin and various associated histone modifications mediate different regulatory functions in a complex higher level fight for DSB repair pathway choice[92,128].

1.3 The MRN complex

Intensive research over the past 25 years, combining different insights from biochemistry, structural biology and related fields, has shaped our understanding of the MRN complex. MRN is sensing, binding to and actively processing DNA double-strand break ends as an integral part of the HR repair pathway, but is also involved in alt-NHEJ. Compared to mammalian cells, where MRN does not take part in c-NHEJ, budding yeast MRX adopts a special role, contributing to c-NHEJ through interactions with Ku70/80 and DNA LigIV[102,136]. The MRN complex consists of the Meiotic recombination 11 homolog 1 (Mre11) nuclease, the Radiation sensitivity 50 (Rad50) ATPase and the regulatory, eukaryote-specific factor Nijmegen breakage syndrome 1 (Nbs1; X-ray sensitive 2, Xrs2, in yeast, denoted MRX), also known as Nibrin[136,137]. The catalytic Mre11-Rad50 (MR) subcomplex exists as a hetero-tetrameric assembly of Mre11 and Rad50 dimers[137-139]. A recent cryo-EM study clearly showed a single Nbs1 bound to the *Chaetomium thermophilum* MR core complex as well as the sole human Mre11 dimer with Rad50 dissociated[139]. Hence, these structures reveal an evolutionary conserved 2:2:1 stoichiometry for the eukaryotic MRN/X complex (Figure 7)[139].

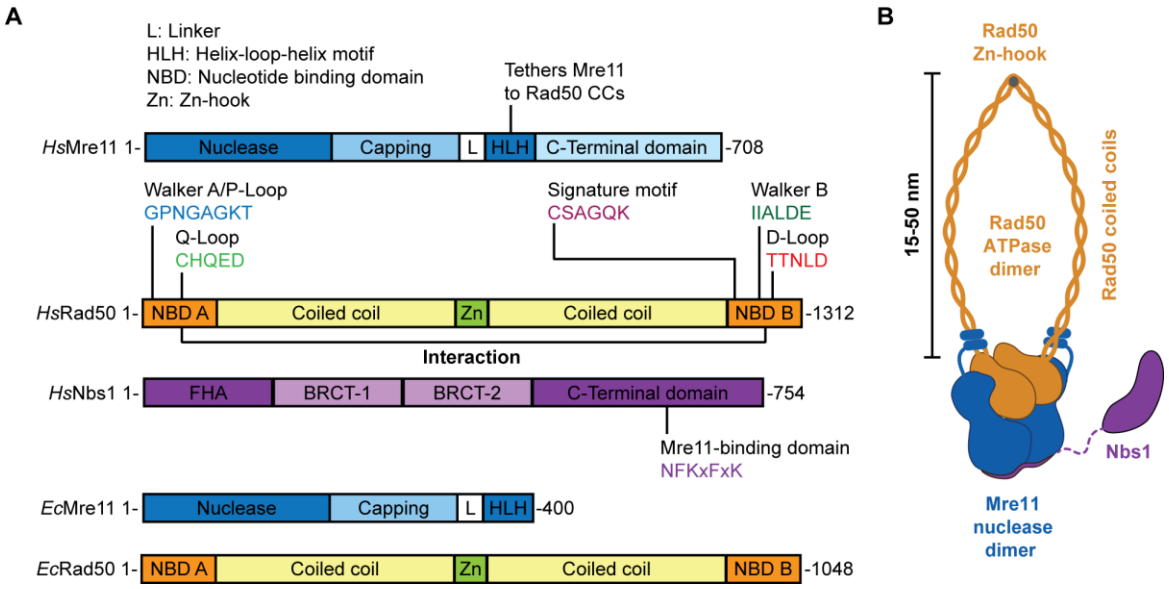

Figure 7: Domains and structural architecture of the MRN complex. (A) Illustration and comparison of the domains in human MRN and *Ec*MR (also known as SbcCD). (B) Model of the MR(N) complex with the globular head domain formed by Mre11 and the Rad50 NBDs, interacting with Nbs1 in eukaryotes, the characteristic long, antiparallel coiled coils and the apical Zn-hook dimerization motif.

Early electron microscopy (EM) and atomic force microscopy (AFM) studies already revealed that the MR(N/X) forms a globular DNA-binding head domain composed of the Mre11 dimer and the globular Rad50 ABC-type ATPase domains, with long protruding and flexible Rad50 coiled coils, joined at an apical Rad50 zinc hook dimerization domain (Figure 7)[140-144].

Intriguingly, MR is conserved throughout all domains of life, with homologs ranging from archaea and eubacteria, to phages and up to eukaryotes[119]. This further underlines MR's essential role as one of the first responders and interactors within a cell's complex DNA damage response and repair networks. MRN performs various tasks to orchestrate and regulate damage recognition, signalling and repair in response to at least four main types of genotoxic and cellular stress: DSBs, stalled replication forks, dysfunctional telomeres and viral invasion[137]. The following chapters will focus on the structural composition, enzymatic functions and cellular roles of the MRN complex and individual components – an overall intriguing, multifunctional molecular machine.

1.3.1 Mre11

Already 30 years ago, Mre11 was first identified and found to be involved in meiotic recombination by a mutational screen in *S. cerevisiae*[145]. Some years later, biochemical studies also identified Mre11 as an active DNA exo-/endonuclease involved in DSB repair, a feature conserved through all homologs of Mre11[120,146,147].
Mre11 can be seen as the core module of the MRN complex as it interacts with both, Rad50 and Nbs1[138]. With the first Mre11 crystal structure derived from the archaeon *Pyrococcus furiosus* it became clear that the Mre11 catalytic core consists of two-domains, embedded in an overall U-shaped dimer architecture (Figure 8)[140]. N-terminal, there is a calcineurin-like phosphoesterase domain, bearing the nuclease catalytic residues as well as a coordination site for two manganese ions, which are essential for nuclease activity. The structure further revealed an adjacent capping domain, involved in strengthening of DNA binding specificities[137,138,140].
In later studies, dimerization was shown to be mediated via a conserved hydrophobic four-helix bundle in the Mre11-Mre11 homodimeric interface[148,149]. The dimerization's functional importance was also shown in yeast, where mutations disrupting the dimer interface mimic a *mre11* knockout[148,150]. To date, several Mre11 crystal structures from homologs of all three domains of life[149-154], as well as a cryo-EM structure of human Mre11 wrapped by a single Nbs1[139] have been solved, showing a conserved overall dimer architecture. Thus, the two-domain and overall dimer architecture seem to be universally conserved features of Mre11, despite the low sequence conservation between species[138].
The described catalytic core of Mre11 is further added by a C-terminal flexible linker and a Rad50-binding domain (RBD), also known as helix-loop-helix (HLH) motif[149,153,155-157]. In eukaryotes, the Mre11 C-terminus comprises some additional domains. First, two additional DNA binding sites – one following the capping domain, which is essential for DSB repair functions and another one positioned at the very C-terminus of Mre11, shown to be critical for meiotic DSB formation and spore viability in yeast[158,159]. The latter was also recently shown to bind DNA in an ATP-independent fashion[139]. Second, a glycine/arginine-rich (GAR) motif that

was shown to be crucial for MRN localization at DNA damage foci *in vivo*, as well as DNA binding and nuclease activity *in vitro*[138,160].

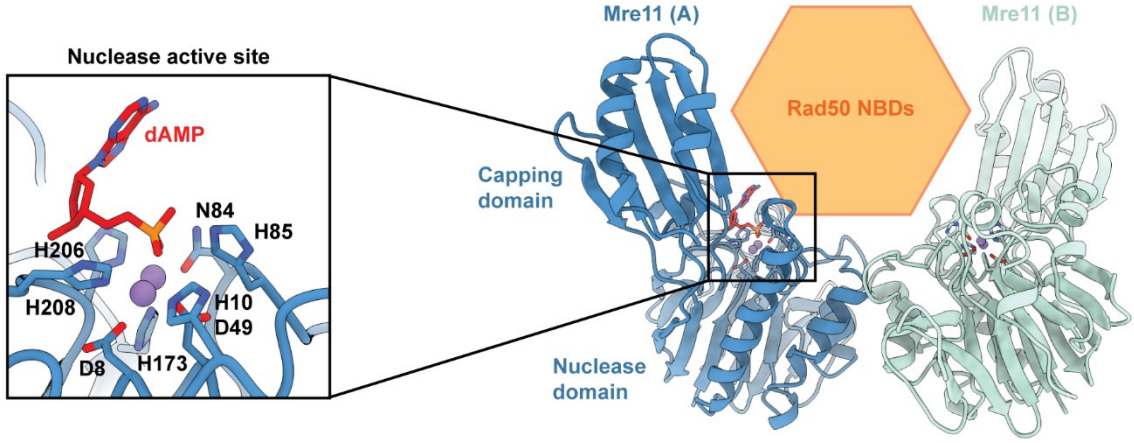

Figure 8: Crystal structure of the Mre11 nuclease dimer. Crystal structure of the *P. furiosus* Mre11 dimer nuclease and capping domains in complex with Mn^{2+} ions (purple) and dAMP (PDB: 1II7) in front view. A closeup on one nuclease active site highlights the metal-coordinating residues, essential for Mre11's nuclease activity. An orange hexagon shows the Rad50 NBD dimer binding site in the assembled MR complex.

As described earlier, the Mre11 dimer forms an evolutionary highly conserved complex with the Rad50 ATPase, supplemented by Nbs1/Xrs2 in eukaryotes[136,137]. In the context of a MR(N) complex, Mre11 shows Mn^{2+}-dependent 3' to 5' dsDNA exonuclease, ssDNA endonuclease and hairpin opening activities in the presence of ATP[146,161-163]. It is further important to note that the MR(N) endonuclease activity requires and is further promoted by Rad50 ATP hydrolysis[93,164,165].

Aside of the apo Mre11 dimer, several DNA bound crystal structures were solved during the last two decades, suggesting that the Mre11 catalytic core can bind DNA in at least two different conformations[148,166]. However, they all show the DNA end structures positioned too far away from either nuclease active site, leaving the mechanism for DNA end processing by Mre11 unresolved[148,166]. The study by *Sung et al.* further suggested that DNA binding would induce a rotation of the Mre11 dimer, resulting in melting of the DNA end to enable its relocation to the Mre11 active site for nucleolytic cleavage[166]. Yet, it is still not clear how this would be possible in a MR(N) complex with Mre11s DNA binding and nuclease active sites blocked by the Rad50 NBDs (Figure 8)[139,153,167].

In HR mediated DSB processing and repair, initial resection should occur in 5' to 3' direction to produce the observed 3' ssDNA overhangs. This stands in contrast to the discussed 3' to 5' exonuclease activity of the MRN complex – a contrariety better known as the "nuclease polarity paradox"[92,136]. An explanation to this paradox can yet be given by the additional MRN cofactor and phosphorylation regulated protein CtIP, also known as Sae2 in yeast MRX. CtIP actively

transforms MRN into a strand-specific endonuclease that preferentially nicks the 5' terminated strand[93,168,169]. Experiments in yeast support this model, showing that the close homologs of human CtIP, Ctp1 (*S. pombe*) and Sae2 (*S. cerevisiae*), are required for the removal of proteins covalently linked to the 5' end of DSBs[63,170,171]. This initial endonucleolytic incision is followed by subsequent 3' to 5' exonuclease resection towards the DSB end to create a 3' ssDNA overhang[93,97,100,172-174]. The described "cutting-from-a-flank" mechanism enables the MRN complex to bypass bound obstacles at the DNA end and initiate DSB repair by HR, even at non-canonical DNA ends[92]. Analysing various DNA end blocks *in vitro*, the endonucleolytic nicking sites were found to be ~15-45 nt away from the DNA end, depending on the nature of the block[92,93,97,135]. However, *in vivo* experiments reported cleavage positions up to ~300-400 nt from the DSB end[92,100]. Due to the diverse nature of DSB ends, including protein adducts such as the meiotic recombination factor Spo11[59,63], DNA hairpins[175] or clean breaks, the MRN-CtIP complex needs to be very versatile to resolve a variety of non-canonical structures[92]. In some cases, where the protein-DNA adduct is not restricted to the 5' end, limited but coordinated cleavage of the opposite 3' strand may further aid to release e.g. a protein adduct and generate a clean 3' end, crucial for downstream HR steps[173].

1.3.2 Rad50

At its core, Rad50 consists of a bipartite nucleotide binding domain (NBD) with a N-terminal Walker A and a C-terminal Walker B motif, interspaced by a 600-900 amino acid long heptad repeat insertion. The N- and C-terminus fold back onto each other to form the globular NBD, also referred to as Rad50 catalytic domain (Rad50cd)[120,176]. NBDs of all Rad50 orthologs show sequence similarity with the class of ABC-type ATPases, thus implying a shared three-dimensional structure and catalytic mechanism[176,177]. Rad50 exhibits ATPase activity upon dimerization in an ATP-regulated manner, where two ATP molecules are sandwiched between the conserved Walker A, B and signature motifs of two opposing Rad50 NBDs (Figure 9 A)[149,156,176]. From the Rad50 head domain flexible antiparallel coiled-coils (CC) are protruding, formed by the heptad repeat insertion. At the apex of these long coiled-coils a second dimer interface, the Zinc hook (Zn-hook), is built by a pair of conserved C-x-x-C motifs forming interlocking hooks around a single Zn^{2+} ion[119,141]. The described architecture with the globular head domain and the long coiled coils closely resembles the Structural Maintenance of Chromosomes (SMC) family of proteins, which are mainly involved in chromatin condensation and chromosome cohesion[120].

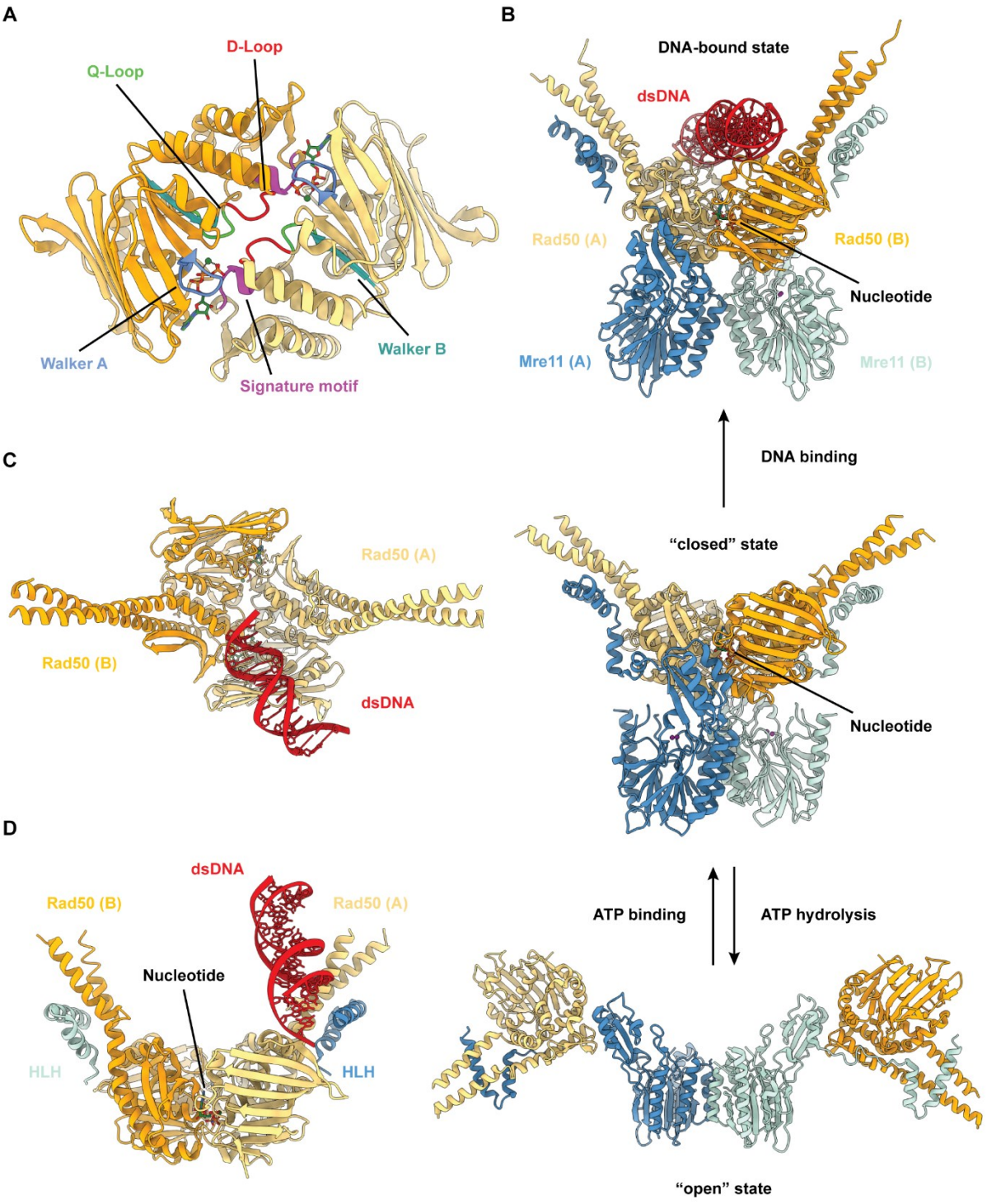

Figure 9: Crystal structures of the Rad50 NBDs bound to DNA substrates and the MR head transition. (A) Crystal structure of the *P. furiosus* Rad50 NBD bound to ATP (NBDs monomers in yellow/orange; PDB: 1F2U) in bottom view. Conserved ATPase motifs are highlighted in color and named consistent with Figure 7 for human Rad50. (B) Illustration of the MR head conformational transitions upon nucleotide binding from an "open" nucleotide free (*T. maritima*, PDB: 3QG5) to a central "closed" ATP-bound (*T. maritima*, PDB: 3THO) and a final closed, DNA-bound state (*M. jannaschii*, PDB: 5DNY). (C) Crystal structure of *C. thermophilum* Rad50 bound to ATPγS (green, sticks) and dsDNA (red), depicted in top view (PDB: 5DAC). (D) Crystal structure of *T. maritima* Rad50 bound to AMP-PNP (green, sticks), dsDNA (red) and peptides of the Mre11 HLH motif (light/dark blue; PDB: 4W9M) in front view.

Despite structural advances for the individual Mre11 and Rad50 subunits, the structural basis of the catalytic MR core complex remained elusive until the first crystal structure of the bacterial MR head domain was solved[102,149]. The structure revealed the tethering of the Mre11 C-terminal HLH motif to the Rad50 CC base, close to the globular ATPase head domain. The overall "open" conformation of this nucleotide-free state displays the Rad50 ATPase domains in a separated state, facing away from each other (Figure 9B)[149]. In contrast to that, ATP-bound structures of the MR complex revealed a "closed" conformation with Mre11 still bound, but the Rad50 ATPase dimer sandwiching two molecules of ATP and two Mg^{2+} between their NBD domains (Figure 9B)[167,178]. This nucleotide-dependent "open to closed" structural rearrangement was also captured by a more recent study, reporting notable conformational changes upon ATP binding and hydrolysis[179]. The nucleotide-state dependent conformational switching of Rad50, was further found to have an impact on MR's biological functions. While the ATP-bound closed conformation is suggested to promote, both, DNA end binding and tethering, the release of the ATP-state during hydrolysis would promote endonuclease activity and DNA end resection[164,179].

The ATP-dependent dimerization of Rad50 forming a closed state further leads to the formation of a DNA binding groove between the extending coiled coils[149,167,176,178]. This is also confirmed by crystal structures of *Thermotoga maritima* and *Chaetomium thermophilum* Rad50 NBDs[156,157] and by the MR head complex of *Methanococcus jannaschii* bound to dsDNA and ATP analogues (Figure 9B-D)[153]. As already visible by the ATP-bound but DNA-free state[167,178], the Mre11 nuclease active sites are occluded by the dimerized Rad50 NBDs sitting on top in the DNA-bound *M. jannaschii* structure (Figure 9B)[153]. Hence, in this conformation of the MR head complex, the DNA duplex can still not access the Mre11 active sites to enable nucleolytic cleavage[153]. So how does DNA access the Mre11 active site?

Structural analysis of the MR structures from *T. maritima* and *M. jannaschii* in concert with biochemical experiments support a model in which ATP hydrolysis induces an opening of the Rad50 NBDs that enables DNA to access the Mre11 active sites[149,153,179]. While the model derived from the *T. maritima* structure suggests a complete "closed to open" transition[149], the *M. jannaschii* model only proposes a partial opening of the Rad50 NBDs upon ATP hydrolysis[153]. Complete $Rad50^{NBD}$ disengagement would either enable the Mre11 active sites to directly access DNA in an open conformation[157,179] or via formation of a transient clamp around the DNA upon binding of new ATP[149]. In case of DNA processing in a closed state or upon mere partial $Rad50^{NBD}$ opening, ATP-hydrolysis induced DNA melting may enable the DNA to access the Mre11 active sites for nucleolytic cleavage[153,167]. However, as structural information of a DNA-bound nuclease active state is still lacking, the structural and mechanistic basis for the nuclease activities of the MR complex remain elusive.

Despite the necessity of ATP hydrolysis for endonucleolytic cleavage, it has been evident for many years that Rad50 is a slow ATPase and thus may occupy the closed ATP-bound state for

relatively long periods *in vivo*[102]. Biochemical studies showed that human and yeast MRN/X share the characteristic of a very slow ATPase with <0.1 ATP/min[164,165,180]. A recent study in *E. coli* further supported this slow ATPase activity, reporting a similar ATPase rate of ~0.48 ATP/min for the bacterial MR homolog SbcCD[165]. Furthermore, the ATPase rate of all three Rad50 homologs can be stimulated by dsDNA – 20-fold in human MRN, 10-fold in yeast MRX and 26-fold in *E. coli* SbcC[164,165,180]. In sum, this shows an evolutionary conserved, slow basal ATPase rate of Rad50, as well as the stimulatory effect of dsDNA binding on ATP hydrolysis[164,165,180]. Intriguingly, the slow ATPase rates could also act as a regulatory mechanism[102]. Especially in the human system for example, where Mre11 was shown to be capable of conducting 3' to 5' exonuclease activity independent of Rad50[102,146].

Another important structural and mechanistic part are the described long coiled coils, protruding from the globular Rad50 head with the apical Zn-hook dimerization domain (Figure 10A and B)[102]. Even though the mechanistic role of the CCs is still not clear, they have been proven to be essential for Rad50 function. This is connected to the fact that they physically tether the globular Rad50 head domain together[102]. Truncations and deletions of the CCs and the apical Zn-hook, respectively, result in abolished telomere maintenance and meiotic DSB formation, as well as severe defects in HR and, notably, NHEJ repair[102,181]. *In vitro* experiments showed that the CCs are important for ATM activation[182] and their removal directly impairs MRN's abilities to hydrolyze ATP, bind dsDNA and tether DNA ends[179,182]. Yet, it is important to note that shortening of the CCs by 243 amino acids, but retaining the Zn-hook, rescued homologous recombination functionality *in vivo*[102,181]. The Zn-hook was further shown to be crucial for the activation of ATM and ATR mediated DNA damage response pathways[183] and loss of its dimerizing interaction also impaired ATM activation[182]. While deletion of the Hook domain showed Rad50 deficiency in budding yeast *in vivo*, replacement with a ligand-inducible FKBP dimerization domain partially mitigated all phenotypes[184].

As already depicted by early EM imaging[141], AFM and time-resolved single molecule analysis also showed that the CCs are highly dynamic and flexible (Figure 10C)[143,144]. Different crystal structures of the apical Rad50 Zn-hook solved to date reveal open and closed, rod-shaped conformations, emphasizing the dynamic nature of the entire CCs (Figure 10B)[141,185,186]. Furthermore, the Zn-hook forming motifs were found to interact not only within a single MR complex, but also in an intercomplex fashion between two complexes. Spanning a long range of ~1,200 Å between complexes in eukaryotes, combined with the DNA binding characteristic of the globular head domain, the MR core complex was proposed to be involved in DNA end tethering[141-144]. These mechanistic features, seem to be further promoted by DNA binding of the globular head domain, which affects the dynamic nature of the CCs and brings them into a rod-shaped orientation, favoring intercomplex associations[102,144].

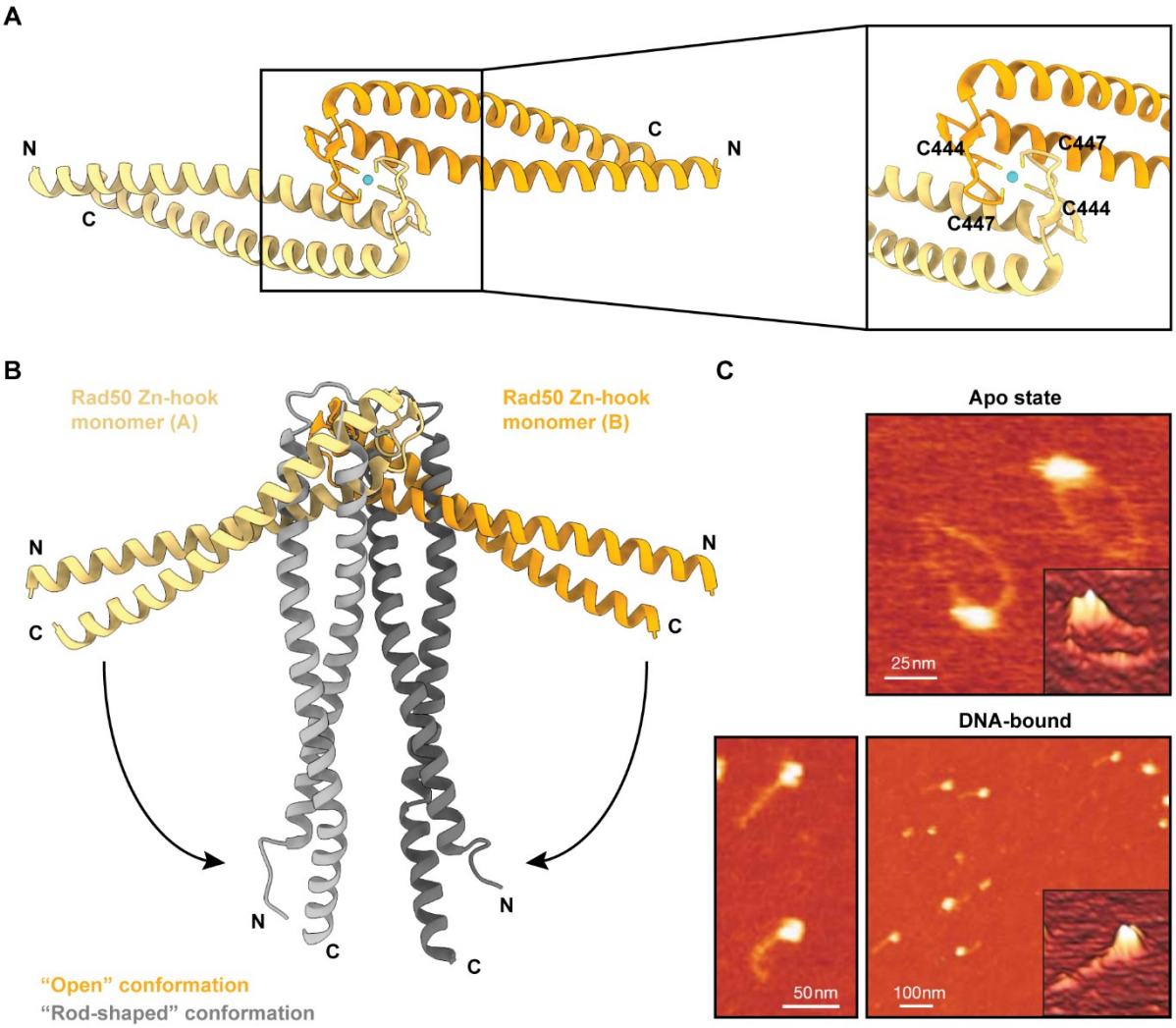

Figure 10: Conserved Rad50 Zn-hook architecture and open to rod-shaped conformational transition. (A) Top view on the crystal structure of the *P. furiosus* Rad50 Zn-hook dimer (monomers in yellow/orange, respectively; PDB: 1L8D) in open conformation. Zn^{2+} (cyan) coordinating cysteines are highlighted in a close-up. (B) Illustration of the Zn-hook "open" to "rod-shape" conformational transition, depicted by structural alignment of the open and rod-shaped *P. furiosus* crystal structures (open in yellow/orange, PDB: 1L8D; rod-shaped in light/dark grey, PDB: 6ZFF) on the coordinated Zn^{2+} ions. Figure based on Soh et al., 2021[186]. (C) AFM images of human MRN in apo and dsDNA-bound states in the presence of the ATP-analogue AMP-PNP. Comparison shows the high flexibility of the coiled-coils and the discussed CC shape changes, from ring to rod, upon DNA binding. Figure adopted from Moreno-Herrero et al., 2005[144].

Even though some AFM studies reported states of transiently opened Zn-hook domains to date[144,187], a recent high-speed AFM study only found complexes of human Rad50 with constantly engaged Zn-hooks, but transiently disconnecting head domains[188]. Additional experiments also showed that the human Rad50 Zn-hook is interchangeable with the structurally related SMC hinge domain of bacterial MukB (Condensin in human) and that this chimeric construct preserves DNA repair functions *in vivo*[188]. This is supported by another study, showing that *B. subtilis* can still grow normally upon exchange of the SMC hinge for the

Rad50 Zn-hook from *P. furiosus*[189]. Thus, it is proposed that the Zn-hook rather serves as a stable dimerization interface, similar to a SMC hinge, than as a transiently opening interface[188]. A recent cryo-EM study on eukaryotic *C. thermophilum* MRN bound to ATPγS reported the 60 nm long Rad50 CCs in a rod configuration without addition of DNA. Intriguingly, the CC apices of two MRN complexes were found to form intercomplex MRN-MRN assemblies via dimerization of their stably interacting Zn-hook domains. Spanning ~120 nm in total, the structure provides a new molecular basis for DNA tethering by MRN without a transient opening of the Zn-hook[139].
In sum, the above described emphasizes the importance of the Rad50 CCs and Zn-hook for a proper biological function of the MR(N) complex[102,181].

1.3.3 Nbs1

The third and eukaryote-specific component of the MRN complex, Nbs1 (Xrs2 in yeast), is a multifunctional protein, associated to the Mre11-Rad50 core complex. Binding of Nbs1 to the eukaryotic MR core complex was shown to be necessary for the re-localization of Mre11-Rad50 to the nucleus and foci formation upon DNA damage[190,191]. In human, Nbs1 is required to promote the MR endonuclease activity on blocked DNA ends and hairpins and adopts a regulatory role for the ATP hydrolysis by Rad50[161,164,173]. Moreover, Nbs1 promotes 3' to 5' exonuclease on blocked DNA ends, while restraining it on free ones[173].
Nbs1 has a structured N-terminus, containing an FHA (fork head associated) domain, followed by two consecutive BRCT (breast cancer associated 1 C-terminus) domains. A region that was found to be involved in binding of phosphorylated substrates and repair foci organization, e.g. the conserved CtIP/Ctp1 pS-x-pT motif (Figure 11A and B)[192-194]. The C-terminus of Nbs1, however, is generally unstructured without recognizable structural folds (Figure 11A). Still, it contains a number of highly conserved and functionally critical motifs, involved in DSB repair via MR and CtIP interactions, as well as ATM recruitment and activation[150,192,195,196].
Biochemical studies further showed that human Nbs1 serves as a main MRN interactor to CtIP, crucial for endonuclease activity[169,194]. Structural studies in yeast showed that this interaction is based on the Nbs1 N-terminal FHA domain binding phosphorylated Ctp1 (CtIP homolog in *S. pombe*; Figure 11B)[192,193].
Recent cryo-EM structures revealed that a single Nbs1 wraps asymmetrically around both Mre11 protomers, suggesting stabilization of the Mre11 dimer as one of its key functions[139]. The interaction is centred around Nbs1's evolutionary conserved KNFKxFxx motif binding to a negatively charged Mre11 binding pocket, which fits well to an earlier *S. pombe* crystal structure[139,150]. Intriguingly, the KNFKxFxx motif directions are reversed for human and *C. thermophilum* protein, highlighting quite significant species-specific adaptations (Figure 11C)[139].

Nbs1-mediated interaction and activation of ATM via an acidic patch and a FxY/F motif triggers the latter to phosphorylate a large number of proteins, including Nbs1 itself[197,198]. This in turn enables MRN to act downstream of ATM in the DNA damage response[192,193]. Nevertheless, the complete structural and mechanistic model for the interactions of Nbs1 with MR, ATM and CtIP, having a central impact on DSB signalling and repair, still remains elusive.

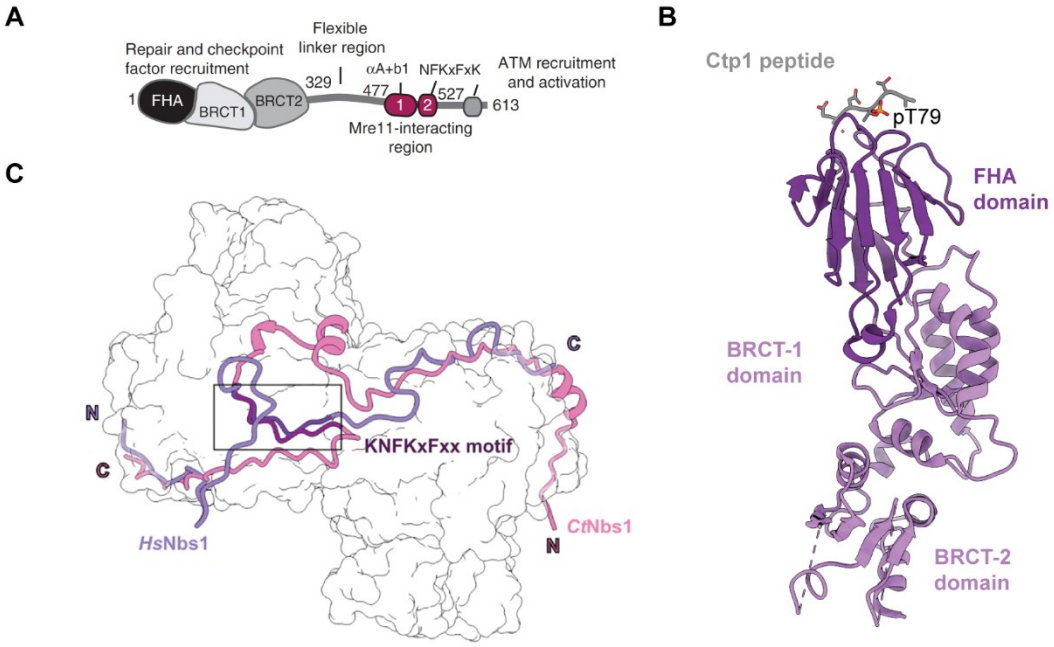

Figure 11: Structural features of Nbs1 and its interactions with the Mre11 nuclease dimer and CtIP/Ctp1. (A) Schematic illustration of the *S. pombe* Nbs1 domains with highlighted Mre11 and ATM (also known as Tel1 in *S. pombe*) interaction sites. Figure taken from Schiller et al., 2012[150]. (B) Crystal structure of the *S. pombe* Nbs1 structured N-terminal domain, composed of an FHA and two consecutive BRCT domains (purple/light purple; PDB: 3HUF). The FHA domain is bound to an interacting Ctp1 phosphopeptide, containing a conserved pS-x-pT motif. (C) Direct comparison of human (purple) and *C. thermophilum* (magenta) Nbs1 paths across the Mre11 dimer (contoured in white). Alignment of both MN complexes highlights the reversed orientation of Nbs1. Figure taken from Rotheneder et al., 2023[139].

1.3.4 CtIP

The eukaryotic CtBP1 interacting protein (CtIP, Ctp1 in fission yeast and Sae2 in budding yeast) combines several functional roles in DSB repair: acting as an important eukaryote-specific MRN cofactor for endonucleolytic cleavage of protein-blocked DSB ends, mediating DNA binding and bridging, as well as forming an interaction platform for important factors of the cell cycle regulatory network[199]. While Sae2 is essential for *S. cerevisiae* MRX endonuclease activity[168], human MRN is only stimulated by CtIP and also requires Nbs1[173].
A major structural characteristic shared among all CtIP homologs is their largely unstructured shape based on expanded low complexity sequence regions. An exception to this is the

structurally conserved and compact N-terminus that bridges CtIP oligomers by forming a tetrameric helical dimer of coiled coil dimers (THDD) domain, also referred to as tetrameric four-helix bundle[199-201] The THDD domain is flexibly adhered to a C-terminal DNA-binding regulatory hub, which e.g. influences MRN/X nuclease activities and thus also affects pathway choice in DSB repair[199-201]. A more recent AFM study also showed that, mediated by the THDD domain interactions, human CtIP forms an overall dumbbell-shaped architecture[202]. Mediated by the THDD domain, the C-terminal DNA binding regions are reported to be able to bridge two DNA molecules in trans (Figure 12)[202].

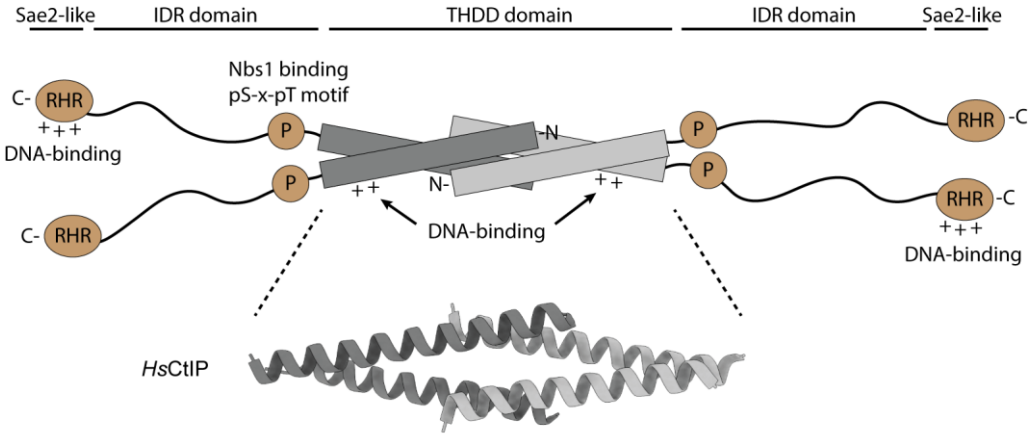

Figure 12: Overall architecture of human CtIP and crystal structure of the N-terminal THDD domain. The schematic highlights the overall dumbbell shape built by the three main domains of CtIP: The N-terminal THDD tetramerization domain, a flexible IDR domain with the phosphorylated pS-x-pT motif for Nbs1 interaction, and the C-terminal Sae2-like domain. A crystal structure of the human CtIP THDD domain (dark/light grey; PDB: 4D2H) shows the conserved tetramerization interface formed by interlocking α-helices. Figure based on Andres and Williams, 2017[199].

Many proteins, e.g. Nbs1[169,192] or BRCA1[194,203], interact with CtIP via short peptide motifs within the interspersed intrinsically disordered region (IDR)[199]. Yeast Ctp1 was shown to interact with the N-terminal FHA domain of *S. pombe* Nbs1 via a conserved, phosphorylated pS-x-pT tandem repeat domain in the IDR[192-194]. Disruption of this Ctp1-Nbs1 interface blocked the Nbs1-mediated recruitment of Ctp1 to DSBs *in vivo*[192] and thus suggests a direct tethering-related coordination mechanism (Figure 12)[192,193,199].

A second conserved region, called Sae2 like domain, is located at the very C-terminus. The Sae2-like domain was found to mediate DNA binding and bridging, regulation of MRN interactions and nuclease activity, as well as G2-M checkpoint activation[93,168,169,200]. It further contains a "RHR" ("RNR" is Sae2) and a Zn^{2+} binding "CxxC" (absent in Sae2) motif (Figure 12). While the RHR motif, based on studies in fission yeast, mediates the DNA binding and bridging activities of the Sae2 like domain[201], the precise function of the Zn^{2+} binding CxxC motif remains elusive[199]. However, despite the recent advances on CtIPs structural and

functional characteristics, a mechanistic basis, especially regarding its essential function for MRNs endonuclease activity, is still lacking.

1.3.5 The MRN complex in health and disease

The MRN complex is a key player acting on the maintenance of essential aspects of genome stability in all cells. This is not least also shown by its discussed conservation through all kingdoms of life[119,137]. Thus, mutations in any genes encoding for MRN components cause diseases, especially in humans. On one hand, studies of the International Cancer Genome Consortium showed that mutations in all three MRN component genes are found in >50 sporadic cancers. A fact that marks MRN, and in particular associated mutations in the individual components, as a risk factor for the development of various cancer types[137]. Germline mutations in Mre11, Nbs1 and Rad50 on the other hand, are known to cause ataxia telangiectasia (A-T)-like disorder (ATLD), Nijmegen breakage syndrome (NBS) and NBS-like disorder, respectively[137,204].
Both, ATLD and NBS cells show phenotypic similarities to those from patients with A-T, inherited by mutations of the central DDR kinase ATM[137,204]. The phenotypes include hypersensitivity to DSB inducing clastogens, defects in DDR cell-cycle checkpoint arrest and chromosomal fragility. However, clinical symptoms of ATLD and NBS patients are distinct[204]. While ATLD patients show neurodegeneration and ataxia like in A-T[205], NBS and NBS-like patients suffer from morphological abnormalities such as “bird-like” faces and microcephaly, accompanied by a high cancer predisposition[204,206].
The described syndromes and disorders connected to MRN mutations, highlight MRNs important cellular functions. Thus, the following chapters will take a closer look at MRNs multifaceted functional roles in cell cycle and DSB response signalling, telomere maintenance and dysfunction, as well as in viral defence and innate immunity mechanisms.

1.3.5.1 MRN as a cell cycle checkpoint mediator in DNA damage signaling

Using Cas9-directed DNA cleavage, it has been demonstrated that already the small number of 1-4 DSBs are sufficient to retard mammalian cell cycle progression due to DDR signaling activation[207]. Budding yeast cells are shown to be even more sensitive, with a single DSB being enough to provoke a robust G2/M arrest[208,209]. Thus, DDR signaling and cell-cycle checkpoint activation upon DSB events are based on sensitive mechanisms, essential for eukaryotic DSB repair and genome maintenance[209].

Aside of being a key modulator in DSB signaling and repair, the MRN complex acts as a cell cycle checkpoint mediator[209]. Upon DSB detection, the C-terminus of Nbs1/Xrs2[192,195,196,210]

but potentially also Mre11-Rad50 themselves[211], activate ATM/Tel1 as shown in mammals and yeast[209]. Furthermore, MRN/X also activates ATR/Mec1. This occurs indirectly after the MRN/X initiated end resection produced RPA coated 3' ssDNA overhangs, where ATR/Mec1 gets recruited to, by their specific binding partners ATRIP/Ddc2[209,212]. Hence, with progressing resection, checkpoint signaling shifts from ATM to ATR dependence[209,213].
Activation of ATM and ATR leads to a broad cellular signaling cascade by phosphorylation mediated activation of numerous substrates, of which many are kinases themselves, and the first substrates being the Checkpoint kinase 2 (CHK2) and 1 (CHK1), respectively[209]. Consequently, via phosphorylation of the central transcription factor p53 and multiple p53-independent mechanisms such as CDC25 phosphatase inhibition, CHK1 and 2 can induce the G2/M checkpoint. This enables the signaling cascade to enforce cell cycle arrest, cell senescence or apoptosis, if multiple or persistent DSBs accumulate[209].
As depicted by these regulatory examples, the MRN complex functions as a cell cycle checkpoint mediator in response to DSBs. Either through direct or indirect signal transduction, to and downstream of the central DDR signaling kinases ATM and ATR[209].

1.3.5.2 MRN in telomere maintenance and dysfunction

Eukaryotic linear chromosomes bear two threats to genomic stability as their ends not only structurally resemble a DSB, but also naturally get shortened with every replication cycle. The chromosome shortening is a side effect of the lagging strand replication, resulting in a short 3' overhang of the opposing strand. To avoid a DSB-related DNA damage response and potential associated loss of genetic information, telomeres protect the ends of eukaryotic linear chromosomes. Yet, reaching a critical telomere length, the cell will be sent to senescence or apoptosis, acting as a tumor suppressing mechanism that limits replication cycles to a finite number[137,214-216].
Telomeres generally consist of long non-coding duplex-DNA with a repetitive sequence of "-TTAGGG" in human[137,215,217]. An attached 3' ssDNA overhang, especially for the blunt-ended leading strand, is generated by Apollo and Exo1 nuclease resection[218]. In case of a functional telomere, MRN senses the newly synthesized ends and promotes resection[215,219]. The overhang not only prevents NHEJ-mediated generation of circular and unstable chromosomes[217], but also serves as a binding platform for the telomere protecting Shelterin complex[137]. The six protein Shelterin complex stabilizes and protects the telomeric ends via t-loop formation, a process where the 3' ssDNA is folded back onto the dsDNA region[137,215].
Eukaryotic MRN/X was shown to be associated with telomeres during S-phase in a DSB-independent fashion, and in case of higher eukaryotes directly interacts with the Shelterin component Telomeric-repeat binding factor 2 (TRF2)[220,221]. A co-crystal structure of the human TRF2 TRF homology domain bound to a Nbs1 peptide (aa 419-449) containing a YQLSP (aa

429-433) motif suggests an interaction also involved in telomeric recruitment of MRN[222]. Intriguingly, S432 gets phosphorylated in S/G2 by CDK2, which disrupts the TRF2-MRN interaction, resulting in TRF2 driven Apollo recruitment to new telomere ends and hence NHEJ prevention. In contrast, during G1, dephosphorylated Nbs1^{S432} binds to TRF2, which prevents MRN-mediated ATM activation and thus again inhibits NHEJ of telomeres[222]. In case of dysfunctional or "uncapped" telomeres, e.g. due to TRF2 depletion, telomeres are recognized as DSBs by the MRN complex. This then results in phosphorylated Nbs1^{S432} dependent ATM activation[222] and MRN mediated removal of the 3' telomeric overhang[223], promoting chromosome segregation and apoptosis due to NHEJ-mediated chromosome fusion[204,215].
Yet, it is still not fully understood to which extent important other MRN-related end-processing cofactors as e.g. CtIP are involved in this process[215]. At *S. cerevisiae* telomeres for example, Sae2's coactivator function for MRX endonuclease activity, and thereby endonucleolytic cleavage itself, is inhibited by the telomeric factor Rif2 (Rap1-Interacting Factor 2)[224-227].

1.3.5.3 MRNs functional role in innate immunity

Another layer to MRNs multifunctionality *in vivo*, is its participation in innate immunity mechanisms involved in viral defense. Among other factors, MRN can detect viral dsDNA and initiate cascades of the described DDR, but also innate immunity signals[137,228]. Due to the small size of viral DNA, and in contrast to canonical DDR, only a local and less amplified MRN-mediated ATM activation is happening. By that MRN helps to avoid cell cycle arrest and global damage responses upon viral infection. Hence, MRN-mediated responses deliver the regulatory basis to block viral replication in the nucleus through a genome related self- and nonself-recognition mechanism[137,229]. Moreover, MRN, in association with NHEJ factors, is able to directly inhibit viral replication via concatenation of viral DNA [137,230,231], forming stretches too big to package and with buried terminal replication origins[137,232-234].
A direct immune response via type I interferons (IFNs) production can also be induced by Mre11-Rad50, while being independent of Nbs1. A study on an ATLD-patient cell line showed that DNA-binding impaired Mre11 induces defects in IFN production[137,235]. MR was further shown to be required for activation of Stimulator of interferon genes (STING), nuclear factor κβ (NF- κβ) and Interferon regulatory factor 3 (IRF3), which are crucial factors for IFN production[137,235]. However, this opens a constant battle between viral defense mechanisms and infecting viruses. For example, oncoproteins from human Adenovirus early region 4 (E4) genes open reading frames 3 and 6 (E4-ORF3 and 6) actively relocalize and mark MRN for degradation to render it inactive[137,232].

1.4 The bacterial Mre11-Rad50 complex

The bacterial MR complex is formed by the Rad50 and Mre11 homologs SbcC (ATPase) and SbcD (nuclease)[119,236]. Already early experiments, using multiple sequence alignments, found conserved motifs of nuclease and ATPase catalytic domains shared among Mre11 and Rad50 protein homologs from e.g. yeast, *E. coli* (further denoted as *Ec*MR; also known as SbcCD) and T4 phages (gp46 ATPase; gp47 nuclease)[119]. This first evidence of evolutionary conservation of the MR complex in prokaryotes was supported by EM imaging, illustrating the typical MR "head-rod-tail" structure for *Ec*MR[120]. Hence, even though the prokaryotic system lacks the important eukaryotic MR cofactors Nbs1 and CtIP, it exhibits structural and functional similarity compared to its eukaryotic counterparts[92,119,172]. As for eukaryotic MRN/X, *in vitro* experiments showed that *Ec*MR detects DNA end structures, processes protein-blocked or obstructed ends, as well as hairpins by nucleolytic cleavage to enable DSB repair by HR (Figure 13)[120,172,237]. *Ec*MR was furthermore shown to bind a stretch of 25-30 bp of dsDNA and having increased affinity towards free DNA ends[165]. Clearance of blocked DNA ends and secondary structures relies on *Ec*MR's 3' to 5' dsDNA exonuclease and a hairpin-opening single-strand 5' endonuclease[172,237]. Whereas *Ec*MR's exonuclease activity only needs ATP binding, but not hydrolysis, the DNA end block stimulated endonuclease activity was biochemically shown to require ATP hydrolysis[165], according to observations made in eukaryotic homologs[93,168,173]. Yet, one has to note that other investigations on *Ec*MR showed that ATPγS is sufficient for endonuclease cleavage[172,238]. Quantitative estimates revealed that multiple ATP hydrolysis cycles are necessary per endonucleolytic cleavage[165]. A putative mechanism was proposed, in which ATP binding and hydrolysis leads to local, but potentially also reversible, melting of the DNA double-strand prior to cleavage[165]. In support of that, ATP-dependent local DNA melting has been observed for other eu- and prokaryotic Mre11 homologs[153,161,239]. Furthermore, the putative DNA melting required for endonuclease activity was shown to likely being dependent on a properly formed *Ec*Mre11 dimer, as mutational weakening of the dimer interface reduced endonuclease, but could be rescued by introduction of a pre-melted DNA bubble[165].

A recent biochemical study revealed that DNA cleavage on opposing 3' and 5' strands, exo- or endonucleolytically, are chemically distinct[165]. This is due to the cleavage-coupled hydrolysis of the DNA phosphodiester bond either happening at the 3' (P-O'5 cleavage) or 5' (3'O-P cleavage) side, looking from a blocked end (Figure 13). Based on this chemical signature, *Ec*MR's binding polarity is suggested to be opposed when binding to a free or a blocked DNA end[165].

Overall, the enzymatic activities are equal to the ones described for eukaryotic MRN/X[172,237]. Thus, deblocking of protein-blocked ends and hairpin-opening activities seem to be evolutionary conserved enzymatic activities of MR[165]. However, due to the lack of prokaryotic counterparts for the important regulatory MR cofactors Nbs1 and CtIP in eukaryotes, *Ec*MR's

enzymatic activity is thought to be less tightly regulated. In contrast to eukaryotic MRN/X, *Ec*MR exhibits an intrinsic, non-cofactor dependent and more robust endonuclease activity that was reported to be binary, cleaving both DNA strands in ~10 bp intervals[238]. As discussed in a previous chapter, this double cleavage of both DNA strands was recently also reported for MRN in a limited way, e.g. helping to release protein blocks bound to the 3' end[173]. Consequently, this further supports the idea of an evolutionary conserved cleavage activity of blocked DNA ends for pro- and eukaryotic Mre11-Rad50 complexes[165].

Additional studies revealed *Ec*MR to cleave topoisomerase DPCs, hairpins and cruciform structures formed by long DNA palindromes, *in vivo* (Figure 13)[236,240,241]. Due to the formation of hairpin-capped ends and cruciform structures, long DNA palindromes are sites of genomic instability, gene amplification and interfere with DNA replication – a threat conserved from prokaryotes to eukaryotes[242,243]. In support of *Ec*MR's capability to resolve hairpin and cruciform structures, the nuclease activity of budding yeast MRX-Sae2 has also been shown to prevent palindrome derived duplications[175,244]. Adding up, mutations of a component of MRX-Sae2, preventing nuclease activity, can result in replication of hairpin-capped ends, inducing formation of di- and acentric chromosomes in mitotic cells[175,240]. In a more recent study, *Ec*MR in cooperation with ExoI has been shown to adopt a crucial role in replication termination. In this case, two convergent replication forks pass each other, which generates a DNA bridge between the duplicated chromosomes, that needs to be resolved by *Ec*MR and ExoI[245].

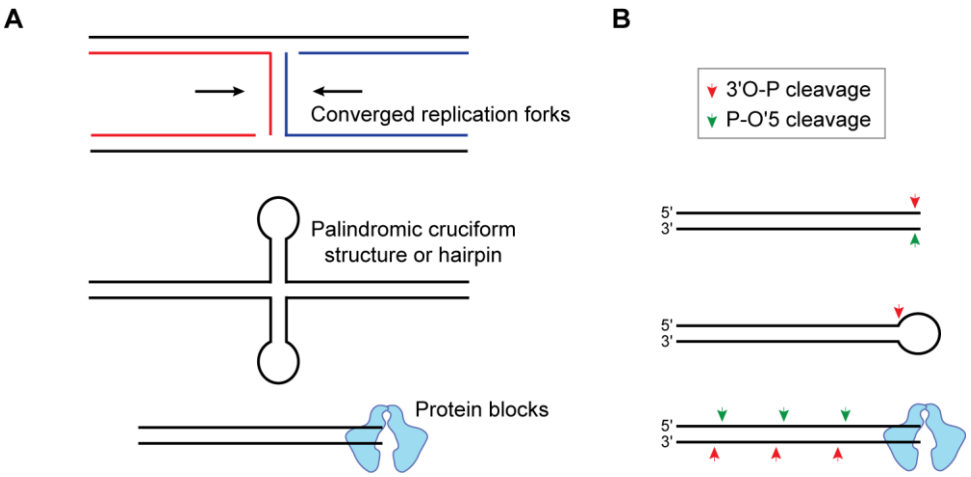

Figure 13: Main DNA substrates and nuclease activities reported for the bacterial MR complex. (A) Schematic illustration of the main DNA substrates processed by the bacterial MR complex SbcCD. (B) Schematic illustration of endo- and exonuclease cleavage reactions at free, hairpin and protein-blocked DNA ends.

1.5 Objectives

The evolutionary conserved MR(N) complex has been extensively studied over the last decades, being a key player in DSB repair. Yet, several structural and mechanistic questions still remain unanswered. Former structural studies on MR core complexes derived from different species could show that in an ATP-bound state, the Rad50 NBDs block DNA entry to the Mre11 nuclease active sites[153,167,178]. Furthermore, the former structural studies were all drawn on protein X-ray crystallography, which required the functionally vital Rad50 CCs to be drastically shortened, likely impairing MR(N)'s overall functionality[153,167,178]. Thus, a structural and mechanistic basis for the MR(N) complex's conserved exo-, endonuclease and hairpin-opening activities remains elusive.

On these grounds, the aim of this thesis was to elucidate the structural and functional characteristics of the MR core complex, using structural and biochemical approaches. Here, the *Ec*MR complex is used as a model system, providing the advantage of conserved structural and enzymatic features compared to the eukaryotic MR(N) orthologs, while being independent of additional cofactors or post-translational modifications[92,119,172]. Hence, the *Ec*MR complex can be used as a simplified model system to investigate the structural and mechanistic principles of the MR core complex. The recent resolution revolution in cryo-EM further enables us to investigate the full-length *Ec*MR complex at near-atomic resolution, without shortening of the functionally essential Rad50 CCs.

Within the course of this thesis, we aimed to obtain structural and mechanistic insights into the Mre11-Rad50 complex with its enigmatic nuclease diversity, able to process a large variety of DNA substrates.

To better understand the structural and functional effects of the flexible CCs on the Rad50 head domain, a cryo-EM structure of the full-length *Ec*MR complex bound to ATPγS should be solved. This then should serve as a ground state in the following, where we aimed to elucidate the structural changes upon DNA binding and processing. Here, the cryo-EM structure of the full-length *Ec*MR complex bound to a free DNA end should be solved. Supported by biochemical assays the structure will help to clarify how the DNA can access the Mre11 nuclease active site, building the mechanistic basis of DNA end sensing and exonucleolytic processing by Mre11-Rad50.

The main goal of this thesis was seized in the second part, where we aimed to investigate the structural mechanism of MR's physiologically important endonuclease, as well as the hairpin-opening activity. Using cryo-EM, we aimed to solve the structures of *Ec*MR bound to a protein-blocked DNA and a DNA hairpin. Supported by biochemical studies, this will help to clarify how Mre11-Rad50 generates an endonucleolytic incision to remove protein blocks and open hairpins. In sum, this work will help to understand the structural and mechanistic basis of Mre11-Rad50's enigmatic nuclease diversity.

2 Publications

2.1 Mechanism of DNA End Sensing and Processing by the Mre11-Rad50 Complex

Lisa Käshammer*, Jan-Hinnerk Saathoff*, Katja Lammens, Fabian Gut, Joseph Bartho, Aaron Alt, Brigitte Kessler, Karl-Peter Hopfner, Mechanism of DNA End Sensing and Processing by the Mre11-Rad50 Complex, *Molecular Cell*, Volume 76, 07 November 2019, Pages 382-394

https://doi.org/10.1016/j.molcel.2019.07.035

* These authors contributed equally

Summary

In this publication we performed cryo-EM on the bacterial *Ec*MR complex (also known as SbcCD) to solve the first full-length Mre11-Rad50 structures. The reported structures depict the *Ec*MR complex in two defined states, a resting and a DNA-bound cutting state. In the ATPγS bound resting state the Mre11 nuclease active sites are blocked by the Rad50 NBDs, resembling previously published crystal structures of the MR head complex. The long protruding Rad50 CCs adopt a ring-like open conformation, but could only be resolved in close proximity to the Rad50 NBDs due to their flexibility. Upon DNA binding, the complex transitions to an active, nuclease-proficient cutting state. Here, the CCs interact and zip up to form a rod-like state that could be resolved up to 200 Å in length, clamping the DNA in close collaboration with the Rad50 NBDs. Consecutively, the Mre11 dimer undergoes a large conformational rearrangement by ~120° to relocate at the side of Rad50, through which a DNA cutting channel is formed. Here, Mre11 binds the DNA end, enabling nucleolytic processing of the free 3' DNA end via MR's conserved 3' to 5' exonuclease activity. This exonuclease state has not been observed in previous crystal structures and hence describes for the first time the structural mechanism of how Mre11-Rad50 can sense and process a free DNA end.
These structural and mechanistic insights on the DNA end sensing and processing by Mre11-Rad50 were further supported by biochemical assays. The exonuclease state showed that DNA binding is mainly mediated by the Rad50 NBDs and CCs. In support of this, mutational analysis

in associated DNA binding residues abolished DNA binding. Furthermore, mutations in the Mre11 fastener, which locks the Mre11 dimer in active conformation, strongly decreased the exo- and endonuclease activities of *Ec*MR, while a charge reversal mutant is able to partially restore activities.
Based on the described results we propose a model in which the *Ec*MR complex scans the DNA for a DSB in an autoinhibited conformation with open CCs. Upon encounter of a DSB end, the CCs close-up to allow relocation of the Mre11 dimer into a nuclease-proficient exonuclease state.

Author Contribution

I performed biochemical assays, in particular nuclease and blocked dsDNA degradation assays, as well as associated quantification and statistical analysis together with Lisa Käshammer to analyse the biochemical properties of *Ec*MR and specific mutants. Furthermore, I was involved in the analysis and discussion of the results with Lisa Käshammer, Karl-Peter Hopfner and all other authors.

Article

Molecular Cell

Mechanism of DNA End Sensing and Processing by the Mre11-Rad50 Complex

Graphical Abstract

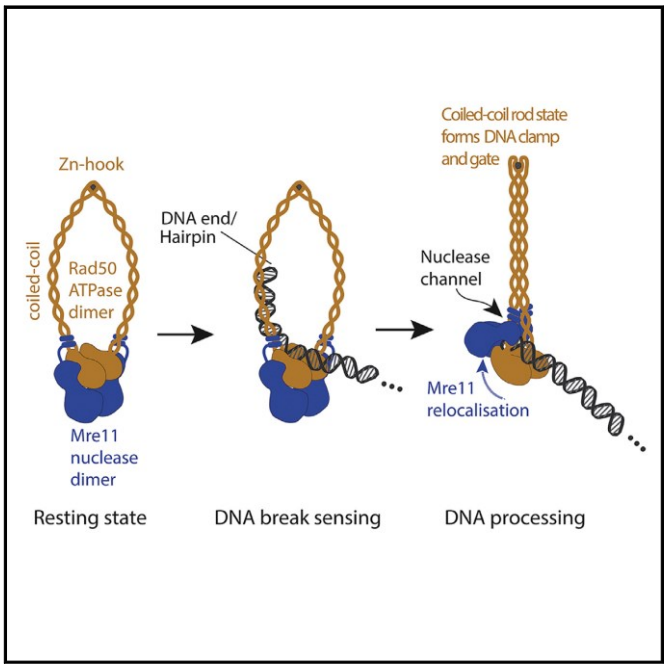

Authors

Lisa Käshammer, Jan-Hinnerk Saathoff, Katja Lammens, ..., Aaron Alt, Brigitte Kessler, Karl-Peter Hopfner

Correspondence

hopfner@genzentrum.lmu.de

In Brief

Käshammer et al. use cryoelectron microscopy and biochemical studies to reveal, at near-atomic resolution, how the ATP-dependent nuclease Mre11-Rad50 can sense and process a wide range of DNA termini to enable repair and recombination of breaks and hairpins in chromosomal DNA.

Highlights

- cryo-EM structure of *Ec*Mre11-Rad50 bound to a DNA break
- Mre11 dimer binds the DNA end at the side of Rad50
- Mre11 and Rad50 assemble a transient DNA cutting channel
- The coiled coils form a rod-shaped DNA gate and clamp

Käshammer et al., 2019, Molecular Cell *76*, 382–394
November 7, 2019 © 2019 Elsevier Inc.
https://doi.org/10.1016/j.molcel.2019.07.035

CellPress

CellPress

Molecular Cell
Article

Mechanism of DNA End Sensing and Processing by the Mre11-Rad50 Complex

Lisa Käshammer,[1,2,4] Jan-Hinnerk Saathoff,[1,2,4] Katja Lammens,[1,2] Fabian Gut,[1,2] Joseph Bartho,[1,2] Aaron Alt,[1,2] Brigitte Kessler,[1,2] and Karl-Peter Hopfner[1,2,3,5,*]
[1]Department of Biochemistry, Ludwig-Maximilians-Universität, 81377 Munich, Germany
[2]Gene Center, Ludwig-Maximilians-Universität, 81377 Munich, Germany
[3]Center for Integrated Protein Science, 81377 Munich, Germany
[4]These authors contributed equally
[5]Lead Contact
*Correspondence: hopfner@genzentrum.lmu.de
https://doi.org/10.1016/j.molcel.2019.07.035

SUMMARY

DNA double-strand breaks (DSBs) threaten genome stability throughout life and are linked to tumorigenesis in humans. To initiate DSB repair by end joining or homologous recombination, the Mre11-nuclease Rad50-ATPase complex detects and processes diverse and obstructed DNA ends, but a structural mechanism is still lacking. Here we report cryo-EM structures of the *E. coli* Mre11-Rad50 homolog SbcCD in resting and DNA-bound cutting states. In the resting state, Mre11's nuclease is blocked by ATP-Rad50, and the Rad50 coiled coils appear flexible. Upon DNA binding, the two coiled coils zip up into a rod and, together with the Rad50 nucleotide-binding domains, form a clamp around dsDNA. Mre11 moves to the side of Rad50, binds the DNA end, and assembles a DNA cutting channel for the nuclease reactions. The structures reveal how Mre11-Rad50 can detect and process diverse DNA ends and uncover a clamping and gating function for the coiled coils.

INTRODUCTION

DNA double-strand breaks (DSBs) are a frequent cause of gross chromosomal aberrations and genome instability in all kingdoms of life (Myung et al., 2001). They are produced by ionizing radiation and genotoxic chemicals, arise at stalled and collapsed replication forks, and are products of abortive topoisomerases. Sensitive detection, signaling, and repair of DSBs is a critical process throughout life to maintain the integrity of genetic information (Blackford and Jackson, 2017; Ciccia and Elledge, 2010).

Repair of DSBs proceeds through homologous recombination (HR) or end joining pathways, typically in a cell cycle-regulated manner in eukaryotes (Chang et al., 2017; Hustedt and Durocher, 2016; Kowalczykowski, 2015; Wright et al., 2018). DNA resection and synthesis in HR and ligation in end joining require chemically "clean" DNA termini, but DSBs can be chemically very heterogeneous, including covalent protein adducts. These "dirty" DNA ends require nucleolytic processing by homologs of the Mre11-Rad50 protein family to enable subsequent repair or DNA damage signaling (Cejka, 2015; Hoa et al., 2016; Mimitou and Symington, 2008; Oh et al., 2016; Paull, 2018; Rahal et al., 2010).

Homologs of Rad50 and Mre11 are found in all kingdoms of life. They form $Mre11_2$-$Rad50_2$ heterotetramers, where two Rad50 ATP-binding cassette (ABC)-type nucleotide binding domains (NBDs) and a Mre11 nuclease dimer assemble as a catalytic head module that binds and cleaves DNA in a reaction regulated by ATP-induced conformational changes between the two NBDs (Hopfner et al., 2001). Rad50 homologs also possess intriguing 15- to 60-nm-long coiled coils (CCs) that can form large proteinaceous rings or rods, joined by an apical Zn-hook dimerization motif (Hopfner et al., 2002; Moreno-Herrero et al., 2005; Park et al., 2017). The CCs are functionally important (Hohl et al., 2011), but their mechanistic role is not understood. Eukaryotic Mre11-Rad50 interacts with Nijmegen breakage syndrome protein 1 (NBS1, known as Xrs2 in yeast), a protein that, among other functions, recruits the DNA damage checkpoint kinase ataxia telangiectasia mutated (ATM) (Carney et al., 1998; Falck et al., 2005).

Prokaryotic Mre11-Rad50 (MR) and eukaryotic Mre11-Rad50-Nbs1/Mre11-Rad50-Xrs2 (MRN/MRX) complexes have the intriguing function to sense both, clean and blocked DNA ends (Paull, 2018). The capability to clear blocked DNA ends is critical in eukaryotes to maintain genome integrity and ensure proper replication. Related functions exist in *E. coli*, where *E. coli* Mre11-Rad50 (*Ec*MR, also called SbcC-SbcD) processes palindromic hairpins, cleaves near protein blocks, and is implicated in the resolution of DNA replication termination structures (Connelly et al., 2003; Eykelenboom et al., 2008; Wendel et al., 2018).

The nature of the block appears to be of no importance and can be, for instance, streptavidin bound to biotinylated DNA termini (Cannavo and Cejka, 2014), the eukaryotic DNA end binding factor Ku (Reginato et al., 2017; Wang et al., 2017), or an abortive topoisomerase (Neale et al., 2005). The hydrolysis of ATP enables MR to cleave DNA 15–25 bp away from diverse blocks through endonuclease activity (Cannavo and Cejka, 2014; Connelly et al., 2003; Deshpande et al., 2016; Neale et al., 2005; Wang et al., 2017). MR(N) complexes also cleave

hairpins and possess 3′→5′ exonuclease activity, either inward from a clean DNA end or toward the DNA end following the internal endonucleolytic 5′ incision (Garcia et al., 2011; Paull and Gellert, 1998). It is mechanistically unclear how MR complexes can detect and process these chemically diverse terminal DNA structures without also cleaving internal DNA containing stable proteins (e.g., nucleosomes). The mechanism of end recognition and cleavage is even more puzzling because human MRN can internally bind to and diffuse along DNA until a DNA block is reached (Myler et al., 2017).

The structural mechanism of how MR(N) complexes sense and process clean and blocked DNA ends is not understood. A number of crystallographic studies with truncated proteins (Rad50$^{\Delta CC}$) revealed the basic architecture of interactions at the catalytic head domain and binding of DNA to Rad50 and Mre11 (Lammens et al., 2011; Lim et al., 2011; Möckel et al., 2012; Williams et al., 2008, 2011). ATP binding to Rad50 leads to a tightly engaged Rad50 NBD dimer, forming a DNA binding platform along the two NBDs (Hopfner et al., 2000; Liu et al., 2016; Seifert et al., 2016). Strangely, the current crystallographic studies suggest that Rad50 blocks Mre11's nuclease active sites in this ATP state (Liu et al., 2016, Möckel et al., 2012; Lim et al., 2011), although ATP is critical for nucleolytic processing by MR/MRN (Cannavo and Cejka, 2014; Herdendorf et al., 2011; Paull and Gellert, 1999; Saathoff et al., 2018). This incompatibility between structural and biochemical data in the processing of DNA ends and a general lack of understanding of DNA end recognition by MR/MRN currently hampers conceptual advances in the mechanism and biology of DSB repair (Paull, 2018).

Here we employed cryoelectron microscopy (cryo-EM) to study the full-length *E. coli* Mre11-Rad50 homolog in resting state (bound to adenosine-5′-o-(3-thio-triphosphate) [ATPγS]) as well as in a DNA end recognition and the cutting state (bound to DNA and ADP after ATP hydrolysis). The structures reveal an unanticipated structural state that resolves the above-mentioned mechanistic discrepancy. Rad50 forms the main DNA binding element through both NBDs and CCs. Upon DNA binding, the two Rad50 CC domains zip up and form a narrow clamp around a single DNA duplex. This structural change allows the Mre11 dimer to move from the bottom to the side of the complex and bind the DNA end. We biochemically show that this state is also involved in the endonucleolytic DNA end processing at blocked DNA ends. Rather than being mere linkers, the CCs act as clamps and gates for the recognition and processing of diverse DNA end structures. Our structures provide a new structural concept and framework for Mre11-Rad50 complex proteins that clarify key aspects of DNA end recognition and processing.

RESULTS

The Cryo-EM Structure of *Ec*MR in the "Resting" State

To reveal the mechanism of ATP-dependent DNA end sensing and processing by MR complexes, we used cryo-electron microscopy and single-particle reconstruction on *Ec*MR. We first addressed the structure of *Ec*MR in the absence of DNA, vitrified the protein in the presence and absence of ATPγS, and recorded transmission electron micrographs. Without nucleotides, we did not obtain homogeneous particles. Addition of ATPγS led to visibly more homogeneous particles and enabled us to obtain a 3.5 Å reconstruction and atomic structure of its DNA binding and processing head module (Figures 1A–1C; Figure S1; Table 1). The catalytic head of *Ec*MR consists of two *Ec*Rad50 NBDs and the *Ec*Mre11 dimer. Both *Ec*Mre11s match the high-resolution crystal structure of the *Ec*Mre11 nuclease extremely well (*Ec*Mre11^{NUC}, composed of phosphodiesterase and capping domains) (Figure S2A) and are anchored to the *Ec*Rad50 CCs via their C-terminal helix-loop-helix (HLH) domains. The *Ec*Rad50^{NBD}s are engaged by jointly binding two Mg^{2+}-ATPγS molecules in their interface and are situated in the DNA binding cleft of the *Ec*Mre11^{NUC} dimer (Figure S4A). The structure recapitulates previous crystal structures of Mre11 bound to the truncated (ΔCCs) Rad50^{NBD} (Lim et al., 2011; Möckel et al., 2012; Figure S2B). Although the head module is well resolved, the ~40-nm-long CCs are apparently flexible and only defined in the reconstruction up to the binding site of *Ec*Mre11^{HLH}. The angle of protrusion of the two CCs from the head suggests that they form wide, presumably flexible proteinaceous rings. The precise shape needs to be determined in future studies. We observed a homogeneous complex of approximately $(Mre11)_2$-$(Rad50)_2$ (M_2R_2) stoichiometry in gel filtration and did not see formation of higher-order complexes through addition of ATP and DNA, supporting a model where the CCs are joined within an M_2R_2 complex (Figure S2C).

In atomic force microscopy (AFM) studies, *Ec*MR forms predominantly V-shaped M_2R_2 complexes, joined at the Zn-hook (de Jager et al., 2004). In the absence of ATP, the *Ec*Mre11 nuclease domains were separated and attached each as monomers to the disengaged *Ec*Rad50 NBDs. Thus, ATP promotes stable head complexes with dimeric Mre11 by joining the two Rad50 NBDs, and we consistently observed slight compaction of the complex by ATP in solution (Figure S2C). Because *Ec*MR is constantly exposed to ATP in the cell but hydrolyzes it only with 0.008 ATP/s/active site (Saathoff et al., 2018), the obtained ATPγS-bound state likely represents a major autoinhibited resting state of the complex with blocked Mre11 nuclease sites.

The Cryo-EM Structure of *Ec*MR in the "Cutting" State

To understand how *Ec*MR recognizes DNA ends, we reconstituted a complex of the nuclease-deficient *Ec*MR mutant H84S (*Ec*M^{H84S}R) with 60-bp double-stranded DNA (dsDNA) in the presence of ATP and recorded transmission electron micrographs. Three-dimensional reconstruction led to a cryo-EM map at a nominal resolution of 4.2 Å that enabled us to derive a near-atomic model of the *Ec*MR catalytic head module and parts of the CCs bound to DNA (Figure 1D–1F; Figure S3; Table 1). The structure captures how *Ec*MR senses and processes DNA ends, and we denoted this condition the cutting state. Inspection of the map at the nucleotide binding sites of the NBDs reveals the presence of Mg^{2+}-ADP. Because ATP binding is critical for DNA binding by *Ec*MR, the structure represents a post-ATP-hydrolysis state, which appears to be quite long-living before ADP → ATP exchange or DNA release (Figures S4B and S4C).

DNA end sensing induces two large conformational changes in the cutting state compared with the resting state (Figures 1D–1F; Figures S1 and S3; Video S1). The CCs move inward,

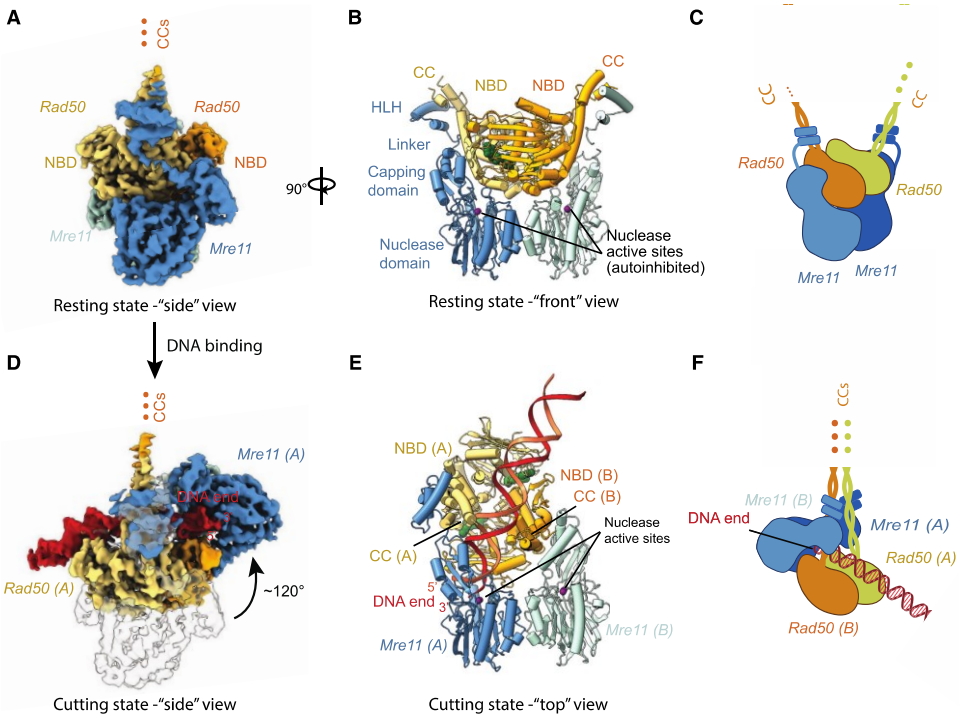

Figure 1. Structure of *Ec*Mre11-Rad50 in the Resting and Cutting States

(A) Density map of the dimeric *Ec*Rad50 ABC ATPase (orange/yellow) bound to the *Ec*Mre11 nuclease dimer (light/dark blue) in the resting state in side view. Subunits as well as the nucleotide binding domain (NBD) and coiled-coils (CC) are annotated. The CCs extend further (dots) but are not visualized in the map.

(B) Atomic model of the resting state catalytic head in front view, using the color code of (A).

(C) Scheme of the resting state catalytic head, using the color code of (A).

(D) Density map model of the cutting state in side view. DNA end binding leads to a large change in the architecture. The *Ec*Mre11 nuclease moves from its autoinhibited location (gray and transparent) with blocked active sites to bind the DNA end in the cutting state. The NBDs and CCs generate a DNA binding clamp and assemble with *Ec*Mre11, forming an active-site channel that harbors the DNA end. Only *Ec*Mre11 protomer A binds DNA (red), whereas *Ec*Mre11 protomer B plays an architectural role. Color code as in (A) with DNA colored in red.

(E) Atomic model of the cutting state in top view using the same color code as in (D).

(F) Scheme of the cutting state catalytic head using the same color code as in (D).

See also Figures S1–S4, Table 1, and Video S1.

zip up, and fold into an apparently rod-like geometry. Intriguingly, in this rod state, the CCs tightly clamp around a single dsDNA duplex, whereas the *Ec*Mre11 dimer relocates from its auto-inhibited position at the "bottom" of the Rad50 NBD dimer to the side of the NBD dimer. Here it forms, together with *Ec*Rad50^{NBD}, an active-site channel that harbors the DNA end. Compared with the resting state, the cutting state can be depicted as an almost rigid body rearrangement of *Ec*Mre11^{NUC} and *Ec*Rad50^{NBD} dimers, enabled by the flexible linker between *Ec*Mre11^{NUC} and *Ec*Mre11^{HLH} (Figure S4D). *Ec*Rad50^{NBD} also undergoes some internal subdomain rotations and changes in loop regions in response to DNA binding and ATP hydrolysis. Repositioning of the *Ec*Mre11^{NUC} dimer at the side of the *Ec*Rad50^{NBD}s sterically requires the inward movement of the CCs; thus, the rod formation of Rad50's CCs presumably precedes or coincides with Mre11 dimer relocalization.

The two *Ec*Rad50^{NBD}s generate a composite dsDNA binding platform that spans 22 bp of a DNA duplex, with dsDNA protruding on both sides (Figures 1D–1F). One dsDNA arm extends from the opposite side of the *Ec*Mre11 dimer location, whereas the other arm is bound by *Ec*Mre11 in the channel. The latter is positioned for nucleolytic cleavage and likely represents the "free DNA end" in the 3′→5′ exonuclease state. The pivotal role of Mre11 in binding the DNA end is consistent with the critical role of human Mre11 in DNA end sensing of MRN (Myler et al., 2017). Interestingly, only one of the two *Ec*Mre11 subunits contacts the DNA end (referred to as subunit "A"), whereas *Ec*Mre11 (subunit "B") helps to position the actively cutting subunit.

In sum, the structures uncover an intriguingly asymmetric and unanticipated structural state as the basis for DNA binding by *Ec*MR that clarifies the prevailing mystery of ATP-dependent detection and processing of DNA ends by MR.

Table 1. Cryo-EM Data Collection, 3D Reconstruction, and Model Refinement Statistics

	*Ec*MR Resting State (EMDB-10107) PDB: 6S6V	*Ec*MR Cutting State (EMDB-10116) PDB: 6S85
Data Collection and Processing		
Magnification	130,000	165,000
Voltage (kV)	300	300
Electron exposure (e–/Å^2)	68	73.6
Defocus range (μm)	–1.0 (–3.5)	–1.0 (–3.5)
Pixel size (Å)	1.06	0.82
Symmetry imposed	C2	C1
Initial particle images (no.)	2,809,916	1,130,635
Final particle images (no.)	142,229	151,271
Map resolution (Å)	3.5	4.2
FSC threshold	0.143	0.143
Refinement		
Initial model used (PDB code)	PDB: 4M0V, homology model of PDB: 3QF7	PDB: 4M0V, Rad50 from resting state
Model resolution (Å)	3.66	4.34
FSC threshold	0.5	0.5
Map sharpening *B* factor (Å^2)	–131	–194
Model Composition		
Non-hydrogen atoms	11,820	12,977
Protein residues	1,498	1,488
Ligands		
Mn^{2+}	4	4
Mg^{2+}	2	2
ATPγS	2	–
ADP	–	2
dsDNA	–	63 nt
B factors (Å^2)		
Protein	83.3	66.03
Ligand		
ATPγS	52.91	–
ADP	–	73.63
dsDNA	–	152.36
RMSDs		
Bond lengths (Å)	0.009	0.007
Bond angles (°)	0.897	0.918
Validation		
MolProbity score	1.82	2.27
Clashscore	6.21	18.66
Poor rotamers (%)	0.24	1.03
Ramachandran Plot		
Favored (%)	92.22	91.87
Allowed (%)	7.78	8.47
Disallowed (%)	0.0	0.34

A Fastener Loop Connects *Ec*Mre11^{NUC} with *Ec*Rad50^{NBD}

To form the cutting state, the phosphodiesterase domain of *Ec*Mre11 (A) is locked onto *Ec*Rad50^{NBD} (B) by a loop in *Ec*Mre11^{NUC}, which we denote "fastener" (amino acids [aa] 137–149) (Figure 2A). The fastener binds the outer β sheet of *Ec*Rad50^{NBD} (B) and holds both domains in place by mainly polar and ionic interactions. To validate this new interface, we mutated the central K149^{EcMre11}-E115^{EcRad50} salt bridge connecting the fastener and Rad50^{NBD}. *Ec*Mre11Rad50^{E115K} and *Ec*Mre11^{K149E}Rad50 display reduced endo/exonuclease and altered DNA binding activity, although the ATPase activity is increased (Figures S4E and S4F). Remarkably, the charge-reverting double mutant *Ec*Mre11^{K149E}Rad50^{E115K} rescues the endonuclease on blocked DNA ends as well as the exonuclease on free ends (Figures 2B and 2C). These data not only validate the cutting state structure but also indicate that the observed conformation is implicated in the endonucleolytic cutting of blocked ends. The increased ATPase rate could be a result of a weaker fastener-NBD interaction causing faster ADP-to-ATP exchange within Rad50's ATP cycle.

The Nuclease Active Site Is Located in a Transient Channel between Mre11 and Rad50

In the active-site channel between *Ec*Mre11^{NUC} and *Ec*Rad50^{NBD}, one DNA strand directly contacts the di-manganese cluster and is properly positioned for nucleolytic cleavage (the actual reaction is prevented by the H84S^{EcMre11} mutation) (Figure 2D; Figure S5A). Difference density analysis is consistent with the presence of two manganese ions, which are added to the buffer prior to plunge freezing (Figures S5B and S5C). The overall recognition is consistent with biochemically prevailing 3′→5′ exonuclease on free DNA ends and shows how DNA binds to Mre11 in the active cutting state. The binding mode is notably different from that obtained in crystallographic studies of prokaryotic Mre11-DNA complexes in the absence of Rad50. There, DNA was bound across the Mre11^{NUC} dimer, suggesting that Mre11 has different DNA binding modes (Figure S5C; Sung et al., 2014; Williams et al., 2008). Some density extends from the di-metal binding site toward the exit of the channel but has a poor quality that does not allow interpretation (Figure 2E). Biochemical data show that *Ec*MR preferentially cleaves the 3′ strand between terminal bases 3 and 4 (Saathoff et al., 2018). Thus, the additional density could stem from DNA that extends ~3 bases beyond the di-metal cluster but may also stem from a disordered *Ec*Mre11 loop (aa 188–203) (Figure S5D). This loop is not critical for cutting per se but seems

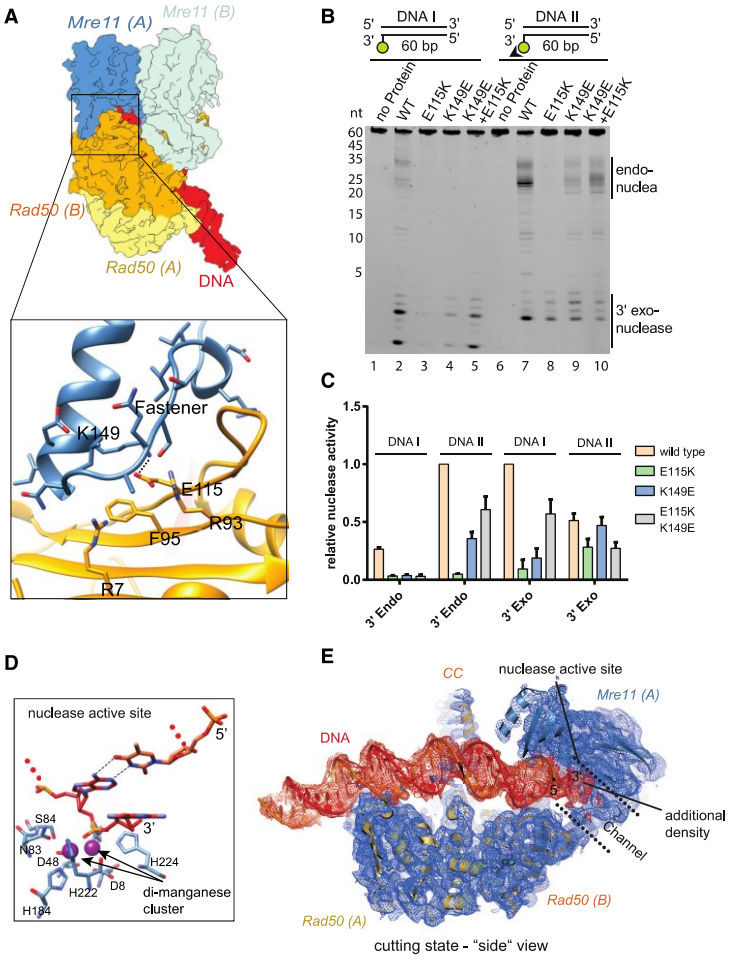

Figure 2. The Fastener Locks a Transient Active-Site Channel between Mre11 and Rad50

(A) The new *Ec*Mre11-EcRad50 interface in the cutting state is stabilized by binding of the *Ec*Mre11 fastener loop (blue) to the *Ec*Rad50 NBD (orange).

(B) Functional analysis of the salt bridge between $E115^{EcRad50}$ and $K149^{EcMre11}$. Although single mutants reduce nuclease activity, both exonuclease (DNA I with a fluorescein label [green]) and endonuclease (DNA II with a fluorescein label and protein block [triangle]) are substantially rescued by a charge-reverting double mutant, $E115^{EcRad50}$+$K149^{EcMre11}$.

(C) Quantification of (B) (n = 3 technical replicates). Error bars indicate the standard deviation.

(D) Details of the interaction of the 3′ strand at or near the DNA end with the di-metal cluster of *Ec*Mre11, showing that the DNA is poised for cleavage in the observed cutting state (prevented by the H84S mutation).

(E) The nuclease active site is located in a channel between *Ec*Rad50 and *Ec*Mre11, which is principally large enough to accommodate hairpins and even extended dsDNA for endonuclease, although bending/melting of DNA or changes in the protein assembly need to occur. Shown is the color-coded density map superimposed with the structural model. Additional density extending into the structure could indicate some promiscuity in DNA end binding.

See also Figures S4 and S5.

to regulate the nuclease specificity (Figure S5E). Importantly, the nuclease channel is wide enough to accommodate longer DNA for endonucleolytic cleavage, as suggested by the biochemistry (Figures 1D and 2B). However, structural alterations in dsDNA (such as melting/unwinding) or changes in the protein are required to accommodate internal DNA and avoid clashes in the current conformation.

In summary, *Ec*Mre11 binds the DNA end through a transiently formed channel, which is consistent with and can explain the broad specificity of MR for diverse types of DNA termini.

The CCs Fold into a Rod Structure upon DNA Binding

To resolve more of the CCs, we employed different classification schemes during the electron microscopy (EM) data evaluation process that enabled us to reconstruct ~1/3 of their macrostructure (Figure 3A). The CCs have a segmented structure and zip up from the more flexible conformations into a closed "rod," clamping around the DNA duplex that is bound at the NBDs (Figure 3B). DNA-induced rod formation matches extremely well the DNA-driven transition of human MRN observed at low resolution by atomic force microscopy (Moreno-Herrero et al., 2005), DNA-bound rods of *Ec*MR in AFM studies (de Jager et al., 2004), and recent analysis of the human Zn-hook (Park et al., 2017; Figure 3A). The Zn-hook dimers joining the apices of the CCs can adopt open V-shaped and closed rod-shaped dimers and, thus, may act as a hinge to allow open, probably ring-like states and closed rod states of the CCs (Hopfner et al., 2002; Park et al., 2017). Although, at this resolution, we cannot assign a sequence at the CCs, a highly conserved sequence region (GEIR motif) in bacterial MR homologs could mark an important site near the first CC-CC "zipper" contact (Figure 3B). We tested several mutations in this motif. Although GEIR→GAIA did not lead to noticeable alteration of the nuclease reactions, GEIR→AEIR robustly reduced endonuclease activity on blocked DNA ends, whereas exonuclease activity on free DNA ends is almost as efficient as in the wild type (WT) (Figure 3C; Figure S5E). Because this mutation still leads to a complex with a stoichiometry and size similar to that of the WT *Ec*MR, the most plausible interpretation is that G→A affects the structure and dynamics of the CCs, which appear

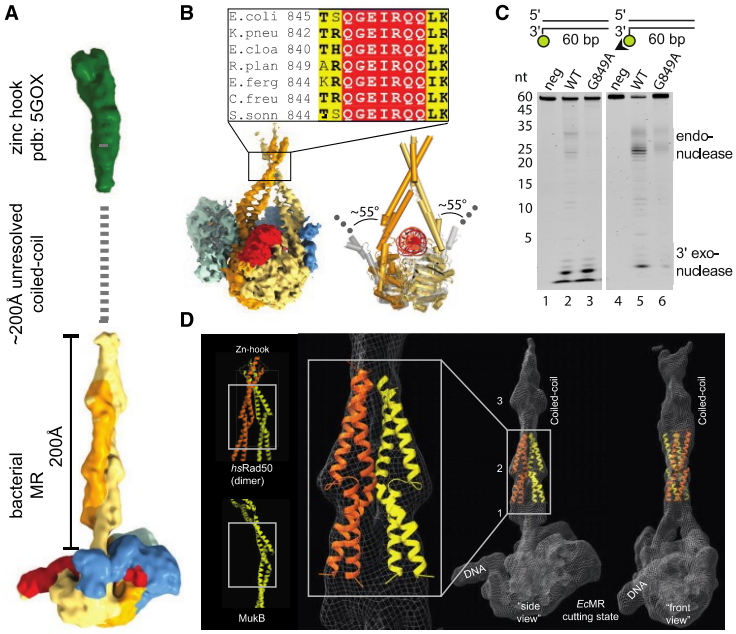

Figure 3. The CCs Form a Long Rod upon DNA Duplex Binding

(A) Low-resolution reconstruction and map showing ~200 Å of the zippered CCs emerging from the DNA binding module (color code of Figure 1). The Zn-hook in rod conformation (PDB: 5GOX) is shown to visualize the approximate site of *Ec*MR.

(B) Left: medium-resolution reconstruction and map showing the CCs up to the first zipper contact. Right: pseudoatomic model visualizing the large ring-to-rod transition of the CCs driven by DNA binding. Top: a conserved sequence motif (GEIR) maps to the region of the first zipper contact.

(C) Mutating the GEIR motif affects endonuclease activity on free and fluorescein-blocked DNA ends (triangle) (see also Figure S5E).

(D) The dimeric CC apex at the human Zn-hook (PDB: 5GOX) and the CC at the MukB elbow region (PDB: 6H2X) harbor a folded CC break element that can be readily docked into the CC zipper contact of *Ec*MR.

See also Figure S5.

to be particularly critical for ATP-dependent endonucleolytic cleavage of blocked DNA.

In our reconstruction, we can visualize two more folded interruptions of the CCs that appear to form CC-CC zipper contacts (Figure 3D). These interaction points match in shape a CC-CC contact of the human hook element in the rod conformation (Park et al., 2017) as well as regions of the "elbow" element of the structural maintenance of chromosome (SMC) ABC-ATPase MukB (Bürmann et al., 2019), indicating wider structural conservation in the Rad50/SMC protein family. Although we cannot assign a sequence motif to these elements yet, secondary structure analysis suggests that *Ec*Rad50 in total has at least five of these folded interruptions in the CCs that could form zipper contacts (Figure S5F).

The CCs Form a Clamp around DNA

The rod conformation is induced and stabilized by joint binding of DNA by the CCs (e.g., K194 and K890) and the NBDs (e.g., R102, K128, and K130) (Figure 4A). Point mutations in DNA binding residues in both NBDs and CCs did not affect basal ATPase rates but nearly abolished DNA binding and DNA-induced ATPase and nuclease activities (Figures 4B–4D). Consistently, *Ec*MR$^{\Delta CC}$ and/or *Ec*MR^{hook} (C506S and C509S mutations in the Zn-hook) lost high-affinity DNA binding (Figure S5G) and linear plasmid degradation activity (Figure S5H). The strong effect of the CC lysines K194 and K890 on DNA binding and ATPase could also be due to the formation of CC-DNA interactions in the pre-hydrolysis ATP state (not visualized here). Alternatively, the cutting state structure could allow more rapid ATP turnover. This is due to the fact, that the NBD dimer is not bound at the Mre11 dimer cleft and, therefore, could more easily open up for ADP→ATP exchange. Together, these data show the CCs, their DNA-clamping activity, and their proper Zn-hook-mediated dimerization are functionally critical for high-affinity DNA binding and ATP-dependent nuclease.

The interaction with the CCs noticeably bends DNA along the NBDs compared with a crystal structure of archaeal MR$^{\Delta CC}$, where DNA is much straighter and is not bound by the CCs (Figures 4E and 4F; Figure S6A; Liu et al., 2016). The observed bent DNA conformation is more difficult to achieve with negatively supercoiled DNA and may add to the sensing of damaged DNA because negatively supercoiled DNA is present in undamaged *E. coli* chromosomes. Consistently, negatively supercoiled DNA stimulates ATP hydrolysis by *Ec*MR much less than relaxed DNA (Saathoff et al., 2018).

Interestingly, the CC-mediated upward bending leads to a single-base-pair registry shift along the NBDs compared with the archaeal MR (ΔCC) ATPγS complex (Figures 4E and 4F). Thus, it is also plausible that ATP-driven conformational changes in the NBDs modulate the way DNA binds in MR and could affect DNA processing. Although the details need to be clarified in future studies, ATP-driven directional registry shifts (like in a DNA translocase to promote directional movement) could help detect the presence of stable protein-DNA adducts through a steric filter by the CCs that allow DNA but not bulky adducts to pass.

Loading onto Linear DNA Is Critical for the Processing of DNA Blocks

Our structural analysis, in conjunction with analysis of the Zn-hook, indicates that, in the cutting state, the CCs form a closed rod all the way from the DNA binding head to the Zn-hooks,

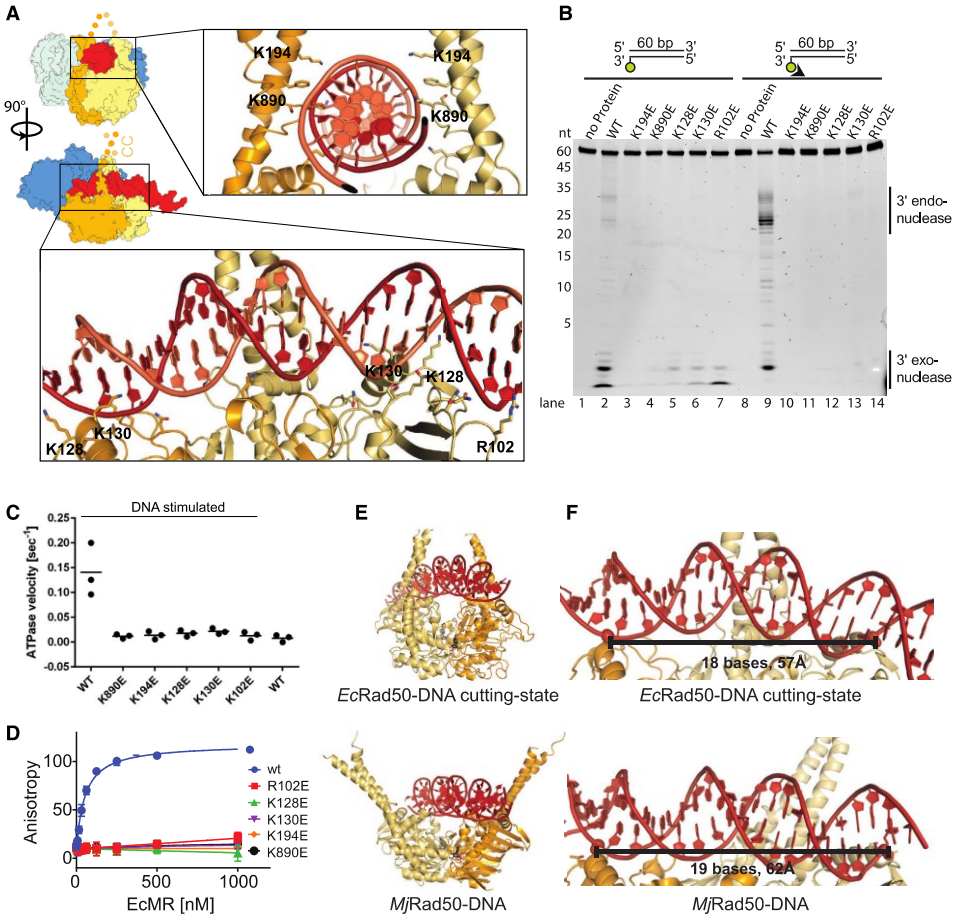

Figure 4. The CCs Form a Chemo-mechanical DNA Clamp

(A) Details of the interaction of DNA with the CCs (top panel) and the NBD (bottom panel) of *Ec*Rad50, showing that the CCs and NBDs form a narrow gate and clamp. Selected DNA binding residues are highlighted.

(B) Nuclease activity of *Ec*MR DNA binding mutants, analyzed with fluorescently labeled 60-bp DNA containing a free DNA end (DNA I) and a DNA end blocked by a single-chain fragment against fluorescein (DNA II). The *Ec*Rad50 DNA-binding lysine and arginine were mutated to glutamate.

(C) Analysis of DNA-stimulated ATPase activity. The DNA binding mutants show no stimulation of ATPase but basal ATPase activity (n = 3 technical replicates). The calculated mean is indicated by a black line. All ATP rates were measured with the nuclease dead $Mre11^{H84Q}$ mutant to avoid DNA degradation.

(D) DNA binding by fluorescence polarization anisotropy reveals that both NBD and CCs DNA binding residues are functionally critical (n = 3 technical repeats). Error bars indicate the standard deviation. All DNA binding measurements were done with the nuclease dead $Mre11^{H84Q}$ mutant to avoid DNA degradation.

(E) Comparison of the DNA interaction of the cryo-EM *Ec*MR cutting-state structure (left) with the X-ray structure of *Methanocaldococcus jannaschii* (Mj) Rad50-DNA (right).

(F) ADP-*Ec*MR cutting state (right) binds DNA with a 1-bp registry shift across the NBDs compared with ATPγS *Mj*Rad50 (left) because of CC-mediated upward bending and distortion of DNA.

See also Figure S6A.

except for a fairly narrow opening near the NBDs that accommodates one DNA duplex (Figure 3A). A second duplex between the CCs (such as through entrapping a loop) would possibly interfere with rod formation by preventing zipper contacts. Because the GEIR motif mutation suggests that CC geometry is very sensitively coupled to functional endonuclease, topological entrapment of a linear DNA end rather than a loop could confer endonuclease specificity toward DNA end structures.

To test this model, we analyzed a DNA fragment that contains biotin moieties on both ends and is either double-blocked in a linear (one streptavidin per end) or circular (both ends bound to one streptavidin) fashion. Addition of *Ec*MR leads to rapid

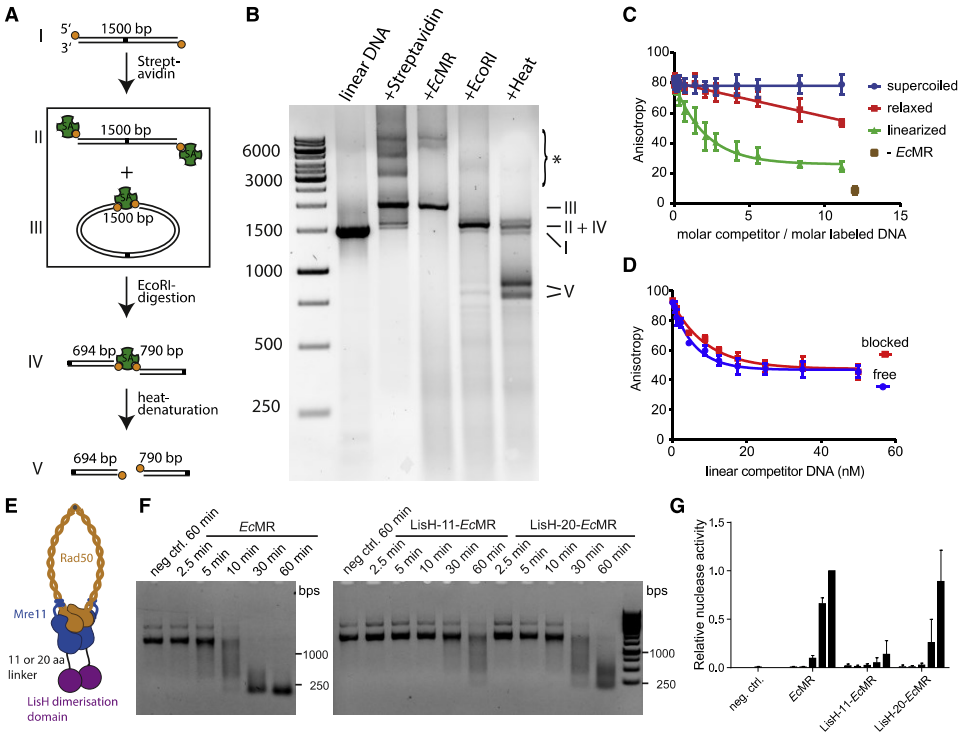

Figure 5. Loading onto Linear DNA Is Critical for the Processing of DNA Blocks

(A) Assay for processing of internal and terminal protein blocks. DNA with 5′ biotin (orange) is incubated with streptavidin (green), forming linear and circular species. After incubation with *Ec*MR, products are analyzed further using EcoRI digestion (black box) and heat denaturation.

(B) Streptavidin addition to linear DNA results in linear (~1,500-bp migration with one or two streptavidin-blocked DNA ends), circular (~2,000-bp migration), and different higher-order linear or circular species (asterisk). *Ec*MR leads to selective digestion of the linear species and some of the higher-order species, presumably the linear ones. In contrast, the circular species is stable. EcoRI addition and heat denaturation confirm the topology of the circular species.

(C) Linear but not relaxed or supercoiled circular DNA efficiently competes for binding to *Ec*MR with linear, 60-bp, fluorescently labeled DNA in fluorescence polarization anisotropy experiments (n = 3 technical replicates). Error bars indicate the standard deviation.

(D) Like (C), but using a linear competitor with free or protein-blocked ends (n = 3 technical replicates). Error bars indicate the standard deviation.

(E) Scheme of the LisH-*Ec*MR fusion approach to conformationally restrict and stabilize the Mre11 dimer.

(F) Time-dependent linear DNA degradation of 1,500-bp linear DNA containing a streptavidin block on both ends. WT *Ec*MR rapidly degrades DNA to short fragments, whereas LisH fusion proteins are severely (11-bp linker) or moderately (20-bp linker) compromised. Error bars indicate the standard deviation.

(G) Quantification of the occurrence of the less than 250-bp product over time in (F) (n = 3 technical replicates).

See also Figure S6.

degradation of the linear but not the circular product in the same reaction mixture, although both contain chemically identical protein-blocked nucleic acid termini (Figures 5A and 5B; Figure S6B). Consistently, *Ec*MR binds to linear plasmid DNA with higher affinity than circular supercoiled and relaxed DNA, regardless of whether the DNA end is free or protein blocked (Figures 5C and 5D). Because the only discriminating feature in these studies is the DNA topology, a plausible role of the CCs and their rod formation is the topological detection of DNA breaks through a gating mechanism; i.e., rods can form when a single duplex, but not a loop, threads through the CCs. In support of topological detection of blocks at linear DNA rather than direct chemical recognition of DNA termini, we also find cleavage of Ku70/80 blocked DNA ends by *Ec*MR with an inward-shifted cut site, as observed for eukaryotic MRN/MRX (Reginato et al., 2017; Wang et al., 2017; Figure S6C). Thus, *Ec*MRs biochemical properties are very similar to the eukaryotic MRN-CtBP-interacting protein (CtIP) in that it, too, cleaves at a defined distance from a stable protein-DNA complex, irrespective of the nature of the protein and the way it is bound to DNA. However, here we show that the block needs to be on linear DNA rather than within a DNA circle for recognition and cleavage, providing a DNA topology/accessibility mechanism for the recognition of broken DNA instead of chemical detection of free DNA termini.

Linking the Mre11 Dimer Slows Down Endonuclease

To load onto blocked DNA, the Mre11 dimer would need to relocate from its autoinhibited conformation over the protein block to

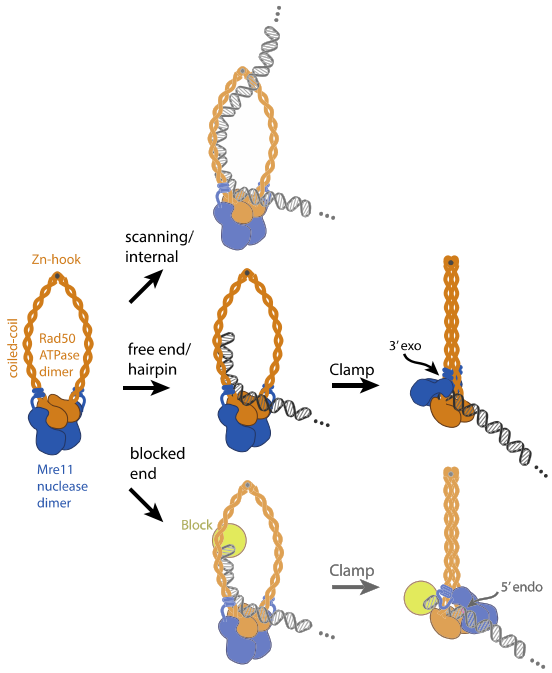

Figure 6. Model of DNA Sensing and Processing by MR

Proposed model of the sensing and cutting of DNA ends by *Ec*MR. Binding of internal DNA could lead to a scanning state (top panel). Encounter of a free (center panels) or blocked (bottom panel) DNA end would allow ring-to-rod transition of the CCs to form the high-affinity cutting state at or near DNA ends. Free DNA ends are bound directly by Mre11, as seen in the cryo-EM structure. Biochemical data suggest that a blocked end is bound in a reversed manner. See also Figure S7.

settle on the other side of DNA. Possibly, the Mre11 dimer transiently opens up for this to occur, which is reasonable because bacterial and archaeal $Mre11^{NUC}$ are monomeric in the absence of Rad50 (Figure S6D; Hopfner et al., 2001; Saathoff et al., 2018). We tested this hypothesis by fusing the Lis1 homology motif (LisH) dimerization domain (Delto et al., 2015) to the N terminus of *Ec*Mre11, which adds an additional tether between the two $Mre11^{NUC}$ domains (Figure 5E). LisH stabilizes the Mre11 dimer without leading to higher-order oligomers in *Ec*MR (Figures S6D and S6E). We assayed DNA degradation for two linker lengths between LisH and Mre11 (11 and 20 residues) using the linear DNA fragment with biotin-streptavidin blocks on both sides (Figure 5F). Degradation of long DNA proceeds by repetitive endonuclease reactions on both strands (Lim et al., 2015), and we consistently observed the appearance of short DNA (<250 bp) fragments. LisH-*Ec*MR degrades plasmids in a delayed manner. LisH-20-*Ec*MR's endonuclease is 3–5 times delayed, although it has normal exonuclease. LisH-11-*Ec*MR hardly shows any endonuclease products (Figure 5G), although its 3′→5′ exonuclease is only ~3 times reduced compared with the WT (Figures S6F and S6G). The lower exonuclease of LisH-11-*Ec*MR could originate from reduced loading on free DNA ends, which might be at least facilitated by dimer dynamics. The residual endonuclease activity of the 20-residue linker could be because it might allow Mre11 dimers to disengage and re-engage on the other side of DNA, with the LisH dimer remaining at the original side of DNA. In any case, our data suggest that the Mre11 dimer interface needs to be dynamic, especially for the endonuclease reaction.

DISCUSSION

Mre11 and Rad50 are phylogenetically conserved DNA end-processing machines (Paull, 2018; Syed and Tainer, 2018), required to clear aberrant or blocked terminal DNA structures and hairpins to enable repair and maintain genome integrity, but the mechanism of end recognition and processing by MR complexes has remained unclear. Using cryo-electron microscopy and biochemical analysis, we visualize resting and DNA cutting states of the *E. coli* MR complex, revealing how MR binds and processes DNA end structures. Our structures show that *Ec*MR adopts a nuclease-autoinhibited resting state in the absence of DNA. DNA binding induces a global conformational change that encompasses both the catalytic head module and the CC region, leading to rod formation of the CCs and repositioning of the Mre11 dimer to the side of the complex, where it assembles a DNA cutting channel and binds the free DNA end.

Combining our cryo-EM structures in the presence of ATPγS with AFM data in the absence of nucleotides (de Jager et al., 2004), a major state in the cellular environment could be M_2R_2, possibly joined into a proteinaceous ring by the Rad50 Zn-hook dimerization domains, although we do not want to rule out other configurations (Figure 6). Linear DNA could then induce the observed rod state in the CCs that enables and perhaps triggers relocalization of the Mre11 protein from an auto-inhibited state beneath the Rad50 NBDs to the active location at the side. The Zn-hooks would act as hinges and remain joined, consistent with crystallographic studies showing open and closed/rod states in the Zn-hooks (Hopfner et al., 2002; Park et al., 2017). Such a model is consistent with *in vivo* studies suggesting that the CCs functionally connect hook and head elements through transmission of structural changes (Hohl et al., 2015). We provide a putative mechanistic basis for this functional coupling *in vivo* because formation of stable zipper contacts along the CCs likely requires properly structured head and hook regions. The previously observed DNA-induced rod formation of human MRN CCs in low-resolution AFM analysis suggests that this global conformational switching is a conserved feature of MR/MRN/MRX complexes (Moreno-Herrero et al., 2005; Park et al., 2017).

The CCs might also act as linkers of distant DNA elements (de Jager et al., 2001; Hopfner et al., 2002; Seeber et al., 2016), in addition to the functions in DNA clamping and gating proposed here. Zn-hook dimerization might switch from intra- to intercomplex configurations, CC rods from different complexes could interact by other means, or additional DNA interactions in the CCs could mediate DNA tethering.

The CCs appear to be a critical structural switch with several functions, including topological gating to DNA ends and assembly of an active clamp for high-affinity DNA binding. The space

between the CCs near the NBDs can accommodate only one DNA duplex. A second duplex within the CCs might prevent, or at least interfere, with formation of a fully engaged rod with multiple zipper contacts, avoiding cutting of internal DNA because the clamp around DNA might not form properly (Figure 6). Evidence of such a global conformational role of CCs is supported by biochemical analysis showing that mutations in the DNA binding residues of the CCs, CC truncation, or mutation of the Zn-hook all have defective nuclease activity and no longer form high-affinity DNA interactions.

Although we do not see degradation of circular DNA, even in the presence of an "internal streptavidin-biotin" connecting two DNA ends (Figures 5A and 5B), *Ec*MR can still bind circular DNA. Circular DNA stimulates *Ec*MRs ATPase, so circular DNA likely interacts with Rad50's ATPase domains even though it is not cleaved (Saathoff et al., 2018). Likewise, human MRN can load to internal sites of DNA, followed by one-dimensional diffusion until a DNA end is reached and DNA cleavage occurs (Myler et al., 2017). Scanning is largely a property of the Rad50 protein and does not even require the full CCs in the human MRN setting, whereas end recognition requires Mre11, in agreement with our structure and consistent with the proposed model (Figure 6) (Myler et al., 2017). These peculiar properties could be explained if interactions with circular DNA, still triggering ATP hydrolysis at the NBDs, and with linear DNA are different. A possible explanation is the apparent restriction of a stable rod conformation to a single passage of DNA through the CCs (Figure 6).

Rod like-states could be a universal mechanistic feature of Rad50/SMC proteins because rod formation and structural changes are also proposed for the distantly related SMC protein family, which forms cohesin and condensin complexes (Diebold-Durand et al., 2017; Uhlmann, 2016). Although there are many underlying functional and structural differences, the general architecture of ABC ATPases coupled to CC rings/rods is quite conserved between SMC proteins and MR. For instance, the structural breaks in the CC rods that mediate the CC-CC zipper contacts are similar to structural elements found in Rad50's hook and MukB's elbow region, suggesting related architectural principles (Bürmann et al., 2019; Park et al., 2017). Thus, although the rod state of *Ec*MR appears to be adapted to passage of a single DNA duplex through the proteinaceous ring, a related mechanistic link between a certain number of DNA duplexes within SMC protein rings (or their absence) and the head module could be relevant for the dynamic interaction of SMC proteins with chromosomal DNA, as shown by recent biochemical analyses (Vazquez Nunez et al., 2019).

Our high-resolution structure of the cutting-state catalytic head reveals how MR detects and processes a DNA end through a new, previously unobserved asymmetric conformational state, where Mre11 binds to the side of Rad50 to assemble a DNA-processing channel (Figure 6). The transient formation of this channel and its structural properties offer an explanation of MR's broad nuclease reactions because it can accommodate different DNA structures. The channel readily accommodates a free DNA end, poised to cleave the 3′ strand exonucleolytically, consistent with the prevalence of 3′ exonuclease on free DNA ends. The channel could also accommodate nicked and bent dsDNA and hairpins, explaining why MR readily opens hairpin structures and can resect DNA 3′→5′ from the nick. The channel is also wide enough to accommodate internal dsDNA. However, internal DNA would need to be bent/melted to fit into the channel, and/or the protein adapts structurally. DNA bending/melting for efficient endonuclease is indeed suggested by biochemical studies (Cannon et al., 2013; Liu et al., 2016, ; Saathoff et al., 2018), and the structural effect of the CCs on DNA geometry and ATP-induced registry shifts of DNA along the NBDs are, in principle, well suited to provide chemo-mechanical means for triggering endonuclease activity. However, additional conformational states during the endonuclease reaction are possible as well. For instance, *Ec*MR-induced endonucleolytic cuts at opposing DNA strands occur with a different cleavage chemistry, suggesting an additional mode of DNA approach to the di-metal center (Saathoff et al., 2018). In addition, crystallographic analysis shows alternative DNA binding modes of the Mre11 nuclease dimer in the absence of Rad50 (Sung et al., 2014; Williams et al., 2008). Although DNA was not bound at the di-metal centers in these structures, these DNA contacts could represent states during DNA end tethering or endonucleolytic reactions. Thus, the requirement of the fastener-NBD interaction for endonucleolytic processing suggests that key aspects of the cutting state are also relevant for endonuclease, the precise mechanism of endonucleolytic processing of blocked DNA by MR requires future studies.

Our results provide some insights into the possible orientation of MR relative to the block in such a reaction. It is unlikely that the block is positioned directly at the exit of the active-site channel; i.e., the location of the DNA end in the observed cutting state. In such a scenario, DNA cleavage should occur closer to the end than observed experimentally. Both the distance between the block and the endonucleolytic cut sites and the cleavage chemistries in biochemical assays argue for location of the block at the Mre11 distal side (Saathoff et al., 2018; Figure 6). This model, suggesting that the CCs clamps are a filter for the block, would explain the fairly consistent distance between endonucleolytic cleavage and block (Cannavo and Cejka, 2014; Deshpande et al., 2016; Saathoff et al., 2018) and mechanistically unify 3′ exo- and 5′ endonuclease through a simple flip of the location of the Mre11 dimer relative to Rad50 on DNA. Loading of *Ec*MR in the flipped orientation would require transient dissociation of the Mre11 dimer, followed by reassembly on the other side of the DNA duplex (Figure 6). Our LisH fusion proteins indeed provide evidence that such transient disassembly is critical for endonuclease reactions but that reassembly of a functional Mre11 dimer on DNA is crucial because mutations that weaken the Mre11 dimer interface cripple *Ec*MR's endonuclease *in vitro* and MRN's function in *S. pombe in vivo* (Williams et al., 2008).

Finally, our results have implications for eukaryotic MRN/X, which requires Nbs1/Xrs2 and CtIP/Sae2 constitutive or transient subunits for efficient DNA processing *in vivo* (Hoa et al., 2016; Mimitou and Symington, 2008; Sartori et al., 2007) and *in vitro* (Anand et al., 2016; Cannavo and Cejka, 2014; Deshpande et al., 2016). Comparison of the bacterial MR cutting state with a model of a putative equivalent eukaryotic complex reveals that the fastener loop of *Ec*Mre11 binds precisely to the surface cluster of residues corresponding to *S. cerevisiae* Rad50S

mutations (Figure S7; Alani et al., 1990). Rad50S mutations phenocopy sae2Δ, cluster on a surface patch on the Rad50 NBDs, and have been proposed early on (Hopfner et al., 2000) and recently demonstrated to disrupt an interaction of Sae2 with Rad50 (Anand et al., 2016). Intriguingly, in *Ct*Mre11 (also *Sp*Mre11), this element is much shorter and conspicuously lacks the long loop that locks *Ec*Mre11^{NUC} to *Ec*Rad50^{NBD} at the "Rad50S" site. It is therefore possible that, instead of a Mre11-intrinsic fastener, the interaction of eukaryotic MRN in the cutting state could be mediated by CtIP/Sae2, which interacts at this site.

In summary, although structures of MRN-CtIP cutting states and structures of MR complexes bound to blocked DNA are needed to clarify activation of the eukaryotic system and the endonuclease activity of MR/MRN, we present structural and biochemical data that provide a new comprehensive framework and mechanistic concept for the detection and processing of diverse DNA ends by the Mre11-Rad50 nuclease complex.

STAR★METHODS

Detailed methods are provided in the online version of this paper and include the following:

- KEY RESOURCES TABLE
- LEAD CONTACT AND MATERIALS AVAILABILITY
- EXPERIMENTAL MODEL AND SUBJECT DETAILS
  - Organisms as source for materials used in experiments
- METHOD DETAILS
  - Expression and purification of EcMR
  - Expression and Purification of *Ct*Ku70/80
  - Nuclease assays
  - ATPase assays
  - DNA binding assays
  - Competitive DNA binding assay
  - Blocked dsDNA degradation assay
  - Circularization Assay
  - Size Exclusion Analysis
  - Cryo electron microscopy grid preparation
  - Cryo electron microscopy data collection
  - Data processing and 3D reconstruction
  - Model building
- QUANTIFICATION AND STATISTICAL ANALYSIS
- DATA AND CODE AVAILABILITY

SUPPLEMENTAL INFORMATION

Supplemental Information can be found online at https://doi.org/10.1016/j.molcel.2019.07.035.

ACKNOWLEDGMENTS

We thank the MPI Biochemistry cryo-EM facility and Mike Strauss for data collection and Dirk Kostrewa, Roland Beckmann, and Christophe Jung for technical help and suggestions. We thank Sebastian Eustermann for insightful discussions and help with modeling of the coiled-coil element. We thank Robert Thomas Byrne for help with data processing and Thomas Fröhlich for mass spectrometry. We thank Sandra Schuller for support in the initial grid preparation. K.-P.H. is supported by the Deutsche Forschungsgemeinschaft (CRC1361), the European Research Council (ERC Advanced Grant ATMMACHINE), the Gottfried-Wilhelm-Leibniz Prize, and the Center for Integrated Protein Sciences Munich (CIPSM). K.L. is supported by CRC1054. L.K. acknowledges support from the International Max Planck Research School of Molecular and Cellular Life Sciences. F.G. acknowledges support from Research Training Group 1721.

AUTHOR CONTRIBUTIONS

L.K. prepared cryo-EM grids and performed structure determination and modeling. J.-H.S., L.K., and F.G. performed the biochemical analysis. L.K., J.-H.S., and K.-P.H. analyzed results. L.K., J.-H.S., and B.K. purified the proteins. A.A. provided Ku70/80. K.L. and J.B. helped with data collection, structure determination, analysis, and modeling. K.P-H. and L.K. wrote the paper with contributions from all other authors. K.-P.H. designed the overall study.

DECLARATION OF INTERESTS

The authors declare no competing interests.

Received: March 22, 2019
Revised: June 17, 2019
Accepted: July 25, 2019
Published: September 3, 2019

SUPPORTING CITATIONS

The following references appear in the Supplemental Information: Ludwiczak et al. (2019); Zimmermann et al. (2018).

REFERENCES

Afonine, P.V., Poon, B.K., Read, R.J., Sobolev, O.V., Terwilliger, T.C., Urzhumtsev, A., and Adams, P.D. (2018). Real-space refinement in PHENIX for cryo-EM and crystallography. Acta Crystallogr. D Struct. Biol. *74*, 531–544.

Alani, E., Padmore, R., and Kleckner, N. (1990). Analysis of wild-type and rad50 mutants of yeast suggests an intimate relationship between meiotic chromosome synapsis and recombination. Cell *61*, 419–436.

Anand, R., Ranjha, L., Cannavo, E., and Cejka, P. (2016). Phosphorylated CtIP Functions as a Co-factor of the MRE11-RAD50-NBS1 Endonuclease in DNA End Resection. Mol. Cell *64*, 940–950.

Biasini, M., Bienert, S., Waterhouse, A., Arnold, K., Studer, G., Schmidt, T., Kiefer, F., Gallo Cassarino, T., Bertoni, M., Bordoli, L., et al. (2014). SWISS-MODEL: modelling protein tertiary and quaternary structure using evolutionary information. Nucleic Acids Res. *42*, W252–W258.

Bieniossek, C., Richmond, T.J., and Berger, I. (2008). MultiBac: multigene baculovirus-based eukaryotic protein complex production. Curr. Protoc. Protein Sci. *Chapter 5*, Unit 5.20.

Blackford, A.N., and Jackson, S.P. (2017). ATM, ATR, and DNA-PK: The Trinity at the Heart of the DNA Damage Response. Mol. Cell *66*, 801–817.

Bürmann, F., Lee, B.G., Than, T., Sinn, L., O'Reilly, F.J., Yatskevich, S., Rappsilber, J., Hu, B., Nasmyth, K., and Löwe, J. (2019). A folded conformation of MukBEF and cohesin. Nat. Struct. Mol. Biol. *26*, 227–236.

Cannavo, E., and Cejka, P. (2014). Sae2 promotes dsDNA endonuclease activity within Mre11-Rad50-Xrs2 to resect DNA breaks. Nature *514*, 122–125.

Cannon, B., Kuhnlein, J., Yang, S.H., Cheng, A., Schindler, D., Stark, J.M., Russell, R., and Paull, T.T. (2013). Visualization of local DNA unwinding by Mre11/Rad50/Nbs1 using single-molecule FRET. Proc. Natl. Acad. Sci. USA *110*, 18868–18873.

Carney, J.P., Maser, R.S., Olivares, H., Davis, E.M., Le Beau, M., Yates, J.R., 3rd, Hays, L., Morgan, W.F., and Petrini, J.H.J. (1998). The hMre11/hRad50 protein complex and Nijmegen breakage syndrome: linkage of double-strand break repair to the cellular DNA damage response. Cell *93*, 477–486.

Cejka, P. (2015). DNA End Resection: Nucleases Team Up with the Right Partners to Initiate Homologous Recombination. J. Biol. Chem. *290*, 22931–22938.

Chang, H.H.Y., Pannunzio, N.R., Adachi, N., and Lieber, M.R. (2017). Non-homologous DNA end joining and alternative pathways to double-strand break repair. Nat. Rev. Mol. Cell Biol. *18*, 495–506.

Ciccia, A., and Elledge, S.J. (2010). The DNA damage response: making it safe to play with knives. Mol. Cell *40*, 179–204.

Connelly, J.C., de Leau, E.S., and Leach, D.R. (2003). Nucleolytic processing of a protein-bound DNA end by the E. coli SbcCD (MR) complex. DNA Repair (Amst.) *2*, 795–807.

de Jager, M., van Noort, J., van Gent, D.C., Dekker, C., Kanaar, R., and Wyman, C. (2001). Human Rad50/Mre11 is a flexible complex that can tether DNA ends. Mol. Cell *8*, 1129–1135.

de Jager, M., Trujillo, K.M., Sung, P., Hopfner, K.-P., Carney, J.P., Tainer, J.A., Connelly, J.C., Leach, D.R.F., Kanaar, R., and Wyman, C. (2004). Differential arrangements of conserved building blocks among homologs of the Rad50/Mre11 DNA repair protein complex. J. Mol. Biol. *339*, 937–949.

Delto, C.F., Heisler, F.F., Kuper, J., Sander, B., Kneussel, M., and Schindelin, H. (2015). The LisH motif of muskelin is crucial for oligomerization and governs intracellular localization. Structure *23*, 364–373.

Deshpande, R.A., Lee, J.H., Arora, S., and Paull, T.T. (2016). Nbs1 Converts the Human Mre11/Rad50 Nuclease Complex into an Endo/Exonuclease Machine Specific for Protein-DNA Adducts. Mol. Cell *64*, 593–606.

Diebold-Durand, M.L., Lee, H., Ruiz Avila, L.B., Noh, H., Shin, H.C., Im, H., Bock, F.P., Burmann, F., Durand, A., Basfeld, A., et al. (2017). Structure of Full-Length SMC and Rearrangements Required for Chromosome Organization. Mol. Cell *67*, 334–347.e5.

Emsley, P., and Cowtan, K. (2004). Coot: model-building tools for molecular graphics. Acta Crystallogr. D Biol. Crystallogr. *60*, 2126–2132.

Eykelenboom, J.K., Blackwood, J.K., Okely, E., and Leach, D.R. (2008). SbcCD causes a double-strand break at a DNA palindrome in the Escherichia coli chromosome. Mol. Cell *29*, 644–651.

Falck, J., Coates, J., and Jackson, S.P. (2005). Conserved modes of recruitment of ATM, ATR and DNA-PKcs to sites of DNA damage. Nature *434*, 605–611.

Garcia, V., Phelps, S.E.L., Gray, S., and Neale, M.J. (2011). Bidirectional resection of DNA double-strand breaks by Mre11 and Exo1. Nature *479*, 241–244.

Goddard, T.D., Huang, C.C., Meng, E.C., Pettersen, E.F., Couch, G.S., Morris, J.H., and Ferrin, T.E. (2018). UCSF ChimeraX: Meeting modern challenges in visualization and analysis. Protein Sci. *27*, 14–25.

Herdendorf, T.J., Albrecht, D.W., Benkovic, S.J., and Nelson, S.W. (2011). Biochemical characterization of bacteriophage T4 Mre11-Rad50 complex. J. Biol. Chem. *286*, 2382–2392.

Hoa, N.N., Shimizu, T., Zhou, Z.W., Wang, Z.Q., Deshpande, R.A., Paull, T.T., Akter, S., Tsuda, M., Furuta, R., Tsutsui, K., et al. (2016). Mre11 Is Essential for the Removal of Lethal Topoisomerase 2 Covalent Cleavage Complexes. Mol. Cell *64*, 1010.

Hohl, M., Kwon, Y., Galván, S.M., Xue, X., Tous, C., Aguilera, A., Sung, P., and Petrini, J.H. (2011). The Rad50 coiled-coil domain is indispensable for Mre11 complex functions. Nat. Struct. Mol. Biol. *18*, 1124–1131.

Hohl, M., Kochańczyk, T., Tous, C., Aguilera, A., Krężel, A., and Petrini, J.H. (2015). Interdependence of the rad50 hook and globular domain functions. Mol. Cell *57*, 479–491.

Hopfner, K.P., Karcher, A., Shin, D.S., Craig, L., Arthur, L.M., Carney, J.P., and Tainer, J.A. (2000). Structural biology of Rad50 ATPase: ATP-driven conformational control in DNA double-strand break repair and the ABC-ATPase superfamily. Cell *101*, 789–800.

Hopfner, K.P., Karcher, A., Craig, L., Woo, T.T., Carney, J.P., and Tainer, J.A. (2001). Structural biochemistry and interaction architecture of the DNA double-strand break repair Mre11 nuclease and Rad50-ATPase. Cell *105*, 473–485.

Hopfner, K.-P., Craig, L., Moncalian, G., Zinkel, R.A., Usui, T., Owen, B.A.L., Karcher, A., Henderson, B., Bodmer, J.-L., McMurray, C.T., et al. (2002). The Rad50 zinc-hook is a structure joining Mre11 complexes in DNA recombination and repair. Nature *418*, 562–566.

Hustedt, N., and Durocher, D. (2016). The control of DNA repair by the cell cycle. Nat. Cell Biol. *19*, 1–9.

Jermutus, L., Honegger, A., Schwesinger, F., Hanes, J., and Plückthun, A. (2001). Tailoring in vitro evolution for protein affinity or stability. Proc. Natl. Acad. Sci. USA *98*, 75–80.

Kowalczykowski, S.C. (2015). An Overview of the Molecular Mechanisms of Recombinational DNA Repair. Cold Spring Harb. Perspect. Biol. *7*, a016410.

Lammens, K., Bemeleit, D.J., Möckel, C., Clausing, E., Schele, A., Hartung, S., Schiller, C.B., Lucas, M., Angermüller, C., Söding, J., et al. (2011). The Mre11:Rad50 structure shows an ATP-dependent molecular clamp in DNA double-strand break repair. Cell *145*, 54–66.

Lim, H.S., Kim, J.S., Park, Y.B., Gwon, G.H., and Cho, Y. (2011). Crystal structure of the Mre11-Rad50-ATPγS complex: understanding the interplay between Mre11 and Rad50. Genes Dev. *25*, 1091–1104.

Lim, C.T., Lai, P.J., Leach, D.R., Maki, H., and Furukohri, A. (2015). A novel mode of nuclease action is revealed by the bacterial Mre11/Rad50 complex. Nucleic Acids Res. *43*, 9804–9816.

Liu, Y., Sung, S., Kim, Y., Li, F., Gwon, G., Jo, A., Kim, A.K., Kim, T., Song, O.K., Lee, S.E., and Cho, Y. (2016). ATP-dependent DNA binding, unwinding, and resection by the Mre11/Rad50 complex. EMBO J. *35*, 743–758.

Ludwiczak, J., Winski, A., Szczepaniak, K., Alva, V., and Dunin-Horkawicz, S. (2019). DeepCoil - a fast and accurate prediction of coiled-coil domains in protein sequences. Bioinformatics. Published online January 2, 2019. https://doi.org/10.1093/bioinformatics/bty1062.

Mastronarde, D.N. (2005). Automated electron microscope tomography using robust prediction of specimen movements. J. Struct. Biol. *152*, 36–51.

Mimitou, E.P., and Symington, L.S. (2008). Sae2, Exo1 and Sgs1 collaborate in DNA double-strand break processing. Nature *455*, 770–774.

Möckel, C., Lammens, K., Schele, A., and Hopfner, K.P. (2012). ATP driven structural changes of the bacterial Mre11:Rad50 catalytic head complex. Nucleic Acids Res. *40*, 914–927.

Moreno-Herrero, F., de Jager, M., Dekker, N.H., Kanaar, R., Wyman, C., and Dekker, C. (2005). Mesoscale conformational changes in the DNA-repair complex Rad50/Mre11/Nbs1 upon binding DNA. Nature *437*, 440–443.

Myler, L.R., Gallardo, I.F., Soniat, M.M., Deshpande, R.A., Gonzalez, X.B., Kim, Y., Paull, T.T., and Finkelstein, I.J. (2017). Single-Molecule Imaging Reveals How Mre11-Rad50-Nbs1 Initiates DNA Break Repair. Mol. Cell *67*, 891–898.e4.

Myung, K., Chen, C., and Kolodner, R.D. (2001). Multiple pathways cooperate in the suppression of genome instability in Saccharomyces cerevisiae. Nature *411*, 1073–1076.

Neale, M.J., Pan, J., and Keeney, S. (2005). Endonucleolytic processing of covalent protein-linked DNA double-strand breaks. Nature *436*, 1053–1057.

Oh, J., Al-Zain, A., Cannavo, E., Cejka, P., and Symington, L.S. (2016). Xrs2 Dependent and Independent Functions of the Mre11-Rad50 Complex. Mol. Cell *64*, 405–415.

Park, Y.B., Hohl, M., Padjasek, M., Jeong, E., Jin, K.S., Krężel, A., Petrini, J.H., and Cho, Y. (2017). Eukaryotic Rad50 functions as a rod-shaped dimer. Nat. Struct. Mol. Biol. *24*, 248–257.

Paull, T.T. (2018). 20 Years of Mre11 Biology: No End in Sight. Mol. Cell *71*, 419–427.

Paull, T.T., and Gellert, M. (1998). The 3′ to 5′ exonuclease activity of Mre 11 facilitates repair of DNA double-strand breaks. Mol. Cell *1*, 969–979.

Paull, T.T., and Gellert, M. (1999). Nbs1 potentiates ATP-driven DNA unwinding and endonuclease cleavage by the Mre11/Rad50 complex. Genes Dev. *13*, 1276–1288.

Pedrazzi, G., Schwesinger, F., Honegger, A., Krebber, C., and Plückthun, A. (1997). Affinity and folding properties both influence the selection of antibodies with the selectively infective phage (SIP) methodology. FEBS Lett. *415*, 289–293.

Pettersen, E.F., Goddard, T.D., Huang, C.C., Couch, G.S., Greenblatt, D.M., Meng, E.C., and Ferrin, T.E. (2004). UCSF Chimera–a visualization system for exploratory research and analysis. J. Comput. Chem. *25*, 1605–1612.

Punjani, A., Rubinstein, J.L., Fleet, D.J., and Brubaker, M.A. (2017). cryoSPARC: algorithms for rapid unsupervised cryo-EM structure determination. Nat. Methods *14*, 290–296.

Rahal, E.A., Henricksen, L.A., Li, Y., Williams, R.S., Tainer, J.A., and Dixon, K. (2010). ATM regulates Mre11-dependent DNA end-degradation and microhomology-mediated end joining. Cell Cycle *9*, 2866–2877.

Reginato, G., Cannavo, E., and Cejka, P. (2017). Physiological protein blocks direct the Mre11-Rad50-Xrs2 and Sae2 nuclease complex to initiate DNA end resection. Genes Dev. *31*, 2325–2330.

Rohou, A., and Grigorieff, N. (2015). CTFFIND4: Fast and accurate defocus estimation from electron micrographs. J. Struct. Biol. *192*, 216–221.

Saathoff, J.H., Käshammer, L., Lammens, K., Byrne, R.T., and Hopfner, K.P. (2018). The bacterial Mre11-Rad50 homolog SbcCD cleaves opposing strands of DNA by two chemically distinct nuclease reactions. Nucleic Acids Res. *46*, 11303–11314.

Sartori, A.A., Lukas, C., Coates, J., Mistrik, M., Fu, S., Bartek, J., Baer, R., Lukas, J., and Jackson, S.P. (2007). Human CtIP promotes DNA end resection. Nature *450*, 509–514.

Scheres, S.H. (2012). RELION: implementation of a Bayesian approach to cryo-EM structure determination. J. Struct. Biol. *180*, 519–530.

Seeber, A., Hegnauer, A.M., Hustedt, N., Deshpande, I., Poli, J., Eglinger, J., Pasero, P., Gut, H., Shinohara, M., Hopfner, K.P., et al. (2016). RPA Mediates Recruitment of MRX to Forks and Double-Strand Breaks to Hold Sister Chromatids Together. Mol. Cell *64*, 951–966.

Seifert, F.U., Lammens, K., Stoehr, G., Kessler, B., and Hopfner, K.P. (2016). Structural mechanism of ATP-dependent DNA binding and DNA end bridging by eukaryotic Rad50. EMBO J. *35*, 759–772.

Sung, S., Li, F., Park, Y.B., Kim, J.S., Kim, A.K., Song, O.K., Kim, J., Che, J., Lee, S.E., and Cho, Y. (2014). DNA end recognition by the Mre11 nuclease dimer: insights into resection and repair of damaged DNA. EMBO J. *33*, 2422–2435.

Syed, A., and Tainer, J.A. (2018). The MRE11-RAD50-NBS1 Complex Conducts the Orchestration of Damage Signaling and Outcomes to Stress in DNA Replication and Repair. Annu. Rev. Biochem. *87*, 263–294.

Tang, G., Peng, L., Baldwin, P.R., Mann, D.S., Jiang, W., Rees, I., and Ludtke, S.J. (2007). EMAN2: an extensible image processing suite for electron microscopy. J. Struct. Biol. *157*, 38–46.

Uhlmann, F. (2016). SMC complexes: from DNA to chromosomes. Nat. Rev. Mol. Cell Biol. *17*, 399–412.

van Dijk, M., and Bonvin, A.M. (2009). 3D-DART: a DNA structure modelling server. Nucleic Acids Res. *37*, W235-9.

Vazquez Nunez, R., Ruiz Avila, L.B., and Gruber, S. (2019). Transient DNA Occupancy of the SMC Interarm Space in Prokaryotic Condensin. Mol. Cell *75*, 209–223.e6.

Wang, W., Daley, J.M., Kwon, Y., Krasner, D.S., and Sung, P. (2017). Plasticity of the Mre11-Rad50-Xrs2-Sae2 nuclease ensemble in the processing of DNA-bound obstacles. Genes Dev. *31*, 2331–2336.

Wendel, B.M., Cole, J.M., Courcelle, C.T., and Courcelle, J. (2018). SbcC-SbcD and ExoI process convergent forks to complete chromosome replication. Proc. Natl. Acad. Sci. USA *115*, 349–354.

Williams, R.S., Moncalian, G., Williams, J.S., Yamada, Y., Limbo, O., Shin, D.S., Groocock, L.M., Cahill, D., Hitomi, C., Guenther, G., et al. (2008). Mre11 dimers coordinate DNA end bridging and nuclease processing in double-strand-break repair. Cell *135*, 97–109.

Williams, G.J., Williams, R.S., Williams, J.S., Moncalian, G., Arvai, A.S., Limbo, O., Guenther, G., SilDas, S., Hammel, M., Russell, P., and Tainer, J.A. (2011). ABC ATPase signature helices in Rad50 link nucleotide state to Mre11 interface for DNA repair. Nat. Struct. Mol. Biol. *18*, 423–431.

Wright, W.D., Shah, S.S., and Heyer, W.D. (2018). Homologous recombination and the repair of DNA double-strand breaks. J. Biol. Chem. *293*, 10524–10535.

Zheng, S.Q., Palovcak, E., Armache, J.P., Verba, K.A., Cheng, Y., and Agard, D.A. (2017). MotionCor2: anisotropic correction of beam-induced motion for improved cryo-electron microscopy. Nat. Methods *14*, 331–332.

Zimmermann, L., Stephens, A., Nam, S.Z., Rau, D., Kübler, J., Lozajic, M., Gabler, F., Söding, J., Lupas, A.N., and Alva, V. (2018). A Completely Reimplemented MPI Bioinformatics Toolkit with a New HHpred Server at its Core. J. Mol. Biol. *430*, 2237–2243.

CellPress

STAR★METHODS

KEY RESOURCES TABLE

REAGENT or RESOURCE	SOURCE	IDENTIFIER
Chemicals, Peptides, and Recombinant Proteins		
ATP	Sigma	A3377
ATPγS	Sigma	A1388
ADP	Sigma	A0752
2-Mercaptoethanol	Carl Roth	4227
DTT	Carl Roth	6908
Imidazole	Carl Roth	3899
b-Octylglycoside	Sigma	O8001
BSA	New England bioLabs	B9000S
FAM-scFv	Prof. Dr. Plückthun, University of Zürich Pedrazzi et al., 1997; Jermutus et al., 2001	N/A
Bradford Roti_Quant	Carl Roth	K015
Urea	Carl Roth	3941
EDTA	VWR International	6381-92-6
Ficoll 400	Carl Roth	CN90.3
Rotiphorese DNA sequencing system	Carl Roth	A431.1
MgCl2	Merck	7791-18-6
$MnCl_2$	Sigma	M3634
Streptavidin	IBA	2-0203-100
Pyruvat kinase/Lactatic dehydrogenase from rabbit muscle	Sigma	P0294
Phosphoenol Pyruvate	ITW Reagents	A2271
NADH	Carl Roth	AE12
TCEP	Sigma	646547
SIGMAFAST Protease Inhibitor Cocktail Tablet, EDTA free	Merck	S8830
GeneRuler 1 kb DNA Ladder	Thermo Fisher Scientific	SM0311
Deposited Data		
*Ec*MR coordinates (resting state)	This Paper	PDB: 6S6V
*Ec*MR head EM map (resting state)	This Paper	EMDB: EMD-10107
*Ec*MR coordinates (cutting state)	This Paper	PDB: 6S85
*Ec*MR head EM map (cutting state)	This Paper	EMDB: EMD-10116
*Ec*MR head with longer coiled coils EM map	This Paper	EMDB: EMD-10114
*Ec*MR head with long coiled coils, low resolution EM map	This Paper	EMDB: EMD-10115
Full Gel Images	This Paper	https://doi.org/10.17632/g5ypj2dyj2.1
Experimental Models: Cell Lines		
E. coli Rosetta	Expression Systems	N/A
E. coli BL21	Expression Systems	N/A
E. coli XL1 Blue	Expression Systems	N/A
Spodoptera frugiperda sf21 cells	Expression Systems	N/A
Trichoplusia ni cells	Expression Systems	N/A

(*Continued on next page*)

CellPress

Continued

REAGENT or RESOURCE	SOURCE	IDENTIFIER
Oligonucleotides		
Oligonucleotides	Metabion	N/A, See Table S1
Recombinant DNA		
pET21b-*Ec*Mre11	Saathoff et al., 2018	N/A
pET29-*Ec*Rad50	Saathoff et al., 2018	N/A
pACEBac1-pIDK-*Ct*Ku70/80	This Paper	N/A
pBR322	Fermentas	SD0041
Software and Algorithms		
SerialEM	Mastronarde, 2005	http://bio3d.colorado.edu/SerialEM/
MotionCor2	Zheng et al., 2017	https://msg.ucsf.edu/em/software/motioncor2.html
CTFFind4.1	Rohou and Grigorieff, 2015	http://grigoriefflab.janelia.org/ctffind4
Relion 2.1b1	Scheres, 2012	https://www3.mrc-lmb.cam.ac.uk/relion/index.php?title=Main_Page
Phenix	Afonine et al., 2018	https://www.phenix-online.org/
UCSF Chimera	Pettersen et al., 2004	https://www.cgl.ucsf.edu/chimera/
Pymol	Schrödinger	https://pymol.org/2/
Chimera X	Goddard et al., 2018	https://www.rbvi.ucsf.edu/chimerax/
COOT	Emsley and Cowtan, 2004	https://www2.mrc-lmb.cam.ac.uk/Personal/pemsley/coot/
Prism	GraphPad	N/A
EMAN2	Tang et al., 2007	http://blake.bcm.tmc.edu/EMAN2/
CryoSPARC	Punjani et al., 2017	https://cryosparc.com/
SWISS-MODEL server	Biasini et al., 2014	https://swissmodel.expasy.org/
3D-DART	van Dijk and Bonvin, 2009	http://haddock.chem.uu.nl/dna/dna.php
Gautomatch	Dr. Jack Zhang	https://www.mrc-lmb.cam.ac.uk/kzhang/

LEAD CONTACT AND MATERIALS AVAILABILITY

Further information and requests for resources and reagents should be directed to and will be fulfilled by the Lead Contact Karl-Peter Hopfner (hopfner@genzentrum.lmu.de).

EXPERIMENTAL MODEL AND SUBJECT DETAILS

Organisms as source for materials used in experiments

E. coli XL1 Blue cells were used for amplification of plasmid DNA.
E. coli BL21 (DE3) and *E.coli* Rosetta2 were used for recombinant protein expression.
Spodoptera frugiperda sf21 insect cells were used for virus production.
Trichoplusia ni insect cells were used for recombinant protein expression.

METHOD DETAILS

Expression and purification of EcMR

*Ec*Mre11^{fl} (cloned in pET21b, 6xHis-tag) and *Ec*Rad50^{fl} (cloned in pET29) were co-transfected into *E. coli* BL21 or Rosetta cells (Novagen). *E. coli* cultures were grown in LB medium at 37°C to an OD_{600} of 0.6. Protein expression was induced with 0.5 mM IPTG and carried out for 16 h at 18°C. The cells were harvested by centrifugation and the pellet was resuspended in lysis buffer (25 mM Tris pH 7.5, 150 mM NaCl, 10 mM Imidazole and 5 mM β-Mercaptoethanol) before cell disruption by sonication. The cell lysate was cleared by centrifugation and the supernatant was applied onto 2.5 mL of pre-equilibrated Ni-NTA (QIAGEN). The beads were washed with 20 mL lysis buffer and 25 mL wash buffer (25 mM Tris pH 7.5, 125 mM NaCl, 20 mM Imidazole and 5 mM β-Mercaptoethanol). The protein was eluted with 10 mL elution buffer (25 mM Tris pH 7.5, 100 mM NaCl, 200 mM Imidazole and 5 mM

β-Mercaptoethanol). The eluate was applied onto a 1 mL HiTrapQ column (GE) and eluted by a step gradient with increasing salt (Buffer A: 100 mM NaCl, 25 mM Tris pH 7.5, Buffer B: 1 M NaCl, 25 mM Tris pH 7.5). The peak fractions were pooled, concentrated and purified via size-exclusion chromatography using a Superose 6 10/300 (GE Healthcare) column in size-exclusion buffer (125 mM NaCl, 20 mM Tris pH 7.5, 10% Glycerol). The protein fractions of interest were pooled, concentrated, flash frozen and stored at −80°C until further use.

Expression and Purification of *Ct*Ku70/80

Codon-optimized synthetic DNA (Genscript, Piscataway, USA) encoding *ct*Ku70 (N-terminal human rhinovirus 3C-protease cleavable 6xHis-tag) and *ct*Ku80 was PCR amplified and cloned into pACEBac1 and pIDC respectively and expressed using the MultiBac technology (Bieniossek et al., 2008). Recombination steps were carried out in *Escherichia coli* XL1Blue cells (Stratagene) under addition of Cre recombinase (NEB). Baculoviruses were generated in *Spodoptera frugiperda* (SF21) insect cells (IPLB-Sf21AE). *Trichoplusia ni* High Five cells (Invitrogen) were co-infected with 1:5000 of baculovirus. Cells were cultured for 72 h at 27°C and harvested by centrifugation.

For purification, cells from 250 mL cells were disrupted in lysis buffer (50 mM HEPES pH 7.5, 1 M NaCl, 400 mM NH_4OAc, 5% glycerol, 0.5 mM TCEP supplemented with a SIGMAFAST Protease Inhibitor Cocktail Tablet, EDTA free (Merck)) and gently sonified. Raw lysate was incubated for 1 h at 50°C and subsequently cleared by centrifugation at 34500 g and 4°C for 30 min. The supernatant was applied onto 2 mL of pre-equilibrated Ni-NTA (QIAGEN). The beads were washed with 20 mL wash buffer (50 mM HEPES pH 7.5, 250 mM NaCl, 10 mM Imidazole and 0.5 mM TCEP). The protein was eluted with 10 mL elution buffer (50 mM HEPES pH 7.5, 250 mM NaCl, 500 mM Imidazole and 0.5 mM TCEP). The affinity tag was cleaved by overnight incubation with human rhinovirus 3C-protease at 4 °C during dialysis into low salt buffer (50 mM HEPES pH 7.5, 150 mM NaCl and 0.5 mM TCEP). The filtered protein was loaded onto a 5 mL HiTrap Heparin HP column (GE Healthcare), equilibrated in the dialysis buffer and eluted with an increasing salt gradient. The peak fractions were pooled, concentrated and purified via size-exclusion chromatography using a Superose 6 16/60 (GE Healthcare) column in size-exclusion buffer (20 mM HEPES pH 7.5, 200 mM NaCl and 0.5 mM TCEP). The protein fractions of interest were identified by SDS-PAGE, pooled, concentrated, flash-frozen in liquid N_2 and stored at −80 °C until required.

Nuclease assays

The nuclease reaction was carried out in assay buffer (25 mM Tris pH 7.5, 50 mM KCl, 5 mM $MgCl_2$, 1 mM $MnCl_2$, 0.1 mg/ml BSA, 1 mM DTT, 1 mM ATP) with 250 nM *Ec*MR and 50 nM 6-FAM labeled 60 bp dsDNA substrate. Where indicated, reactions were supplemented with a 15-fold excess of a single-chain variable fragment against fluorescein (FAM-scFv) to generate a blocked DNA end (Pedrazzi et al., 1997). Prior to each nuclease reaction, the precise *Ec*MR-concentration was determined according to Bradford using the Roti-Quant solution (Roth). The reaction was started by protein addition and incubated at 37°C for 5 min for a blocked dsDNA end and for 15 min for an unblocked dsDNA. 10 μL of each reaction was terminated by mixing equal volume of loading buffer (8 M Urea, 20 mM EDTA, 6% Ficoll 400). The reaction products were resolved on 12% denaturing polyacrylamide gels (Rotiphorese® DNA sequencing system) in 1x TBE buffer. Gels were run at 90 min at a constant power of 32 W and scanned by a Typhoon fluorescence imager (GE healthcare). FAM-labeled substrates were imaged with a 473 nm Laser and 510 nm filter. The images were analyzed and integrated with the ImageJ software.

ATPase assays

We applied an NADH-coupled assay to monitor the ATP-hydrolysis rate of *Ec*Mre11-Rad50. *Ec*MR (250 nM) was incubated at 37°C in assay buffer (25 mM Tris pH 7.5, 50 mM KCl, 5 mM $MgCl_2$, 1 mM $MnCl_2$, 1 mM ATP, 0.1 mg/ml BSA, 1 mM DTT) in the presence of NADH (0.35 mM), pyruvate kinase/lactate dehydrogenase (20 U/ml PK, 30 U/ml LDH, Sigma) and Phosphoenol Pyruvate (2 mM). To stimulate *Ec*MR's ATPase activity, a 60 bp DNA (1000 nM) was added. The rate of NADH oxidation was monitored fluorometrically by measuring the absorbance at 340 nm on an Infinite M1000 microplate reader (Tecan) over a period of 20 minutes. ATP turnover was calculated using the steady-state rate and corrected for a buffer blank. All ATP rates were measured with the nuclease dead $Mre11^{H84Q}$ mutant to avoid DNA degradation.

DNA binding assays

Fluorescence polarization anisotropy was used to monitor the interaction between *Ec*MR and 35 bp DNA. 2.5 nM of 5′ Fluorescein-labeled DNA was incubated with increasing concentrations of *Ec*MR in assay buffer (25 mM Tris pH 7.5, 50 mM KCl, 1 mM ATP, 5 mM $MgCl_2$, 1 mM $MnCl_2$, 1 mM DTT). After 20 minutes at 25°C, the fluorescence anisotropy was measured at an excitation wavelength of 470 nM and emission wavelength of 520 nM. All DNA binding measurements were measured with the nuclease dead $Mre11^{H84Q}$ mutant to avoid DNA degradation. Data were analyzed with Prism (GraphPad) and K_D values determined by fitting the anisotropy data to a bimolecular equilibrium model:

$$Y = Af - (Af - Ab)\frac{x}{Kd - x}$$

CellPress

Competitive DNA binding assay

For the competition assays, fluorescence polarization anisotropy was used to monitor the interaction between *Ec*MR and long DNA substrates. 2.5 nM of 35 bp 5′ Fluorescein-labeled DNA was incubated with 50 nM $EcM^{H84Q}R$ for 20 minutes at 25°C in assay buffer (25 mM Tris pH 7.5, 50 mM KCl, 1 mM ATP, 5 mM MgCl2, 1 mM MnCl2, 1 mM DTT). For the competition reaction, increasing concentrations of plasmid DNA (pBR322) or 5′ biotinylated 1500 bp were added and incubated for 20 minutes at 25°C. The fluorescence anisotropy was measured at an excitation wavelength of 470 nM and emission wavelength of 520 nM. The anisotropy data were fit with Prism (GraphPad).

Blocked dsDNA degradation assay

To test for degradation of linear and circular DNA with a protein block, a 1500 basepair fragment was amplified by PCR using pET21b vector as template and 5′ biotinylated primers (for: ccgcgcacatttccccgaaaagtgcc, rev: ccagttgatcggcgcgagatttaatcg). DNA ends were blocked in assay buffer (25 mM Tris pH 7.5, 50 mM KCl, 1mM ATP, 5 mM $MgCl_2$, 1 mM $MnCl_2$, 0.1 mg/ml BSA, 1 mM DTT) with 52 nM DNA and 5 μM streptavidin at 20°C. The nuclease reaction was started by adding 50 nM of *Ec*MR and incubated at 37°C. Quenching of the reaction was done after 0, 2.5, 5, 10, 30 and 60 minutes by adding 1.5 μl 200 mM EDTA per 6 μl reaction mix. For agarose gel electrophoresis 6 μl reaction mix were diluted with 14 μl 1.6x loading dye and 8 μl of each sample were then separated by horizontal agarose gel electrophoresis. The DNA and degradation products were separated by horizontal agarose gel electrophoresis and imaged with a Typhoon fluorescence imager (GE healthcare) using 473 nm Laser and 510 nm filter. Degradation products and educts were quantified using ImageJ.

Circularization Assay

Circularization of 5′ biotinylated 1500 bp dsDNA was carried out in assay buffer (25 mM Tris pH 7.5, 50 mM KCl, 1mM ATP, 5 mM $MgCl_2$, 1 mM $MnCl_2$, 0.1 mg/ml BSA, 1 mM DTT) with 20 nM DNA and 10 nM streptavidin at 20°C. The nuclease reaction was started by adding 200 nM of *Ec*MR and incubated 10 minutes at 37°C. The DNA and degradation products were separated by horizontal agarose gel electrophoresis and imaged with a Typhoon fluorescence imager (GE healthcare) using 473 nm Laser and 510 nm filter.

Size Exclusion Analysis

For the size exclusion analysis of *Ec*MR without ATP and DNA, 20 μl of *Ec*MR were mixed with 30 μl SEC buffer I (50 mM KCl, 20 mM Tris pH 7.5). For *Ec*MR in complex with ATP, 20 μl *Ec*MR were mixed with 5 μl 10x buffer (10 mM ATP, 10 mM $MnCl_2$, 50 mM $MgCl_2$) and 25 μl SEC buffer I. For *Ec*MR in complex with ATP and DNA, 20 μl of *Ec*MR were mixed with 5 μl 10x buffer and 25 μl DNA (18 μM, 60 bp). All three samples were incubated at room temperature for 30 min and centrifuged with a table top centrifuge at full speed for 10 min. 50 μl of the mixture were injected onto a S6 5/150 column. For the sample without ATP and DNA SEC buffer I was used. For the samples with ATP and ATP and DNA SEC buffer II was used (50 mM KCl, 20 mM Tris pH 7.5, 5 mM $MgCl_2$, 1 mM $MnCl_2$, 1 mM ATP).

Cryo electron microscopy grid preparation

For the resting state *Ec*MR:ATPγS complex, full length *Ec*MR was purified as described previously with the exception that for the buffers 2 mM DTT instead of 5 mM β-mercaptoethanol were used. After the ion exchange chromatography, the protein was pooled, aliquoted and snap-frozen in liquid nitrogen. Prior to grid preparation the *Ec*MR was thawed and purified via size exclusion chromatography using a S6 5/150 column (buffer: 50 mM KCl, 20 mM HEPES, pH 7.5). The peak fraction was diluted to a final concentration of 0.4 mg/ml and mixed with 10x buffer (10 mM $MnCl_2$, 25 mM $MgCl_2$ and 10 mM ATPγS). Right before grid preparation 5 μL β-octyl glucoside were added to a final concentration of 0.05%. 4.5 μL of the protein solution were applied to Quantifoil R2/1 holey carbon grids and frozen in liquid ethane using a Leica EM GP (Leica, 15°C and 95% humidity).

For the cutting state *Ec*MR:DNA complex, 10x Buffer (10 mM $MnCl_2$, 25 mM $MgCl_2$ and 10 mM ATP) were mixed with 60 bp dsDNA (fwd: 5′-CGCTTTATCAGAAGCCAGACATTAACGCTTC TGGAGAAACTCAACGAGCTGGACGCGGAT-3′) and the peak fraction of $EcM^{H84S}R$ was added. Two datasets were collected on the *Ec*MR:DNA complex with a protein:DNA ratio of 1:5 (dataset I) and 1:3 (dataset II) and protein concentrations of 0.3 mg/ml and 0.5 mg/ml, respectively. For incubation the complex was left on ice for at least 30 min and the protein solution was applied to Quantifoil R2/1 holey carbon grids and frozen in liquid ethane using a Vitrobot IV (FEI, 4°C and 95% humidity).

Cryo electron microscopy data collection

Data was collected with a FEI Titan Krios transmission electron microscope (300 kV) using a Gatan K2 detector and a Gatan GIF Quantum energy filter (slit width 20 eV). SerialEM was used for data acquisition using customized scripts from Mike Strauss (Mastronarde, 2005). For the resting state *Ec*MR:ATPγS complex 8186 micrographs were collected with a pixel size of 1.06 Å and a total electron dose of 68 $e^-/Å^2$. A defocus from −1.0 to −3.5 μM was used and 50 frames were collected in 10 s (0.2 s/frame).

For the cutting state $EcM^{H84S}R$:DNA complex two datasets were collected with 9336 (dataset I) and 3475 (dataset II) micrographs. Both datasets were collected with a pixel size of 0.82 Å and a total electron dose of 73.6 $e^-/Å^2$ dataset I and II. A defocus from −1.0 to −3.5 μm was used and 25 frames were collected in 5 s (0.2 s/frame).

CellPress

Data processing and 3D reconstruction

Motioncor2 (Zheng et al., 2017) was used to align the micrographs. Subsequently, the aligned micrographs were used for determining the correlation transfer function with CTFFind 4.1 (Rohou and Grigorieff, 2015). Respectively, 6895 micrographs were selected for the resting state reconstruction. Unless stated otherwise all processing steps were performed with RELION 2.1b1 (Scheres, 2012). The gold standard Fourier shell correlation 0.143 criterion was used to determine the resolutions of the reconstructions. RELION was used for automatic B-factor determination. The exact processing schemes including particle numbers are illustrated in Figure S1 and S3. For the resting state reconstruction, initial manual picking was performed with EMAN2 (Tang et al., 2007) and 1607 particles were picked manually. From the picked particles, 2D classes were calculated using RELION2.1b1. The four best classes were low pass filtered to 20 Å and used for autopicking on a subset of 2935 micrographs (subset I). From these micrographs, 998 166 particles were picked and subjected to 2D classification and classes with clearly defined features were selected. A subset of these particles was used to calculate an initial 3D model using CryoSPARC (Punjani et al., 2017). An initial 3D classification with six classes and C1 symmetry resulted in a reconstruction that was further used as reference. In parallel 2D classes calculated from subset I and low pass filtered to 20 Å were used for autopicking on all 6895 micrographs and in total 2 809 916 particles were picked. After 2D classification 1 187 179 particles were subjected to 3D classification (C2 symmetry) and from these four classes, the best two classes were selected for further processing. Further sorting and 2D classification, yielded a dataset with 472836 particles. 3D Classification into two classes resulted in two reconstructions, one with well-defined *Ec*Mre11 HLH motif and beginning of the *Ec*Rad50 coiled-coils (30%) and one where this part is less well defined (70%). The map with a well defined HLH motif contained 142229 particles and was used for further refinement. The final resolution of this reconstruction after solvent mask post-processing was 3.5 Å.

For the cutting state reconstruction, 7762 micrographs were selected from the initial recorded 9336 micrographs based on manual inspection of the CTF. Gautomatch (developed by K. Zhang, MRC Laboratory of Molecular Biology, Cambridge, UK, https://www.mrc-lmb.cam.ac.uk/kzhang/Gautomatch) was used for initial particle picking. The four best classes with 54 556 particles were low-pass filtered to 20 Å in RELION and used for autopicking in RELION. After several rounds of autopicking and 2D classification 149 098 particles were used to reconstruct an initial model in CryoSPARC. In the initial 3D classification 489 112 particles were classified into four classes using C1 symmetry and one class with 100 194 particles was selected. Further classification yielded a final subset of 58 385 particles. Using the 2D classes generated from dataset I, 696 512 particles were picked in dataset II with RELION from 3178 micrographs (initial 3475). After 2D classification the selected 342 737 particles were subjected to 3D classification with the initial model from a refinement run from dataset I. After particle polishing and movie processing the particles were joined together and solvent masked post-processing resulted in a 4.2 Å reconstruction. After application of a larger mask covering a longer segment of the coiled-coils, the same particles gave a lower overall resolution reconstruction, where the course of the coiled coils could be traced to nine helical turns away from the head complex. To calculate the low resolution (~15 Å) reconstruction with longer coiled-coils, particles from dataset I were subjected to 3D classification and the one class with elongated coiled-coils (24 055 particles) was selected. The box size of these particles was increased to 800 pixel and the particles were further classified with 2D and 3D classification yielding in a reconstruction with 18833 particles.

Model building

UCSF Chimera (Pettersen et al., 2004) was used to dock the existing crystal structure of the *Ec*Mre11 nuclease and capping domain (PDB: 4M0V) into the electron density. For *Ec*Rad50 an initial model calculated from the *Thermotoga maritima* structure (PDB: 3QF7) with the SWISS-MODEL server. The resolution during refinement was restricted to 3.5 Å. The helix-loop-helix (HLH) motif was built from poly-alanine helices generated in COOT (Emsley and Cowtan, 2004) and the linker between the two helices and the linker between capping domain and HLH motif were built manually.

For the cutting state reconstruction, UCSF Chimera was used to dock the crystal structure of the *Ec*Mre11 nuclease and capping domain (PDB: 4M0V) into the electron density. The *Ec*Rad50 model from the resting state cryo-EM structure was used to build *Ec*Rad50 in the processing state structure. Similarly, the HLH motif was fitted into the processing state structure. The linker was built manually into the density of the Mre11 (A) monomer. For the Mre11 (B) monomer the resolution was too low to allow building of the linker. COOT was used for model building alternating with real space refinement in PHENIX 1.14 (Afonine et al., 2018) using the *Ec*Mre11 crystal structure (4m0v) as reference model. Since the directionality and registry of DNA binding could not be determined from the structure dsDNA we used an arbitrary registry from the DNA model generated using the webserver 3D-DART (van Dijk and Bonvin, 2009) on the basis of our experimental sequence. This website was also used to bend the DNA using parameters for bend angle (30), bend zone (9-20) and origin (8). COOT was used to refine the DNA using libg restraints alternating with real-space refinement in PHENIX where base pairs as well as base stacking pairs were defined for refinement.

QUANTIFICATION AND STATISTICAL ANALYSIS

ImageJ was used for quantification of nuclease and plasmid assay products and educts. GraphPad Prism was used for plotting the resulting quantification values (in Figures 2C, 5G, and S6G). Error bars are given as standard deviation of the mean.

GraphPad Prism was used for plotting triplicates of the DNA binding assay (in Figures 4D, 5C, 5D, S4C, S4F, and S5G). Error bars are given as standard deviation of the mean.

GraphPad Prism was used for plotting triplicates of the ATPase assay (Figures 4C and S4E). The calculated mean is indicated by a black line.

DATA AND CODE AVAILABILITY

The coordinate files generated during this study are available at the protein data bank (https://www.rcsb.org/) with the accession codes PDB: 6S6V (resting state) and PDB: 6S85 (cutting state).

The calculated reconstructions generated during this study are available at the Electron Microscopy Data Bank (https://www.ebi.ac.uk/pdbe/emdb/) with the accession codes EMDB: EMD-10107 (resting state), EMDB: EMD-10116 (cutting state head complex at 4.2A), EMDB: EMD-10114 (cutting state head complex at 4.3A) and EMDB: EMD-10115 (cutting state head complex at 15A with long coiled coils). Full gel images are deposited under the following https://doi.org/10.17632/g5ypj2dyj2.1

Molecular Cell, Volume *76*

Supplemental Information

Mechanism of DNA End Sensing and Processing by the Mre11-Rad50 Complex

Lisa Käshammer, Jan-Hinnerk Saathoff, Katja Lammens, Fabian Gut, Joseph Bartho, Aaron Alt, Brigitte Kessler, and Karl-Peter Hopfner

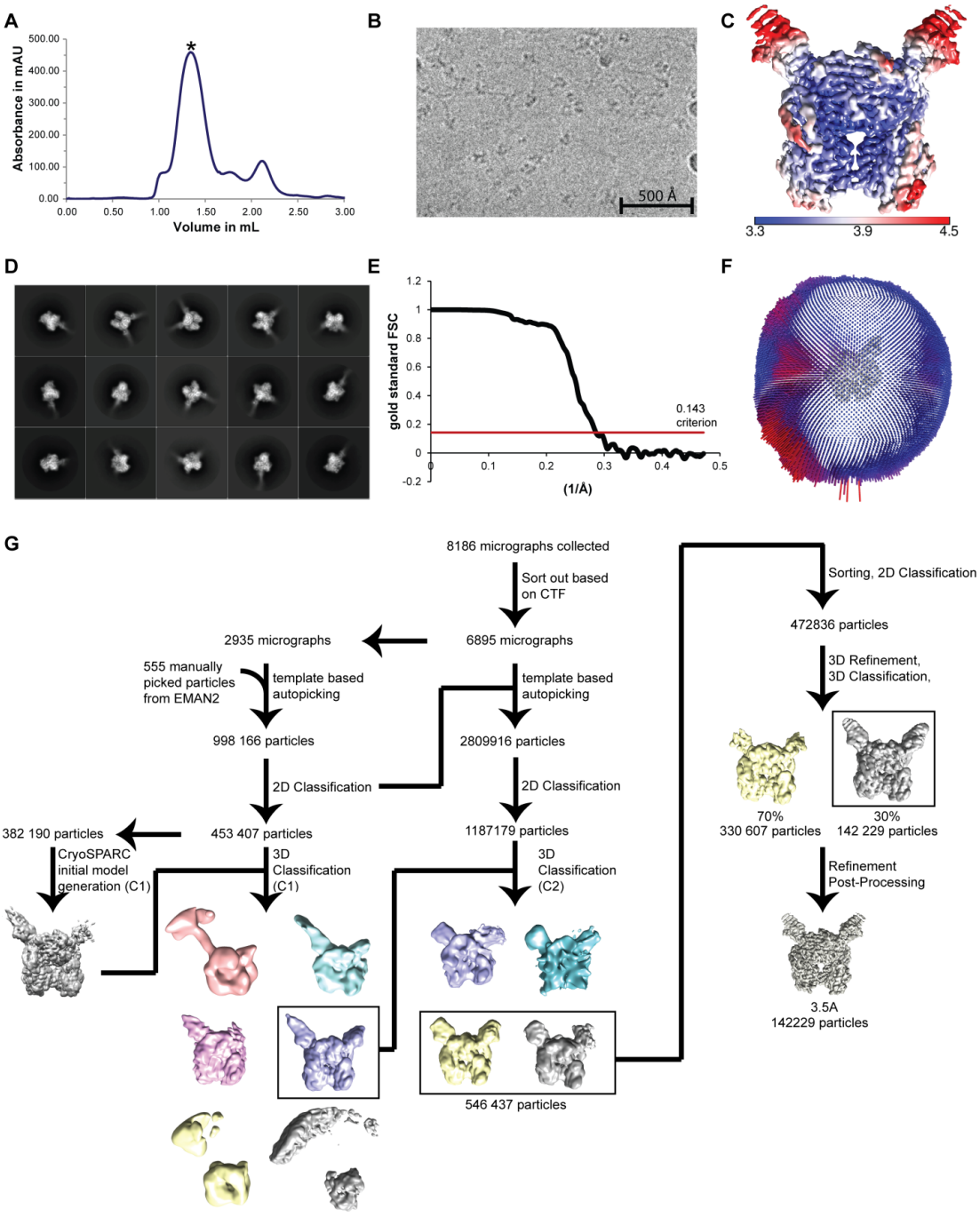
A
Absorbance in mAU
500.00
400.00
300.00
200.00
100.00
0.00
0.00
0.50
1.00
1.50
2.00
2.50
3.00
Volume in mL
B
500 Å
C
3.3
3.9
4.5
D
E
gold standard FSC
1.2
1
0.8
0.6
0.4
0.2
0
-0.2
0
0.1
0.2
0.3
0.4
0.5
(1/Å)
0.143
criterion
F
G
8186 micrographs collected
Sort out based on CTF
6895 micrographs
2935 micrographs
555 manually picked particles from EMAN2
template based autopicking
template based autopicking
998 166 particles
2809916 particles
2D Classification
2D Classification
382 190 particles
453 407 particles
1187179 particles
CryoSPARC initial model generation (C1)
3D Classification (C1)
3D Classification (C2)
546 437 particles
Sorting, 2D Classification
472836 particles
3D Refinement, 3D Classification,
70%
330 607 particles
30%
142 229 particles
Refinement Post-Processing
3.5A
142229 particles

Figure S1 Related to Figure 1| Cryo-EM processing scheme of the resting state

(A) Size exclusion profile of full-length *Ec*MR. The peak used for grid preparation is indicated by an asterisk.

(B) Representative micrograph of the resting state *Ec*MR complex bound to ATPγS.

(C) The local resolution of the resting state reconstruction was calculated using ResMap and is shown as color-coded surface representation.

(D) The fifteen highest populated classes from the 2D classification of the *Ec*MR in resting state are shown.

(E) Gold-standard Fourier shell correlation (FSC) for the resting state. The red line indicates the 0.143 cutoff criterion which indicates a nominal resolution of 3.5 Å.

(F) Angular distribution of the particles used for the resting state reconstruction

(G) Flow chart showing the image-processing pipeline for the cryo-EM data analysis of the *Ec*MR resting state.

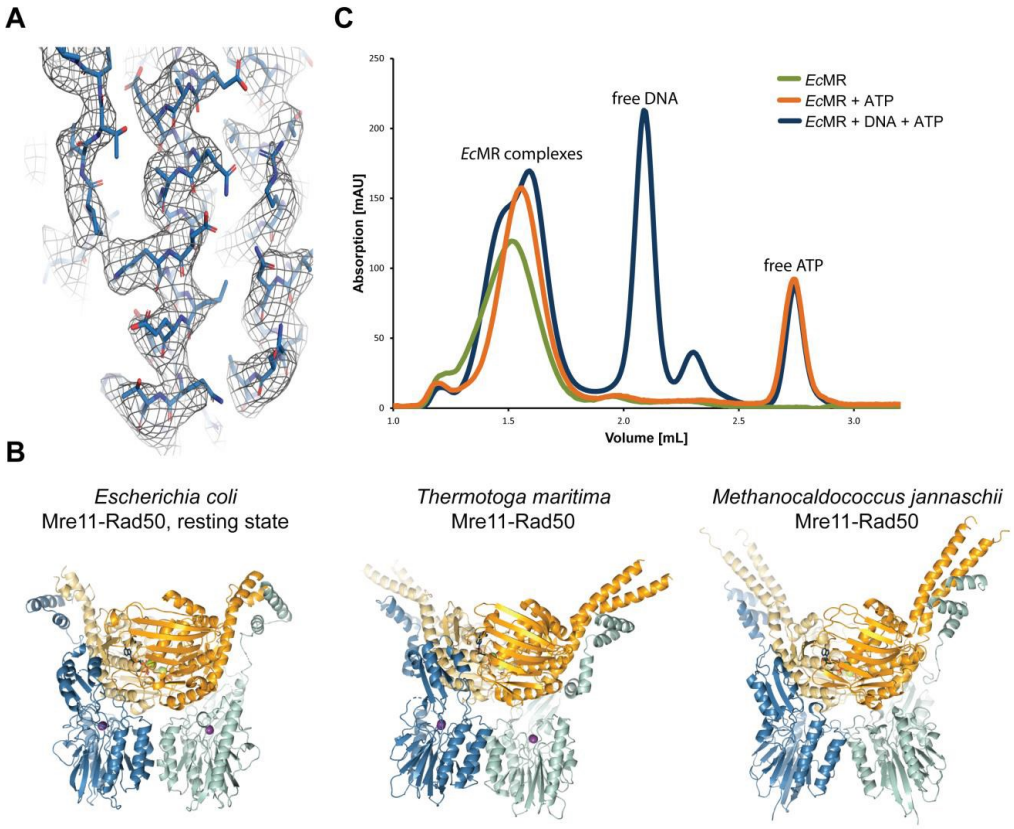

Figure S2 Related to Figure 1| Resting State Analysis

(A) Portion of the electron density superimposed with the 1.8 Å X-ray structure of *Ec*Mre11 (4M0V) shows the quality of the map. This starting model was subsequently adjusted and refined.

(B) Gel filtration retention volumes of *Ec*MR in absence and presence of ATP and/or DNA shows homogeneous species and no formation of stable higher order oligomers as a function of ATP or DNA. ATP/DNA leads to a slight reduction of hydrodynamic radius.

(B) Comparison of the resting state *Ec*MR head with X-ray structures of the MR head from *Thermotoga maritima* (PDB: 3THO) and *Methanocaldococcus jannaschii* (PDB: 3AV0). All three structures show a related fold with slightly different orientations of the coiled coil.

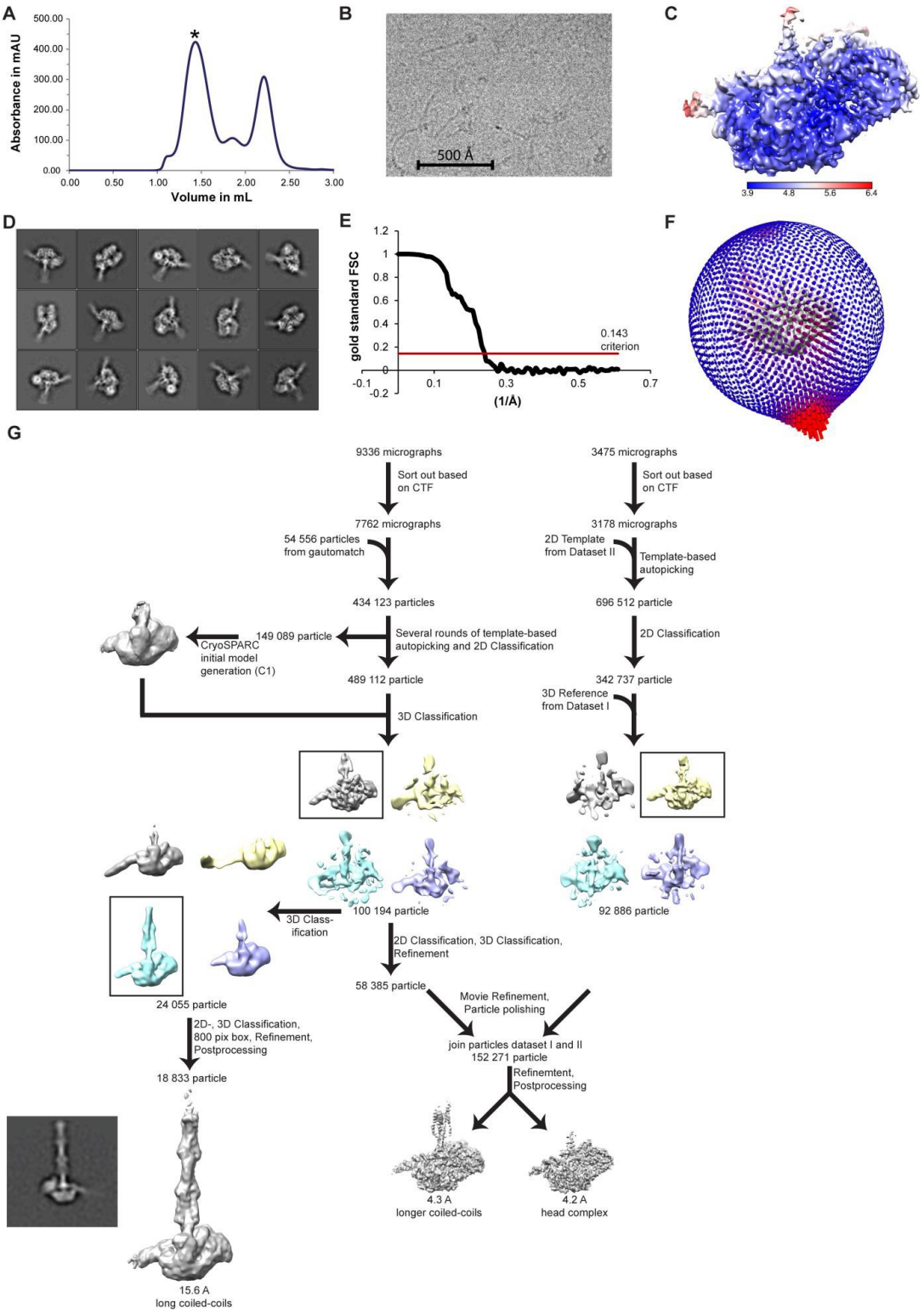
A
Absorbance in mAU
Volume in mL
B
500 Å
C
3.9
4.8
5.6
6.4
D
E
gold standard FSC
0.143
criterion
(1/Å)
F
G
9336 micrographs
Sort out based on CTF
7762 micrographs
54 556 particles from gautomatch
434 123 particles
149 089 particle
CryoSPARC initial model generation (C1)
Several rounds of template-based autopicking and 2D Classification
489 112 particle
3D Classification
100 194 particle
3D Class-ification
24 055 particle
2D-, 3D Classification, 800 pix box, Refinement, Postprocessing
18 833 particle
15.6 A
long coiled-coils
2D Classification, 3D Classification, Refinement
58 385 particle
Movie Refinement, Particle polishing
3475 micrographs
Sort out based on CTF
3178 micrographs
2D Template from Dataset II
Template-based autopicking
696 512 particle
2D Classification
342 737 particle
3D Reference from Dataset I
92 886 particle
join particles dataset I and II
152 271 particle
Refinemtent, Postprocessing
4.3 A
longer coiled-coils
4.2 A
head complex

Figure S3 Related to Figure 1| Cryo-EM processing scheme of the cutting state

(A) Size exclusion profile of full-length EcMR^{H84S}. The peak used for grid preparation is indicated by an asterisk.

(B) Representative micrograph with the cutting state EcMR^{H84S} in complex with ADP and DNA.

(C) The local resolution of the cutting state reconstruction was calculated using ResMap and is shown as a color-coded surface representation.

(D) The fifteen highest populated classes from the 2D classification of the *Ec*MR in the cutting state are shown.

(E) Gold standard Fourier shell correlation (FSC) for the cutting state reconstruction. The red line indicates the 0.143 cutoff criterion which indicates a nominal resolution of 4.2 Å.

(F) Angular distribution of the cutting state reconstruction particles.

(G) Sorting scheme that was used to obtain the 4.2 Å reconstruction of the cutting state.

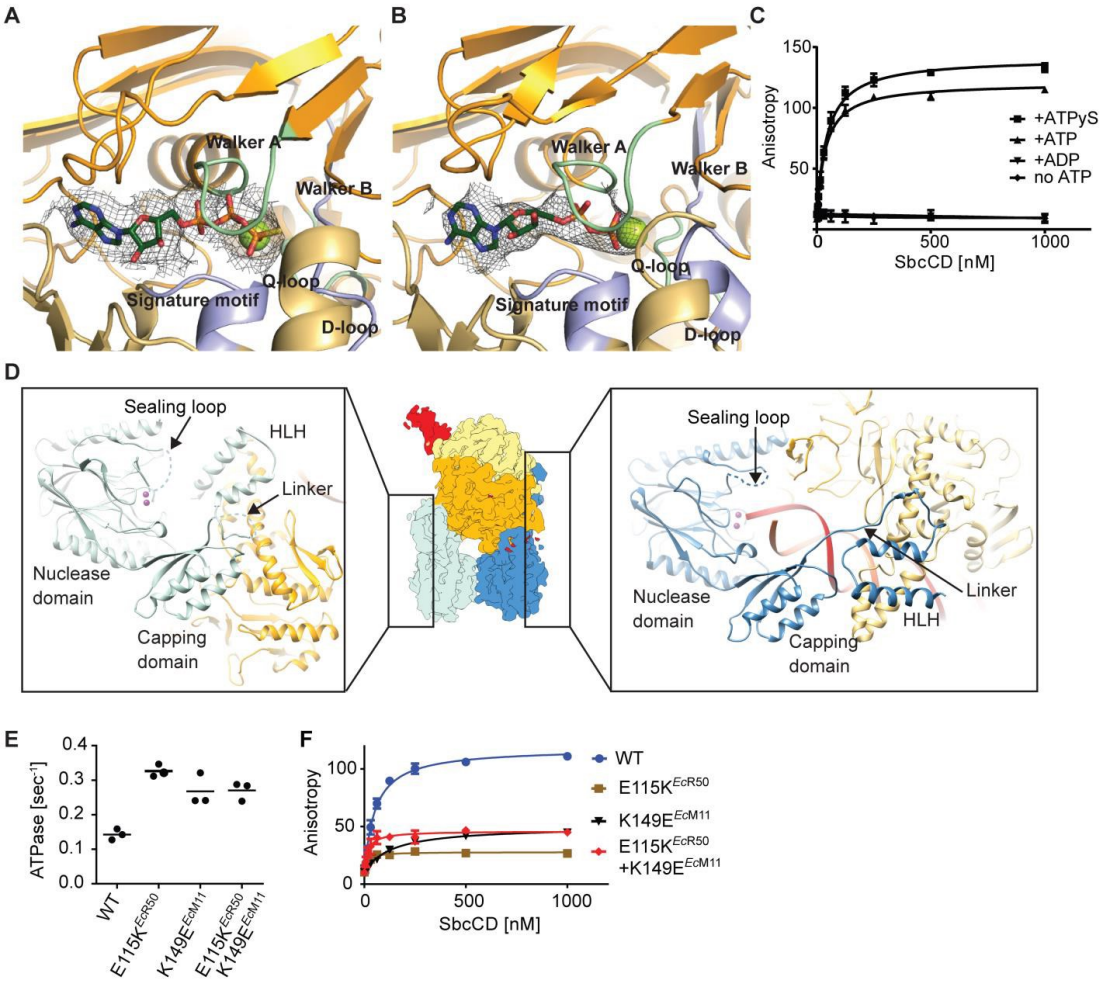

Figure S4 Related to Figure 1 and 2| Structural details of nucleotide and metal binding

(A) ATPγS-Mg^{2+} is visible in the nucleotide binding domain of the resting state reconstruction. The density for the nucleotide is shown and important nucleotide binding motifs are highlighted and color coded.

(B) ADP-Mg^{2+} is visible in the nucleotide binding domain of the cutting state reconstruction.

(C) Interaction of *Ec*MR to fluorescein-labeled 60 bp DNA in the presence of ATP, ADP, ATPγS and no nucleotides monitored by the change in fluorescence anisotropy. DNA binding was detected in the presence of ATP and ATPγS, but not ADP. The data were fit to a 1 to 1 binding equation. Mean and standard deviation are indicated (n = 3, technical replicates).

(D) The linker between the HLH motif and the capping domain of Mre11 adopt different conformations in both monomers. In monomer B (left) no DNA is bound and the linker adopts a

closed conformation while in the DNA binding monomer A (right) an extended conformation is formed.

(E) Steady-state ATPase rates of *Ec*MR charge reverse mutants *Ec*Rad50^{E115K}, *Ec*Mre11^{K149E} and *Ec*Mre11^{K149E}Rad50^{E115K}, stimulated by 60 bp DNA. Mean and individual data point (*n* = 3, technical replicates).

(F) Interaction of *Ec*MR charge reverse mutants with double-stranded DNA monitored by the change in fluorescence anisotropy. The data were fit to a 1 to 1 binding equation. Mean and standard deviation are indicated (*n* = 3, technical replicates). The following K_d values were calculated: *Ec*MR: 51 ± 5 nM; *Ec*MR^{E115K}: 14 ± 4 nM; *Ec*M^{K149E}R: 132 ± 17 nM; *Ec*M^{K149E}R^{E115K}: 17 ± 4 nM.

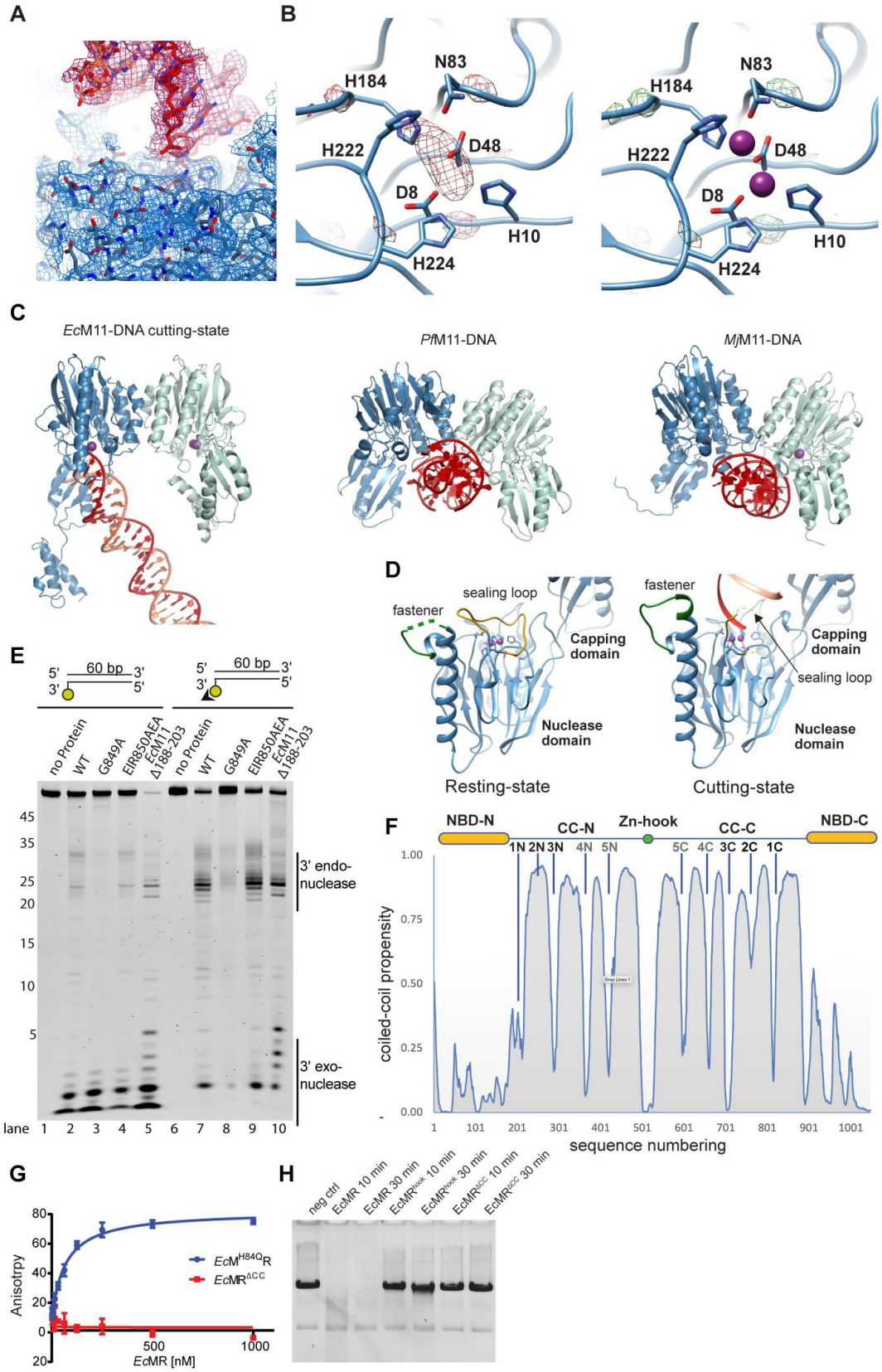
A
B
N83
H184
H222
D48
D8
H10
H224
C
EcM11-DNA cutting-state
PfM11-DNA
MjM11-DNA
D
fastener
sealing loop
Capping domain
Nuclease domain
Resting-state
Cutting-state
E
5' 60 bp 3'
3' 5'
no Protein
WT
G849A
EIR850AEA
EcM11 Δ188-203
3' endo-nuclease
3' exo-nuclease
lane 1 2 3 4 5 6 7 8 9 10
F
NBD-N
CC-N
Zn-hook
CC-C
NBD-C
1N 2N 3N 4N 5N 5C 4C 3C 2C 1C
coiled-coil propensity
sequence numbering
G
Anisotrpy
EcM^H84QR
EcMR^ΔCC
EcMR [nM]
H
neg ctrl
EcMR 10 min
EcMR 30 min
EcMR^hook 10 min
EcMR^hook 30 min
EcMR^ΔCC 10 min
EcMR^ΔCC 30 min

Figure S5 Related to Figure 2 and 3| Mutational analysis of Fastener-NBD interface and coiled-coil

(A) Map at the *Ec*Mre11 active site (blue) bound to DNA (red).
(B) Difference density analysis of *Ec*MR in the cutting shows robust density (left panel) at the di-metal site where crystallographic analysis of *Ec*Mre11 showed two manganese ions (right panel). The difference density was calculated using the command phenix.real_space_diff_map, for pdb maps without (left) and with (right) manganese ions.
(C) Comparison of the Mre11 resting state to Mre11-DNA orientation of the cryo-EM *Ec*MR cutting state and to the X-ray structures of *Pyrococcus furiosus* Mre11-DNA (pdb: 3DSC; bottom, left) and *Methanocaldococcus jannaschii* Mre11-DNA (pdb: 4TUG; bottom, right).
(D) Rearrangement of the *Ec*Mre11 sealing loop (yellow) and *Ec*Mre11 fastener (green) in the resting- and cutting-state respectively.
(E) Nuclease activity of *Ec*MR mutants analyzed with fluorescently labeled 60 bp DNA containing a free DNA end (DNA I) and a DNA end which is blocked by a single-chain fragment against fluorescein (DNA II). To prevent exonucleolytic degradation, the unlabeled 3' DNA end is protected by 10 consecutive phosphothioate linkages. The residues of *Ec*Mre11$^{\text{sealing loop}}$ are deleted in the *Ec*Mre11$^{\Delta 188\text{-}203}$ mutant.
(F) Analysis of coiled-coil propensity along the protein sequence using DeepCoil (Ludwiczak et al., 2019) as implemented in the MPI ToolKit (Zimmermann et al., 2018). NBD's N and C-terminal regions as well as the Zn-hook have low CC propensity as expected. However, the N- and C-terminal parts of the CC domain have another 4 (1N,3N,4N,5N) and 5 (5C,4C,3C,2C,1C) regions of low CC propensity. 2N still has high CC propensity, but in our cryo-EM map pairs with 2C to form the CC break element 2. In total our density shows three CC break elements (1,2,3 in Figure 3D) matching the sequence regions of 1N:1C, 2N:2C, 3N:3C. 4N:4C and 5N:5C might form two additional CC break elements towards the Zn-hook.
(G) Interaction of *Ec*MR$^{\Delta CC}$ with double-stranded DNA monitored by the change in fluorescence anisotropy. The data were fit to a 1 to 1 binding equation. Mean and standard deviation are indicated (n = 3, technical replicates).
(H) Plasmid assay of linearised pBR322 with the coiled-coil mutants *Ec*MR$^{\text{hook}}$ and *Ec*MR$^{\Delta CC}$. Time points were taken after 10 and 30 min.

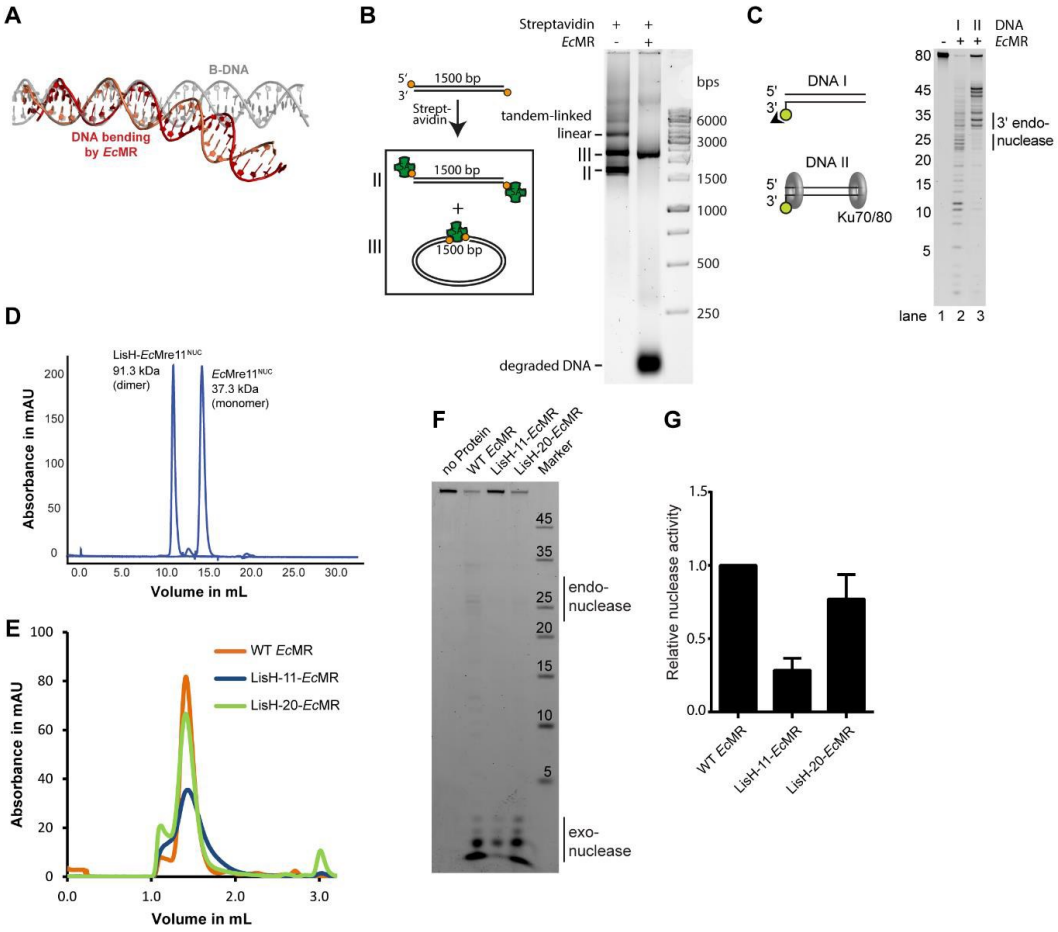

Figure S6 Related to Figure 4 and 5| Characterization of the LisH-*Ec*MR constructs

(A) Comparison of standard B-form -DNA (gray) to the DNA structure in the*Ec*MR cutting-state structure (red).

(B) Nuclease activity assays as in Figure 3A, B but with different DNA/streptavidin ratio leading to a larger fraction of the double-blocked linear species (II) over the circular (III). *Ec*MR selectively degrades linear DNA.

(C) Nuclease activity of *Ec*MR wild type analyzed with 5' fluorescently labeled 80 bp DNA containing a DNA end which is terminally-blocked by a single-chain fragment against fluorescein, scFv (DNA I) and in the presence *Chaetomium thermophilum* Ku70/80 (DNA II). The 3' endonuclease shifts from 25 nucleotides (scFv-bound) to 35 nucleotides (Ku70/80-bound) approximately 10 bp inwards.

(D) Size exclusion profiles of LisH-*Ec*Mre11^{NUC} and *Ec*Mre11^{NUC}.

(E) Size exclusion profiles of LisH-*Ec*MR with 11 and 20 residue linker and *Ec*MR. The runs were done with a S6 5/150 column.
(F) Nuclease activity of LisH-*Ec*MR with 11 and 20 residue linker and *Ec*MR analyzed with fluorescently labeled 60 bp DNA containing a free DNA end. To prevent exonucleolytic degradation, the unlabeled 3' DNA end is protected by 10 consecutive phosphothioate linkages.
(G) Quantification of the exonuclease activity shown in (F), (n=3, technical replicates)

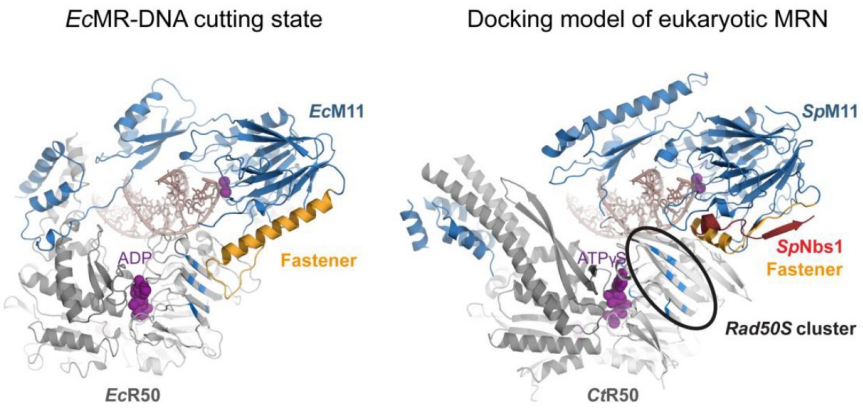

Figure S7 Related to Figure 6| Comparison of EcMR and a model for eukaryotic MRN.

Structural alignment of *Ec*MR cutting-state (left) with a model for eukaryotic MRN (right, obtained by docking the ATPγS bound (*Chaetomium thermophilum*) *Ct*Rad50^{NBD}-Mre11^{HLH} complex (PDB: 5DA9), the CtMre11^{NUC} dimer (PDB: 4YKE), and the Mre11-interacting region of *S. pombe* Nbs1 (PDB: 4FBW) onto the *Ec*MR cutting state model, the relevant *rad50*S residues are shown as blue backbone patches. The *Ec*Mre11^{fastener} helix binds to *Ec*Rad50 at precisely the surface location that harbors the Rad50S cluster of residues. The fastener loop (orange) is much shorter in eukaryotic Mre11 and binds Nbs1 (red). Thus, the bacterial Mre11^{fastener}-Rad50 interaction could be replaced by a Mre11-Nbs1/CtIP-Rad50 interaction, explaining a wide range of biochemical data.

Table S1 Related to Key Resource Table| DNA oligomers used for the assays and the cryo-EM sample

Oligonucleotide	Sequence 5' to 3'
60 bp DNA fwd for nuclease	CGGGTAGTAGATGAGCGCAGGGACACCGAGGTCAA GTACATTACCCTCTC*A*T*A*G*G*A*G*G*T*G
60 bp DNA rev for nuclease	CACCTCCTATGAGAGGGTAATGTACTTGACCTCGGT GTCCCTGCGCTCATCTACTACCCG-6-FAM
60 bp DNA fwd for size exclusion analysis	CGGGTAGTAGATGAGCGCAGG*G*A*C*A*C*C*G*A*G *GTCAAGTACATTACCCTCTCATAGGAGGTG
60 bp DNA rev for size exclusion analysis	CACCTCCTATGAGAGGGTAATGTACTTGACCTCGGT GTCCCTGCGCTCATCTACTACCCG
80 bp DNA fwd for nuclease with Ku70/80	CGGGTAGTAGATGAGCGCAGGGACACCGAGGTCAA GTACATTACCCTCTCATAGGAGGTGCGCTTTATCAG AAGCCAGAC
80 bp DNA rev for nuclease with Ku70/80	GTCTGGCTTCTGATAAAGCGCACCTCCTATGAGAGG GTAATGTACTTGACCTCGGTGTCCCTGCGCTCATCT ACTACCCG-6-FAM
60 bp DNA fwd for ATPase assay	CGCTTTATCAGAAGCCAGACATTAACGCTTCTGGAG AAACTCAACGAGCTGGACGCGGAT
60 bp DNA rev for ATPase assay	ATCCGCGTCCAGCTCGTTGAGTTTCTCCAGAAGCGT TAATGTCTGGCTTCTGATAAAGCG
35 bp DNA fwd for DNA binding assay	CGCTTTATCAGAAGCCAGACATTAACGCTTCTGGA
35 bp DNA rev for DNA binding assay	6-FAM-TCCAGAAGCGTTAATGTCTGGCTTCTGATAAAGCG
60 bp DNA for EM fwd	CGCTTTATCAGAAGCCAGACATTAACGCTTC TGGAGAAACTCAACGAGCTGGACGCGGAT
60 bp DNA for EM rev	ATCCGCGTCCAGCTCGTTGAGTTTCTCCAGAAGCGT TAATGTCTGGCTTCTGATAAAGCG

Movie S1 Related to Figure 1| Depiction of the conformational changes occurring upon DNA binding in *Ec*MR

The first part of the movie explains the structure of *Ec*MR in the resting state and the movement of the Mre11 dimer upon DNA binding. Additionally, it depicts important structural features of the cutting state structure. The second part of the movie explains closing of the CCs using a morph between the resting state and the cutting state of *Ec*MR.

2.2 Structural mechanism of endonucleolytic processing of blocked DNA ends and hairpins by Mre11-Rad50

Fabian Gut*, Lisa Käshammer*, Katja Lammens, Joseph D. Bartho, Anna-Maria Boggusch, Erik van de Logt, Brigitte Kessler, Karl-Peter Hopfner, Structural mechanism of endonucleolytic processing of blocked DNA ends and hairpins by Mre11-Rad50, *Molecular Cell*, Volume 82, 19 August 2022, Pages 3513-3522

https://doi.org/10.1016/j.molcel.2022.07.019

* These authors contributed equally

Summary

In this publication we use cryo-EM on the bacterial *Ec*MR complex (also known as SbcCD) to reveal how the Mre11-Rad50 nuclease removes protein blocks from a DSB end via its conserved endonuclease activity, to enable DSB repair. We report a cryo-EM structure of *Ec*MR bound to a protein-blocked DNA end in 5' endonuclease mode, which closely resembles the previously reported exonuclease state. The endonuclease state further reveals that Mre11-Rad50 bends DNA for endonucleolytic cleavage. This is supported by biochemical assays, which show that *Ec*MR preferentially cleaves at DNA sites with higher flexibility. Furthermore, we show that MR is loaded onto blocked DNA ends with opposing polarity compared to free DNA ends, resulting in Mre11 pointing away from the block. This is sufficient to explain a broad range of previous biochemical data, for example, the reversal of cleavage strands in 3' exo- and 5' endonuclease activities, through the way MR interacts with different DNA ends.
Furthermore, we report a cryo-EM structure of *Ec*MR bound to a DNA hairpin, explaining the structural and mechanistic basis for MR's hairpin-opening activity. The observed conformation of the hairpin-bound state is again very similar to the reported exo- and endonuclease states of *Ec*MR. Thus, the structures show how Mre11-Rad50 is able to process internal DNA, free DNA ends, and hairpins through a similar ATP-regulated conformational state. In summary, our results provide the structural and mechanistic basis for how blocked DNA ends and hairpins are processed by Mre11-Rad50 and unify its enigmatic nuclease diversity in a single structural framework.

Author Contribution

Together with Lisa Käshammer and Brigitte Kessler, I purified the proteins used within this study. I prepared cryo-EM grids and performed data collection, structure determination, analysis and modelling together with Lisa Käshammer, Katja Lammens and Joseph Bartho.

With the help of Anna-Maria Boggusch and Erik van de Logt, I performed biochemical nuclease assays. I wrote the manuscript together with Karl-Peter Hopfner, Lisa Käshammer and with contributions from all other authors.

Short article

Molecular Cell

Structural mechanism of endonucleolytic processing of blocked DNA ends and hairpins by Mre11-Rad50

Graphical abstract

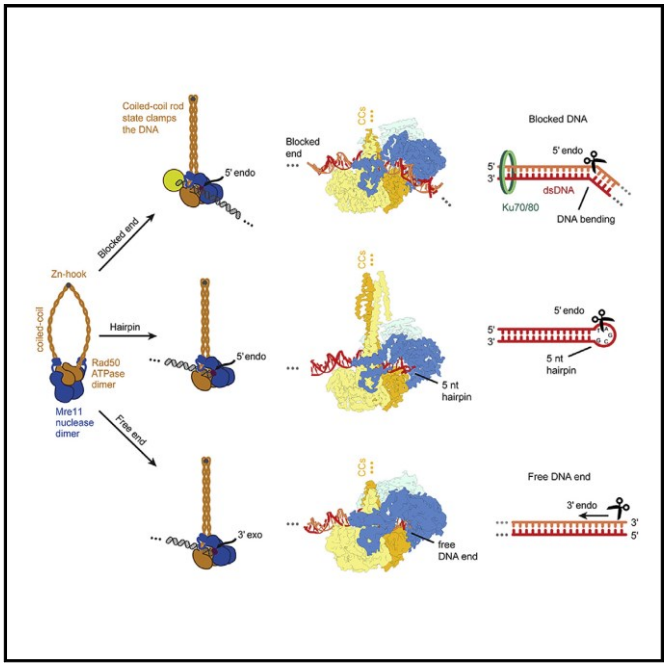

Highlights

- Cryo-EM structures of *Ec*Mre11-Rad50 bound to a protein-blocked DNA end and a hairpin
- A single structural framework unifying Mre11-Rad50's enigmatic nuclease diversity
- Mre11-Rad50 is loaded onto blocked DNA ends with Mre11 pointing away from the block
- Mre11-Rad50 strongly bends internal dsDNA for endonucleolytic cleavage

Authors

Fabian Gut, Lisa Käshammer, Katja Lammens, ..., Erik van de Logt, Brigitte Kessler, Karl-Peter Hopfner

Correspondence

hopfner@genzentrum.lmu.de

In brief

Gut et al. use cryoelectron microscopy and biochemical studies to reveal how the Mre11-Rad50 (MR) nuclease generates an endonucleolytic incision to remove protein blocks from a DNA double-strand break, providing also a unified mechanistic basis for MR's endonuclease, exonuclease, and hairpin-opening activities.

Gut et al., 2022, Molecular Cell *82*, 1–10
September 15, 2022 © 2022 Elsevier Inc.
https://doi.org/10.1016/j.molcel.2022.07.019

CellPress

Please cite this article in press as: Gut et al., Structural mechanism of endonucleolytic processing of blocked DNA ends and hairpins by Mre11-Rad50, Molecular Cell (2022), https://doi.org/10.1016/j.molcel.2022.07.019

Molecular Cell

CellPress

Short article

Structural mechanism of endonucleolytic processing of blocked DNA ends and hairpins by Mre11-Rad50

Fabian Gut,[1,2,3] Lisa Käshammer,[1,2,3,4] Katja Lammens,[1,2] Joseph D. Bartho,[1,2] Anna-Maria Boggusch,[1,2] Erik van de Logt,[1,2] Brigitte Kessler,[1,2] and Karl-Peter Hopfner[1,2,5,*]

[1]Gene Center, Ludwig-Maximilians-Universität, 81377 Munich, Germany
[2]Department of Biochemistry, Ludwig-Maximilians-Universität, 81377 Munich, Germany
[3]These authors contributed equally
[4]Present address: MRC Laboratory of Molecular Biology, Structural Studies Division, Cambridge Biomedical Campus, Cambridge, UK
[5]Lead contact
*Correspondence: hopfner@genzentrum.lmu.de
https://doi.org/10.1016/j.molcel.2022.07.019

SUMMARY

DNA double-strand breaks (DSBs) threaten genome stability and are linked to tumorigenesis in humans. Repair of DSBs requires the removal of attached proteins and hairpins through a poorly understood but physiologically critical endonuclease activity by the Mre11-Rad50 complex. Here, we report cryoelectron microscopy (cryo-EM) structures of the bacterial Mre11-Rad50 homolog SbcCD bound to a protein-blocked DNA end and a DNA hairpin. The structures reveal that Mre11-Rad50 bends internal DNA for endonucleolytic cleavage and show how internal DNA, DNA ends, and hairpins are processed through a similar ATP-regulated conformational state. Furthermore, Mre11-Rad50 is loaded onto blocked DNA ends with Mre11 pointing away from the block, explaining the distinct biochemistries of 3′ → 5′ exonucleolytic and endonucleolytic incision through the way Mre11-Rad50 interacts with diverse DNA ends. In summary, our results unify Mre11-Rad50's enigmatic nuclease diversity within a single structural framework and reveal how blocked DNA ends and hairpins are processed.

INTRODUCTION

DNA double-strand breaks (DSBs) are a threat to genome integrity and cell viability and are linked to cancerogenesis in humans (Carbone et al., 2020). DSBs are repaired either by template-independent end-joining-type reactions (Chang et al., 2017; Della et al., 2004; Zhao et al., 2020) or by homology-directed repair (HDR) such as homologous recombination (Chen et al., 2018; Haber, 2018; Wright et al., 2018). Challenges for the repair of DSBs, which are formed by ionizing radiation, genotoxic chemicals, or various enzymatic processes, are obstructions in the form of chemical alterations, hairpins, or covalent protein adducts such as abortive topoisomerases (Johnson et al., 2021; Morimoto et al., 2019).

Obstructed DNA termini require processing by the Mre11-Rad50 (MR) complex, an ATP-dependent DSB sensor and nuclease that is found in all kingdoms of life (Hoa et al., 2016; Paull, 2018; Syed and Tainer, 2018). In eukaryotes, MR associates with Nbs1 to form the Mre11-Rad50-Nbs1 (MRN, MRX in yeast) complex (Carney et al., 1998), which is implicated in various DNA end reactions (Cejka and Symington, 2021; Delamarre et al., 2020; Kim et al., 2020; Marie and Symington, 2022), DNA damage signaling (Cassani et al., 2019; Hailemariam et al., 2019; Lee and Paull, 2005), and DNA tethering (Mojumdar et al., 2019; Seeber et al., 2016). The role of prokaryotic MR homologs (known as SbcCD in *Escherichia coli* [*E. coli*]) is less understood, but they are implicated in dealing with aberrant DNA structures formed by palindromes and over-replicated DNA (Eykelenboom et al., 2008; Wendel et al., 2018).

MR consists of two Rad50 ATP-binding cassette (ABC)-type ATPases and two Mre11 nucleases. Rad50 nucleotide binding domains (NBDs) together with Mre11 subunits assemble a DNA binding and processing "head" module (Hopfner et al., 2001). The 15–60 nm long Rad50 coiled-coil (CC) domains form long ring or rod structures, joined via an apical Zn-hook dimerization motif (Hopfner et al., 2002; Park et al., 2017). The ring shape is proposed to function as a topological gate to restrict nucleolytic cleavage to DSB and not intact genomic DNA. After DSB entry into the ring, the CCs switch to a rod and enable a cutting conformation of the head (Käshammer et al., 2019).

On clean DNA ends, MR/MRN possess 3′ → 5′ exonuclease activity (Paull and Gellert, 1998). Both MR and MRN can also open hairpin structures (Eykelenboom et al., 2008; Lobachev et al., 2002; Paull and Gellert, 1998). On blocked DNA ends, however, MR/MRN show 5′ endonuclease activity around 25–35 base pairs (bp) away from the block (Cannavo and Cejka, 2014; Deshpande et al., 2016). Furthermore, 3′ → 5′ back

Please cite this article in press as: Gut et al., Structural mechanism of endonucleolytic processing of blocked DNA ends and hairpins by Mre11-Rad50, Molecular Cell (2022), https://doi.org/10.1016/j.molcel.2022.07.019

resection from the 5′ nick toward the DNA end can generate short regions of ssDNA for the assembly of long-range resection machinery (Garcia et al., 2011; Mimitou and Symington, 2008), whereas repetitive endonuclease activity may lead to multiple incisions farther away from the block (Cannavo et al., 2019; Käshammer et al., 2019; Lim et al., 2015). *E. coli* MR (*Ec*MR) cleaves and possibly deprotects both 3′ and 5′ strands by generating a "clean" DSB (Connelly et al., 2003; Lim et al., 2015; Saathoff et al., 2018). A common basis for this broad and mechanistically confusing range of activities has not been established.

Recent work revealed how *Ec*MR binds a clean DNA end in 3′ exonuclease mode (Käshammer et al., 2019), but it remained unclear how physiologically more important endonuclease and hairpin-opening activities are carried out. Here, we use cryoelectron microscopy (cryo-EM) and biochemistry to investigate the *Ec*MR complex both in endonuclease and hairpin-opening states. Our results provide a structural basis for a unified nuclease mechanism of the Mre11-Rad50 complex through identification of a DNA cutting channel that can accommodate free DNA ends, hairpins, but—intriguingly—also bent internal sites of DNA. The mechanism can explain a broad range of prior biochemical data, for instance, the reversal of cleavage strands in 3′ exonuclease and 5′ endonuclease activities and the long cutting distances to the physical edge of the block.

RESULTS

Cryo-EM structure of *Ec*MR bound to a blocked DNA end in endonuclease mode

To reveal how Mre11-Rad50 detects obstructed DNA ends, we used cryo-EM and single-particle reconstruction on the *Ec*MR complex. We incubated 120 bp dsDNA with *Chaetomium thermophilum* Ku70/80 (Ku) to generate protein-blocked dsDNA ends (Figure 1A). Ku, a physiological block for eukaryotic MRN (Reginato et al., 2017; Wang et al., 2017), stimulates *Ec*MR's endonuclease similar to that of MRN (Käshammer et al., 2019). Compared with obstacles that are attached via a flexible linker to the 3′- or 5′-terminal base (e.g., DNA-biotin:streptavidin), DNA ends bound by the ring molecule Ku are cleaved farther inward, matching the DNA footprint of Ku (Käshammer et al., 2019). We incubated Ku-bound 120 bp DNA with the nuclease-deficient mutant *Ec*M^{H84Q}R (Figure S1A) and ATP prior to vitrification (Figure 1A), resulting in the three reconstructions: an *Ec*M^{H84Q}R endonucleolytic cutting state at 3.4 Å (Figures 1B, 1C, and S1; Tables 1 and S1), Ku bound to dsDNA at 3.5 Å (Figure S2), and a Ku-RM-MR-Ku state of two *Ec*M^{H84Q}R and Ku complexes bound to a single 120 bp dsDNA (Figure S2).

The 3.4 Å map showed a well-resolved *Ec*M^{H84Q}R catalytic head module bound to DNA. The overall architecture is similar to that in the exonuclease state (Käshammer et al., 2019, PDB: 6S85) (Figures 1B, 1C, and S3A). The Rad50^{NBDs} are dimerized and bind two Mg^{2+}-ADP. The CCs are in a rod configuration with a narrow opening for dsDNA next to the Rad50^{NBDs}. The Mre11 dimer is relocated from the autoinhibited state to one side of the Rad50^{NBD} dimer, forming a nuclease channel between one Mre11 (denoted "Mre11 (A)") and one Rad50 (denoted "Rad50 (A)") subunit. DNA binds along both Rad50^{NBDs} between the CCs and traverses the active site channel. In contrast to the exonuclease state, where the DNA ended at the nucleolytic di-metal center of *Ec*Mre11, we now see density for DNA that exits the channel on the other side (Figure 1B). A lower resolution reconstruction and LAFTER filtering resolved the extended path of DNA even further (Figure S1; Table 1), consistent with this configuration representing MR bound to internal DNA.

DNA in the endonuclease state forms more extensive contacts with Rad50 than the exonuclease state, since it also binds Rad50^{NBD} (B) at the exit of the nuclease channel. A symmetry-related site on Rad50^{NBD} (A) binds DNA on the distal site of the complex. Thus, only in the endonuclease all DNA binding sites on Rad50 are fully occupied (Figure S3A). DNA is well structured in the active site channel with a backbone phosphate contacting the di-metal moiety (likely Mn^{2+}). The metal coordination and active site geometry are very similar to that observed in the exonuclease state (Figures 1D and S3B), as well as in a high-resolution *Ec*Mre11 crystal structure in complex with Mn^{2+} in the absence of DNA (Liu et al., 2014; PDB: 4M0V). A water molecule, positionally inferred from the high-resolution crystal structure, would attack the DNA backbone in such a way as to cleave the 3′O–P bond, which is consistent with the biochemistry of the 5′ endonuclease and 3′ → 5′ exonuclease activities (Figures 1D and S3B) (Saathoff et al., 2018).

MR binds to free and blocked DNA ends with reversed polarity

It is yet unclear on which side of MR the block is located. To address this, we first biochemically assessed the binding of *Ec*M^{H84Q}R to the Ku-blocked dsDNA. Electrophoretic mobility shift assay (EMSA) showed efficient binding of *Ec*MR to both 2:1 and 1:1 Ku:DNA complexes with a saturating concentration of 40 nM *Ec*MR (Figure S3C). We also performed nuclease assays, which have shown that Ku efficiently stimulates the endonuclease activity of *Ec*MR, consistent with prior work (Käshammer et al., 2019). At a ratio of 2× Ku over DNA, we observe stimulation of endonuclease activity but also exonuclease products. Further, 4× Ku reduces exonuclease products and still leads to robust endonuclease, whereas 6× or higher Ku inhibits also endonuclease activity (Figure 1E). Likely, multiple Ku loading prevents *Ec*MR's DNA access (Bliss and Lane, 1997). The main endonuclease cleavage reactions are in the range of 30–45 bp (3′ 6-FAM label), which would correspond to a cleavage distance of 50–35 bp from the 5′ end. Please note that the endonuclease cleavage reactions around 45 bp might stem from 3′ endonuclease activities of *Ec*MR bound to the "other" end (Saathoff et al., 2018). Thus, Ku-bound DNA is an efficient endonuclease substrate for *Ec*MR.

To assess whether the block is situated at the Mre11 proximal or distal site, we made use of a subset of 2D classes that had two *Ec*MR complexes loaded onto a single DNA (Figure 1F). These particles led to an 8.2 Å reconstruction (Figure S2) that revealed the orientation of *Ec*MRs on the DNA and also showed density for Ku on both ends. We calculated a composite map combining the better-resolved individual reconstructions of Ku and *Ec*MR (Figures 1F, S1, and S2). Interestingly, both *Ec*MR complexes are oriented such that the Mre11 dimer points away from Ku, i.e., the Mre11 dimer is oriented on blocked DNA in

Please cite this article in press as: Gut et al., Structural mechanism of endonucleolytic processing of blocked DNA ends and hairpins by Mre11-Rad50, Molecular Cell (2022), https://doi.org/10.1016/j.molcel.2022.07.019

Molecular Cell
Short article

CellPress

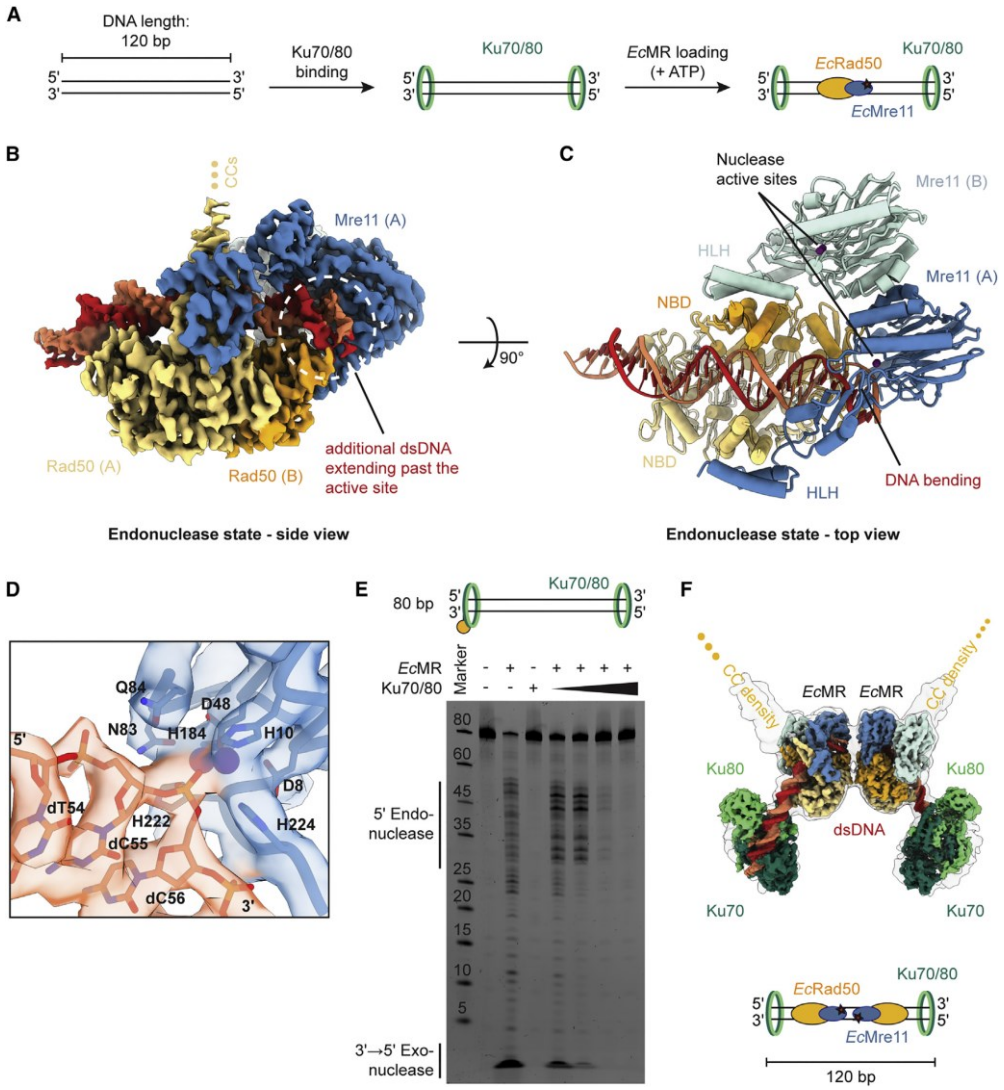

Figure 1. Structure and enzymatic activity of *Ec*Mre11-Rad50 in the endonuclease state

(A) Scheme of cryo-EM sample preparation to trap *Ec*MR in the endonuclease state.

(B) 3.4 Å density map of the *Ec*MR complex (Rad50 orange/yellow; Mre11 light/dark blue) bound to blocked DNA (red) in the endonuclease state. Rad50 and Mre11 dimers assemble a DNA channel that contains the nuclease active site. Extending coiled coils (CCs) are not resolved (dots).

(C) Atomic model of the endonuclease state.

(D) Nuclease active site of Mre11(A) in endonuclease state, (Mre11: blue; DNA: orange; Mn^{2+}: purple). Overlay: 3.4 Å cryo-EM map.

(E) Nuclease assay of *Ec*MR WT on an 80 bp 3′ 6-FAM-labeled, Ku-blocked DNA substrate with increasing excess of Ku over DNA (2×, 4×, 6×, and 10×), showing a strong reduction in endonuclease activity at higher Ku concentrations. Mild increase of Ku:DNA from 2× to 4× reduces unspecific nuclease products while the primary endonuclease activity remains intact.

(F) Composite map (top) and scheme (bottom) of the Ku-RM-MR-Ku assembly with two *Ec*MR complexes bound to one Ku-blocked 120 bp DNA. Semitransparent overlay: initial 8.2 Å cryo-EM map.

See also Figures S1 and S2, Table 1, and Video S1.

Please cite this article in press as: Gut et al., Structural mechanism of endonucleolytic processing of blocked DNA ends and hairpins by Mre11-Rad50, Molecular Cell (2022), https://doi.org/10.1016/j.molcel.2022.07.019

CellPress

Molecular Cell
Short article

Table 1. Cryo-EM data collection, 3D reconstruction and model refinement statistics

	*Ec*MR endonuclease state (EMDB-14391) PDB: 7YZO	*Ec*MR endonuclease state with extended DNA (EMDB-14403) PDB: 7Z03	Ku-RM-MR-Ku state (EMDB-14392)	*Ec*MR hairpin-bound state (EMDB-14393) PDB: 7YZP	Ku70/80 DNA-bound state (EMDB-14394)
Data collection and processing					
Magnification	130,000	–	–	130,000	130,000
Voltage (kV)	300	–	–	300	300
Electron exposure (e–/Å^2)	44.68/44.90 45.27/37.92	–	–	46.60/47.01	44.68/44.90 45.27/37.92
Defocus range (μm)	−1.2 (−2.8)	–	–	−1.2 (−2.8)	−1.2 (−2.8)
Pixel size (Å)	1.059	–	–	1.059	1.059
Symmetry imposed	C1	–	–	C1	C1
Initial particle images (No.)	7,268,469	612,619	2,340,662	1,219,810	7,268,469
Final particle images (No.)	199,751	57,747	10,494	54,504	211,512
Map resolution (Å)	3.4	3.7	8.2	4.0	3.5
FSC threshold	0.143	0.143	0.143	0.143	0.143
Refinement					
Initial model (PDB code)	6S85	–	–	6S85/1DGO	–
Model resolution (Å)	3.5	–	–	4.1	–
FSC threshold	0.5	–	–	0.5	–
Map sharpening B factor (Å^2)	−119.2	–	–	−97.9	−96.9
Model composition					
Non-hydrogen atoms	13,072	13,072	–	14,101	–
Protein residues	1,497	1,497	–	1,633	–
Nucleic acid residues	62	78	–	59	–
Ligands					
Mn^{2+}	4	4	–	4	–
Mg^{2+}	2	2	–	2	–
ADP	2	2	–	2	–
dsDNA	1	1	–	1	–
RMSDs					
Bond lengths (Å)	0.004	–	–	0.002	–
Bond angles (°)	0.704	–	–	0.538	–
Validation					
MolProbity score	1.51	–	–	1.74	–
Clashscore	5.68	–	–	8.36	–
Poor rotamers (%)	0.08	–	–	0	–
Ramachandran plot					
Favored (%)	96.75	–	–	95.84	–
Allowed (%)	3.25	–	–	4.16	–
Disallowed (%)	0	–	–	0	–

endonuclease modes "inward" relative to the end. For comparison, it was oriented "outward" on a free DNA end (Figure S3D). *Ec*MR's active site is around ~55 nt from the 5′ end, which corresponds well to the ~50 nt incisions observed biochemically (Figure 1E), considering that there is still some space between Ku and *Ec*MR in these reconstructions.

The rather defined, central MR oligomer in the Ku-RM-MR-Ku assembly on the 120 bp DNA raises the question whether the RM:MR interaction is stable or merely a product of the molecular crowding on the short DNA. Using a 240 bp Ku-blocked dsDNA, we could not observe any 2D classes having multiple MR complexes. Thus, the interaction between adjacent *Ec*MR complexes is likely transient, if there is an interaction at all. We do not want to rule out other forms of oligomerization, for which there is at least evidence for eukaryotic MRN (Kissling et al., 2022; Moreno-Herrero et al., 2005).

A plausible explanation for the observed DNA Ku-RM-MR-Ku assembly is simultaneous loading of an MR complex from both

Please cite this article in press as: Gut et al., Structural mechanism of endonucleolytic processing of blocked DNA ends and hairpins by Mre11-Rad50, Molecular Cell (2022), https://doi.org/10.1016/j.molcel.2022.07.019

Molecular Cell
Short article

CellPress

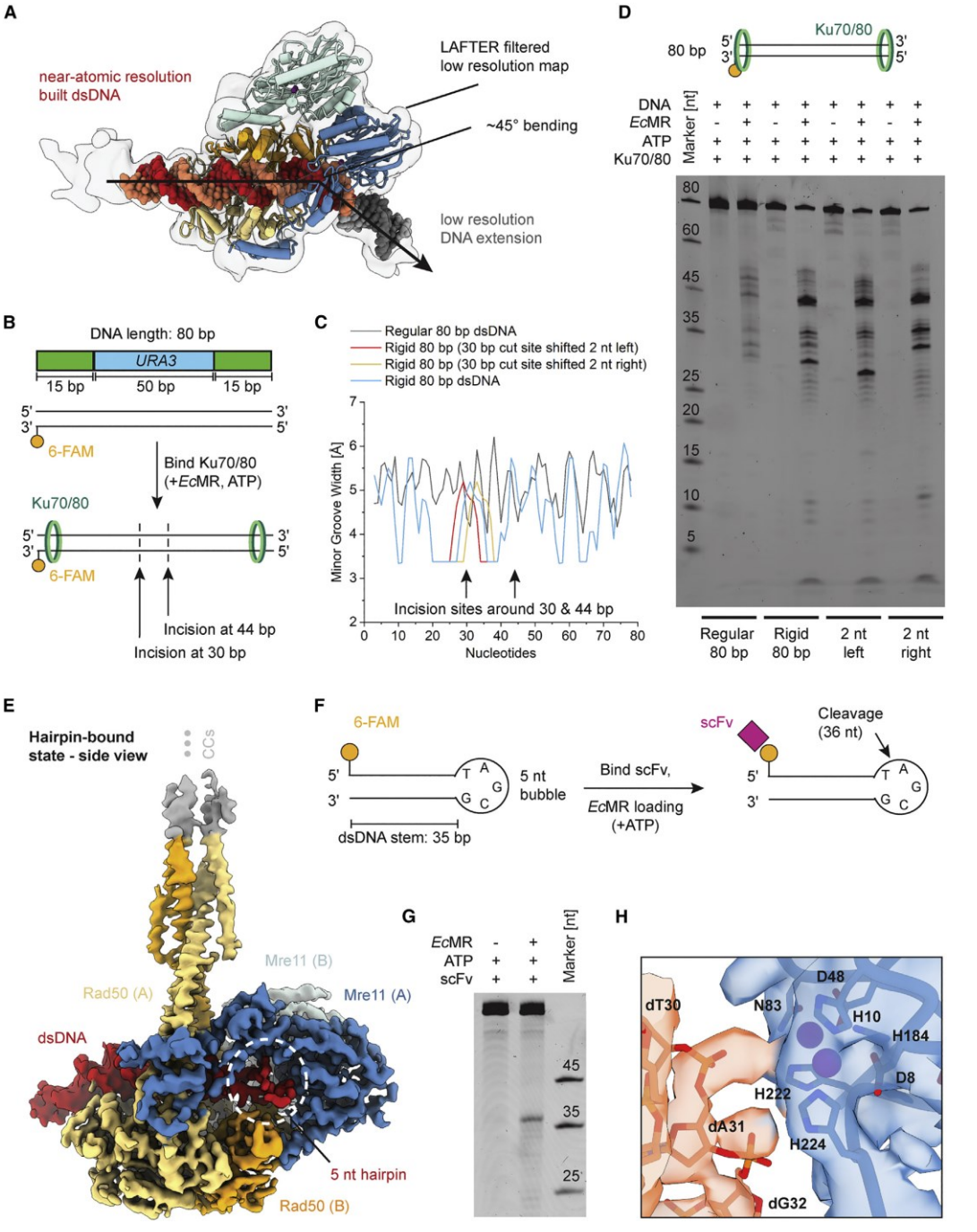

(legend on next page)

Please cite this article in press as: Gut et al., Structural mechanism of endonucleolytic processing of blocked DNA ends and hairpins by Mre11-Rad50, Molecular Cell (2022), https://doi.org/10.1016/j.molcel.2022.07.019

ends, resulting in the double-inward-facing RM:MR assembly. It should be noted that this is a result of the short two-ended DNA substrate; in a genomic context, *Ec*MR might only load unidirectionally and not form this RM-MR assembly. Nevertheless, the inward-facing configuration is consistent with and sufficient to explain a large body of biochemical data that showed differences between 3′ → 5′ exonuclease and 5′ endonuclease, such as cleavage site locations, cleavage chemistry, and strand preference. Thus, biochemical and topological differences between endonuclease and exonuclease are not caused by differences in the architecture of the underlying cutting states but by the polarity of how *Ec*MR binds at or near the DNA end.

MR bends DNA for endonucleolytic cutting

DNA passing through the active site channel is bent by ~45° (Figure 2A), which resolves our previous notation that linear continuation of DNA in the exonuclease structure would result in a clash with Mre11 (Käshammer et al., 2019). To interrogate the mechanistic relevance of DNA bending, we tested the effect of DNA mechanical properties through nuclease assays on rigid poly(dA·dT)-rich 80 bp dsDNA, based on the *URA3* promoter sequence (Rohs et al., 2009; Suter et al., 2000) (Figure 2B). The enhanced DNA rigidity is proposed to be a result of the reduced minor groove width of poly(dA·dT) (Figures 2C and S3E). *Ec*MR cleaves Ku-bound *URA3*-derived 80 bp dsDNA at two distinct positions, 30 and 44 nt from the labeled 3′ end (Figures 2B–2D), whereas a generic 80 bp dsDNA shows a broader cleavage pattern around 33 and 45 nt (Käshammer et al., 2019). The 30 and 44 nt sites in the *URA3*-derived dsDNA correspond to interspersed flexible regions within the poly(dA·dT) stretches, which have a predicted higher flexibility (Zhou et al., 2013) (Figures 2C and S3E). Intriguingly, shifting the predicted flexible region at 30 nt two nucleotides backward and forward resulted in respective 2 nt shifts of the preferential cleavage site at 30 nt, but not at 44 nt (Figures 2C, 2D, and S3E).

Cryo-EM structure of *Ec*MR bound to a hairpin

Besides free and protein-blocked DNA termini, a third, physiologically relevant, substrate for MR/MRN are hairpins (Connelly et al., 2003; Lim et al., 2015; Paull and Gellert, 1998; Trujillo and Sung, 2001). To determine the cryo-EM structure of the *Ec*MR complex bound to a dsDNA hairpin, we vitrified the *Ec*M^{H84Q}R mutant in the presence of ATP with a dsDNA hairpin, featuring a 35 bp stem and 5 nt loop (Figures 2E and S4). The 5′ 6-FAM-labeled hairpin substrate was incubated with a single-chain variable fragment (FAM-scFv) against fluorescein to block the other end (Figure 2F) (Pedrazzi et al., 1997). MR cleaves the hairpin with predominant incision in the loop, suggesting that *Ec*MR either preferentially loads directly onto the hairpin, or it is loaded onto the scFv-blocked end and slides (in inward conformation) a few bases to settle on the hairpin (Figures 2F, 2G, and S3F). The 4 Å reconstruction revealed again a structure that is very similar to endonuclease and exonuclease modes (Figures 2E and 2H). Density for DNA is well resolved at the nuclease active site. Compared with the exonuclease state, some additional density in the nuclease channel likely results from the hairpin loop (Figure S3G). At this stage, the map does not allow determination of the precise hairpin geometry, which might be flexible. However, the structural fitting is consistent with an incision occurring between the first two nucleotides of the hairpin loop, as determined by nuclease assays (Figures 2F–2H). As with the endonuclease state, clear density for both Mg^{2+}-ADP moieties in the Rad50^{NBDs} could be observed, indicating again a post-hydrolysis state.

After completion of exonuclease (Käshammer et al., 2019), endonuclease (this study), and hairpin (this study) states, we conclude that all of them involve a highly similar DNA-*Ec*MR geometry up to the DNA contacts at the di-metal center. Significant differences are only seen for the parts of DNA after the di-metal site, exiting the active site channel. The results show that MR's cutting channel can accommodate a wide range of DNA structures, while DNA cleavage is carried out by a highly similar MR conformation (Figure 3).

DISCUSSION

The Mre11-Rad50 complex detects and clears aberrant or blocked DNA termini to enable further repair and maintain genome integrity (Cejka and Symington, 2021; Paull, 2018; Syed and Tainer, 2018). To endonucleolytically cleave DNA at diverse termini, but not in intact genomic DNA, MR needs to topologically, but not chemically, recognize a particular block or DNA end. Such a topological recognition was indicated in a recent study, showing that DNA ends traverse a narrow channel formed by Mre11 and Rad50 to reach the nuclease site (Käshammer et al., 2019).

Here, we present structures of *Ec*MR bound to a blocked DNA end and a hairpin. MR's nuclease channel emerges as a versatile entity that can accommodate free ends, internal DNA, as well as hairpins, all recognized by a similar configuration of MR, consistent with the biochemically observed cleavage sites and chemistry (Saathoff et al., 2018). Thus, MR does not have different types of structurally distinct nuclease modes, rather the way MR is loaded onto DNA determines the mode of DNA cleavage. In

Figure 2. DNA bending in endonuclease state and structure of *Ec*MR in complex with a hairpin

(A) LAFTER-filtered map illustrates extended DNA and a 45° bending at the nuclease active site (map threshold of 0.0045).
(B) Schematic representation of the rigid poly(dA·dT) (T-tract) 80 bp dsDNA used to investigate DNA bending by *Ec*MRs.
(C) DNA shape predictions (Zhou et al., 2013), illustrating rigid and more flexible regions.
(D) Nuclease assay of *Ec*MR WT on different (regular and rigid) 3′ 6-FAM-labeled, Ku-blocked 80 bp DNA substrates (4:1 ratio Ku:DNA), showing predominant nuclease cleavage at sites consistent with more flexible regions, mapped in (C).
(E) 4 Å density map of the *Ec*MR complex bound to a DNA hairpin (red). Extending, but not resolved, CCs are depicted by the dots.
(F) Scheme illustrating the hairpin sample and experimental cleavage position.
(G) Nuclease assay of *Ec*MR WT on the 5′ 6-FAM-labeled, scFv-blocked DNA hairpin, showing predominant nuclease cleavage at 36 nt, as illustrated in (F).
(H) Nuclease active site of Mre11 (A) bound to a DNA hairpin (color code of Figure 1D). Overlay: 4 Å cryo-EM map.
See also Figures S1, S3, and S4, Table 1, and Video S1.

Please cite this article in press as: Gut et al., Structural mechanism of endonucleolytic processing of blocked DNA ends and hairpins by Mre11-Rad50, Molecular Cell (2022), https://doi.org/10.1016/j.molcel.2022.07.019

Molecular Cell
Short article

CellPress

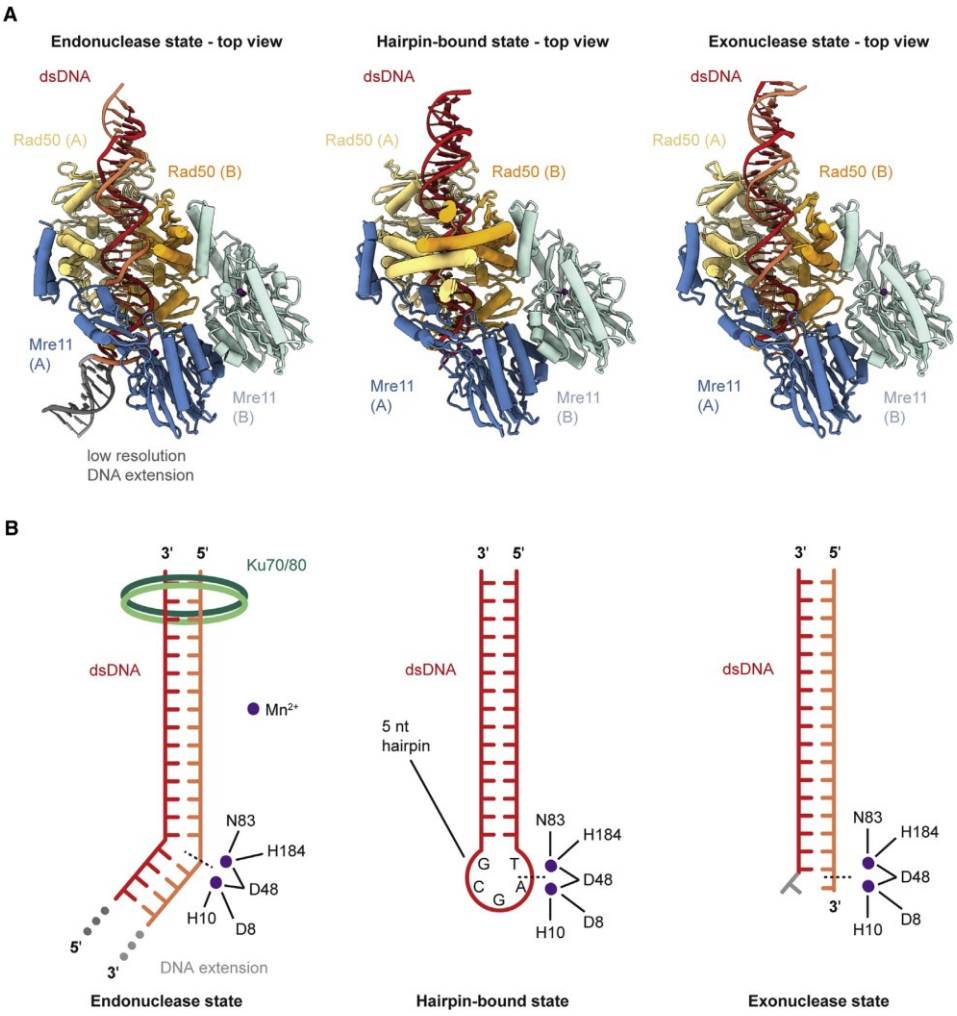

Figure 3. A unified nuclease mechanism as the basis for the processing of different DNA substrates

(A) Comparative view of all three nuclease active states of *Ec*MR shows a unified nuclease mechanism.

(B) Illustration of the nucleolytic cleavage positioning and active site residues on protein-blocked, hairpin, or free DNA termini.

See also Figure S3.

fact, our Ku-RM-MR-Ku structure points to an ATP-dependent loading reaction on Ku-bound DNA that leads to an inward-facing polarity where the Mre11 dimer is pointing away from the DSB. Based on the Ku-RM-MR-Ku structure (likely formed through symmetric loading of an inward-facing MR complex from either end), the inward-facing orientation of both *Ec*MRs positions the nuclease active site with ~55 nt from the 5′ end. Biochemically, we observe predominant 50 nt incisions, although they might be biased by local sequence/shape. Studies with MRX showed predominant cleavage at ~35 nt (Reginato et al., 2017; Wang et al., 2017), which one can achieve, based on our model, simply by sliding MR closer to Ku until the proteins almost touch.

The inward-facing configuration clarifies why in the endonuclease mode the 5′ strand is incised, whereas in the exonuclease mode (outward-facing configuration) it is the 3′ strand (Cannavo and Cejka, 2014; Deshpande et al., 2016). Furthermore, it explains the cleavage chemistry where in exonuclease mode, the phosphates are part of the leaving dNMPs, while in endonuclease mode, the phosphates remain attached to the newly formed DNA termini at the *Ec*MR-bound strand (Saathoff et al., 2018). Furthermore, the outward-facing orientation at the free end/hairpin may be a result of an inward-facing loading at the other end of the DNA oligos, followed by lateral sliding. So, it is possible that MR always loads with the same inward-facing polarity;

Please cite this article in press as: Gut et al., Structural mechanism of endonucleolytic processing of blocked DNA ends and hairpins by Mre11-Rad50, Molecular Cell (2022), https://doi.org/10.1016/j.molcel.2022.07.019

CellPress

Molecular Cell
Short article

however, it may result in outward-facing polarity on the typical double-ended short DNA molecules used in biochemical assays. Structural alignments of human Rad50 and Mre11 AlphaFold2 models on the endonuclease-state structure further showed that the predicted human models are sterically able to adopt a very similar conformation than *Ec*MR (Figure S3H). Although details of the cutting state of eukaryotic MRN/X must await future experimental work, our proposed unified nuclease-cutting-state mechanism might be applicable to eukaryotic Mre11-Rad50 homologs.

An unexpected result was the DNA bending by MR in the endonuclease state. We estimate around 45°–50° in individual MR particles and Ku-MR-MR-Ku complexes, respectively. Several studies biochemically observed influence of DNA melting and unwinding in nuclease activities or DNA binding studies (Gobbini et al., 2018; Liu et al., 2016; Sharma et al., 2021; Zabolotnaya et al., 2020). We do not see evidence for active DNA melting in the endonuclease state, rather DNA is bent in a base-paired manner. However, as MR/MRN may form oligomers, DNA melting could take place in close vicinity or between complexes to compensate torsional stress forced onto the DNA. Internal bubbles or regions that are more easily meltable could also lead to preferential binding and cutting at these sites. Furthermore, the need for DNA bending could explain the promotion of endonuclease by a nick in the opposite strand (Deshpande et al., 2016). In any case, local DNA mechanical or shape properties, or the width of the minor groove, can apparently influence the position and effectivity of the DNA strand incision reaction. As these features can also be a function of local DNA sequence, an interesting area for future studies will be the physiological relevance of DNA mechanical properties or sequence in DSB processing by MRN/X. For instance, it could be linked to the recently observed local sequence-dependent cleavage of mitotic DSBs by MRX *in vivo* (Bazzano et al., 2021).

In summary, we reveal how MR structurally binds obstructed DNA termini and cuts them with endonuclease activity, unifying MR's distinct nuclease reactions in a common mechanistic framework.

Limitations of the study

We do not yet understand the precise mechanism of the ATP-dependent loading mechanism of Mre11-Rad50 onto DNA ends, why it cleaves near the DSB and does not slide inward, whether and how oligomerization is involved, and how MR additionally cleaves the 3′ strand opposing the 5′ incision with a different cleavage chemistry.

STAR★METHODS

Detailed methods are provided in the online version of this paper and include the following:

- KEY RESOURCES TABLE
- RESOURCE AVAILABILITY
  - Lead contact
  - Materials availability
  - Data and code availability
- EXPERIMENTAL MODEL AND SUBJECT DETAILS
  - Organisms as source for materials used in experiments
- METHOD DETAILS
  - Expression and purification of *Ec*MR
  - Expression and purification of Ku70/80
  - DNA substrates
  - Nuclease assay
  - Electrophoretic mobility shift assay (EMSA)
  - Grid preparation for cryo-electron microscopy
  - Electron microscopy data collection and processing
  - Model building
- QUANTIFICATION AND STATISTICAL ANALYSIS

SUPPLEMENTAL INFORMATION

Supplemental information can be found online at https://doi.org/10.1016/j.molcel.2022.07.019.

ACKNOWLEDGMENTS

EM data were collected at the Cryo-EM Core Facility of the Gene Center, Department of Biochemistry, LMU, Munich. We thank all members of the Hopfner lab for helpful discussions. K.-P.H. is supported by the Deutsche Forschungsgemeinschaft (CRC1361, HO2489/11-1) and the Gottfried-Wilhelm-Leibniz Prize. F.G. acknowledges the support from the Research Training Group 1721. L.K. acknowledges support from the International Max Planck Research School of Molecular and Cellular Life Sciences. K.L. is supported by the Deutsche Forschungsgemeinschaft (CRC1054, Project-ID 210592381) E.v.d.L. is supported by a PhD fellowship from Boehringer Ingelheim Fonds (BIF).

AUTHOR CONTRIBUTIONS

F.G. and L.K. prepared cryo-EM grids and performed structure determination and modeling. F.G., L.K., A.-M.B., and E.v.d.L. performed the biochemical analysis. F.G., L.K., and K.-P.H. analyzed results. F.G., L.K., and B.K. purified the proteins. K.L. and J.D.B. helped with data collection, structure determination, analysis, and modeling. K.-P.H. and F.G. wrote the paper with contributions from all other authors. K.-P.H. designed the overall study.

DECLARATION OF INTERESTS

The authors declare no competing interests.

Received: March 3, 2022
Revised: June 10, 2022
Accepted: July 23, 2022
Published: August 19, 2022

SUPPORTING CITATIONS

The following references appear in the supplemental information: Kashammer et al. (2019); Zhou et al. (2013); Tan et al. (2017); Evans et al., [https://doi.org/10.1101/2021.10.04].

REFERENCES

Afonine, P.V., Poon, B.K., Read, R.J., Sobolev, O.V., Terwilliger, T.C., Urzhumtsev, A., and Adams, P.D. (2018). Real-space refinement in PHENIX for cryo-EM and crystallography. Acta Crystallogr. D Struct. Biol. *74*, 531–544.

Asarnow, D., Palovcak, E., and Cheng, Y. (2019). UCSF pyem v0. 5. Zenodo. https://doi.org/10.5281/zenodo.3576630.

Bazzano, D., Lomonaco, S., and Wilson, T.E. (2021). Mapping yeast mitotic 5′ resection at base resolution reveals the sequence and positional dependence of nucleases in vivo. Nucleic Acids Res. *49*, 12607–12621.

Please cite this article in press as: Gut et al., Structural mechanism of endonucleolytic processing of blocked DNA ends and hairpins by Mre11-Rad50, Molecular Cell (2022), https://doi.org/10.1016/j.molcel.2022.07.019

Molecular Cell
Short article

Bepler, T., Morin, A., Rapp, M., Brasch, J., Shapiro, L., Noble, A.J., and Berger, B. (2019). Positive-unlabeled convolutional neural networks for particle picking in cryo-electron micrographs. Nat. Methods *16*, 1153–1160.

Bliss, T.M., and Lane, D.P. (1997). Ku selectively transfers between DNA molecules with homologous ends. J. Biol. Chem. *272*, 5765–5773.

Burnley, T., Palmer, C.M., and Winn, M. (2017). Recent developments in the CCP-EM software suite. Acta Crystallogr. D Struct. Biol. *73*, 469–477.

Cannavo, E., and Cejka, P. (2014). Sae2 promotes dsDNA endonuclease activity within Mre11-Rad50-Xrs2 to resect DNA breaks. Nature *514*, 122–125.

Cannavo, E., Reginato, G., and Cejka, P. (2019). Stepwise 5′ DNA end-specific resection of DNA breaks by the Mre11-Rad50-Xrs2 and Sae2 nuclease ensemble. Proc. Natl. Acad. Sci. USA *116*, 5505–5513.

Carbone, M., Arron, S.T., Beutler, B., Bononi, A., Cavenee, W., Cleaver, J.E., Croce, C.M., D'Andrea, A., Foulkes, W.D., Gaudino, G., et al. (2020). Tumour predisposition and cancer syndromes as models to study gene-environment interactions. Nat. Rev. Cancer *20*, 533–549.

Carney, J.P., Maser, R.S., Olivares, H., Davis, E.M., Le Beau, M., Yates, J.R., Hays, L., Morgan, W.F., and Petrini, J.H. (1998). The hMre11/hRad50 protein complex and Nijmegen breakage syndrome: linkage of double-strand break repair to the cellular DNA damage response. Cell *93*, 477–486.

Cassani, C., Vertemara, J., Bassani, M., Marsella, A., Tisi, R., Zampella, G., and Longhese, M.P. (2019). The ATP-bound conformation of the Mre11-Rad50 complex is essential for Tel1/ATM activation. Nucleic Acids Res. *47*, 3550–3567.

Cejka, P., and Symington, L.S. (2021). DNA end resection: mechanism and control. Annu. Rev. Genet. *55*, 285–307.

Chang, H.H.Y., Pannunzio, N.R., Adachi, N., and Lieber, M.R. (2017). Non-homologous DNA end joining and alternative pathways to double-strand break repair. Nat. Rev. Mol. Cell Biol. *18*, 495–506.

Chen, C.C., Feng, W., Lim, P.X., Kass, E.M., and Jasin, M. (2018). Homology-directed repair and the role of BRCA1, BRCA2, and related proteins in genome integrity and cancer. Annu. Rev. Cancer Biol. *2*, 313–336.

Connelly, J.C., de Leau, E.S., and Leach, D.R. (2003). Nucleolytic processing of a protein-bound DNA end by the E. coli SbcCD (MR) complex. DNA Repair (Amst) *2*, 795–807.

Croll, T.I. (2018). Isolde: a physically realistic environment for model building into low-resolution electron-density maps. Acta Crystallogr. D Struct. Biol. *74*, 519–530.

Delamarre, A., Barthe, A., de la Roche Saint-André, C., Luciano, P., Forey, R., Padioleau, I., Skrzypczak, M., Ginalski, K., Géli, V., Pasero, P., and Lengronne, A. (2020). MRX increases chromatin accessibility at stalled replication forks to promote nascent DNA resection and cohesin loading. Mol. Cell *77*, 395–410.e3.

Della, M., Palmbos, P.L., Tseng, H.M., Tonkin, L.M., Daley, J.M., Topper, L.M., Pitcher, R.S., Tomkinson, A.E., Wilson, T.E., and Doherty, A.J. (2004). Mycobacterial Ku and ligase proteins constitute a two-component NHEJ repair machine. Science *306*, 683–685.

Deshpande, R.A., Lee, J.H., Arora, S., and Paull, T.T. (2016). Nbs1 converts the human Mre11/Rad50 nuclease complex into an Endo/exonuclease machine specific for protein-DNA adducts. Mol. Cell *64*, 593–606.

Emsley, P., and Cowtan, K. (2004). Coot: model-building tools for molecular graphics. Acta Crystallogr. D Biol. Crystallogr. *60*, 2126–2132.

Evans, R., O'Neill, M., Pritzel, A., Antropova, N., Senior, A.W., Green, T., Žídek, A., Bates, R., Blackwell, S., and Yim, J. (2021). Protein complex prediction with AlphaFold-Multimer. BioRxiv.

Eykelenboom, J.K., Blackwood, J.K., Okely, E., and Leach, D.R. (2008). SbcCD causes a double-strand break at a DNA palindrome in the Escherichia coli chromosome. Mol. Cell *29*, 644–651.

Garcia, V., Phelps, S.E.L., Gray, S., and Neale, M.J. (2011). Bidirectional resection of DNA double-strand breaks by Mre11 and Exo1. Nature *479*, 241–244.

Ghosh, M., Vinay Kumar, N., Varshney, U., and Chary, K.V. (2000). Structural basis for uracil DNA glycosylase interaction with uracil: NMR study. Nucleic Acids Res. *28*, 1906–1912.

Gobbini, E., Vertemara, J., and Longhese, M.P. (2018). Local unwinding of double-strand DNA ends by the MRX complex promotes Exo1 processing activity. Mol. Cell. Oncol. *5*, e1511208.

Grant, T., Rohou, A., and Grigorieff, N. (2018). cisTEM, user-friendly software for single-particle image processing. eLife *7*, e35383.

Haber, J.E. (2018). DNA repair: the search for homology. BioEssays *40*, e1700229.

Hailemariam, S., Kumar, S., and Burgers, P.M. (2019). Activation of Tel11ATM kinase requires Rad50 ATPase and long nucleosome-free DNA but no DNA ends. J. Biol. Chem. *294*, 10120–10130.

Hoa, N.N., Shimizu, T., Zhou, Z.W., Wang, Z.Q., Deshpande, R.A., Paull, T.T., Akter, S., Tsuda, M., Furuta, R., Tsutsui, K., et al. (2016). Mre11 is essential for the removal of lethal topoisomerase 2 covalent cleavage complexes. Mol. Cell *64*, 1010.

Hopfner, K.P., Craig, L., Moncalian, G., Zinkel, R.A., Usui, T., Owen, B.A.L., Karcher, A., Henderson, B., Bodmer, J.L., McMurray, C.T., et al. (2002). The Rad50 zinc-hook is a structure joining Mre11 complexes in DNA recombination and repair. Nature *418*, 562–566.

Hopfner, K.P., Karcher, A., Craig, L., Woo, T.T., Carney, J.P., and Tainer, J.A. (2001). Structural biochemistry and interaction architecture of the DNA double-strand break repair Mre11 nuclease and Rad50-ATPase. Cell *105*, 473–485.

Johnson, D., Crawford, M., Cooper, T., Claeys Bouuaert, C., Keeney, S., Llorente, B., Garcia, V., and Neale, M.J. (2021). Concerted cutting by Spo11 illuminates meiotic DNA break mechanics. Nature *594*, 572–576.

Jumper, J., Evans, R., Pritzel, A., Green, T., Figurnov, M., Ronneberger, O., Tunyasuvunakool, K., Bates, R., Žídek, A., Potapenko, A., et al. (2021). Highly accurate protein structure prediction with AlphaFold. Nature *596*, 583–589.

Käshammer, L., Saathoff, J.H., Lammens, K., Gut, F., Bartho, J., Alt, A., Kessler, B., and Hopfner, K.P. (2019). Mechanism of DNA end sensing and processing by the Mre11-Rad50 complex. Mol. Cell *76*, 382–394.e6.

Kim, J.J., Lee, S.Y., Choi, J.H., Woo, H.G., Xhemalce, B., and Miller, K.M. (2020). PCAF-mediated histone acetylation promotes replication fork degradation by MRE11 and EXO1 in BRCA-deficient cells. Mol. Cell *80*, 327–344.e8.

Kissling, V.M., Reginato, G., Bianco, E., Kasaciunaite, K., Tilma, J., Cereghetti, G., Schindler, N., Lee, S.S., Guérois, R., Luke, B., et al. (2022). Mre11-Rad50 oligomerization promotes DNA double-strand break repair. Nat. Commun. *13*, 2374.

Lee, J.H., and Paull, T.T. (2005). ATM activation by DNA double-strand breaks through the Mre11-Rad50-Nbs1 complex. Science *308*, 551–554.

Liebschner, D., Afonine, P.V., Baker, M.L., Bunkóczi, G., Chen, V.B., Croll, T.I., Hintze, B., Hung, L.W., Jain, S., McCoy, A.J., et al. (2019). Macromolecular structure determination using X-rays, neutrons and electrons: recent developments in Phenix. Acta Crystallogr. D Struct. Biol. *75*, 861–877.

Lim, C.T., Lai, P.J., Leach, D.R., Maki, H., and Furukohri, A. (2015). A novel mode of nuclease action is revealed by the bacterial Mre11/Rad50 complex. Nucleic Acids Res. *43*, 9804–9816.

Liu, S., Tian, L.F., Liu, Y.P., An, X.M., Tang, Q., Yan, X.X., and Liang, D.C. (2014). Structural basis for DNA recognition and nuclease processing by the Mre11 homologue SbcD in double-strand breaks repair. Acta Crystallogr. D Biol. Crystallogr. *70*, 299–309.

Liu, Y., Sung, S., Kim, Y., Li, F., Gwon, G., Jo, A., Kim, A.K., Kim, T., Song, O.K., Lee, S.E., and Cho, Y. (2016). ATP-dependent DNA binding, unwinding, and resection by the Mre11/Rad50 complex. EMBO J. *35*, 743–758.

Lobachev, K.S., Gordenin, D.A., and Resnick, M.A. (2002). The Mre11 complex is required for repair of hairpin-capped double-strand breaks and prevention of chromosome rearrangements. Cell *108*, 183–193.

Marie, L., and Symington, L.S. (2022). Mechanism for inverted-repeat recombination induced by a replication fork barrier. Nat. Commun. *13*, 32.

Please cite this article in press as: Gut et al., Structural mechanism of endonucleolytic processing of blocked DNA ends and hairpins by Mre11-Rad50, Molecular Cell (2022), https://doi.org/10.1016/j.molcel.2022.07.019

CellPress

Molecular Cell
Short article

Mimitou, E.P., and Symington, L.S. (2008). Sae2, Exo1 and Sgs1 collaborate in DNA double-strand break processing. Nature *455*, 770–774.

Mojumdar, A., Sorenson, K., Hohl, M., Toulouze, M., Lees-Miller, S.P., Dubrana, K., Petrini, J.H.J., and Cobb, J.A. (2019). Nej1 interacts with Mre11 to regulate tethering and Dna2 binding at DNA double-strand breaks. Cell Rep. *28*, 1564–1573.e3.

Moreno-Herrero, F., de Jager, M., Dekker, N.H., Kanaar, R., Wyman, C., and Dekker, C. (2005). Mesoscale conformational changes in the DNA-repair complex Rad50/Mre11/Nbs1 upon binding DNA. Nature *437*, 440–443.

Morimoto, S., Tsuda, M., Bunch, H., Sasanuma, H., Austin, C., and Takeda, S. (2019). Type II DNA topoisomerases cause spontaneous double-strand breaks in genomic DNA. Genes (Basel) *10*, 868.

Park, Y.B., Hohl, M., Padjasek, M., Jeong, E., Jin, K.S., Krężel, A., Petrini, J.H., and Cho, Y. (2017). Eukaryotic Rad50 functions as a rod-shaped dimer. Nat. Struct. Mol. Biol. *24*, 248–257.

Paull, T.T. (2018). 20 years of Mre11 biology: no end in sight. Mol. Cell *71*, 419–427.

Paull, T.T., and Gellert, M. (1998). The 3′ to 5′ exonuclease activity of Mre 11 facilitates repair of DNA double-strand breaks. Mol. Cell *1*, 969–979.

Pedrazzi, G., Schwesinger, F., Honegger, A., Krebber, C., and Plückthun, A. (1997). Affinity and folding properties both influence the selection of antibodies with the selectively infective phage (SIP) methodology. FEBS Lett. *415*, 289–293.

Pettersen, E.F., Goddard, T.D., Huang, C.C., Couch, G.S., Greenblatt, D.M., Meng, E.C., and Ferrin, T.E. (2004). UCSF Chimera–a visualization system for exploratory research and analysis. J. Comput. Chem. *25*, 1605–1612.

Pettersen, E.F., Goddard, T.D., Huang, C.C., Meng, E.C., Couch, G.S., Croll, T.I., Morris, J.H., and Ferrin, T.E. (2021). UCSF ChimeraX: structure visualization for researchers, educators, and developers. Protein Sci. *30*, 70–82.

Punjani, A., Rubinstein, J.L., Fleet, D.J., and Brubaker, M.A. (2017). cryoSPARC: algorithms for rapid unsupervised cryo-EM structure determination. Nat. Methods *14*, 290–296.

Punjani, A., Zhang, H., and Fleet, D.J. (2020). Non-uniform refinement: adaptive regularization improves single-particle cryo-EM reconstruction. Nat. Methods *17*, 1214–1221.

Ramlaul, K., Palmer, C.M., and Aylett, C.H.S. (2019). A local agreement filtering algorithm for transmission EM reconstructions. J. Struct. Biol. *205*, 30–40.

Reginato, G., Cannavo, E., and Cejka, P. (2017). Physiological protein blocks direct the Mre11-Rad50-Xrs2 and Sae2 nuclease complex to initiate DNA end resection. Genes Dev. *31*, 2325–2330.

Rohou, A., and Grigorieff, N. (2015). CTFFIND4: fast and accurate defocus estimation from electron micrographs. J. Struct. Biol. *192*, 216–221.

Rohs, R., West, S.M., Sosinsky, A., Liu, P., Mann, R.S., and Honig, B. (2009). The role of DNA shape in protein-DNA recognition. Nature *461*, 1248–1253.

Saathoff, J.H., Käshammer, L., Lammens, K., Byrne, R.T., and Hopfner, K.P. (2018). The bacterial Mre11-Rad50 homolog SbcCD cleaves opposing strands of DNA by two chemically distinct nuclease reactions. Nucleic Acids Res. *46*, 11303–11314.

Scheres, S.H. (2012). RELION: implementation of a Bayesian approach to cryo-EM structure determination. J. Struct. Biol. *180*, 519–530.

Seeber, A., Hegnauer, A.M., Hustedt, N., Deshpande, I., Poli, J., Eglinger, J., Pasero, P., Gut, H., Shinohara, M., Hopfner, K.P., et al. (2016). RPA mediates recruitment of MRX to forks and double-strand breaks to hold sister chromatids together. Mol. Cell *64*, 951–966.

Sharma, S., Anand, R., Zhang, X., Francia, S., Michelini, F., Galbiati, A., Williams, H., Ronato, D.A., Masson, J.Y., Rothenberg, E., et al. (2021). MRE11-RAD50-NBS1 complex is sufficient to promote transcription by RNA polymerase II at double-strand breaks by melting DNA ends. Cell Rep. *34*, 108565.

Suter, B., Schnappauf, G., and Thoma, F. (2000). Poly(dA.dT) sequences exist as rigid DNA structures in nucleosome-free yeast promoters in vivo. Nucleic Acids Res. *28*, 4083–4089.

Syed, A., and Tainer, J.A. (2018). The MRE11-RAD50-NBS1 complex conducts the orchestration of damage signaling and outcomes to stress in DNA replication and repair. Annu. Rev. Biochem. *87*, 263–294.

Tan, Y.Z., Baldwin, P.R., Davis, J.H., Williamson, J.R., Potter, C.S., Carragher, B., and Lyumkis, D. (2017). Addressing preferred specimen orientation in single-particle cryo-EM through tilting. Nat. Methods *14*, 793–796.

Trujillo, K.M., and Sung, P. (2001). DNA structure-specific nuclease activities in the Saccharomyces cerevisiae Rad50*Mre11 complex. J. Biol. Chem. *276*, 35458–35464.

Wang, W., Daley, J.M., Kwon, Y., Krasner, D.S., and Sung, P. (2017). Plasticity of the Mre11-Rad50-Xrs2-Sae2 nuclease ensemble in the processing of DNA-bound obstacles. Genes Dev. *31*, 2331–2336.

Wendel, B.M., Cole, J.M., Courcelle, C.T., and Courcelle, J. (2018). SbcC-SbcD and ExoI process convergent forks to complete chromosome replication. Proc. Natl. Acad. Sci. USA *115*, 349–354.

Wood, C., Burnley, T., Patwardhan, A., Scheres, S., Topf, M., Roseman, A., and Winn, M. (2015). Collaborative computational project for electron cryo-microscopy. Acta Crystallogr. D Biol. Crystallogr. *71*, 123–126.

Wright, W.D., Shah, S.S., and Heyer, W.D. (2018). Homologous recombination and the repair of DNA double-strand breaks. J. Biol. Chem. *293*, 10524–10535.

Zabolotnaya, E., Mela, I., Williamson, M.J., Bray, S.M., Yau, S.K., Papatziamou, D., Edwardson, J.M., Robinson, N.P., and Henderson, R.M. (2020). Modes of action of the archaeal Mre11/Rad50 DNA-repair complex revealed by fast-scan atomic force microscopy. Proc. Natl. Acad. Sci. USA *117*, 14936–14947.

Zhao, B., Rothenberg, E., Ramsden, D.A., and Lieber, M.R. (2020). The molecular basis and disease relevance of non-homologous DNA end joining. Nat. Rev. Mol. Cell Biol. *21*, 765–781.

Zheng, S.Q., Palovcak, E., Armache, J.P., Verba, K.A., Cheng, Y., and Agard, D.A. (2017). MotionCor2: anisotropic correction of beam-induced motion for improved cryo-electron microscopy. Nat. Methods *14*, 331–332.

Zhou, T., Yang, L., Lu, Y., Dror, I., Dantas Machado, A.C., Ghane, T., Di Felice, R., and Rohs, R. (2013). DNAshape: a method for the high-throughput prediction of DNA structural features on a genomic scale. Nucleic Acids Res. *41*, W56–W62.

Please cite this article in press as: Gut et al., Structural mechanism of endonucleolytic processing of blocked DNA ends and hairpins by Mre11-Rad50, Molecular Cell (2022), https://doi.org/10.1016/j.molcel.2022.07.019

Molecular Cell
Short article

CellPress

STAR★METHODS

KEY RESOURCES TABLE

REAGENT or RESOURCE	SOURCE	IDENTIFIER
Chemicals, peptides, and recombinant proteins		
ATP	Sigma (Merck)	A3377
ATPγS	Sigma (Merck)	A1388
2-Mercaptoethanol	Carl-Roth	4227
DTT	Carl Roth	6908
Imidazole	Carl Roth	3899
β-Octylglycoside	Sigma (Merck)	O8001
BSA	New England bioLabs	B9000S
6-FAM scFv	Prof. Dr. Plückthun, University of Zürich (Pedrazzi et al., 1997)	N/A
Urea	Carl Roth	3941
EDTA	VWR International	6381-92-6
Ficoll 400	Carl Roth	CN90.3
Rotiphorese DNA sequencing system	Carl Roth	A431.1
$MgCl_2$	Merck	7791-18-6
$MnCl_2$	Sigma (Merck)	M3634
TCEP	Sigma (Merck)	646547
SIGMAFAST Protease Inhibitor Cocktail Tablet, EDTA free	Merck	S8830
Deposited data		
*Ec*MR coordinates (Endonuclease state)	This Paper	PDB: 7YZO
*Ec*MR head EM map (Endonuclease state)	This Paper	EMDB-14391
*Ec*MR head coordinates with extended DNA (Endonuclease state)	This Paper	PDB: 7Z03
*Ec*MR head EM map with extended DNA (Endonuclease state)	This Paper	EMDB-14403
Ku70/80 (bound to dsDNA) EM map	This Paper	EMDB-14394
Ku-RM-MR-Ku state EM map	This Paper	EMDB-14392
Ku-RM-MR-Ku state EM composite map	This Paper	EMDB-14392
*Ec*MR coordinates (Hairpin-bound)	This Paper	PDB: 7YZP
*Ec*MR head EM map (Hairpin-bound)	This Paper	EMDB-14393
Full Gel Images	This Paper	https://doi.org/10.17632/kdvrdjvz7d.1
Experimental models: Organisms/strains		
E. coli XL1 Blue	Expression System	N/A
E. coli Rosetta2	Expression System	N/A
E. coli BL21 (DE3)	Expression System	N/A
Spodoptera frugiperda sf21 cells	Expression System	N/A
Trichoplusia ni cells	Expression System	N/A
Oligonucleotides		
Oligonucleotides	Metabion	See Table S1
Primer	Metabion	See Table S1
Recombinant DNA		
pET21b-*Ec*Mre11	Saathoff et al., 2018	N/A
pET29-*Ec*Rad50	Saathoff et al., 2018	N/A

(*Continued on next page*)

Please cite this article in press as: Gut et al., Structural mechanism of endonucleolytic processing of blocked DNA ends and hairpins by Mre11-Rad50, Molecular Cell (2022), https://doi.org/10.1016/j.molcel.2022.07.019

Continued

REAGENT or RESOURCE	SOURCE	IDENTIFIER
pACEBac1-pIDK-*Ct*Ku70/80	Käshammer et al., 2019	N/A
Software and algorithms		
MotionCor2	Zheng et al., 2017	https://msg.ucsf.edu/em/software/motioncor2.html
CTFFIND4.1	Rohou and Grigorieff, 2015	http://grigoriefflab.janelia.org/ctffind4
Relion 3.0.8	Scheres, 2012	https://www3.mrc-lmb.cam.ac.uk/relion/index.php?title=Main_Page
Phenix	Afonine et al., 2018; Liebschner et al., 2019	https://www.phenix-online.org/
UCSF Chimera	Pettersen et al., 2004	https://www.cgl.ucsf.edu/chimera/
ChimeraX	Pettersen et al., 2021	https://www.rbvi.ucsf.edu/chimerax/
COOT	Emsley and Cowtan, 2004	https://www2.mrc-lmb.cam.ac.uk/Personal/pemsley/coot/
OriginPro	OriginLab	N/A
CryoSPARC v3.2.0	Punjani et al., 2017	https://cryosparc.com/
Topaz	Bepler et al., 2019	https://emgweb.nysbc.org/topaz.html
CisTEM v1.0.2	Grant et al., 2018	https://cistem.org/
High-throughput DNA Shape Prediction	Zhou et al., 2013	https://rohslab.usc.edu/DNAshape/index.html
AlphaFold v2.1.0	Jumper et al., 2021	https://colab.research.google.com/github/deepmind/alphafold/blob/main/notebooks/AlphaFold.ipynb
CCP-EM	Burnley et al., 2017	https://www.ccpem.ac.uk/
LAFTER v1.1	Ramlaul et al., 2019	https://github.com/StructuralBiology-ICLMedicine/lafter
pyEM v0.5	Asarnow et al., 2019	https://github.com/asarnow/pyem/tree/v0.5
ISOLDE	Croll, 2018	https://isolde.cimr.cam.ac.uk/static/isolde/doc/isolde.html
3DFSC	Tan et al., 2017	https://3dfsc.salk.edu/

RESOURCE AVAILABILITY

Lead contact

Further information and requests for resources and reagents should be directed to and will be fulfilled by the lead contact Karl-Peter Hopfner (hopfner@genzentrum.lmu.de).

Materials availability

This study did not generate new unique reagents.

Data and code availability

- The coordinate files generated during this study are available at the Protein Data Bank (https://www.rcsb.org/) with the accession codes PDB: 7YZO (Endonuclease state), PDB: 7Z03 (Endonuclease state with extended DNA) and PDB: 7YZP (Hairpin-bound state). The cryo-EM reconstructions generated during this study are available at the Electron Microscopy Data Bank (https://www.ebi.ac.uk/pdbe/emdb/) with the accession codes EMDB: EMD-14391 (Endonuclease state head complex at 3.4 Å), EMDB: EMD-14403 (LAFTER-filtered endonuclease state head complex with extended DNA), EMDB: EMD-14392 (Composite map and Ku-RM-MR-Ku state at 8.2 Å), EMDB: EMD-14394 (Ku70/80 bound to dsDNA at 3.5 Å) and EMDB: EMD-14393 (Hairpin-bound state head complex at 4 Å). Full gel images are deposited under the following https://doi.org/10.17632/kdvrdjvz7d.1.
- This paper does not report original code.
- Any additional information required to reanalyse the data reported in this paper is available from the lead contact upon request.

Please cite this article in press as: Gut et al., Structural mechanism of endonucleolytic processing of blocked DNA ends and hairpins by Mre11-Rad50, Molecular Cell (2022), https://doi.org/10.1016/j.molcel.2022.07.019

Molecular Cell
Short article

CellPress

EXPERIMENTAL MODEL AND SUBJECT DETAILS

Organisms as source for materials used in experiments

E. coli XL1 Blue cells were used for amplification of plasmid DNA.
E. coli BL21 (DE3) and *E. coli* Rosetta2 were used for recombinant protein expression.
Spodoptera frugiperda sf21 insect cells were used for virus production.
Trichoplusia ni insect cells were used for recombinant protein expression.

METHOD DETAILS

Expression and purification of *Ec*MR

Expression and purification of full-length *Ec*Mre11 (pET21b expression vector; C-terminal 6xHis-tag) and *Ec*Rad50 (pET29 expression vector) was performed as described in a previous publication (Käshammer et al., 2019). Both expression vectors were co-transfected into *E. coli* BL21 (DE3) or Rosetta2 bacterial cells for protein expression. Bacterial cultures were grown in LB media at 37°C to an OD_{600} of 0.6. Protein expression was induced using 0.5 mM IPTG and carried out at 18°C for 16 hours. Cells were harvested by centrifugation and resuspended in lysis buffer (25 mM Tris pH 7.5, 150 mM NaCl, 10 mM Imidazole, 5 mM β-Mercaptoethanol) before cell disruption by sonication. Cell lysate was cleared by centrifugation and the supernatant was applied onto 2.5 mL of pre-equilibrated Ni-NTA resin (QIAGEN). The protein immobilized on the resin was then washed with 20 mL lysis buffer and 25 mL wash buffer (25 mM Tris pH 7.5, 125 mM NaCl, 20 mM Imidazole and 5 mM β-Mercaptoethanol). Captured protein was eluted with 10 mL elution buffer (25 mM Tris pH 7.5, 100 mM NaCl, 200 mM Imidazole and 5 mM β-Mercaptoethanol) and loaded onto a 1 mL HiTrapQ column (GE). Elution from the anion exchange column was done by a step gradient with increasing salt concentration (Buffer A: 100 mM NaCl, 25 mM Tris pH 7.5, Buffer B: 1 M NaCl, 25 mM Tris pH 7.5). Ion exchange chromatography peak fractions were pooled, concentrated and purified via size-exclusion chromatography using a Superose 6 10/300 (GE Healthcare) column pre-equilibrated in size-exclusion buffer (125 mM NaCl, 20 mM Tris pH 7.5, 10% Glycerol). The protein fractions of interest were identified by SDS-PAGE, pooled, concentrated and stored at -80°C.

Expression and purification of Ku70/80

Expression and purification of full-length *Chaetomium thermophilum* Ku70/80 was performed as described in a previous publication (Käshammer et al., 2019). Codon-optimized synthetic DNA (Genscript, Piscataway, USA) encoding Ku70 (N-terminal human rhinovirus 3C-protease cleavable 6xHis-tag) and Ku80 was PCR amplified and cloned into pACEBac1 and pIDC respectively and expressed using the MultiBac technology. Recombination steps were carried out in *E. coli* XL1 Blue cells under addition of Cre recombinase (NEB). Baculovirus generation was done in *Spodoptera frugiperda* (sf21) insect cells (IPLB-Sf21AE). For protein expression, *Trichoplusia ni* High Five cells were co-infected using 1:5000 of baculovirus. Cells were cultured for 72 hours at 27°C and harvested by centrifugation. Cells were re-suspended in lysis buffer (50 mM HEPES pH 7.5, 1 M NaCl, 400 mM NH_4OAc, 5% glycerol, 0.5 mM TCEP supplemented with a SIGMAFAST Protease Inhibitor Cocktail Tablet, EDTA free (Merck)) and gently sonified for cell disruption. The lysate was incubated for 1 hour at 50°C and subsequently cleared by centrifugation at 34500 g and 4°C for 30 min. The cleared supernatant was applied onto 2 mL of pre-equilibrated Ni-NTA (QIAGEN) and the immobilized protein was then washed with 20 mL wash buffer (50 mM HEPES pH 7.5, 250 mM NaCl, 10 mM Imidazole and 0.5 mM TCEP). The protein was eluted in 10 mL elution buffer (50 mM HEPES pH 7.5, 250 mM NaCl, 500 mM Imidazole and 0.5 mM TCEP) before cleavage of the affinity tag by overnight incubation with human rhinovirus 3C-protease at 4°C during dialysis into low salt buffer (50 mM HEPES pH 7.5, 150 mM NaCl and 0.5 mM TCEP). The filtered protein was then loaded onto a 5 mL HiTrap Heparin HP column (GE Healthcare), equilibrated in dialysis buffer and eluted with an increasing salt gradient before purification via size-exclusion chromatography using a Superose 6 16/60 (GE Healthcare) column equilibrated in size-exclusion buffer (20 mM HEPES pH 7.5, 200 mM NaCl and 0.5 mM TCEP). Protein fractions of interest were identified by SDS-PAGE, pooled, concentrated and stored at -80°C.

DNA substrates

All oligonucleotides were purchased HPLC-purified from Metabion (Planegg, Germany) and additionally purified via PAGE if fluorescently labeled. For annealing, the complementary oligo mix was heated to 95°C and then slowly cooled down to 25°C with a gradual decrease of 0.1°C per second using a PCR cycler. Unlabeled oligos were mixed in a 1:1 ratio for annealing. If labeled oligos were used, a ratio of 1.1 to 1 of unlabeled to labeled was used. The used oligonucleotide sequences are listed in Table S1.

Nuclease assay

The nuclease reaction was carried out in assay buffer (25 mM Tris pH 7.5, 50 mM KCl, 5 mM $MgCl_2$, 2 mM $MnCl_2$, 0.2 mg/ml BSA,1 mM DTT, 1 mM ATP) with 250 nM *Ec*MR and 50 nM 6-FAM labeled 80 bp dsDNA or hairpin DNA substrate (Table S1). To investigate endonuclease activity of the *Ec*MR complex, the DNA termini of the 3′ 6-FAM labeled 80 bp dsDNA were blocked using 200 nM of Ku70/80 (4:1 ratio of Ku70/80:DNA), if not stated otherwise. Prior to the addition of *Ec*MR, the dsDNA was incubated with Ku70/80 for 30 min at 25°C. When using the 5′ 6-FAM labeled hairpin DNA, reactions were supplemented with a 15-fold excess of a single-chain variable fragment (scFv) against the 6-FAM label (Pedrazzi et al., 1997) to block the opposing dsDNA end. To ensure

Please cite this article in press as: Gut et al., Structural mechanism of endonucleolytic processing of blocked DNA ends and hairpins by Mre11-Rad50, Molecular Cell (2022), https://doi.org/10.1016/j.molcel.2022.07.019

binding of the scFv, the sample was incubated at 25°C for 15 to 30 min. The reaction was started by *Ec*MR addition and incubated at 37°C for 5 min. Reactions were terminated by mixing with an equal volume of loading buffer (8 M Urea, 20 mM EDTA, 6% Ficoll 400). Reaction products were resolved on 12% denaturing polyacrylamide gels (Rotiphorese DNAsequencing system) in 1x TBE buffer. Gels were run for 90 min at constant 32 W and scanned by a Typhoon fluorescence imager (GE healthcare) using a 473 nm Laser and 510 nm filter.

Electrophoretic mobility shift assay (EMSA)

For the EMSA of *Ec*MR (Mre11^{H84Q}, nuclease dead) with Ku70/80 end-blocked 120 bp dsDNA a 1:2 dilution series of *Ec*MR in assay buffer (50 mM KCl, 25 mM TRIS pH 7.5, 5 mM $MgCl_2$, 1 mM $MnCl_2$, 1 mM DTT, 0.2 mg/ml BSA, 5 mM ATP, 10% glycerol) was prepared ranging from 0 to 640 nM as final protein concentrations. The 5′ 6-FAM 120 bp dsDNA substrate was amplified by PCR from a pET21b expression vector using DNA primers (Table S1) purchased from Metabion (Planegg, Germany). For the 5′ 6-FAM labelled 120 bp dsDNA substrate a final concentration of 10 nM was used, incubated with a 2x molar excess of Ku70/80 to block the free DNA ends. The dsDNA:Ku70/80 mixture was incubated for 30 min at 25°C, before adding *Ec*MR. After addition of *Ec*MR, the reaction mix was incubated for additional 30 min at 25°C before loading onto a 4% non-denaturing acrylamide gel supplemented with 10 mM Mg-Acetate and 2 mM ATP. The acrylamide gels were run for 2 – 2.5 hours at 80V and 4°C using 0.5x TB running buffer supplemented with 10 mM Mg-Acetate.

Grid preparation for cryo-electron microscopy

Protein for grid preparation was purified as described with the exception that after ion exchange chromatography, the protein was pooled and snap-frozen in liquid nitrogen. Prior to grid preparation, the full length *Ec*MR was purified via size-exclusion chromatography using a S6 5/150 column (buffer: 50 mM KCl, 20 mM HEPES, pH 7.5). For the endonuclease samples, 10x Buffer (10 mM $MnCl_2$, 50 mM $MgCl_2$ and 10 mM ATP) was mixed with 120 bp dsDNA (Table S1) and Ku70/80 to final concentrations of 0.49 μM and 0.97 μM, respectively. To ensure binding of Ku to the DNA ends, the sample was incubated at 25°C for 15 to 30 min. The collected peak fraction of *Ec*MR was then added to a final concentration of 1.47 μM, resulting in a 1:2:3 molar ratio of DNA:Ku70/80:*Ec*MR. For the DNA hairpin samples, 10x Buffer (10 mM $MnCl_2$, 50 mM $MgCl_2$ and 10 mM ATP) was mixed with hairpin dsDNA (Table S1) and an anti–6-FAM scFv (Pedrazzi et al., 1997) to final concentrations of 0.41 μM and 4 μM, respectively. To ensure binding of the scFv to the 6-FAM labeled 5' DNA end, the sample was incubated at 25°C for 15 to 30 min. The collected peak fraction of *Ec*MR was added to a final concentration of 0.41 μM, resulting in a 1:10:1 molar ratio of DNA:scFv:*Ec*MR. For the hairpin sample, ß-OG was included as a detergent with a final concentration of 0.05% (w/v). After *Ec*MR addition, the samples were incubated for additional 15 min at 25°C and then kept on ice until grid preparation. We applied the protein solution to Quantifoil Cu 200 R2/1 or UltraAU R2/2 grids (tilted datasets, endonuclease state), previously glow discharged for 20 (endonuclease state) or 7 s (hairpin state) at 20 mA (GloQube, Quorum). Grids were prepared using a Leica EM GP plunge freezer (Leica) at 10°C and 95% humidity. For each prepared grid, 4.5 μl of sample was applied to the grids and blotted for 2.5 s before vitrification in liquid ethane.

Electron microscopy data collection and processing

Datasets were collected on a Titan Krios G3 transmission electron microscope (Thermo Fisher Scientific) operated at 300 kV with a K2 Summit direct electron detector (Gatan). All datasets were collected using the EPU software package (TFS) with an applied defocus range of -2.8 to -1.2 μM and a magnified pixel size of 1.059 Å. For the endonuclease state, we collected 2 untilted data subsets of 2,775 and 7,257 micrographs (10,032 micrographs in total; dataset 1) with respective total doses of 44.68 e^- Å^{-2} and 44.9 e^- Å^{-2}, as well as 2 tilted datasets of 2521 (dataset 2) and 2414 micrographs (dataset 3) with respective total doses of 45.27 e^- Å^{-2} and 37.92 e^- Å^{-2} and an applied stage tilt of -25°. Micrograph movies were motion-corrected and dose-weighted using MotionCor2 (Zheng et al., 2017) and CTF parameters were estimated using CTFFIND4 (Rohou and Grigorieff, 2015). For -25° tilt micrographs, additional patch CTF estimation was performed, using the patch CTF estimation job integrated in the cryoSPARC software framework (Punjani et al., 2017). The described micrographs were also used to process the cryo-EM reconstructions of the Ku-RM-MR-Ku and the DNA-bound Ku70/80 states. For the hairpin-bound state, we collected 2 untilted data sets of 6,768 and 10,098 micrographs (16,866 micrographs in total; datasets 4 and 5) with respective total doses of 46.6 e^- Å^{-2} and 47.01 e^- Å^{-2}. Micrograph movies were motion-corrected and dose-weighted using MotionCor2 (Zheng et al., 2017) and CTF parameters were estimated using CTFFIND4 (Rohou and Grigorieff, 2015). Unless stated otherwise, all cryo-EM data processing steps were conducted using cryoSPARC (v3.2.0 and former versions) and Relion v3.0.8 (Scheres, 2012), as illustrated in the processing schemes (Figures S1, S2, and S4). All reported resolutions are based on the gold standard FSC 0.143 criterion.

For the *Ec*MR endonuclease state structure, the micrographs of datasets 1-3 were processed. Extracted particle subsets were only merged into one particle set at later processing stages, after CTF refinement and particle polishing in RELION. For an initial round of particle picking, the cryoSPARC blob picker was used, followed by particle filtering via 2D classification using a 320-pixel box, yielding subsets of 124,161, 82,225 and 63,303 particles for the respective datasets. These particles were then separately used to train Topaz models (Bepler et al., 2019) for convolutional neural-network based particle picking and extraction, again using a 320-pixel box, yielding new particle subsets of 2,785,335, 628,444 and 607,004 particles for the respective datasets. Additional particle filtering via 2D classification was applied as described above, followed by 3D particle classification into 4 classes by cryoSPARC ab-initio reconstruction and heterogeneous refinement. Selection of the best classes after heterogeneous refinement led to particle

Please cite this article in press as: Gut et al., Structural mechanism of endonucleolytic processing of blocked DNA ends and hairpins by Mre11-Rad50, Molecular Cell (2022), https://doi.org/10.1016/j.molcel.2022.07.019

Molecular Cell
Short article

CellPress

subsets of 102,929, 57,747 and 44,712 particles for the respective datasets 1, 2 and 3. The particle subsets were used to reconstruct initial cryo-EM electron densities for each data set and the initial densities were further refined in cryoSPARC, using homogeneous & non-uniform refinements (Punjani et al., 2020). At this stage, the three particle subsets were transferred to RELION, using the UCSF pyEM script (Asarnow et al., 2019), for CTF refinement and particle polishing. For particle subsets 2 and 3, an additional round of 2D classification was performed in RELION to sort-out junk particles, reducing the particle number to 55,301 and 41,521, respectively. The cryoSPARC densities were used as initial references (down sampled to 60 Å) for a first round of masked 3D refinements in RELION, followed by two iterative rounds of CTF refinement and particle polishing. Afterwards, the polished particle subsets were merged into a single subset of 199,751 particles, yielding a cryo-EM map of the *Ec*MR endonuclease state at 3.4 Å resolution (EMDB-14391), after an additional masked 3D refinement and solvent mask post-processing. The cryo-EM map was also post-processed by local filtering using the LAFTER software (Ramlaul et al., 2019), integrated into the CCP-EM software suite (Burnley et al., 2017; Wood et al., 2015), to better resolve flexible parts and loop regions within the map. The LAFTER-filtered map was used where indicated (see model building). Additionally, the refined cryoSPARC reconstruction from dataset 2 at 3.7 Å showed extended DNA density after the Mre11 nuclease active site (Figure S1E). Therefore, we applied local filtering using the LAFTER software (Ramlaul et al., 2019), yielding a cryo-EM map of the *Ec*MR endonuclease state with extended DNA (EMDB-14403).

Processing the Ku-RM-MR-Ku state structure, due to data quality reasons, only the micrographs of datasets 2 and 3 were included. Furthermore, processing was done solely using cryoSPARC. An initial round of particle picking using the blob picker and subsequent particle sorting by multiple rounds of 2D classification yielded in 3,043 good particles divided among 4 2D classes with an extraction box size of 320 pixel. This particle set was then used to train a Topaz model for convolutional neural-network based particle picking and extraction. Particle picking with the new Topaz model yielded in initial 286,192 particles, with a now increased extraction box size of 600-pixel, Fourier-cropped to 150 pixels. Again, particle sorting by multiple rounds of 2D classification were performed, leaving 18,803 good particles which could then be subjected to an ab-initio reconstruction with 2 classes, followed by heterogeneous refinement. Here, only the particles of the second class (64.4% of the original 18,803 particles) were further processed. The particle set was once more sorted by a 2D classification leaving a new particle set with 10,494 particles, which were re-extracted with a box size of 600-pixel without Fourier-crop. The particles were further refined using the cryoSPARC global and local CTF refinements and duplicate particles were removed within 100 Å (Punjani et al., 2017). A final refinement cycle using homogeneous and masked refinements (in use of the local refinement job implemented in cryoSPARC) yielded a final reconstruction at 8.2 Å (EMDB-14392). This cryo-EM map of the Ku-RM-MR-Ku state was then used to calculate a composite map using the better resolved maps of the *Ec*MR endonuclease state (EMDB-14391) and Ku70/80 bound to a DNA end (EMDB-14394). The composite map was calculated using the combine focused maps routine implemented in Phenix v1.17 (Liebschner et al., 2019).

For the Ku70/80 structure, the micrographs of datasets 1-3 described above were separately processed. Extracted particle subsets were only merged into one particle set at later processing stages, after CTF refinement and particle polishing in RELION v3.0.8. For an initial round of particle picking, blob picker implemented in cryoSPARC was used, followed by particle filtering in several rounds of 2D classification using a 320-pixel box, yielding subsets of 151,496, 83,893 and 89,088 particles for the respective datasets. These particles were then separately used to train Topaz models for convolutional neural-network based particle picking and extracted in a 320-pixel box. This led to new particle subsets of 2,989,830, 686,412 and 721,275 particles for the respective datasets. Afterwards, particle filtering via 2D classification was applied as described above, followed by 3D particle classification into 4 classes by cryoSPARC ab-initio reconstruction and heterogeneous refinement. Selection of the best classes after heterogeneous refinement led to new particle subsets of 173,314, 65,373 and 69,335 particles. The latter were used to reconstruct cryo-EM electron densities using cryoSPARC ab-initio reconstruction. These densities were further refined in cryoSPARC, using homogeneous & non-uniform refinements. At this stage, the three particle subsets were transferred to RELION, using the UCSF pyEM script, for movie refinement and particle polishing, followed by another polishing 2D classification and a 3D focused classification with 5 classes, after merging the polished subsets. Classes 2 to 5 were selected after the 3D focused classification, removing further low-quality particles. The resulting particle subset was subjected to a last round of polishing 2D classification. This then resulted in a final particle subset of 211,512 particles. After an intermediate masked 3D refinement run in CisTEM v1.0.2 (Grant et al., 2018), solvent mask post-processing in Relion resulted in a cryo-EM map of Ku70/80 bound to dsDNA at 3.5 Å resolution (EMDB-14394).

For the hairpin-bound structure, micrographs of datasets 4 and 5 were processed. Micrographs of datasets 4 and 5 were merged from the start. For an initial round of particle picking, again, the cryoSPARC blob picker was used. We performed initial particle sorting in several rounds of 2D classification using a 320-pixel box and by 3D ab initio reconstructions with several classes, yielding a total subset of 46,726 particles. These particles were used to train a Topaz model for convolutional neural-network based particle picking and extraction, again using a 320-pixel box, yielding a new subset with 1,299,536 particles. Those particles were sorted as described above, leading to a new particle subset of 61,845 particles. The particles were used to reconstruct an initial cryo-EM electron density, further refined using homogeneous & non-uniform refinements, which could then be used as an initial reference map. We transferred the particles to RELION, using the UCSF pyEM script, for masked 3D refinement, CTF refinement and particle polishing. The polished particle set was once more filtered by 2D classification, after two iterative polishing cycles, further reducing the particle number to 54,504. This final particle subset could then be used to reconstruct a cryo-EM map of the hairpin-bound state at 4.0 Å resolution (EMDB-14393), using masked 3D refinement and solvent mask post-processing. The cryo-EM map was also post-processed by local filtering using the LAFTER software to better resolve flexible parts and loop regions within the map. The LAFTER-filtered map was used where indicated (see model building).

Please cite this article in press as: Gut et al., Structural mechanism of endonucleolytic processing of blocked DNA ends and hairpins by Mre11-Rad50, Molecular Cell (2022), https://doi.org/10.1016/j.molcel.2022.07.019

CellPress

Molecular Cell
Short article

Reconstructed cryo-EM maps were rendered using ChimeraX (Pettersen et al., 2021).

Model building

For the endonuclease state model (PDB: 7YZO), we performed rigid body fitting in UCSF Chimera (Pettersen et al., 2004) using the available cryo-EM structure of *Ec*MR in the exonuclease cutting state (PDB code: 6S85). Model building was performed manually in COOT (Emsley and Cowtan, 2004) using secondary structure restraints for protein and libg restraints for DNA, alternating with iterative rounds of real-space refinement in PHENIX 1.19 (Afonine et al., 2018; Liebschner et al., 2019) and molecular dynamics simulations in ISOLDE v1.3 (Croll, 2018). Since the registry of DNA binding could not be determined from the dsDNA densities, we used an arbitrary registry based on our experimental sequence.

For the model of the low-resolution endonuclease map with extended DNA (PDB: 7Z03), the further extending DNA after the Mre11 active site was manually built using the endonuclease state model as a starting point (PDB: 7YZO). We used the low-resolution cryoSPARC density (Figure S1, labeled with an asterisk) as well as the LAFTER-filtered cryo-EM densities. The extending dsDNA sequence was built as a separate B-DNA based on our experimental sequence. The created B-DNA stretch was connected to the 3.4 Å endonuclease model DNA and initially refined against the cryoSPARC 3.7 Å map (Figure S1E) using PHENIX 1.19 and libg DNA restraints. The extended dsDNA was further manually refined against the LAFTER-filtered map, whereas the protein was adapted from the 3.4 Å endonuclease state structure and not further edited.

For the DNA hairpin state (PDB: 7YZP), the dsDNA was built manually, using the hairpin DNA structure of 1DGO (Ghosh et al., 2000) as an initial template, which could be rigid-body docked into the template protein structure 6S85. An initial round of manual DNA refinement was performed in COOT and the DNA sequence was adjusted according to our experimental sequence. As for the endonuclease state, further model building was performed manually in COOT using secondary structure restraints for protein and libg restraints for DNA, alternating with iterative rounds of real-space refinement in PHENIX 1.19 and molecular dynamics simulations in ISOLDE v1.3. Furthermore, the *Ec*Rad50 CCs of the hairpin state could be extended by 34 and 39 amino acids on the n- and c-terminal parts, respectively, in comparison to the endo- and exonuclease states (PDB: 7YZO and 6S85). The stated residues were initially modelled using AlphaFold2 (Jumper et al., 2021), connecting the n- and c-terminal parts of the anti-parallel CCs by an artificial 6 amino acid PAS-Linker that was removed after rigid-body docking into the cryo-EM density. The protein main chains and the CC extensions were connected and included in a final round of refinement as described above.

For the DNA-bound Ku70/80 reconstruction, structural models were calculated using AlphaFold2 for both subunits (not deposited) and rigid-body docked into the density to structurally validate the Ku70/80 reconstruction. The derived models showed a good overall density fit except for the c-terminal parts of Ku70 and Ku80, which are not resolved by the map. The calculated Ku70/80 AlphaFold2 models were also used for the atomic model depicted in the supplementary movie (Video S1). Here, the atomic models were rigid-body docked into the composite map of the Ku-RM-MR-Ku state structure and the c-terminal portions not resolved by the cryo-EM reconstruction were truncated at residues A575 and E575, for Ku70 and 80, respectively. B-DNA was fitted into the clear dsDNA density of the Ku70/80 reconstruction first and refined using PHENIX 1.19 and manually in COOT using libg DNA restraints, before rigid-body docking into the composite map. The adapted dsDNA could then be connected to the DNA of the rigid-body docked *Ec*MR endonuclease model (PDB: 7YZO), completing the model used for the supplementary movie (Video S1). Due to clashes with the fitted dsDNA, the n-terminal parts of the Ku70 (residues 1-26) and Ku80 (residues 1-3) were truncated.

For the structural alignment of the *Ec*MR endonuclease state and the human Mre11-Rad50 homolog we calculated dimer models of each protein individually (*Hs*Rad50: amino acids 1-200 and 1133-1312 connected by a G_6 linker; *Hs*Mre11: amino acids 1-356) using a local installation of AlphaFold-Multimer (Evans et al., 2021)

Models were rendered using ChimeraX (Pettersen et al., 2021).

QUANTIFICATION AND STATISTICAL ANALYSIS

Directional Fourier shell correlation (FSC) determination was performed for the Endonuclease state head complex, the Ku70/80 bound to dsDNA and the Hairpin-bound state head complex, using the 3DFSC software (Tan et al., 2017) (Figures S1, S2, and S4).

OriginPro was used to plot the results of the high-throughput DNA shape prediction (Figures 2C and S3E).

Molecular Cell, Volume *82*

Supplemental information

Structural mechanism of endonucleolytic processing of blocked DNA ends and hairpins by Mre11-Rad50

Fabian Gut, Lisa Käshammer, Katja Lammens, Joseph D. Bartho, Anna-Maria Boggusch, Erik van de Logt, Brigitte Kessler, and Karl-Peter Hopfner

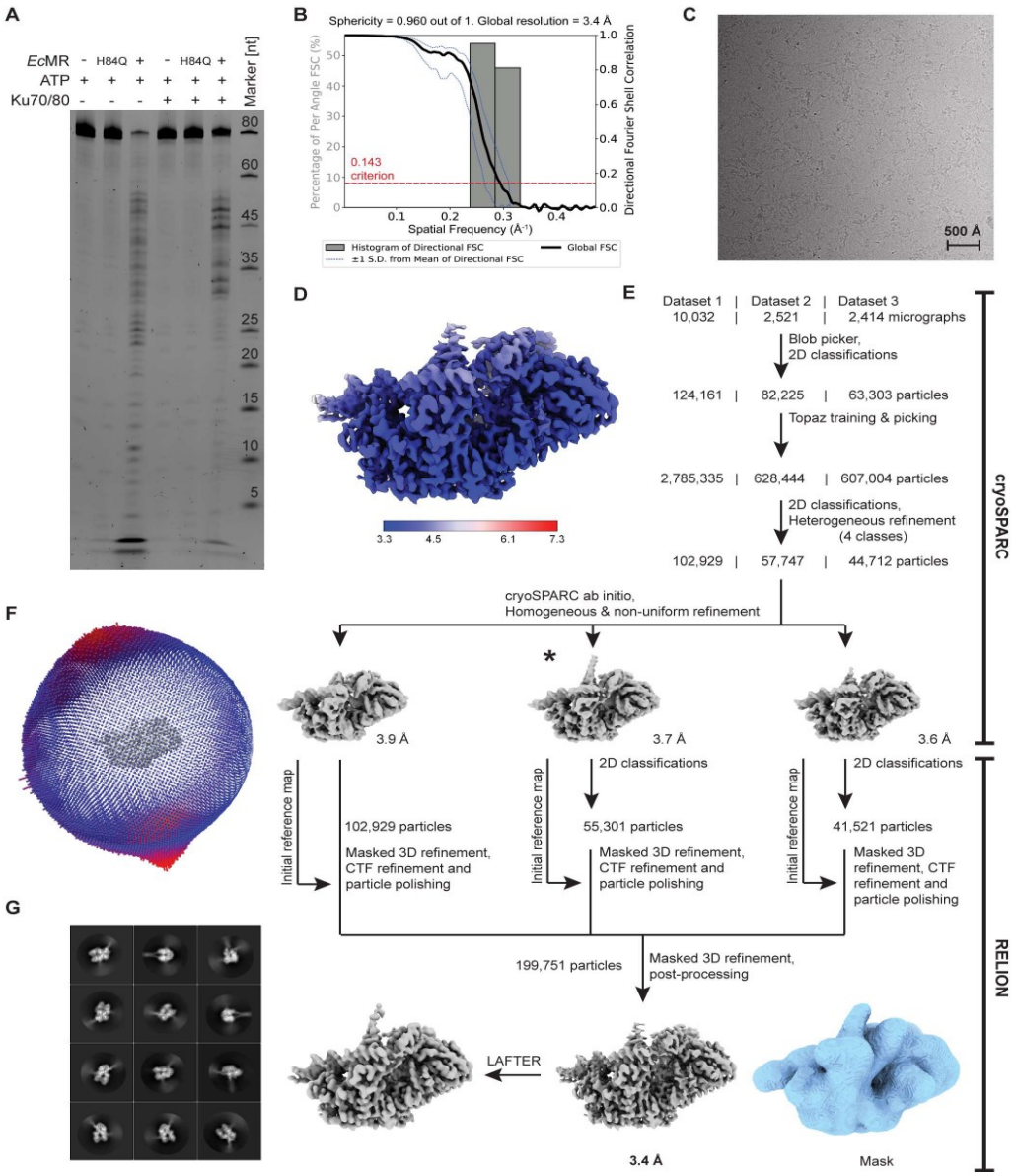

Figure S1 Related to Figure 1| Endonuclease State processing scheme

(A) Nuclease assay of *Ec*MR WT and H84Q nuclease dead on an 80 bp 3' 6-FAM labeled DNA substrate with free and Ku blocked ends (100 nM Ku, 2:1 Ku:DNA) which shows that the H84Q mutant is exo- and endonuclease nuclease deficient.

(B) Histogram and directional Fourier shell correlation (FSC) for the endonuclease state head complex. Directional FSC determination was performed with the 3DFSC software (Tan et al., 2017). A sphericity of 0.96 was determined indicating very isotropic angular distribution (a value of 1 stands

for completely isotropic angular distribution). The red line shows the 0.143 cut-off criterion which indicates a nominal resolution of 3.4 Å.

(C) Representative micrograph of the endonuclease sample containing *Ec*MR bound to Ku blocked 120 bp dsDNA in the presence of ATP.

(D) The local resolution of the endonuclease state head complex, calculated using ResMap and shown as color-coded surface representation.

(E) Flow chart showing the image-processing pipeline for the cryo-EM data analysis of the *Ec*MR endonuclease state. The asterisk marks the endonuclease state head complex reconstruction with extended DNA at 3.7 Å.

(F) Angular distribution of the particles used for the endonuclease state reconstruction.

(G) The twelve highest populated classes from the 2D classification of the *Ec*MR endonuclease state are shown.

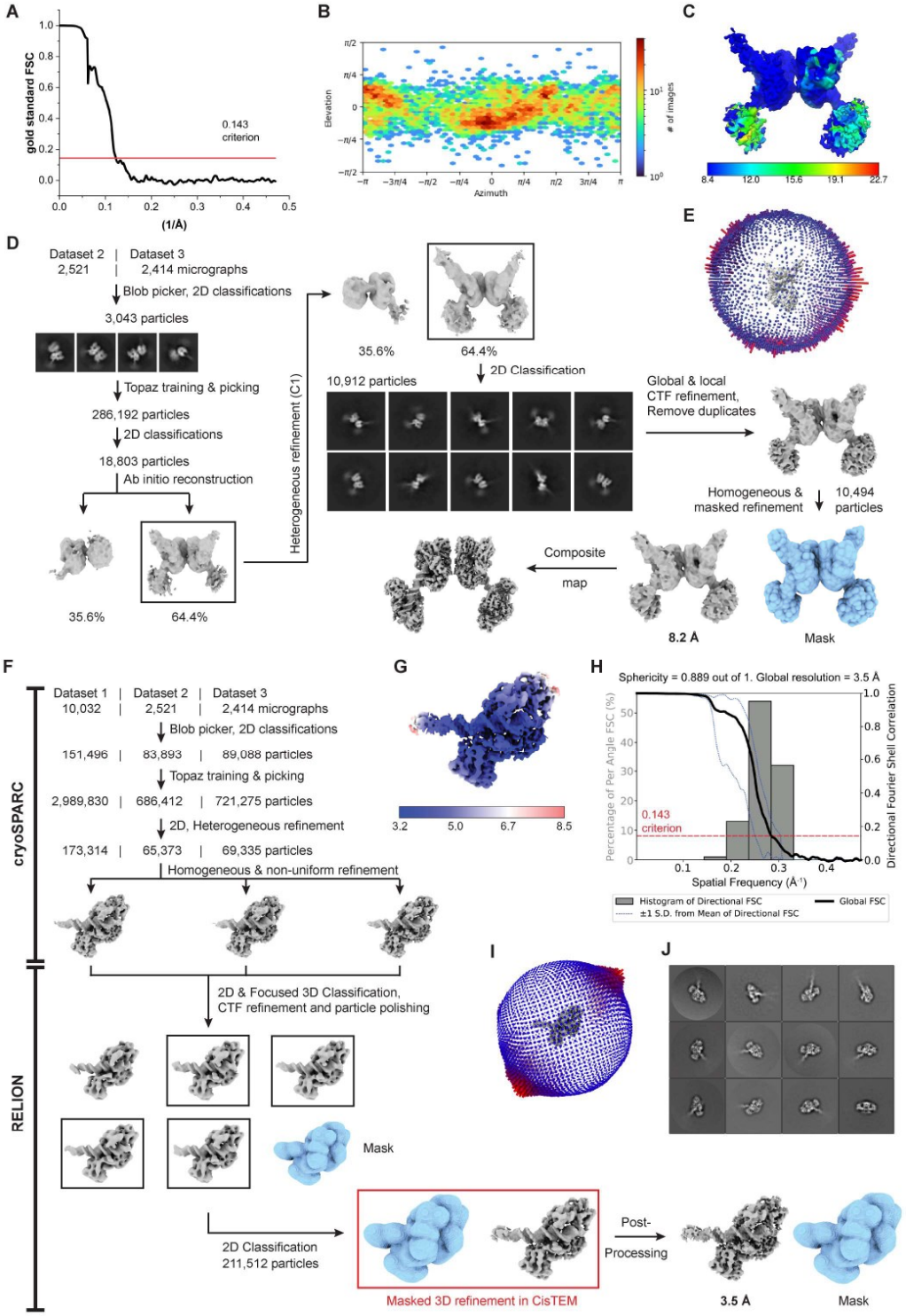
A
gold standard FSC
0.143
criterion
(1/Å)
B
Elevation
Azimuth
# of images
C
8.4
12.0
15.6
19.1
22.7
D
Dataset 2 | Dataset 3
2,521 | 2,414 micrographs
Blob picker, 2D classifications
3,043 particles
Topaz training & picking
286,192 particles
2D classifications
18,803 particles
Ab initio reconstruction
35.6%
64.4%
Heterogeneous refinement (C1)
10,912 particles
2D Classification
Global & local
CTF refinement,
Remove duplicates
Homogeneous &
masked refinement
10,494
particles
Composite
map
8.2 Å
Mask
E
F
cryoSPARC
Dataset 1 | Dataset 2 | Dataset 3
10,032 | 2,521 | 2,414 micrographs
Blob picker, 2D classifications
151,496 | 83,893 | 89,088 particles
Topaz training & picking
2,989,830 | 686,412 | 721,275 particles
2D, Heterogeneous refinement
173,314 | 65,373 | 69,335 particles
Homogeneous & non-uniform refinement
RELION
2D & Focused 3D Classification,
CTF refinement and particle polishing
Mask
2D Classification
211,512 particles
Masked 3D refinement in CisTEM
Post-
Processing
3.5 Å
Mask
G
3.2
5.0
6.7
8.5
H
Sphericity = 0.889 out of 1. Global resolution = 3.5 Å
Percentage of Per Angle FSC (%)
Directional Fourier Shell Correlation
0.143
criterion
Spatial Frequency (Å⁻¹)
Histogram of Directional FSC
±1 S.D. from Mean of Directional FSC
Global FSC
I
J

Figure S2 Related to Figure 1| Ku-RM-MR-Ku State and Ku70/80 processing schemes

(A) Gold-standard Fourier shell correlation (FSC) for the Ku-RM-MR-Ku complex. The red line shows the 0.143 cut-off criterion which indicates a nominal resolution of 8.2 Å.

(B) Angular distribution plot of the particles used for the Ku-RM-MR-Ku state 8.2 Å reconstruction.

(C) The local resolution of the Ku-RM-MR-Ku state, calculated with the cryoSPARC implementation and shown as color-coded surface representation.

(D) Flow chart showing the image-processing pipeline for the cryo-EM data analysis of the Ku-RM-MR-Ku state.

(E) Angular distribution of the particles used for the 8.2 Å reconstruction.

(F) Flow chart showing the image-processing pipeline for the cryo-EM data analysis of the Ku70/80 complex bound to DNA.

(G) The local resolution of the Ku70/80 complex, calculated using ResMap and shown as color-coded surface representation.

(H) Histogram and directional Fourier shell correlation (FSC) for the Ku70/80 DNA-bound state reconstruction. Directional FSC determination was performed with the 3DFSC software (Tan et al., 2017). A sphericity of 0.889 was determined indicating an isotropic angular distribution (a value of 1 stands for completely isotropic angular distribution). The red line shows the 0.143 cut-off criterion which indicates a nominal resolution of 3.5 Å.

(I) Angular distribution of the particles used for the Ku70/80 reconstruction.

(J) The twelve highest populated classes from the 2D classification of the Ku70/80 complex bound to DNA are shown.

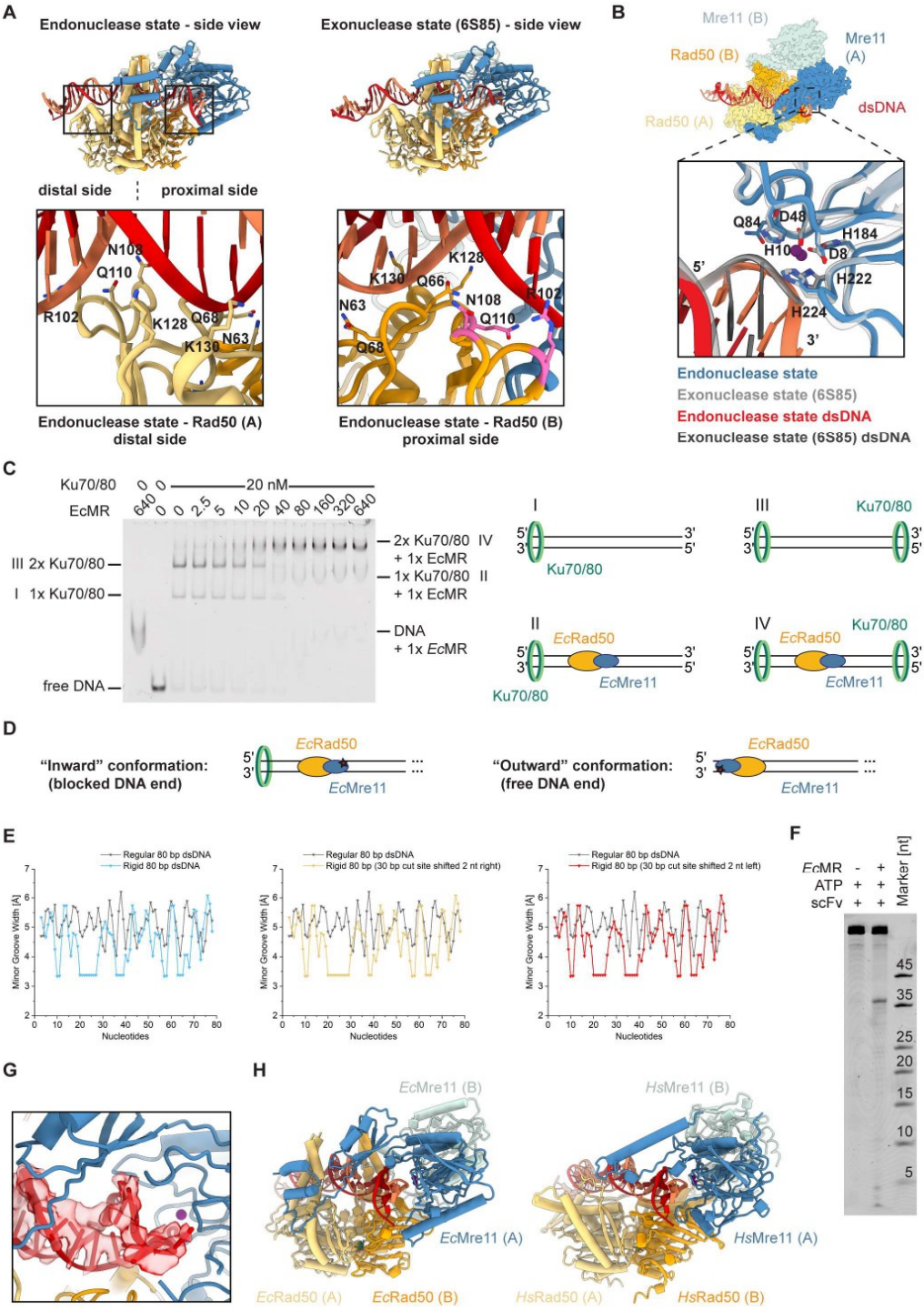
A
Endonuclease state - side view
Exonuclease state (6S85) - side view
distal side
proximal side
N108
Q110
R102
K128
Q68
K130
N63
Endonuclease state - Rad50 (A)
distal side
Endonuclease state - Rad50 (B)
proximal side
B
Mre11 (B)
Mre11 (A)
Rad50 (B)
Rad50 (A)
dsDNA
Q84
D48
H184
H10
D8
H222
H224
5'
3'
Endonuclease state
Exonuclease state (6S85)
Endonuclease state dsDNA
Exonuclease state (6S85) dsDNA
C
Ku70/80
EcMR
20 nM
III 2x Ku70/80
I 1x Ku70/80
free DNA
2x Ku70/80 + 1x EcMR
1x Ku70/80 + 1x EcMR
DNA + 1x EcMR
Ku70/80
EcRad50
EcMre11
D
"Inward" conformation:
(blocked DNA end)
"Outward" conformation:
(free DNA end)
E
Regular 80 bp dsDNA
Rigid 80 bp dsDNA
Rigid 80 bp (30 bp cut site shifted 2 nt right)
Rigid 80 bp (30 bp cut site shifted 2 nt left)
Minor Groove Width [A]
Nucleotides
F
EcMR
ATP
scFv
Marker [nt]
45
35
25
20
15
10
5
G
H
EcMre11 (B)
HsMre11 (B)
EcMre11 (A)
HsMre11 (A)
EcRad50 (A)
EcRad50 (B)
HsRad50 (A)
HsRad50 (B)

Figure S3 Related to Figure 1, 2 and 3| Structural and biochemical analysis of the Endonuclease and Hairpin-bound States

(A) The upper panel shows a comparison of endonuclease and exonuclease state (PDB: 6S85) models in side view. Subunits are illustrated using the same color code as in Figure 1 (Rad50 orange/yellow; Mre11 light/dark blue; DNA red). The lower panel shows interactions of Rad50 (A) and (B) with DNA in endonuclease state. DNA binding residues are depicted as sticks and residues involved in endonuclease state DNA binding, but not in exonuclease, are highlighted in pink.

(B) Nuclease active site comparison of Mre11(A) in endonuclease and exonuclease ((Kashammer et al., 2019); PDB: 6S85) state models. The Mre11(A) subunit is colored in dark blue (endonuclease) and light grey (exonuclease), the DNA in orange/red (endonuclease) and dark grey (exonuclease) and the Mn^{2+} ions in purple. DNA and enzymatically important residues are annotated and illustrated as sticks.

(C) Electrophoretic mobility shift assay of *Ec*M^{H84Q}R bound to Ku blocked 120 bp dsDNA. Illustration of the 4 different observed binding species.

(D) Illustration showing the different orientation of the *Ec*MR complex in the discussed “inward” and “outward” conformations, relative to the blocked or free DNA end.

(E) High-throughput DNA shape prediction (Zhou et al, 2013) of the regular and rigid 80 bp dsDNA, illustrating rigid and more flexible regions within the DNA oligos.

(F) Full gel image of the nuclease assay of *Ec*MR WT on the 5' 6-FAM labeled, scFv blocked DNA hairpin, showing predominant nuclease cleavage at 36 nt, illustrated in Figure 2F.

(G) Nuclease active site of Mre11 (A) bound to a DNA hairpin. Mre11 (A) is colored in dark blue, Rad50 (B) in orange and the hairpin DNA in red. The atomic model of the hairpin DNA is overlaid by the 4 Å cryo-EM density.

(H) Structural alignment of the *Ec*MR endonuclease state and human Rad50 (amino acids 1-200 and 1133-1312 connected by a G_6 linker) and Mre11 (amino acids 1-356) AlphaFold-Multimer (Evans et al., DOI:10.1101/2021.10.04.463034) predictions by rigid-body docking of the predicted models on the *Ec*MR endonuclease model. Rad50 is generally displayed in orange/yellow, Mre11 in light/dark blue and endonuclease state DNA in red. The Mn^{2+} ions of the endonuclease model are illustrated as purple spheres and the Mg^{2+}-ADP as green sticks and spheres, respectively. The predicted models support the concept that our proposed unified nuclease cutting state mechanism might also be applicable to eukaryotic Mre11-Rad50 homologs.

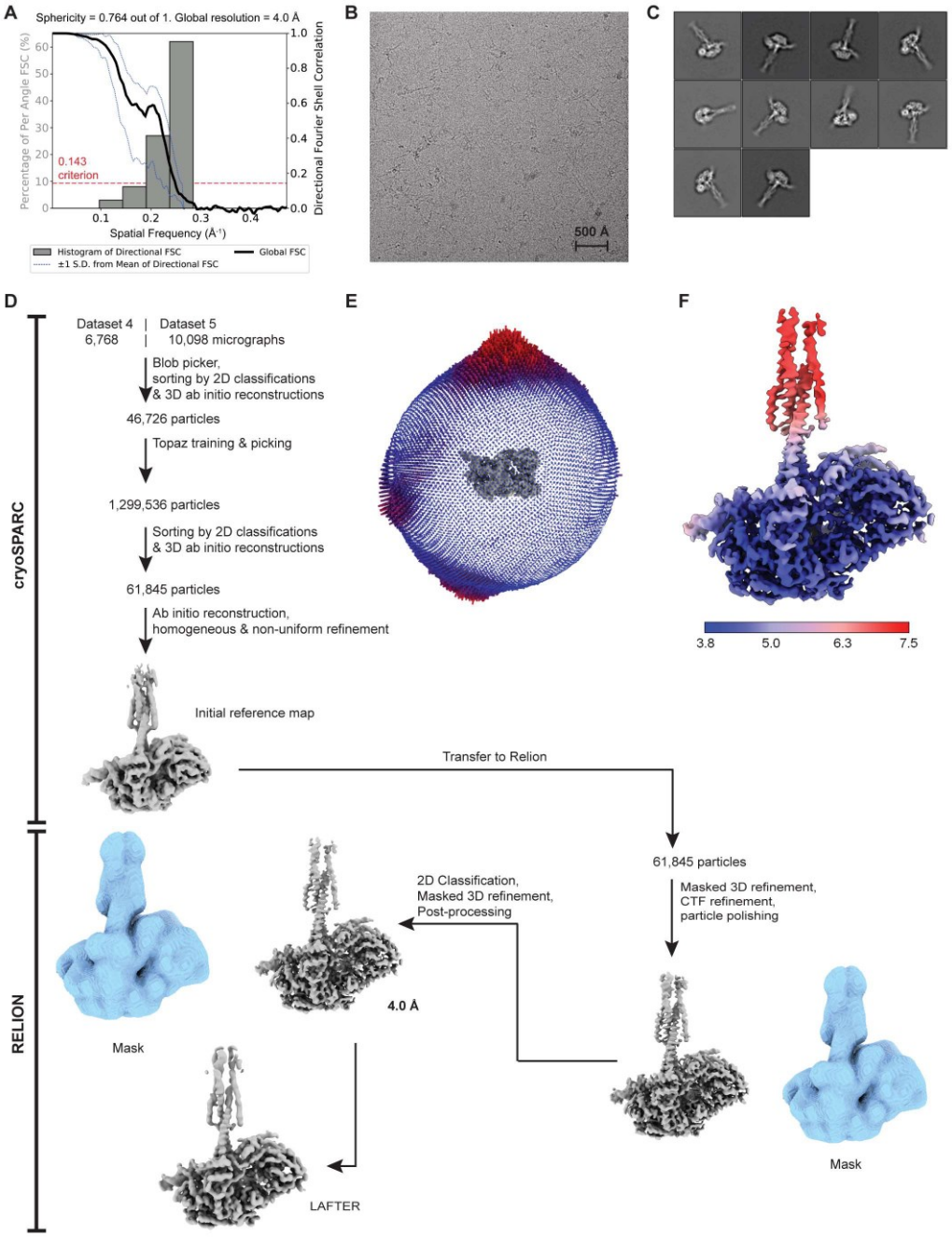

Figure S4 Related to Figure 2| Hairpin-bound State processing scheme

(A) Histogram and directional Fourier shell correlation (FSC) for the hairpin-bound state head complex. Directional FSC determination was performed with the 3DFSC software (Tan et al., 2017). A sphericity of 0.764 was determined indicating a mostly isotropic angular distribution (a value of 1

stands for completely isotropic angular distribution). The red line shows the 0.143 cut-off criterion which indicates a nominal resolution of 4 Å.

(B) Representative micrograph of the DNA hairpin sample containing *Ec*MR bound to the DNA hairpin in the presence of ATP.

(C) The ten highest populated classes from the 2D classification of the *Ec*MR hairpin-bound state are shown.

(D) Flow chart showing the image-processing pipeline for the cryo-EM data analysis of the *Ec*MR hairpin-bound state.

(E) Angular distribution of the particles used for the hairpin-bound state reconstruction.

(F) The local resolution of the *Ec*MR hairpin-bound state head complex, calculated using ResMap and shown as color-coded surface representation.

Table S1 Related to STAR Methods |PCR Primer and DNA oligomers used for cryo-EM samples and assays

Oligonucleotide	Sequence 5' to 3'
120 bp DNA for EM (fwd)	GCGTGGCACAACAACTGGCGGGCAAACAGTCGTTGCTGATTG GCGTTGCCACCTCCAGTCTGGCCCTGCACGCGCCGTCGCAAATT GTCGCGGCGATTAAATCTCGCGCCGATCAACTGG
120 bp DNA for EM (rev)	CCAGTTGATCGGCGCGAGATTTAATCGCCGCGACAATTTGCGA CGGCGCGTGCAGGGCCAGACTGGAGGTGGCAACGCCAATCAG CAACGACTGTTTGCCCGCCAGTTGTTGTGCCACGC
75 bp DNA hairpin for EM with 35 bp dsDNA stem and 5 nt bubble	6FAM-CGCTTTATCAGAAGCCAGACATTAACGCTTCTGGATAGC GTCCAGAAGCGTTAATGTCTGGCTTCTGATAAAGCG
80 bp DNA (fwd) for nuclease assays with Ku70/80	CGGGTAGTAGATGAGCGCAGGGACACCGAGGTCAAGTACATT ACCCTCTCATAGGAGGTGCGCTTTATCAGAAGCCAGAC
80 bp DNA (rev) for nuclease assays with Ku70/80	GTCTGGCTTCTGATAAAGCGCACCTCCTATGAGAGGGTAATGT ACTTGACCTCGGTGTCCCTGCGCTCATCTACTACCCG-6FAM
80 bp rigid DNA (fwd) for nuclease assays with Ku70/80	ACAGATGAACTTTAAAGAAAAAAAAAAAAACAAGAAAAAAAAACT AAGGCCAAAGAAACTTTAAAAAAAACCTATCTTATAGT
80 bp rigid DNA (rev) for nuclease assays with Ku70/80	ACTATAAGATAGGTTTTTTTAAAGTTTCTTTGGCCTTAGTTTTTT TTCTTGTTTTTTTTTTTTCTTTAAAGTTCATCTGT-6FAM
80 bp rigid DNA (fwd) 2nt left for nuclease assays with Ku70/80	ACAGATGAACTTTAAAGAAAAAAAAAACAAGAAAAAAAAAACT AAGGCCAAAGAAACTTTAAAAAAAACCTATCTTATAGT
80 bp rigid DNA (rev) 2nt left for nuclease assays with Ku70/80	ACTATAAGATAGGTTTTTTTAAAGTTTCTTTGGCCTTAGTTTTTT TTTTCTTGTTTTTTTTTTCTTTAAAGTTCATCTGT-6FAM
80 bp rigid DNA (fwd) 2nt right for nuclease assays with Ku70/80	ACAGATGAACTTTAAAGAAAAAAAAAAAAAACAAGAAAAAAACT AAGGCCAAAGAAACTTTAAAAAAAACCTATCTTATAGT
80 bp rigid DNA (rev) 2nt right for nuclease assays with Ku70/80	ACTATAAGATAGGTTTTTTTAAAGTTTCTTTGGCCTTAGTTTTTT CTTGTTTTTTTTTTTTTCTTTAAAGTTCATCTGT-6FAM
Primer (fwd) for 5'-6FAM 120 bp dsDNA (pET21b) for EMSA	6-FAM-GCGTGGCACAACAACTGGCGGG
Primer (rev) for 5'-6FAM 120 bp dsDNA (pET21b) for EMSA	CCAGTTGATCGGCGCGAGATTTAATCG
PCR product (fwd) 5'-6FAM 120 bp dsDNA (pET21b) for EMSA	GCGTGGCACAACAACTGGCGGGCAAACAGTCGTTGCTGATTG GCGTTGCCACCTCCAGTCTGGCCCTGCACGCGCCGTCGCAAATT GTCGCGGCGATTAAATCTCGCGCCGATCAACTGG
PCR product (rev) 5'-6FAM 120 bp dsDNA (pET21b) for EMSA	CCAGTTGATCGGCGCGAGATTTAATCGCCGCGACAATTTGCGA CGGCGCGTGCAGGGCCAGACTGGAGGTGGCAACGCCAATCAG CAACGACTGTTTGCCCGCCAGTTGTTGTGCCACGC

3 Discussion

As a key player in DSBs repair, the MRN complex has been extensively studied over the last 25 years. Combining structural, biochemical and biophysical approaches, major advances have been made towards a structural and mechanistic understanding of the MRN complex. Yet, several questions still remain unanswered, especially in regard of the DNA binding and processing mechanisms of the full-length MR(N) complex.

Structurally, the MR(N) complex and its individual components have been mainly studied by X-ray crystallography over the last decades. As a result, several structures of the MR(N) complex with and without DNA[149,153,167,178], sole Mre11[140,148,166,246], but also in complex with Nbs1 peptides[139,150], and sole Rad50[156,157,176] could be solved for various organisms. A recent study also reported a cryo-EM structure of the full-length *C. thermophilum* MRN complex bound to ATPγS[139]. However, the solved structures of the MR(N) complex in ATP-bound states all show, that the Mre11 dimer remains underneath the Rad50 head domain, with or without DNA bound to Rad50. Hence, an autoinhibitory state is formed, where the Mre11 nuclease active sites cannot be accessed by the DNA[153,167,178]. Due to the prevalent limitations in protein crystallization, the highly dynamic and functionally crucial coiled coils (CCs) with the apical Zn-hook always needed to be drastically shortened. However, the latter were shown to affect the biological and enzymatic functions of the complex[179,181,182,184].
Despite the major structural and biochemical advances during the last two decades, many more questions concerning the MRN complex remained elusive. Four enigmatic, but previously unresolved questions tackled within this work are:

(I) How does the dsDNA enter the Mre11 nuclease active site?
(II) What is the underlying structural mechanism of the MR(N)'s conserved exo- and endonuclease activities?
(III) Is there a uniform structural basis to MR(N)'s nuclease diversity?
(IV) What is the functional and mechanistic role of the CCs?

3.1 From resting to cutting state – a unified nuclease mechanism for different DNA substrates

The bacterial *Ec*MR complex provides a good model system to study the structural and biochemical mechanisms of the MRN complex. Even though it is lacking eukaryote-specific interaction partners, such as Nbs1 or CtIP, it still shows highly conserved structural and biochemical properties compared to eukaryotic MRN/X[92,119,120,172]. Enzymatically, this mainly includes the conserved 3' to 5' dsDNA exonuclease, the single-strand 5' endonuclease on hairpin-capped and blocked DNA ends and the coupled ATPase activity[120,172,237]. With the advent of the so-called "resolution-revolution" in cryo-EM, structural biology obtained a new arm, enabling structural studies on the full-length MR complex. Hence, we set out to answer the above mentioned, still unsolved questions by investigation of the full-length *Ec*MR complex using cryo-EM and biochemical approaches.

Using cryo-EM we solved the globular head domain of full-length *Ec*MR in an ATPγS bound state (Section 2.1, Figure 1; Figure 14). The overall conformation matches the previously solved MR crystal structures from several different organisms, resembling ATP-bound states (Section 2.1, Figure S2)[153,167,178]. The Rad50 NBDs adopt a closed state, sandwiching two ATPγS molecules coordinated by two Mg^{2+} ions. Mre11 is kept in an autoinhibitory state underneath the Rad50 head, where the Rad50 NBDs block DNA access to the Mre11 nuclease active sites. Thus, the ATPγS state has been further referred to as "resting state". The high structural conservation compared to previously solved crystal structures not only further highlights the structural conservation of the MR complex, but also indicates a rather minor impact of the CCs on the MR head conformation of the resting state. Underlining the flexibility observed in previous studies, only a short part of the CCs could be reconstructed[143,144]. Moreover, they clearly point outwards from the Rad50 NBDs, which matches the crystallographic observations[153,167,178] and suggests a ring-shaped conformation (Section 2.1, Figure 1; Figure 14). However, this ring-shape is further dependent on joined apical Rad50 Zn-hook motifs, forming a second stable dimerization domain. This was not only shown in AFM studies for the M_2R_2 complex[143,188], but also in recent structural studies on eukaryotic MRN and the Zn-hook in particular[139,141,185,186]. Yet, it is important to note that there are also studies that showed an opening of the Zn-hook[144,187].

Intriguingly, the ATPγS-bound resting state of prokaryotic *Ec*MR with open CCs stands in contrast to a recent structure of the eukaryotic *C. thermophilum* MRN complex. The eukaryotic MRN complex revealed an ATPγS-bound auto-inhibited resting state structure with closed, rod-shaped CCs[139]. This underlines the potential structural and mechanistic influence of eukaryote-specific cofactors, such as Nbs1.

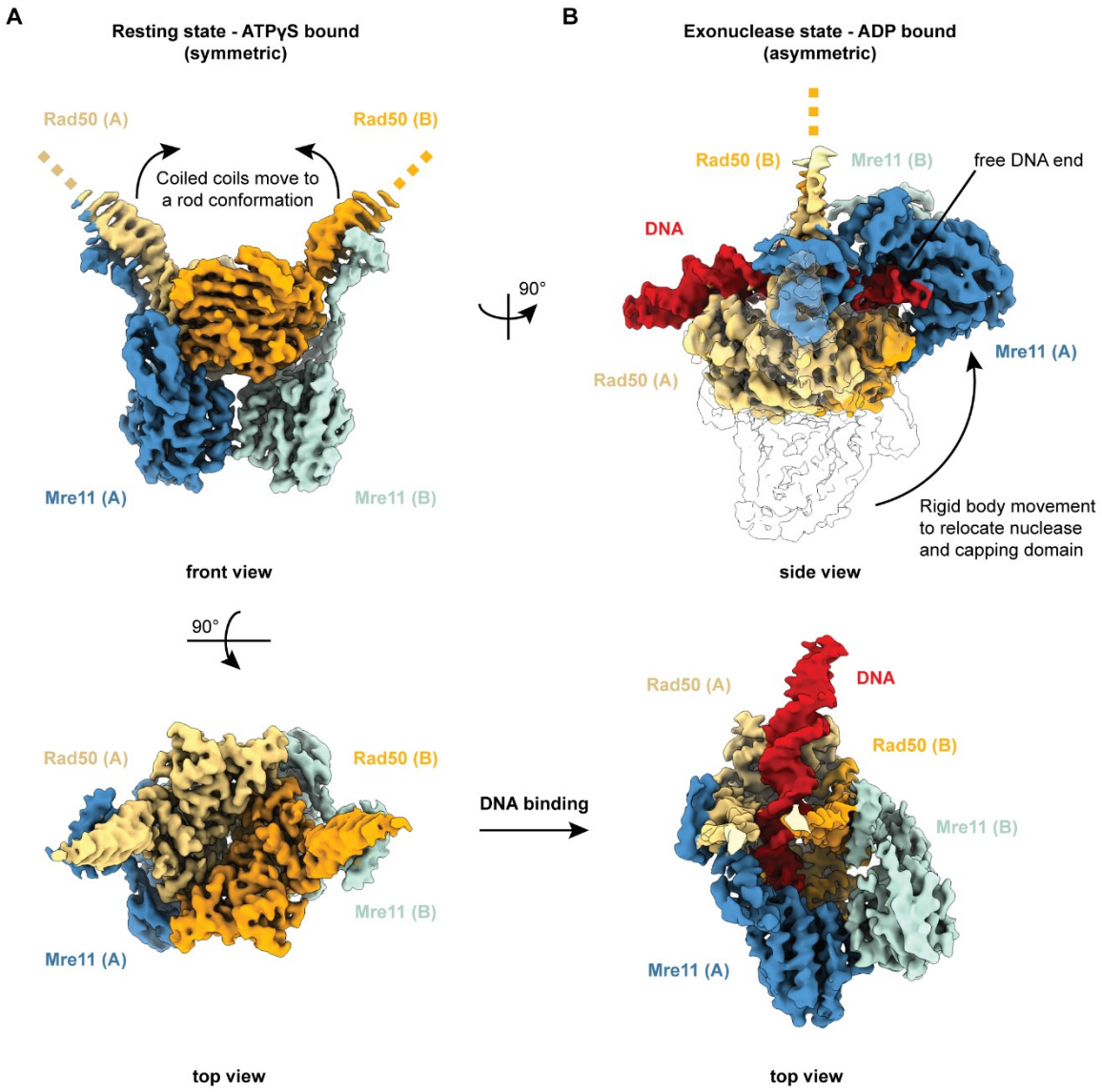

Figure 14: Cryo-EM reconstructions of *Ec*MR in resting and DNA-bound exonuclease state. (A) The ATPγS bound resting state of *Ec*MR depicted in two different views – front and top view. The Rad50 and Mre11 subunits are colored in shades of orange and blue, respectively. The Mre11 dimer remains in an autoinhibited resting state underneath the Rad50 head module. The flexible, unresolved CCs are implied by orange dots. (B) The dsDNA and ADP bound exonuclease state of *Ec*MR depicted in two different views – front and top view. The subunits of the MR complex are colored according to panel A with the dsDNA colored in red. In the side view, a transparent overlay of the resting state reconstruction is shown. This illustrates the relocation of the Mre11 dimer in the asymmetric exonuclease state conformation with the Mre11 (A) active site contacting the DNA end.

Using ATP and 60 bp dsDNA, the structure of *Ec*MR bound to a free DNA double-strand in a nuclease proficient "cutting state" was solved (Section 2.1, Figure 1; Figure 14). In comparison to the resting state structure, large conformational rearrangements take place in the cutting state. The Mre11 nuclease and capping domains undergo a large movement of ~120° to relocate to the side of Rad50, forming an active site channel that harbours the DNA end. Intriguingly, this further holds the transition from an overall symmetric resting to an asymmetric cutting state

(Section 2.1, Figure 1; Figure 14). Here, the Mre11 C-terminal linker domain, inserted between the capping domain and the HLH motif, plays a crucial role acting as a flexible tethering element between Mre11 and Rad50. The described conformational change brings the nuclease active site of Mre11 (A) with its two coordinated Mn^{2+} ions in close proximity to the free 3' dsDNA end (Section 2.1, Figure 1, 2 and S5). Hence, this likely represents a nuclease-proficient 3' to 5' exonuclease state (further denoted as exonuclease state) - a conformation that has not been observed in any of the previous structural studies[148,153,166]. Structural analysis showed, that exonucleolytic cleavage would occur between the last two terminal bases at the 3' end. Based on recent biochemical data, the 3'O-P bond is cleaved in this 3' to 5' exonuclease state, leaving a 3'-OH on the residual DNA strand and a 5' phosphate on the leaving dNMPs[165]. The positioning of the Mre11 dimer on the DNA end helps to explain *Ec*MR's elevated affinity towards dsDNA ends (Section 2.1, Figure 5). Here, Mre11 adopts a central role in DNA end sensing and binding, which is also consistent with results from single molecule imaging on human MRN[96].

The majority of the dsDNA is bound by residues of the Rad50 NBDs and the adjacent CCs, which partially matches observations from previous crystal structures[153,156,157]. Furthermore, this indicates a conserved DNA binding mode for Rad50 from different species. Point mutations at NBD and CC DNA binding residues drastically diminished DNA binding, DNA induced stimulation of ATPase activity and nuclease activities (Section 2.1, Figure 4). This further underlines the tight mechanistic interaction between Rad50 DNA binding, ATP hydrolysis and nuclease activity. Crystal structures of Rad50:DNA complexes indicate a footprint of ~20 bp[153,156,157], while biochemical data indicates a minimum of 25-30 bp for DNA binding and ATPase stimulation[165]. In sum, this matches the observed footprint of the *Ec*MR exonuclease state structure, with the 22 bp spanning DNA binding platform formed by the Rad50 NBDs (Section 2.1, Figure 1 and 4).

The conformational changes are not restricted to the globular head domain of *Ec*MR. Upon DNA binding and triggering of the conformational rearrangements, the CCs move inwards in close cooperation with the Mre11 dimer relocation (Figure 14). By interacting with one another, they transition from an open ring-shaped to a rod-like conformation, clamping the $Rad50^{NBD}$ bound DNA duplex. As a result, the CCs are more rigid and could be resolved to ~1/3 of their total length, which corresponds to ~200 Å (Section 2.1, Figure 3). A previous AFM study revealed DNA-driven structural transitions between free and DNA-bound human MRN[144], which matches the described DNA-induced rod-formation very well. Hence, the ring to rod transition of the CCs might also likely be a feature conserved from pro- to eukaryotes. This is further supported by crystal structures of the human and *P. furiosus* Zn-hook domains, showing open ring- and closed rod-shaped conformations[141,185,186]. Thus, the Zn-hook likely acts as a dynamic hinge, allowing the CCs to transition between open and closed states[141,185,186]. Moreover, the ring to rod transition may explain MR's topological specificity for DNA ends,

irrespective of the type of block. While a single DNA duplex fits through the small opening at the base of the clamped CCs, presence of a second DNA duplex, e.g. upon binding of internal or circular DNA, might prevent rod formation and thus also formation of the cutting state to enable nuclease cleavage (Section 2.1, Figure 4 and 6).

A recent study also showed that the rod-shaped Zn-hook apices of two eukaryotic MRN complexes can dimerize. Forming 120 nm spanning MRN-MRN structures, this mechanism is likely to be involved in DSB repair DNA tethering[139]. However, gel filtration experiments merely showed a M_2R_2 stoichiometry for the bacterial MR complex without higher-order complex formation by ATP or DNA addition (Section 2.1, Figure S2). This supports the model where the CCs are stably connected by the Zn-hook within a M_2R_2 complex[188], but opposes Zn-hook mediated higher-order complex formation for *Ec*MR, as observed for eukaryotic MRN[139].

To examine *Ec*MR in an endonuclease state conformation, we needed to switch to a protein-blocked DNA substrate. It was already shown in previous biochemical studies that Ku70/80 (further referred to as Ku) serves as a suitable DNA end block and specifically stimulates MR's endonuclease activity (Section 2.1, Figure S6)[95-99]. Using a 120 bp dsDNA substrate with *C. thermophilum* Ku70/80 blocked ends and ATP, we were able to solve the structure of *Ec*MR in "endonuclease state".

The structure revealed the *Ec*MR head complex bound to 31 bp of internal dsDNA in endonuclease mode (Section 2.2, Figure 1; Figure 15). Overall, the head complex adopts a highly similar conformation compared to the exonuclease state. The DNA, again, binds along both Rad50 NBDs and is further bound by the clamping conformation of the CCs, before traversing through the active site channel. In this state, Rad50 makes more extensive DNA contacts, compared to the exonuclease state. Residues R102, N108 and Q110 additionally contact the DNA phosphate backbone on the proximal $Rad50^{NBD}$ (B) side, near the active site channel (Section 2.2 Figure S3; Figure 15). This suggests, that *Ec*MR bound to a free DNA end in exonuclease mode does not fully occupy all Rad50 DNA binding sites. The active site geometry and coordination of the Mn^{2+} di-metal moiety contacting a DNA backbone phosphate are highly similar to the exonuclease state structure (Section 2.2, Figure 1 and S3). Using a structurally inferred water molecule from a high resolution *Ec*Mre11 crystal structure from Liu and colleagues (PDB: 4M0V)[152], clearly identifies the biochemical cleavage positioning, characteristic of a 5' endonuclease cleavage. As described in a recent biochemical study, the 5' endonuclease shows consistent biochemistry with the 3' to 5' exonuclease activity, as both cleave the 3'O-P bond of the DNA phosphate backbone[165]. Most importantly, in contrast to the exonuclease state, the DNA is now clearly extending past the nuclease active site and exits the channel on the opposite side of the Mre11 di-metal center. This is even further elucidated by a lower resolution reconstruction depicting extended density of the post-active site DNA (Section 2.2, Figure 2; Figure 15). Both densities revealed that the continuous dsDNA is bent sideways to exit the active site channel and not end at the Mre11 nuclease di-metal center. Monitoring

nuclease cleavage events on Ku-blocked and more rigid poly(dA·dT) dsDNA substrates[247] showed that endonucleolytic cleavage predominantly occurs in regions with higher flexibility (Section 2.2, Figure 2; Figure 15). Hence, the active DNA bending seems to be a mechanistic feature of the MR endonuclease state, as already proposed from structural analysis of the exonuclease state (Section 2.1, Figure 2). Here, a simple extension of the dsDNA past the Mre11 active site in exonuclease state would lead to a steric clash, even though the nuclease channel is principally wide enough. To overcome this, active bending is needed to accommodate continuous DNA in the endonuclease state (Section 2.1, Figure 1 and 2). The need for active DNA bending, has also been implied by the observation that nicks in the opposing strand, which lead to increased flexibility, promote endonuclease cleavage of the other strand[173].

In a recent biochemical study, weakening of the Mre11 dimer interaction by a *Ec*Mre11^{V68D} mutation drastically reduced endonuclease activity *in vitro*[165]. Introduction of a pre-melted DNA bubble compensates for this endonuclease defect, interpreted as a hint towards DNA melting in wild-type protein[165]. However, it may also be that the weakening Mre11 interface mutation impairs *Ec*MR's capability of active DNA bending in endonuclease mode. In that case, introduction of the DNA bubble would compensate for the reduced bending capability of *Ec*MR due to the increased local DNA flexibility.

During the last years several studies reported biochemical evidence for DNA binding and nuclease activity related DNA melting or unwinding by the MR(N) complex[153,161,187,239,248,249]. However, based on our structural work, we do not have any evidence for active DNA melting or winding. Rather, the dsDNA is bent in a manner that conserves the base-pairing. Nevertheless, based on our structural and biochemical data, it is not excluded that DNA melting could occur. This in particular holds true for scenarios where MR/MRN may form oligomers on DNA, e.g. mediated by intercomplex Rad50 β-sheet interactions, as reported recently for *S. cerevisiae* MR(X)[250]. Intriguingly, MR oligomerization was shown to drive 5' endonucleolytic cleavage at multiple sites, while leaving exonuclease activity unaffected[250]. Oligomerization could force torsional stress on the internally bound dsDNA that is released via DNA melting. This in turn could also aid the proposed endonuclease mechanism, as the partially melted dsDNA may be more flexible and thus also more easily bendable in endonuclease mode.

Aside of influencing the endonuclease cleavage efficiency of the MR complex, local DNA characteristics may apparently also have an effect on cleavage positioning. As DNA with a more rigid poly(dA·dT) sequence revealed preferential cleavage at regions with predicted higher flexibility of the DNA, this apparently also shifted the cleavage pattern with respect to a generic DNA (Section 2.2, Figure 2). Structurally rigid poly(dA·dT) sequences have been shown to exist *in vivo* and are proposed to affect nucleosome positioning and remodelling and thereby also contribute to transcriptional regulation[247]. Thus, sequence-based DNA mechanical and shape properties can influence the cleavage reaction positioning *in vitro* and potentially

also *in vivo*. Recent *in vivo* and *in vitro* experiments in yeast suggested a direct sequence-dependence in the resection of mitotic DSBs by MRX[251,252]. However, in our structures *Ec*MR only interacts with the DNA phosphate backbone without evidence of any direct protein-nucleobase contact that could serve as part of a sequence recognition mechanism. Hence, on the contrary, it might be that DNA sequence rather directly influences mechanistic DNA parameters, and thus also DNA shape, than the cleavage pattern itself. To further elucidate the physiological relevance of that will be an interesting area for future studies.

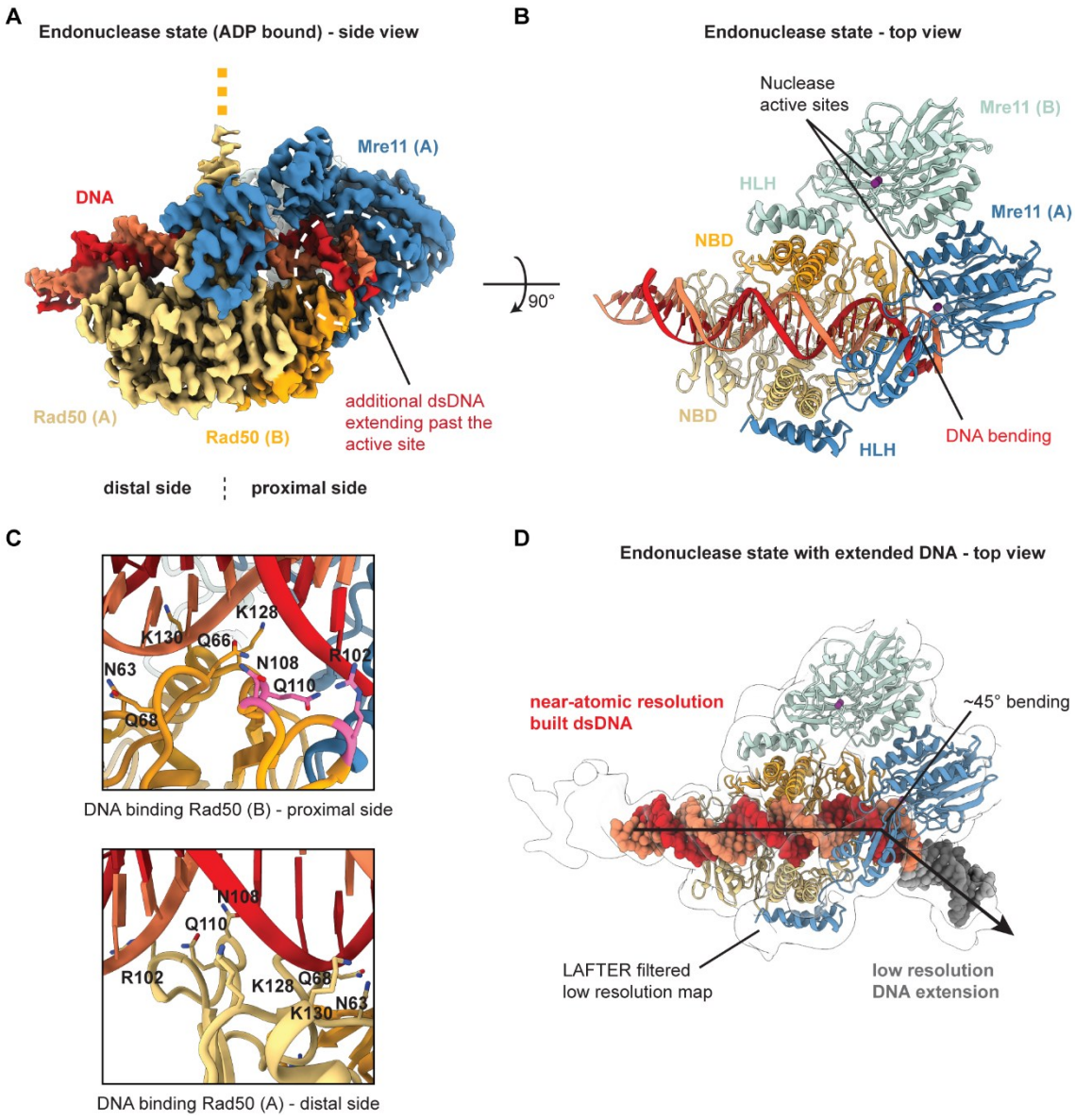

Figure 15: Cryo-EM reconstruction and DNA binding properties of *Ec*MR in endonuclease state. (A) The ADP and DNA-bound endonuclease state of *Ec*MR shown in side view. Rad50, Mre11 and dsDNA are colored in shades of orange, blue and red, respectively. The flexible, unresolved CCs are implied by orange dots. Additional dsDNA extending past the active site is illustrated by a white dotted circle. (B) Top view of the *Ec*MR structural model with color coding according to panel A. The Mre11 nuclease active sites are highlighted and contain the Mn^{2+} ions shown as purple spheres. (C) Close-up views on the Rad50 DNA

binding sites in endonuclease mode. DNA contacting residues are depicted as sticks. Endonuclease-specific DNA binding residues on the proximal side are highlighted in pink. (D) Top view of the *Ec*MR endonuclease state with extended dsDNA, illustrating the active ~45° DNA bending. The extended DNA based on the low resolution reconstruction is highlighted in shades of grey.

Another cryo-EM structure determined in the course of this study is the *Ec*MR complex in a "hairpin-bound state" using a DNA hairpin and ATP. Intriguingly, *Ec*MR adopts a highly similar overall conformation, again, as already described for the 3' to 5' exo- and the 5' endonuclease states (Section 2.2, Figure 2 and 3). Structural fitting is in accordance with a positioning for endonucleolytic cleavage between the first two nucleotides of the hairpin loop, seen from the 5' end. This agrees well with our presented biochemical data (Section 2.2, Figure 2 and S3) and several other biochemically observed MR hairpin cleavage patterns[120,172]. It is further important to note, that a study on human MR reported primary incisions at the 3' side of the hairpin loop[146]. A possible explanation for this would be the flexible nature of the ssDNA hairpin loops, which may result in a different binding and cleavage conformation at the Mre11 active site, depending on the hairpin substrate. Furthermore, additional ~100 Å of the rod-shaped, interacting CCs could be resolved and modeled compared to the exo- and endonuclease structures, further supporting their proposed general DNA gating and clamping function (Section 2.1, Figure 1 and 3; Section 2.2, Figure 2).

While ATPγS is bound in the resting state structure, ADP is present in all three active cutting states (Section 2.1, Figure S4 and Section 2.2). As the cryo-EM sample preparation for the exo-, endonuclease and hairpin-bound states included ATP, the bound ADP molecules indicate the latter as post-hydrolysis states. Given the presence of dsDNA in the samples, this is further supported by the reported dsDNA dependent 26-fold increase of *Ec*MR's ATPase activity[165]. A characteristic that was also shown to be conserved in human and yeast MR complexes by similar stimulation rates[164,180].

Surprisingly, all three active cutting state structures, forming the exo-, endonuclease and hairpin-bound states, share the characteristic of highly similar large conformational rearrangements (Section 2.2, Figure 3). The active site DNA cutting channel formed by Mre11 and Rad50 with the CCs acting as a molecular DNA clamp, revealed Mre11's ability to accommodate and process a variety of different DNA substrates in a single conformational state. Hence, these structures not only reveal a structural basis for DNA end sensing and processing by MR, but also provide a unified mechanistic basis for MR's nuclease diversity.

3.2 Reversed polarity of MR on free versus blocked DNA ends

The Ku-RM-MR-Ku state revealed that both *Ec*MR complexes are oriented on the DNA with the active, re-located Mre11 dimer pointing away from the protein-blocked end. Thus, Mre11 is oriented "inwards", looking from the DNA end – an orientation that stands in contrast to the "outward" orientation of the exonuclease state on a free DNA end (Section 2.2, Figure 1 and S3; Figure 16). This change in orientation was already hypothesized in a former biochemical study[165] and explains a whole body of biochemical results. It not only clarifies differences in cleavage site locations and strand preference for the 3' to 5' exo- and the 5' endonuclease activities, incising either the 3' or 5' ended strand, but also explains the shared 3'O-P cleavage chemistry (Section 2.1, Figure 1 and 2; Section 2.2, Figure 1 and S3)[165]. Moreover, it structurally clarifies why biochemically in exonuclease mode the phosphates are part of the leaving dNMPs, while in endonuclease they are attached to the newly formed DNA end[165]. Hence, biochemical and topological differences between exo- and endonuclease activities are not based on conformational differences, but on the polarity of *Ec*MR binding to internal dsDNA or free ends (Section 2.2, Figure 3 and S3; Figure 16).

*Ec*MR's inwards orientation with the active Mre11 dimer pointing away from the block, supports MR's suggested role within the described "nuclease polarity paradox" in HR repair[92,136]. In the observed 5' endonuclease mode, MR is able to nick the 5' strand adjacent to the blocked end, while subsequently being able to exonucleolytically back-resect in 3' to 5' direction. This orchestrated enzymatic mechanism was also shown *in vitro* for yeast MRX-Sae2[97,174]. Combining those two nuclease functions in a single conformational state is possible due to the revealed unified nuclease mechanism (Section 2.2). Yet, it is still unclear how a protein block covalently bound to the 3' or both DNA ends would be removed by MR. While a block bound to the 5' end, e.g. Spo11 in meiotic recombination[62], can be resolved by exonucleolytic back resection from the initial nick site[63,64], blocks associated with the 3' end would remain attached. Here, the cleavage of the opposing strand by *Ec*MR's 3' endonuclease, which was also reported for human MRN in a limited amount[173], would further aid to release the protein-DNA adduct[92]. However, the structural basis for this conserved 3' endonuclease activity remains elusive.

The inwards orientation of both *Ec*MR complexes on the Ku-blocked DNA positions the Mre11 nuclease active site of either complex ~55 bp from the respective end (Figure 16). This matches the biochemically observed incision sites at ~50 nt from the 5' end (Section 2.1, Figure S6, Section 2.2, Figure 1 and 2). Analysing various blocks *in vitro*, the MRN/X endonucleolytic nicking sites were found to be ~15-45 nt away from the DNA end[92,93,97,135]. Depending on the nature of the block *in vitro*, e.g. using a Streptavidin bound 5' biotin tethered to the DNA end via a short chemical spacer, the observed cleavage position will change compared to Ku-blocked ends[97]. *In vitro* experiments on yeast MRX reported a robust cleavage pattern at ~35

nt from the Ku-blocked DNA end[97,174]. Given the observed space between *Ec*MR and Ku in the Ku-RM-MR-Ku state, this ~35 nt cleavage pattern could also be achieved by just sliding the MR complex back towards the blocked end until the proteins just touch. In support of this, human MRN was shown to be able to diffuse along DNA until a block is reached[96]. So far, we have no structural evidence for a direct interaction between *Ec*MR and Ku, or a protein block in general. The same holds true for the two loaded *Ec*MR complexes, where we do not see evidence for an intercomplex interaction between MR complexes. However, such interactions could still occur, especially in the eukaryotic MR system, where e.g. oligomerization was shown to drive 5' endonucleolytic cleavage at multiple sites[250].

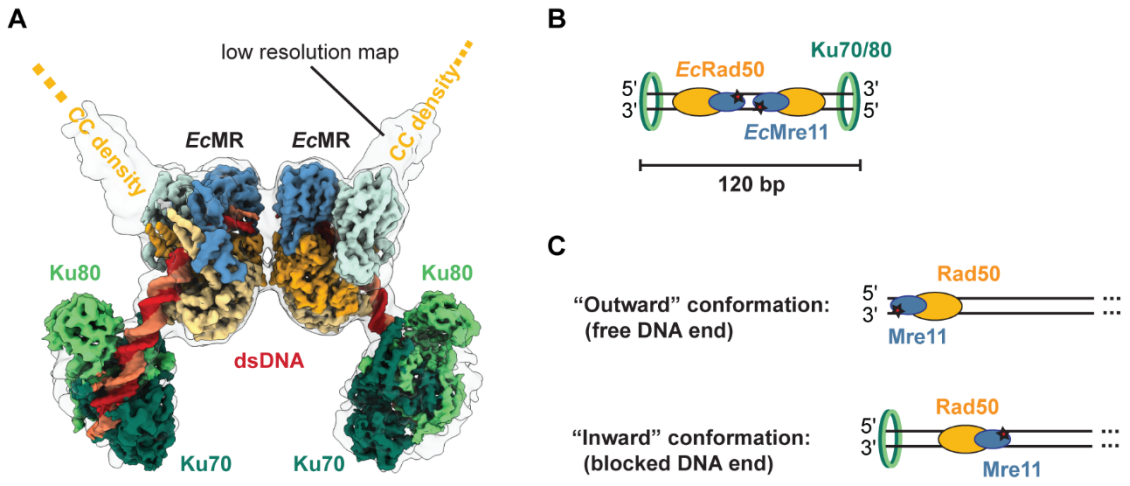

Figure 16: The Ku-RM-MR-Ku state reveals the reversed polarity of MR on free versus blocked DNA ends. (A) Low resolution recontruction and derived composite map of the Ku-RM-MR-Ku state. (B) Schematic illustration of the Ku-RM-MR-Ku state on 120 bp dsDNA. (C) Schematic illustration depicting the reversed polarity of MR on free versus blocked DNA ends.

In their *in vitro* study on yeast MRX, Wang *et al.* not only reported a predominant cleavage event at ~35 nt, but also a second cleavage event at ~65 nt when increasing the DNA length from 70 to 100 bp[174]. This result is further supported by a recent *in vivo* study on yeast MRX that also reported cleavage at ~65 nt[251]. This cleavage pattern fits our observed incision sites considering potential influences of local DNA sequence and shape variations or sliding of the MR complex on DNA[96,251]. Furthermore, the consecutive incisions in combination with observations of cleavage sites up to 300-400 bp from the DNA end *in vivo*[100], suggest a stepwise endonuclease mechanism by the MRN/X complex to initiate DSB resection[253]. However, we do not see any structural evidence for such a mechanism at the moment.

3.3 Towards a structural model for the full MR reaction cycle

The discussed results illustrate that the MR complex undergoes large conformational movements. Thereby, it transitions from an open ring-shaped resting state to a rod-shaped and unified nuclease-active conformation, enabling processing of several different DNA substrates. However, the mechanistic bases for the resting to cutting state, as well as the "reverse" cutting to resting state transitions, still remain elusive. Hence, it will be the task of future research to fill in the gaps and progress towards a complete structural model for the full MR reaction cycle. In regard to this, the following chapter will focus on mechanistic hypotheses for the transition between the different structural states.

Starting from a point in the reaction cycle where a DSB end is sensed and the DNA is bound by MR, the complex needs to transition from resting to an active cutting state. Thinking of a free DNA end, the Mre11 dimer could, in theory, relocate across the break end to adopt the unified nuclease active conformation. However, on a blocked DSB end things appear to be more complex. Due to the reversed polarity of the MR complex on free versus blocked DNA ends, with a continuous DNA duplex in the latter, a simple relocation of the Mre11 dimer is prevented. Thus, based on our current *Ec*MR structures, there are three possible mechanistic theories that could explain the conformational rearrangements via an intermediate transition state.

A first model suggests a transient opening of the Mre11 dimer interface, to relocate over the dsDNA duplex and reassemble on the other side in endonuclease mode. In this scenario, the Mre11 monomers would stay flexibly attached to the DNA-bound Rad50 dimer via the C-terminal linker and the HLH motif (Figure 17). Our biochemical experiments on fusion proteins of *Ec*MR and the LisH (Lis1 homology) dimerization domain[254,255], further support a transient opening of the Mre11 dimer. Here, N-terminal fusions of LisH domains to the respective Mre11 subunits were done, connected by different length linkers, tethering the nuclease dimer together. Using a short 11 amino acid linker severely compromised *Ec*MR's endonuclease activity on blocked 1500 bp linear dsDNA, while an extended linker length of 20 amino acids showed residual endonuclease activity (Section 2.1, Figure 5 and S6). While the shorter 11-aa linker might prevent a Mre11 dimer opening and relocation, the 20-aa linker might be long enough to allow more conformational freedom. Overall, this biochemically supports a potential involvement of the transient Mre11 dimer opening in the transition state mechanism.

The second model would need detachment of at least one HLH motif from the Rad50 binding site. This transient HLH detachment would enable the Mre11 dimer to swing around the DNA as a whole and relocate to the other side of the DNA in endonuclease state. Afterwards, the HLH-motif would need to bind to the Rad50 head again, to form the observed active nuclease state conformation (Figure 17). In principle, it would also be possible that not one but both HLHs detach from the Rad50 head domain, disrupting the MR complex as a whole. However,

based on our current biochemical and cryo-EM experiments, there is at least no evidence of pronounced *Ec*MR complex dis- and reassociation upon addition of DNA and ATP (Section 2.1 and 2.2).

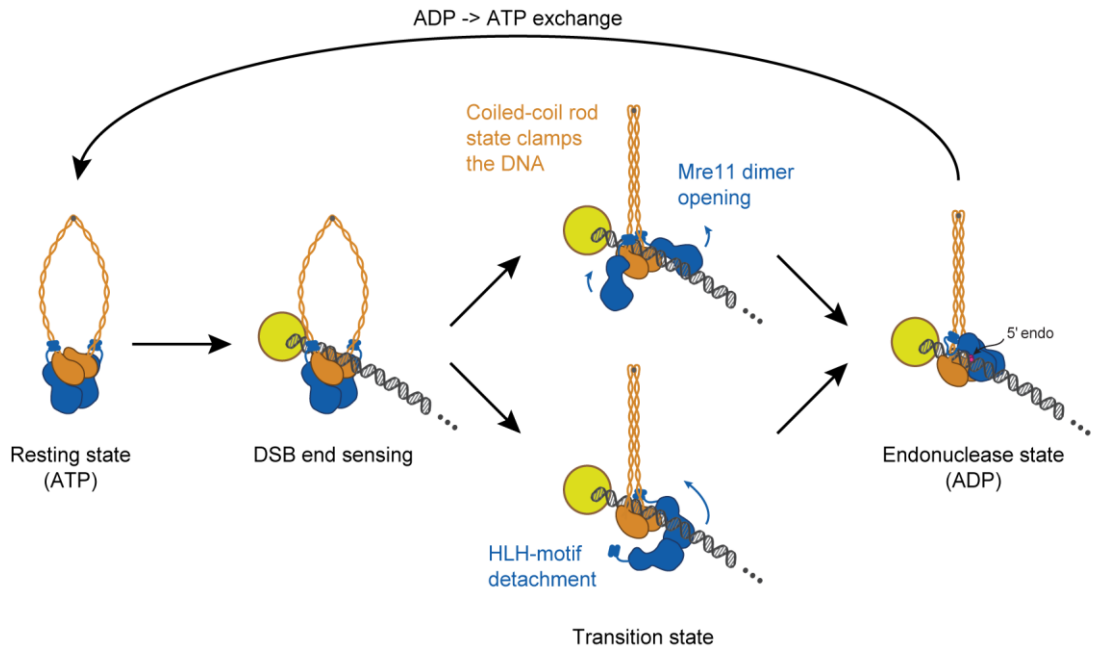

Figure 17: Schematic illustration of the full MR reaction cycle and potential structural models for the unsolved resting to active transition state.

In a third potential mechanistic model, the transition state would be coupled to an additional ATP hydrolysis cycle and an associated opening of the Rad50 head domain to allow nucleotide exchange. Starting from the point where a DSB end is sensed and DNA is bound to the Rad50 head, but the Mre11 dimer is still in the autoinhibited resting state (Figure 17), ATP would be hydrolysed by Rad50. This may induce the opening of the Rad50 head domain to release ADP+P_i, leading to a conformation which resembles the nucleotide-free open state crystal structure of the *T. maritima* MR head complex[149]. During this time frame, the disengaged Rad50 NBDs could relocate to the other side of the DNA double-strand, before binding of two new ATP molecules would induce head engagement again. However, the Rad50 dimer would still need to flip by 180° over the DSB end for the CCs to be able to clamp and gate the DNA as depicted in the unified nuclease active state model. This might be further aggravated in a scenario where the MR complex might act several hundred bases upstream of the break site[100], with the continuous DNA blocking a simple flipping mechanism. Here, the Zn-hook would either be forced to remain on the side of the Rad50 head or would also need to dissociate, as shown in several AFM studies[143,144,187], followed by re-association on the other side of the DNA. The described ADP-release and Rad50 head disengagement is also necessary for the

ADP to ATP exchange to complete the full MR reaction cycle (Figure 17). However, the mechanistic basis for the induction of the nucleotide release is missing to date.

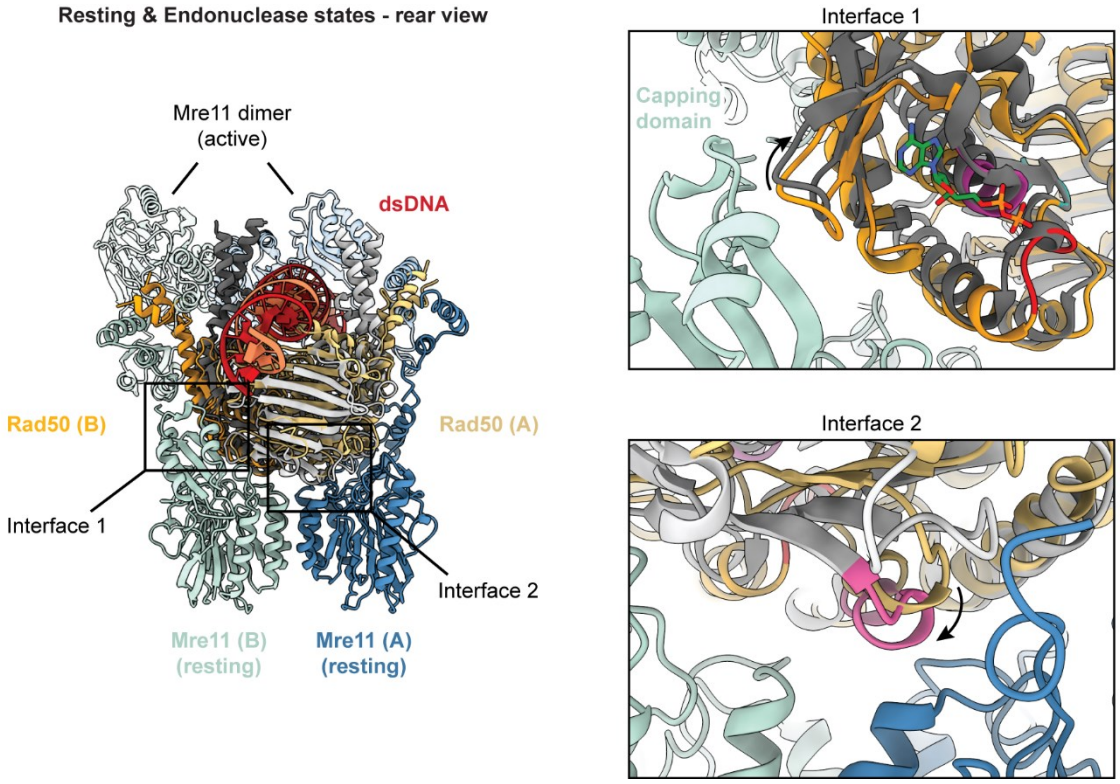

Figure 18: Structural alignment of the *Ec*MR resting and endonuclease states and associated structural changes of the Rad50 NBDs. Structural alignment of the ATPγS bound resting and the ADP and dsDNA-bound endonuclease states of *Ec*MR, aligned on the Rad50 NBDs. Resting state Rad50 and Mre11 are colored in shades of orange and blue, respectively. Endonuclease state Rad50, Mre11 and dsDNA are colored in shades of grey, transparent blue and red, respectively, with the bound ADP shown as green sticks. For clarity reasons, the resting state ATPγS is not shown. Domain movements at interface 1 and 2, likely coupled to ATP hydrolysis, are illustrated by black arrows. In interface 1, the Rad50 signature and Walker A motifs are highlighted in purple and red, respectively.

Structural alignment of the resting and endonuclease states on the Rad50 head modules may support a mechanistic basis for the Mre11 dimer opening model. Comparing the two conformational states, at least two noticeable structural rearrangements became apparent.
First, in interface 1, a loop formed by Rad50$^{938\text{-}944}$ moves inwards and away from the resting state Mre11 capping domain, when ATP is hydrolysed (Figure 18). In resting state, this loop seems to interact with Mre11 via Ala942^{Rad50} binding to a small hydrophobic patch formed by the Mre11 capping domain, complemented by surrounding polar interactions. A structurally similar interface was described for the *T. maritima* MR complex and suggested to stabilize a nucleotide and DNA free open conformation[149]. The loop is also directly connected to the ATPase catalytically important Rad50 signature motif (Figure 18). Hence, there might be a direct connection between ATP hydrolysis, induced structural changes transitioning from the

Rad50 signature motif towards the loop and a resulting destabilization of the resting state Rad50-Mre11 interface 1.
Second, in interface 2, the C-terminal helix of Rad50$^{1017\text{-}1025}$ gets pushed down towards the Mre11 dimer interface upon transition from ATP to ADP state (Figure 18). This may further destabilize the Mre11-Rad50, but also the Mre11 dimer interface interaction. A process that is potentially further amplified by clamping of the CCs and resulting potential pulling forces, transmitted via the Mre11 linker and HLH-motif. In sum, the described ATP hydrolysis induced structural rearrangements may lead to an overall destabilization of the MR resting state and could result in a Mre11 dimer opening.
It is important to note that the loop movement can only be observed in the Rad50 (B) subunit, while the C-terminal helix is only relocated in the distal Rad50 (A). This one-sided movements may add the possibility for an active directionality in the resting to active state transition mechanism. However, it is also possible that these movements do happen in both Rad50 monomers and may be masked by the large conformational rearrangements associated with active state formation. It will be the task of future studies to structurally and biochemically elucidate the proposed models and clarify the missing pieces of the complete MR reaction cycle.

3.4 A model for the 3' endonucleolytic cleavage activity based on the existing 5' endonuclease structure

While we were able to solve the structural and mechanistic basis for *Ec*MR's 5' endonuclease activity, we still do not understand how MR additionally cleaves the opposing 3' strand. This 3' endonuclease cleavage, although reported in a limited way, was shown to be conserved in eukaryotic MRN[173], but in comparison to the 5' endonuclease depends on a different cleavage chemistry[165]. Even though, the structural basis of the 3' endonuclease still remains unclear to date, a mechanistic model can be derived based on the existing 5' endonuclease structure combined with recent biochemical insights.
During repair of obstructed DNA ends, the MR(N) complex endonucleolytically incises the 5' strand, followed by 3' to 5' exonucleolytic back resection towards the end[92,94,100,173]. This combined nuclease activity is also matching our unified structural and mechanistic basis for the 5' endo- and 3' to 5' exonuclease activities (Section 2.2, Figure 3). Based on the described biochemical insights, a model was drawn that suggests the 3' endonucleolytic incision as a secondary cleavage event, after the initial incision and back resection (Figure 19)[173]. Structural analysis of our 5' endonuclease state shows that the two closest DNA backbone phosphates of the opposing 3' strand are only ~13.5 Å away from the 5' strand phosphate positioned for cleavage (Figure 19). However, 3' to 5' back resection from the initial 5' strand incision will

leave this part of the opposing 3' strand as ssDNA with increased flexibility. Thus, in a secondary reaction, the DNA phosphate backbone of the 3' strand might be relocated to the Mre11 active site and positioned for nucleolytic cleavage.

Nevertheless, it might be that the MR(N) complex adopts a different conformation than the one depicted by the unified nuclease mechanism. This might in particular be the case in the alternative scenario, where the initial endonuclease incision is executed on the opposing 3' strand, as reported for human MRN[173]. Furthermore, it is still not understood how eukaryote specific cofactors such as CtIP contribute and potentially influence certain conformational states. Thus, it will be the task of future structural studies to further elucidate the conformational state of MR(N)'s 3' endonuclease activity.

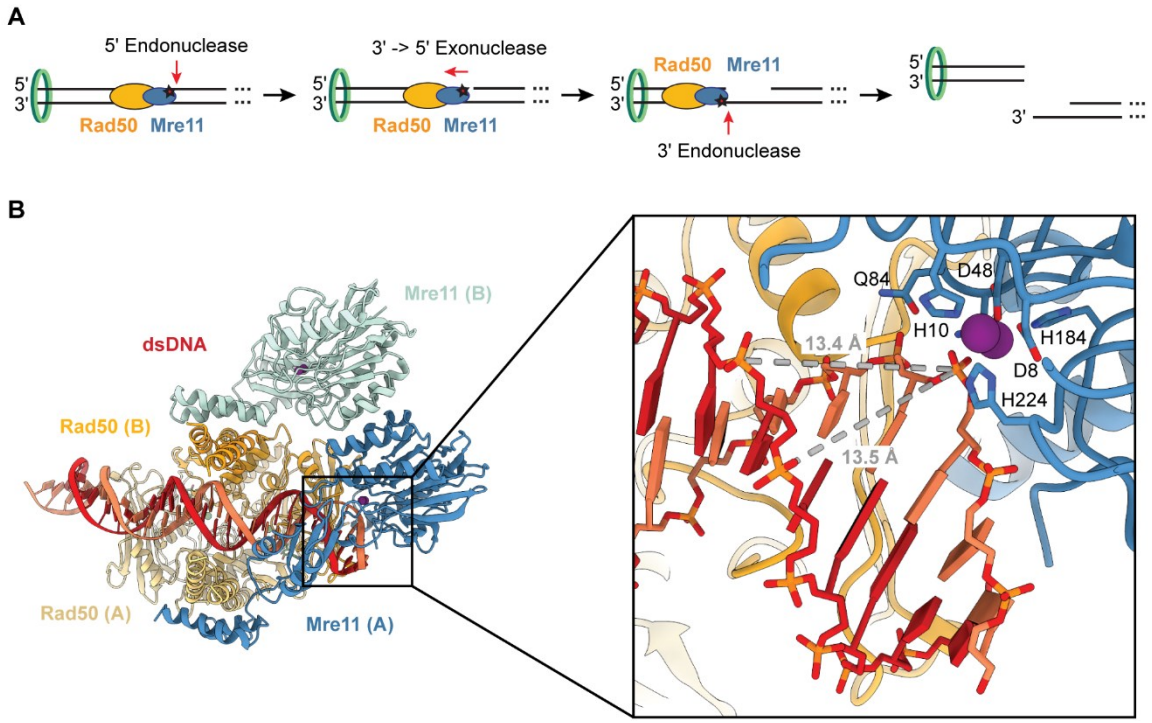

Figure 19: Model for the 3' endonucleolytic cleavage activity based on biochemical and structural insights. (A) Schematic illustration of MR(N)'s stepwise resection of a blocked DNA end, combining MR(N)'s different nuclease activities. Panel based on Deshpande et al., 2016[173]. (B) Top view of *Ec*MR in endonuclease state. Rad50, Mre11, dsDNA and Mn^{2+} ions are colored in shades of orange, blue, red and purple, respectively. Close-up on the Mre11 (A) nuclease active site with highlighted distances of the nearest DNA backbone phosphates of the opposing 3' strand.

3.5 *Ec*MR as a model system for MRN - transferring the unified nuclease mechanism to eukaryotes

Our results also have implications for eukaryotic MRN/X, as the *Ec*MR nuclease active states with the derived unified mechanistic framework can serve as a structural model system. We performed structural alignments of eukaryotic MR crystal structures and human AlphaFold2 models on the *Ec*MR exo- and endonuclease states, respectively. These showed that the eukaryotic models are sterically able to adopt a very similar DNA-bound active conformation (Section 2.1, Figure S7; Section 2.2, Figure S3). However, it is still not clear how the eukaryote-specific and enzymatically important cofactors CtIP/Sae2 and Nbs1/Xrs2, which was also shown to be essential for resection in humans[93,173], are structurally involved in this process.

In the *Ec*MR exo- and endonuclease states, the *Ec*Mre11$^{\text{fastener}}$ loop (amino acids 137-149) binds to the outer β-sheet of the *Ec*Rad50 NBD, locking the complex in the nuclease active conformation (Section 2.1, Figure 2 and S7; Section 2.2., Figure S3). In *C. thermophilum* and human Mre11 models, this element is much shorter and lacks the *Ec*Mre11 specific loop, acting as a conformational latch. Moreover, the fastener bound Rad50 NBD surface cluster corresponds to the sites of yeast Rad50S mutations[256], which phenocopy a Sae2 knockout[176,257]. It is therefore possible that in the absence of an intrinsic fastener, the cutting state interactions between eukaryotic Mre11$^{\text{Nuc}}$ and Rad50$^{\text{NBD}}$ are mediated by CtIP/Sae2 (Section 2.1, Figure S7)[258]. Supporting this, experiments with yeast MRX showed a phosphorylation dependent physical interaction of the Sae2 C-terminus with Rad50, which is important for DNA end resection and can be impaired by the Rad50S mutation K81I[93,168,259]. A recent study mapped this C-terminal region further down to a conserved 15 amino acid long CtIP/Ctp1 polypeptide, sufficient to stimulate the endonuclease activity of human and *S. pombe* MRN[258]. An AlphaFold2 (AF2)[260] model of a human CtIP$^{831\text{-}860}$ C-terminal part, including the conserved 15 amino acids with the endonuclease critical T847 and adjacent T859 phosphorylation sites[129,135,258,261,262], shows binding to the Rad50 NBD (amino acids 1-228 and 1079-1312) outer β-sheets (Figure 20). The model suggests binding of T847 to a polar pocket formed by Rad50 β-sheet residues Q81, R83 and Q97. R83 is the human counterpart to yeast K81$^{\text{Rad50}}$, and thus helps to structurally explain the observed Rad50S mutant K81I induced inhibition of MRN/X DNA end resection (Figure 20)[227,263]. Structural alignment of the CtIP$^{831\text{-}860}$ model on the AF2 model of human MR pre-aligned on the *Ec*MR endonuclease state (Section 2.2, Figure S3) shows, that the N-terminal part of the CtIP peptide wraps closely underneath the nuclease domain of the active Mre11 (A) at the DNA exit site (Figure 20). Hence, this conformation may give an idea how the CtIP C-terminus might structurally bridge the interaction between Rad50 and Mre11, replacing the bacterial fastener in an active cutting state conformation.

Adding up on this, the telomeric factor Rif2 was recently shown to inhibit MRX endonuclease activity in yeast[226,264]. Genetic and structural modelling approaches found yeast Rad50 residues K6, N18, K81 and I93 to be important for the inhibiting Rad50-Rif2 interaction[226,227,264]. As Rad50^{K81} is also an important residue in MRX-Sae2 binding, Rif2 likely competes with Sae2 for Rad50 binding to limit MRX endonuclease stimulation[263]. In mammals, it was speculated that the telomeric factor TRF2 may adopt Rif2's inhibitory role[227]. Interestingly, this idea is further supported by an AF2 model of a human TRF2$^{448-474}$ inhibitor of DDR (iDDR) domain[265] polypeptide bound to Rad50 that shows an overlapping binding position compared to the human CtIP model (Figure 20). Two very recent studies published on bioRxiv, focusing on the inhibition of MRN/X-CtIP/Sae2 by TRF2/Rif2 binding at telomeres, support the above discussed prediction results for the CtIP/TRF2-Rad50 binding[266,267].

Taken together, this supports a model in which CtIP/Sae2 may act as an evolutionary conserved Rad50^{NBD} bound fastener surrogate, promoting stabilization of an MRN/X active nuclease cutting state similar to *Ec*MR (Section 2.1, Figure S7; Section 2.2 Figure S3)[258]. Nevertheless, future studies will be needed to clarify the resection-related interactions and mechanistic interplay of CtIP with Mre11 and Nbs1.

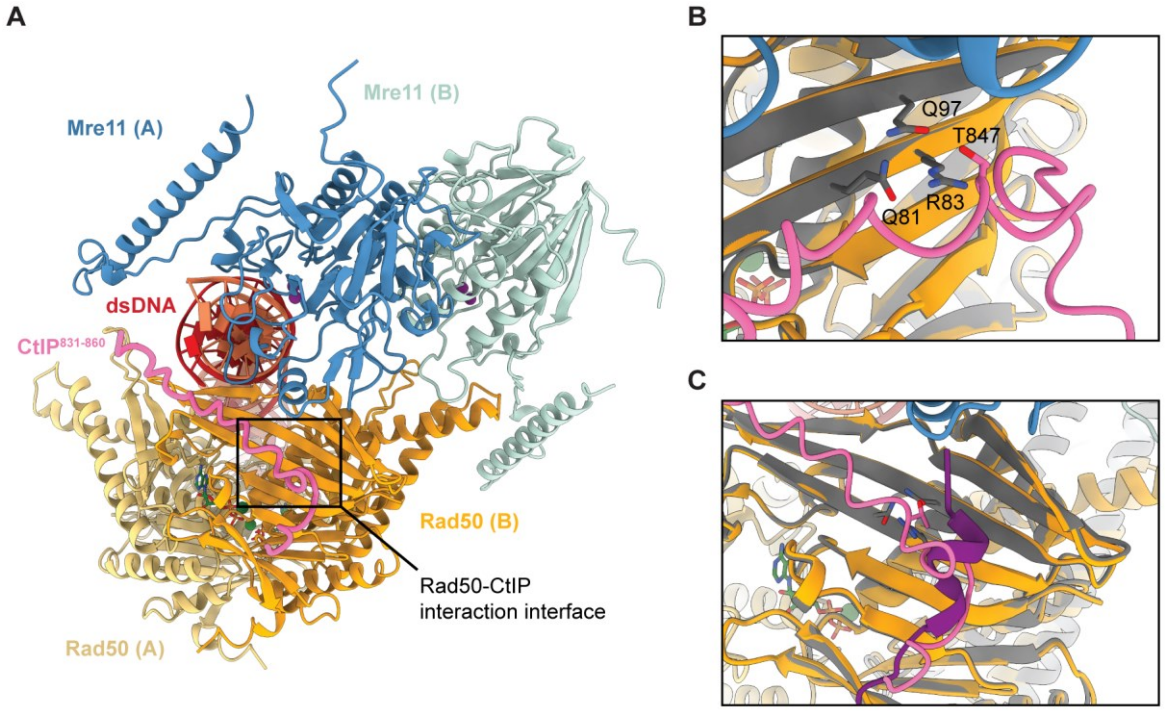

Figure 20: Structural alignments of pre-aligned AlphaFold2 models of the human MR complex in active state with CtIP and TRF2 binding to the outer β-sheets of the Rad50 NBD. (A) AlphaFold2 models of human Rad50 (amino acids 1-200 and 1133-1312 connected by a G_6 linker) and Mre11 (1-356) dimers, structurally aligned on the *Ec*MR endonuclease state and coloured in shades of orange and blue, respectively. The dsDNA in red is positionally inferred from the *Ec*MR endonuclease state and the CtIP$^{831-860}$ C-terminal peptide (pink) from structural alignment of a predicted monomeric Rad50-CtIP$^{831-860}$ AF2 model. (B) Close-up on the structural alignment of the Rad50-CtIP$^{831-860}$ and human MR nuclease active state AF2

models. Rad50 (B) and Mre11 (A) of the human MR are coloured in orange and blue. Rad50 and CtIP$^{831-860}$ of the human MR are coloured in dark grey and pink. Interacting residues around the essential CtIP phosphosite T847 are depicted as sticks. (C) Structural overlay of a Rad50-TRF2$^{448-474}$ AF2 model on the alignment of panel B, showing positional overlap of the binding locations of CtIP and TRF on the Rad50 NBD. Colouring according to panel B with TRF2$^{448-474}$ depicted in purple.

In sum, the results generated within this thesis not only provide the first structures of the full-length *E. coli* Mre11-Rad50 complex, but also reveal a unified structural mechanism as basis for MR's nuclease diversity. The presented data allows further structural and mechanistic insights into the exo-, endonuclease and hairpin-opening activities of the bacterial MR, which can also be extrapolated to eukaryotic MRN/X. These insights build the basis for future studies on the remaining elusive parts of the full MR reaction cycle, as well as for the DNA end sensing and processing mechanism by eukaryotic MRN/X.

4 References

1 Basu, A. K. DNA Damage, Mutagenesis and Cancer. *Int J Mol Sci* **19**, doi:10.3390/ijms19040970 (2018).

2 Yousefzadeh, M. *et al.* DNA damage-how and why we age? *Elife* **10**, doi:10.7554/eLife.62852 (2021).

3 De Bont, R. & van Larebeke, N. Endogenous DNA damage in humans: a review of quantitative data. *Mutagenesis* **19**, 169-185, doi:10.1093/mutage/geh025 (2004).

4 Lindahl, T. Instability and decay of the primary structure of DNA. *nature* **362**, 709-715 (1993).

5 Hoeijmakers, J. H. J. DNA Damage, Aging, and Cancer. *New England Journal of Medicine* **361**, 1475-1485, doi:10.1056/NEJMra0804615 (2009).

6 Kirkwood, T. B. Understanding the odd science of aging. *Cell* **120**, 437-447 (2005).

7 Schumacher, B., Garinis, G. A. & Hoeijmakers, J. H. Age to survive: DNA damage and aging. *Trends in Genetics* **24**, 77-85 (2008).

8 Doll, R. & Peto, R. The causes of cancer: quantitative estimates of avoidable risks of cancer in the United States today. *JNCI: Journal of the National Cancer Institute* **66**, 1192-1308 (1981).

9 Trichopoulos, D. & Petridou, E. Epidemiologic studies and cancer etiology in humans. *Medicine Exercise Nutrition and Health* **3**, 206-225 (1994).

10 Jackson, A. L. & Loeb, L. A. The contribution of endogenous sources of DNA damage to the multiple mutations in cancer. *Mutation Research/Fundamental and Molecular Mechanisms of Mutagenesis* **477**, 7-21 (2001).

11 Friedberg, E. C., Walker, G. C., Siede, W. & Wood, R. D. *DNA repair and mutagenesis*. (American Society for Microbiology Press, 2005).

12 Frankenberg-Schwager, M. Review of repair kinetics for DNA damage induced in eukaryotic cells in vitro by ionizing radiation. *Radiotherapy and Oncology* **14**, 307-320 (1989).

13 Oleinick, N. L., Chiu, S.-m., Friedman, L. R., Xue, L.-y. & Ramakrishnan, N. in *Mechanisms of DNA damage and repair* 181-192 (Springer, 1986).

14 Chiu, S.-M., Oleinick, N. L., Friedman, L. R. & Stambrook, P. J. Hypersensitivity of DNA in transcriptionally active chromatin to ionizing radiation. *Biochimica et Biophysica Acta (BBA)-Gene Structure and Expression* **699**, 15-21 (1982).

15 Drabløs, F. *et al.* Alkylation damage in DNA and RNA—repair mechanisms and medical significance. *DNA repair* **3**, 1389-1407 (2004).

16 Fu, D., Calvo, J. A. & Samson, L. D. Balancing repair and tolerance of DNA damage caused by alkylating agents. *Nature Reviews Cancer* **12**, 104-120 (2012).

17 IARC-MONOGRAPHS. On the Evaluation of Carcinogenic Risks to Humans Tobacco Smoking. *World Health Organization* **vol. 38** (1986).

18 Friedberg, E. C., McDaniel, L. D. & Schultz, R. A. The role of endogenous and exogenous DNA damage and mutagenesis. *Current opinion in genetics & development* **14**, 5-10 (2004).

19 Jin, Y. H. *et al.* Cadmium is a mutagen that acts by inhibiting mismatch repair. *Nature genetics* **34**, 326-329 (2003).

20 Epe, B. Role of endogenous oxidative DNA damage in carcinogenesis: what can we learn from repair-deficient mice? (2002).

21 Floyd, R. A. Measurement of oxidative stress in vivo. *In: K.J.A. Daview, F. Ursini (Eds.), The Oxygen Paradox, Cleup University Press, Cleup*, 89-103 (1995).

22 Klebanoff, S. Phagocytic cell: products of oxygen metabolism. *In: J.I. Gallin, I.M. Goldstein, R. Snyderman (Eds.) Inflammation: basic principles and clinical correlates. Raven Press, New York*, 391-444 (1988).

23 T.G. Newcomb, L. A. L. Oxidative DNA damage and mutagenesis. *In: J.A. Nickoloff, M.F. Hoekstra (Eds.), DNA Damage and Repair in Prokaryotes and Lower Eukaryotes, Humana Press, Totowa, NJ*, 1-18 (1998).

24 Purmal, A. A., Kow, Y. W. & Wallace, S. S. Major oxidative products of cytosine, 5-hydroxycytosine and 5-hydroxyuracil, exhibit sequence context-dependent mispairing in vitro. *Nucleic acids research* **22**, 72-78 (1994).

25 Cadet, J. & Berger, M. Radiation-induced decomposition of the purine bases within DNA and related model compounds. *International Journal of Radiation Biology and Related Studies in Physics, Chemistry and Medicine* **47**, 127-143 (1985).

26 Pourquier, P. & Pommier, Y. Topoisomerase I-mediated DNA damage. (2001).

27 Champoux, J. J. DNA is linked to the rat liver DNA nicking-closing enzyme by a phosphodiester bond to tyrosine. *Journal of Biological Chemistry* **256**, 4805-4809 (1981).

28 Lynn, R. M., Bjornsti, M.-A., Caron, P. R. & Wang, J. C. Peptide sequencing and site-directed mutagenesis identify tyrosine-727 as the active site tyrosine of Saccharomyces cerevisiae DNA topoisomerase I. *Proceedings of the National Academy of Sciences* **86**, 3559-3563 (1989).

29 Xu, Y. & Her, C. Inhibition of topoisomerase (DNA) I (TOP1): DNA damage repair and anticancer therapy. *Biomolecules* **5**, 1652-1670 (2015).

30 Wall, M. E. & Wani, M. C. Camptothecin and taxol: discovery to clinic—thirteenth Bruce F. Cain Memorial Award Lecture. *Cancer research* **55**, 753-760 (1995).

31 Pommier, Y. DNA topoisomerase I inhibitors: chemistry, biology, and interfacial inhibition. *Chemical reviews* **109**, 2894-2902 (2009).

32 Chatterjee, N. & Walker, G. C. Mechanisms of DNA damage, repair, and mutagenesis. *Environmental and molecular mutagenesis* **58**, 235-263 (2017).

33 Lange, S. S., Takata, K.-i. & Wood, R. D. DNA polymerases and cancer. *Nature reviews cancer* **11**, 96-110 (2011).

34 Waters, L. S. *et al.* Eukaryotic translesion polymerases and their roles and regulation in DNA damage tolerance. *Microbiology and Molecular Biology Reviews* **73**, 134-154 (2009).

35 Bielas, J. H., Loeb, K. R., Rubin, B. P., True, L. D. & Loeb, L. A. Human cancers express a mutator phenotype. *Proceedings of the National Academy of Sciences* **103**, 18238-18242 (2006).

36 Masutani, C. *et al.* Xeroderma pigmentosum variant (XP-V) correcting protein from HeLa cells has a thymine dimer bypass DNA polymerase activity. *The EMBO journal* **18**, 3491-3501 (1999).

37 Johnson, R. E., Washington, M. T., Prakash, S. & Prakash, L. Fidelity of human DNA polymerase η. *Journal of Biological Chemistry* **275**, 7447-7450 (2000).

38 Biertümpfel, C. *et al.* Structure and mechanism of human DNA polymerase η. *Nature* **465**, 1044-1048 (2010).

39 Silverstein, T. D. *et al.* Structural basis for the suppression of skin cancers by DNA polymerase η. *Nature* **465**, 1039-1043 (2010).

40 Limoli, C. L., Giedzinski, E., Bonner, W. M. & Cleaver, J. E. UV-induced replication arrest in the xeroderma pigmentosum variant leads to DNA double-strand breaks, γ-H2AX formation, and Mre11 relocalization. *Proceedings of the National Academy of Sciences* **99**, 233-238 (2002).

41 Mehta, A. & Haber, J. E. Sources of DNA double-strand breaks and models of recombinational DNA repair. *Cold Spring Harbor perspectives in biology* **6**, a016428 (2014).

42 Vilenchik, M. M. & Knudson, A. G. Endogenous DNA double-strand breaks: production, fidelity of repair, and induction of cancer. *Proceedings of the National Academy of Sciences* **100**, 12871-12876 (2003).

43 Sonoda, E., Morrison, C., Yamashita, Y. M., Takata, M. & Takeda, S. Reverse genetic studies of homologous DNA recombination using the chicken B–lymphocyte line, DT40. *Philosophical Transactions of the Royal Society of London. Series B: Biological Sciences* **356**, 111-117 (2001).

44 Koster, D. A., Palle, K., Bot, E. S., Bjornsti, M.-A. & Dekker, N. H. Antitumour drugs impede DNA uncoiling by topoisomerase I. *Nature* **448**, 213-217 (2007).

45 Mirkin, E. V. & Mirkin, S. M. Replication fork stalling at natural impediments. *Microbiology and molecular biology reviews* **71**, 13-35 (2007).

46 Bétermier, M., Borde, V. & de Villartay, J.-P. Coupling DNA damage and repair: an essential safeguard during programmed DNA double-strand breaks? *Trends in Cell Biology* **30**, 87-96 (2020).

47 Jung, D., Giallourakis, C., Mostoslavsky, R. & Alt, F. W. Mechanism and control of V (D) J recombination at the immunoglobulin heavy chain locus. *Annual review of immunology* **24**, 541-570 (2006).

48 Zhang, Y. *et al.* Transposon molecular domestication and the evolution of the RAG recombinase. *Nature* **569**, 79-84 (2019).

49 Schatz, D. G. & Swanson, P. C. V (D) J recombination: mechanisms of initiation. *Annual review of genetics* **45**, 167-202 (2011).

50 Lieber, M. R. The mechanism of double-strand DNA break repair by the nonhomologous DNA end joining pathway. *Annual review of biochemistry* **79**, 181 (2010).

51 De Villartay, J.-P., Fischer, A. & Durandy, A. The mechanisms of immune diversification and their disorders. *Nature Reviews Immunology* **3**, 962-972 (2003).

52 Yu, K. & Lieber, M. R. Current insights into the mechanism of mammalian immunoglobulin class switch recombination. *Critical reviews in biochemistry and molecular biology* **54**, 333-351 (2019).

53 Yu, K. & Lieber, M. R. Nucleic acid structures and enzymes in the immunoglobulin class switch recombination mechanism. *DNA repair* **2**, 1163-1174 (2003).

54 Bransteitter, R., Pham, P., Scharff, M. D. & Goodman, M. F. Activation-induced cytidine deaminase deaminates deoxycytidine on single-stranded DNA but requires the action of RNase. *Proceedings of the National Academy of Sciences* **100**, 4102-4107 (2003).

55 Petersen-Mahrt, S. K., Harris, R. S. & Neuberger, M. S. AID mutates E. coli suggesting a DNA deamination mechanism for antibody diversification. *Nature* **418**, 99-104 (2002).

56 Liu, M. *et al.* Two levels of protection for the B cell genome during somatic hypermutation. *Nature* **451**, 841-845 (2008).

57 Han, L. & Yu, K. Altered kinetics of nonhomologous end joining and class switch recombination in ligase IV–deficient B cells. *The Journal of experimental medicine* **205**, 2745-2753 (2008).

58 Alberts, B. *et al. Molecular Biology of the Cell*. (Garland Science, 2008).

59 Keeney, S., Giroux, C. N. & Kleckner, N. Meiosis-specific DNA double-strand breaks are catalyzed by Spo11, a member of a widely conserved protein family. *Cell* **88**, 375-384 (1997).

60 Diaz, R. L., Alcid, A. D., Berger, J. M. & Keeney, S. Identification of residues in yeast Spo11p critical for meiotic DNA double-strand break formation. *Molecular and cellular biology* **22**, 1106-1115 (2002).

61 Keeney, S. in *Recombination and meiosis* 81-123 (Springer, 2007).

62 Keeney, S. & Neale, M. Initiation of meiotic recombination by formation of DNA double-strand breaks: mechanism and regulation. *Biochemical Society Transactions* **34**, 523-525 (2006).

63 Neale, M. J., Pan, J. & Keeney, S. Endonucleolytic processing of covalent protein-linked DNA double-strand breaks. *Nature* **436**, 1053-1057 (2005).

64 Hodgson, A. *et al.* Mre11 and Exo1 contribute to the initiation and processivity of resection at meiotic double-strand breaks made independently of Spo11. *DNA repair* **10**, 138-148 (2011).

65 Hakem, R. DNA-damage repair; the good, the bad, and the ugly. *The EMBO journal* **27**, 589-605 (2008).

66 Sedgwick, B., Bates, P. A., Paik, J., Jacobs, S. C. & Lindahl, T. Repair of alkylated DNA: recent advances. *DNA repair* **6**, 429-442 (2007).

67 Jiricny, J. The multifaceted mismatch-repair system. *Nature reviews Molecular cell biology* **7**, 335-346 (2006).

68 Stojic, L., Brun, R. & Jiricny, J. Mismatch repair and DNA damage signalling. *DNA repair* **3**, 1091-1101 (2004).

69 Wallace, S. S. Base excision repair: a critical player in many games. *DNA repair* **19**, 14-26 (2014).

70 Krokan, H. E. & Bjørås, M. Base excision repair. *Cold Spring Harbor perspectives in biology* **5**, a012583 (2013).

71 Marteijn, J. A., Lans, H., Vermeulen, W. & Hoeijmakers, J. H. Understanding nucleotide excision repair and its roles in cancer and ageing. *Nature reviews Molecular cell biology* **15**, 465-481 (2014).

72 Caldecott, K. W. Single-strand break repair and genetic disease. *Nature Reviews Genetics* **9**, 619-631 (2008).

73 Walker, J. R., Corpina, R. A. & Goldberg, J. Structure of the Ku heterodimer bound to DNA and its implications for double-strand break repair. *Nature* **412**, 607-614 (2001).

74 Yin, X., Liu, M., Tian, Y., Wang, J. & Xu, Y. Cryo-EM structure of human DNA-PK holoenzyme. *Cell research* **27**, 1341-1350 (2017).

75 Chaplin, A. K. *et al.* Cryo-EM of NHEJ supercomplexes provides insights into DNA repair. *Molecular cell* **81**, 3400-3409. e3403 (2021).

76 Chen, S. *et al.* Structural basis of long-range to short-range synaptic transition in NHEJ. *Nature* **593**, 294-298 (2021).

77 Chaplin, A. K. *et al.* Dimers of DNA-PK create a stage for DNA double-strand break repair. *Nature Structural & Molecular Biology* **28**, 13-19 (2021).

78 Chiruvella, K. K., Liang, Z. & Wilson, T. E. Repair of double-strand breaks by end joining. *Cold Spring Harbor perspectives in biology* **5**, a012757 (2013).

79 Goodarzi, A. A. *et al.* DNA-PK autophosphorylation facilitates Artemis endonuclease activity. *The EMBO journal* **25**, 3880-3889 (2006).

80 Moon, A. F. *et al.* Structural insight into the substrate specificity of DNA polymerase μ. *Nature structural & molecular biology* **14**, 45-53 (2007).

81 Caracciolo, D., Riillo, C., Di Martino, M. T., Tagliaferri, P. & Tassone, P. Alternative non-homologous end-joining: Error-prone DNA repair as cancer's Achilles' heel. *Cancers* **13**, 1392 (2021).

82 Trenner, A. & Sartori, A. A. Harnessing DNA double-strand break repair for cancer treatment. *Frontiers in oncology* **9**, 1388 (2019).

83 Yang, G. *et al.* Super-resolution imaging identifies PARP1 and the Ku complex acting as DNA double-strand break sensors. *Nucleic acids research* **46**, 3446-3457 (2018).

84 Paddock, M. *et al.* Competition between PARP-1 and Ku70 control the decision between high-fidelity and mutagenic DNA repair. *DNA repair* **10**, 338-343 (2011).

85 Boboila, C. *et al.* Alternative end-joining catalyzes class switch recombination in the absence of both Ku70 and DNA ligase 4. *Journal of Experimental Medicine* **207**, 417-427 (2010).

86 Lenhart, J. S., Schroeder, J. W., Walsh, B. W. & Simmons, L. A. DNA repair and genome maintenance in Bacillus subtilis. *Microbiology and molecular biology reviews* **76**, 530-564 (2012).

87 Aravind, L. & Koonin, E. V. Prokaryotic homologs of the eukaryotic DNA-end-binding protein Ku, novel domains in the Ku protein and prediction of a prokaryotic double-strand break repair system. *Genome research* **11**, 1365-1374 (2001).

88 Gong, C. *et al.* Mechanism of nonhomologous end-joining in mycobacteria: a low-fidelity repair system driven by Ku, ligase D and ligase C. *Nature structural & molecular biology* **12**, 304-312 (2005).

89 Pitcher, R. S., Tonkin, L. M., Green, A. J. & Doherty, A. J. Domain structure of a NHEJ DNA repair ligase from Mycobacterium tuberculosis. *Journal of molecular biology* **351**, 531-544 (2005).

90 Wright, W. D., Shah, S. S. & Heyer, W.-D. Homologous recombination and the repair of DNA double-strand breaks. *Journal of Biological Chemistry* **293**, 10524-10535 (2018).

91 Sun, Y., McCorvie, T. J., Yates, L. A. & Zhang, X. Structural basis of homologous recombination. *Cellular and Molecular Life Sciences* **77**, 3-18 (2020).

92 Cejka, P. & Symington, L. S. DNA end resection: mechanism and control. *Annual Review of Genetics* **55**, 285-307 (2021).

93 Anand, R., Ranjha, L., Cannavo, E. & Cejka, P. Phosphorylated CtIP functions as a co-factor of the MRE11-RAD50-NBS1 endonuclease in DNA end resection. *Molecular cell* **64**, 940-950 (2016).

94 Mimitou, E. P. & Symington, L. S. Sae2, Exo1 and Sgs1 collaborate in DNA double-strand break processing. *Nature* **455**, 770-774 (2008).

95 Chanut, P., Britton, S., Coates, J., Jackson, S. P. & Calsou, P. Coordinated nuclease activities counteract Ku at single-ended DNA double-strand breaks. *Nature communications* **7**, 1-12 (2016).

96 Myler, L. R. *et al.* Single-molecule imaging reveals how Mre11-Rad50-Nbs1 initiates DNA break repair. *Molecular cell* **67**, 891-898. e894 (2017).

97 Reginato, G., Cannavo, E. & Cejka, P. Physiological protein blocks direct the Mre11–Rad50–Xrs2 and Sae2 nuclease complex to initiate DNA end resection. *Genes & development* **31**, 2325-2330 (2017).

98 Langerak, P., Mejia-Ramirez, E., Limbo, O. & Russell, P. Release of Ku and MRN from DNA ends by Mre11 nuclease activity and Ctp1 is required for homologous recombination repair of double-strand breaks. *PLoS genetics* **7**, e1002271 (2011).

99 Mimitou, E. P. & Symington, L. S. Ku prevents Exo1 and Sgs1-dependent resection of DNA ends in the absence of a functional MRX complex or Sae2. *The EMBO journal* **29**, 3358-3369 (2010).

100 Garcia, V., Phelps, S. E., Gray, S. & Neale, M. J. Bidirectional resection of DNA double-strand breaks by Mre11 and Exo1. *Nature* **479**, 241-244 (2011).

101 Shibata, A. *et al.* DNA double-strand break repair pathway choice is directed by distinct MRE11 nuclease activities. *Molecular cell* **53**, 7-18 (2014).

102 Paull, T. T. & Deshpande, R. A. The Mre11/Rad50/Nbs1 complex: recent insights into catalytic activities and ATP-driven conformational changes. *Exp Cell Res* **329**, 139-147, doi:10.1016/j.yexcr.2014.07.007 (2014).

103 Zeman, M. K. & Cimprich, K. A. Causes and consequences of replication stress. *Nat Cell Biol* **16**, 2-9, doi:10.1038/ncb2897 (2014).

104 Shinohara, A. & Ogawa, T. Stimulation by Rad52 of yeast Rad51-mediated recombination. *Nature* **391**, 404-407 (1998).

105 Baumann, P. & West, S. C. The human Rad51 protein: polarity of strand transfer and stimulation by hRP-A. *The EMBO journal* **16**, 5198-5206 (1997).

106 Carreira, A. *et al.* The BRC repeats of BRCA2 modulate the DNA-binding selectivity of RAD51. *Cell* **136**, 1032-1043 (2009).

107 Gupta, R. C., Folta-Stogniew, E., O'Malley, S., Takahashi, M. & Radding, C. M. Rapid exchange of A: T base pairs is essential for recognition of DNA homology by human Rad51 recombination protein. *Molecular cell* **4**, 705-714 (1999).

108 Folta-Stogniew, E., O'Malley, S., Gupta, R., Anderson, K. S. & Radding, C. M. Exchange of DNA base pairs that coincides with recognition of homology promoted by E. coli RecA protein. *Molecular cell* **15**, 965-975 (2004).

109 Morrical, S. W. DNA-pairing and annealing processes in homologous recombination and homology-directed repair. *Cold Spring Harbor perspectives in biology* **7**, a016444 (2015).

110 Nimonkar, A. V., Sica, R. A. & Kowalczykowski, S. C. Rad52 promotes second-end DNA capture in double-stranded break repair to form complement-stabilized joint molecules. *Proceedings of the National Academy of Sciences* **106**, 3077-3082 (2009).

111 Kadyk, L. C. & Hartwell, L. H. Sister chromatids are preferred over homologs as substrates for recombinational repair in Saccharomyces cerevisiae. *Genetics* **132**, 387-402 (1992).

112 Manthei, K. A. & Keck, J. L. The BLM dissolvasome in DNA replication and repair. *Cellular and molecular life sciences* **70**, 4067-4084 (2013).

113 Chen, X.-B. *et al.* Human Mus81-associated endonuclease cleaves Holliday junctions in vitro. *Molecular cell* **8**, 1117-1127 (2001).

114 Fekairi, S. *et al.* Human SLX4 is a Holliday junction resolvase subunit that binds multiple DNA repair/recombination endonucleases. *Cell* **138**, 78-89 (2009).

115 Ip, S. C. *et al.* Identification of Holliday junction resolvases from humans and yeast. *Nature* **456**, 357-361 (2008).

116 Wyatt, H. D. & West, S. C. Holliday junction resolvases. *Cold Spring Harbor perspectives in biology* **6**, a023192 (2014).

117 Bhargava, R., Onyango, D. O. & Stark, J. M. Regulation of single-strand annealing and its role in genome maintenance. *Trends in Genetics* **32**, 566-575 (2016).

118 Kowalczykowski, S. C. An overview of the molecular mechanisms of recombinational DNA repair. *Cold Spring Harbor Perspectives in Biology* **7**, a016410 (2015).

119 Sharples, G. J. & Leach, D. R. Structural and functional similarities between the SbcCD proteins of Escherichia coli and the RAD50 and MRE11 (RAD32) recombination and repair proteins of yeast. *Molecular microbiology* **17**, 1215-1217 (1995).

120 Connelly, J. C., Kirkham, L. A. & Leach, D. R. The SbcCD nuclease of Escherichia coli is a structural maintenance of chromosomes (SMC) family protein that cleaves hairpin DNA. *Proceedings of the National Academy of Sciences* **95**, 7969-7974 (1998).

121 Bell, J. C., Plank, J. L., Dombrowski, C. C. & Kowalczykowski, S. C. Direct imaging of RecA nucleation and growth on single molecules of SSB-coated ssDNA. *Nature* **491**, 274-278 (2012).

122 Forget, A. L. & Kowalczykowski, S. C. Single-molecule imaging of DNA pairing by RecA reveals a three-dimensional homology search. *Nature* **482**, 423-427 (2012).

123 Hiom, K. & West, S. C. Branch migration during homologous recombination: assembly of a RuvAB-Holliday junction complex in vitro. *Cell* **80**, 787-793 (1995).

124 Stasiak, A. *et al.* The Escherichia coli RuvB branch migration protein forms double hexameric rings around DNA. *Proceedings of the National Academy of Sciences* **91**, 7618-7622 (1994).

125 Rafferty, J. B. *et al.* Crystal structure of DNA recombination protein RuvA and a model for its binding to the Holliday junction. *Science* **274**, 415-421 (1996).

126 Harmon, F. G., DiGate, R. J. & Kowalczykowski, S. C. RecQ helicase and topoisomerase III comprise a novel DNA strand passage function: a conserved mechanism for control of DNA recombination. *Molecular cell* **3**, 611-620 (1999).

127 Bennett, R. J., Dunderdale, H. J. & West, S. C. Resolution of Holliday junctions by RuvC resolvase: cleavage specificity and DNA distortion. *Cell* **74**, 1021-1031 (1993).

128 Scully, R., Panday, A., Elango, R. & Willis, N. A. DNA double-strand break repair-pathway choice in somatic mammalian cells. *Nature reviews Molecular cell biology* **20**, 698-714 (2019).

129 Huertas, P., Cortés-Ledesma, F., Sartori, A. A., Aguilera, A. & Jackson, S. P. CDK targets Sae2 to control DNA-end resection and homologous recombination. *Nature* **455**, 689-692 (2008).

130 Chapman, J. R., Taylor, M. R. & Boulton, S. J. Playing the end game: DNA double-strand break repair pathway choice. *Mol Cell* **47**, 497-510, doi:10.1016/j.molcel.2012.07.029 (2012).

131 Paull, T. T. Reconsidering pathway choice: a sequential model of mammalian DNA double-strand break pathway decisions. *Current Opinion in Genetics & Development* **71**, 55-62 (2021).

132 Shim, E. Y. *et al.* Saccharomyces cerevisiae Mre11/Rad50/Xrs2 and Ku proteins regulate association of Exo1 and Dna2 with DNA breaks. *The EMBO journal* **29**, 3370-3380 (2010).

133 Sun, J., Lee, K.-J., Davis, A. J. & Chen, D. J. Human Ku70/80 protein blocks exonuclease 1-mediated DNA resection in the presence of human Mre11 or Mre11/Rad50 protein complex. *Journal of Biological Chemistry* **287**, 4936-4945 (2012).

134 Kochan, J. A. *et al.* Meta-analysis of DNA double-strand break response kinetics. *Nucleic acids research* **45**, 12625-12637 (2017).

135 Deshpande, R. A. *et al.* DNA-dependent protein kinase promotes DNA end processing by MRN and CtIP. *Science advances* **6**, eaay0922 (2020).

136 Paull, T. T. 20 years of Mre11 biology: no end in sight. *Molecular cell* **71**, 419-427 (2018).

137 Syed, A. & Tainer, J. A. The MRE11–RAD50–NBS1 complex conducts the orchestration of damage signaling and outcomes to stress in DNA replication and repair. *Annual review of biochemistry* **87**, 263 (2018).

138 Schiller, C. B., Seifert, F. U., Linke-Winnebeck, C. & Hopfner, K.-P. Structural studies of DNA end detection and resection in homologous recombination. *Cold Spring Harbor Perspectives in Biology* **6**, a017962 (2014).

139 Rotheneder, M. *et al.* Cryo-EM structure of the Mre11-Rad50-Nbs1 complex reveals the molecular mechanism of scaffolding functions. *Molecular Cell* **83**, 167-185. e169 (2023).

140 Hopfner, K.-P. *et al.* Structural biochemistry and interaction architecture of the DNA double-strand break repair Mre11 nuclease and Rad50-ATPase. *Cell* **105**, 473-485 (2001).

141 Hopfner, K.-P. *et al.* The Rad50 zinc-hook is a structure joining Mre11 complexes in DNA recombination and repair. *Nature* **418**, 562-566 (2002).

142 Chen, L., Trujillo, K., Ramos, W., Sung, P. & Tomkinson, A. E. Promotion of Dnl4-catalyzed DNA end-joining by the Rad50/Mre11/Xrs2 and Hdf1/Hdf2 complexes. *Molecular cell* **8**, 1105-1115 (2001).

143 de Jager, M. *et al.* Human Rad50/Mre11 is a flexible complex that can tether DNA ends. *Molecular cell* **8**, 1129-1135 (2001).

144 Moreno-Herrero, F. *et al.* Mesoscale conformational changes in the DNA-repair complex Rad50/Mre11/Nbs1 upon binding DNA. *Nature* **437**, 440-443 (2005).

145 Ajimura, M., Leem, S. & Ogawa, H. Identification of new genes required for meiotic recombination in Saccharomyces cerevisiae. *Genetics* **133**, 51-66 (1993).

146 Paull, T. T. & Gellert, M. The 3′ to 5′ exonuclease activity of Mre11 facilitates repair of DNA double-strand breaks. *Molecular cell* **1**, 969-979 (1998).

147 Hopfner, K.-P. *et al.* Mre11 and Rad50 from Pyrococcus furiosus: cloning and biochemical characterization reveal an evolutionarily conserved multiprotein machine. *Journal of bacteriology* **182**, 6036-6041 (2000).

148 Williams, R. S. *et al.* Mre11 dimers coordinate DNA end bridging and nuclease processing in double-strand-break repair. *Cell* **135**, 97-109 (2008).

149 Lammens, K. *et al.* The Mre11: Rad50 structure shows an ATP-dependent molecular clamp in DNA double-strand break repair. *Cell* **145**, 54-66 (2011).

150 Schiller, C. B. *et al.* Structure of Mre11–Nbs1 complex yields insights into ataxia-telangiectasia–like disease mutations and DNA damage signaling. *Nature structural & molecular biology* **19**, 693-700 (2012).

151 Das, D. *et al.* Crystal structure of the first eubacterial Mre11 nuclease reveals novel features that may discriminate substrates during DNA repair. *Journal of molecular biology* **397**, 647-663 (2010).

152 Liu, S. *et al.* Structural basis for DNA recognition and nuclease processing by the Mre11 homologue SbcD in double-strand breaks repair. *Acta Crystallographica Section D: Biological Crystallography* **70**, 299-309 (2014).

153 Liu, Y. *et al.* ATP-dependent DNA binding, unwinding, and resection by the Mre11/Rad50 complex. *The EMBO journal* **35**, 743-758 (2016).

154 Seifert, F. U., Lammens, K. & Hopfner, K.-P. Structure of the catalytic domain of Mre11 from Chaetomium thermophilum. *Acta Crystallographica Section F: Structural Biology Communications* **71**, 752-757 (2015).

155 Williams, G. J. *et al.* ABC ATPase signature helices in Rad50 link nucleotide state to Mre11 interface for DNA repair. *Nat Struct Mol Biol* **18**, 423-431, doi:10.1038/nsmb.2038 (2011).

156 Seifert, F. U., Lammens, K., Stoehr, G., Kessler, B. & Hopfner, K. P. Structural mechanism of ATP-dependent DNA binding and DNA end bridging by eukaryotic Rad50. *The EMBO journal* **35**, 759-772 (2016).

157 Rojowska, A. *et al.* Structure of the Rad50 DNA double-strand break repair protein in complex with DNA. *The EMBO journal* **33**, 2847-2859 (2014).

158 Furuse, M. *et al.* Distinct roles of two separable in vitro activities of yeast Mre11 in mitotic and meiotic recombination. *The EMBO journal* **17**, 6412-6425 (1998).

159 Usui, T. *et al.* Complex formation and functional versatility of Mre11 of budding yeast in recombination. *Cell* **95**, 705-716 (1998).

160 Déry, U. *et al.* A glycine-arginine domain in control of the human MRE11 DNA repair protein. *Molecular and cellular biology* **28**, 3058-3069 (2008).

161 Paull, T. T. & Gellert, M. Nbs1 potentiates ATP-driven DNA unwinding and endonuclease cleavage by the Mre11/Rad50 complex. *Genes & development* **13**, 1276-1288 (1999).

162 Trujillo, K. M., Yuan, S.-S. F., Eva, Y.-H. L. & Sung, P. Nuclease activities in a complex of human recombination and DNA repair factors Rad50, Mre11, and p95. *Journal of Biological Chemistry* **273**, 21447-21450 (1998).

163 Trujillo, K. M. & Sung, P. DNA Structure-specific Nuclease Activities in theSaccharomyces cerevisiae Rad50· Mre11 Complex. *Journal of Biological Chemistry* **276**, 35458-35464 (2001).

164 Deshpande, R. A., Lee, J.-H. & Paull, T. T. Rad50 ATPase activity is regulated by DNA ends and requires coordination of both active sites. *Nucleic acids research* **45**, 5255-5268 (2017).

165 Saathoff, J.-H., Käshammer, L., Lammens, K., Byrne, R. T. & Hopfner, K.-P. The bacterial Mre11–Rad50 homolog SbcCD cleaves opposing strands of DNA by two chemically distinct nuclease reactions. *Nucleic acids research* **46**, 11303-11314 (2018).

166 Sung, S. *et al.* DNA end recognition by the Mre11 nuclease dimer: insights into resection and repair of damaged DNA. *The EMBO journal* **33**, 2422-2435 (2014).

167 Möckel, C., Lammens, K., Schele, A. & Hopfner, K.-P. ATP driven structural changes of the bacterial Mre11: Rad50 catalytic head complex. *Nucleic acids research* **40**, 914-927 (2012).

168 Cannavo, E. & Cejka, P. Sae2 promotes dsDNA endonuclease activity within Mre11–Rad50–Xrs2 to resect DNA breaks. *Nature* **514**, 122-125 (2014).

169 Sartori, A. A. *et al.* Human CtIP promotes DNA end resection. *Nature* **450**, 509-514 (2007).

170 Hartsuiker, E., Neale, M. J. & Carr, A. M. Distinct requirements for the Rad32Mre11 nuclease and Ctp1CtIP in the removal of covalently bound topoisomerase I and II from DNA. *Molecular cell* **33**, 117-123 (2009).

171 Hartsuiker, E. *et al.* Ctp1CtIP and Rad32Mre11 nuclease activity are required for Rec12Spo11 removal, but Rec12Spo11 removal is dispensable for other MRN-dependent meiotic functions. *Molecular and cellular biology* **29**, 1671-1681 (2009).

172 Connelly, J. C., De Leau, E. S. & Leach, D. R. Nucleolytic processing of a protein-bound DNA end by the E. coli SbcCD (MR) complex. *DNA repair* **2**, 795-807 (2003).

173 Deshpande, R. A., Lee, J.-H., Arora, S. & Paull, T. T. Nbs1 converts the human Mre11/Rad50 nuclease complex into an endo/exonuclease machine specific for protein-DNA adducts. *Molecular cell* **64**, 593-606 (2016).

174 Wang, W., Daley, J. M., Kwon, Y., Krasner, D. S. & Sung, P. Plasticity of the Mre11–Rad50–Xrs2–Sae2 nuclease ensemble in the processing of DNA-bound obstacles. *Genes & development* **31**, 2331-2336 (2017).

175 Lobachev, K. S., Gordenin, D. A. & Resnick, M. A. The Mre11 complex is required for repair of hairpin-capped double-strand breaks and prevention of chromosome rearrangements. *Cell* **108**, 183-193 (2002).

176 Hopfner, K.-P. *et al.* Structural biology of Rad50 ATPase: ATP-driven conformational control in DNA double-strand break repair and the ABC-ATPase superfamily. *Cell* **101**, 789-800 (2000).

177 Aravind, L., Walker, D. R. & Koonin, E. V. Conserved domains in DNA repair proteins and evolution of repair systems. *Nucleic acids research* **27**, 1223-1242 (1999).

178 Lim, H. S., Kim, J. S., Park, Y. B., Gwon, G. H. & Cho, Y. Crystal structure of the Mre11–Rad50–ATPγS complex: understanding the interplay between Mre11 and Rad50. *Genes & development* **25**, 1091-1104 (2011).

179 Deshpande, R. A. *et al.* ATP-driven Rad50 conformations regulate DNA tethering, end resection, and ATM checkpoint signaling. *The EMBO journal* **33**, 482-500 (2014).

180 Trujillo, K. M. *et al.* Yeast xrs2 binds DNA and helps target rad50 and mre11 to DNA ends. *Journal of Biological Chemistry* **278**, 48957-48964 (2003).

181 Hohl, M. *et al.* The Rad50 coiled-coil domain is indispensable for Mre11 complex functions. *Nature structural & molecular biology* **18**, 1124-1131 (2011).

182 Lee, J.-H. *et al.* Ataxia telangiectasia-mutated (ATM) kinase activity is regulated by ATP-driven conformational changes in the Mre11/Rad50/Nbs1 (MRN) complex. *Journal of Biological Chemistry* **288**, 12840-12851 (2013).

183 He, J. *et al.* Rad50 zinc hook is important for the Mre11 complex to bind chromosomal DNA double-stranded breaks and initiate various DNA damage responses. *Journal of Biological Chemistry* **287**, 31747-31756 (2012).

184 Wiltzius, J. J., Hohl, M., Fleming, J. C. & Petrini, J. H. The Rad50 hook domain is a critical determinant of Mre11 complex functions. *Nature structural & molecular biology* **12**, 403-407 (2005).

185 Park, Y. B. *et al.* Eukaryotic Rad50 functions as a rod-shaped dimer. *Nature structural & molecular biology* **24**, 248-257 (2017).

186 Soh, Y. M., Basquin, J. & Gruber, S. A rod conformation of the Pyrococcus furiosus Rad50 coiled coil. *Proteins: Structure, Function, and Bioinformatics* **89**, 251-255 (2021).

187 Zabolotnaya, E. *et al.* Modes of action of the archaeal Mre11/Rad50 DNA-repair complex revealed by fast-scan atomic force microscopy. *Proceedings of the National Academy of Sciences* **117**, 14936-14947 (2020).

188 Tatebe, H. *et al.* Rad50 zinc hook functions as a constitutive dimerization module interchangeable with SMC hinge. *Nature communications* **11**, 1-11 (2020).

189 Bürmann, F. *et al.* Tuned SMC arms drive chromosomal loading of prokaryotic condensin. *Molecular cell* **65**, 861-872. e869 (2017).

190 Carney, J. P. *et al.* The hMre11/hRad50 protein complex and Nijmegen breakage syndrome: linkage of double-strand break repair to the cellular DNA damage response. *Cell* **93**, 477-486 (1998).

191 Desai-Mehta, A., Cerosaletti, K. M. & Concannon, P. Distinct functional domains of nibrin mediate Mre11 binding, focus formation, and nuclear localization. *Molecular and cellular biology* **21**, 2184-2191 (2001).

192 Williams, R. S. *et al.* Nbs1 flexibly tethers Ctp1 and Mre11-Rad50 to coordinate DNA double-strand break processing and repair. *Cell* **139**, 87-99 (2009).

193 Lloyd, J. *et al.* A supramodular FHA/BRCT-repeat architecture mediates Nbs1 adaptor function in response to DNA damage. *Cell* **139**, 100-111 (2009).

194 Chen, L., Nievera, C. J., Lee, A. Y.-L. & Wu, X. Cell cycle-dependent complex formation of BRCA1· CtIP· MRN is important for DNA double-strand break repair. *Journal of Biological Chemistry* **283**, 7713-7720 (2008).

195 Stracker, T. H., Morales, M., Couto, S. S., Hussein, H. & Petrini, J. H. The carboxy terminus of NBS1 is required for induction of apoptosis by the MRE11 complex. *Nature* **447**, 218-221 (2007).

196 Falck, J., Coates, J. & Jackson, S. P. Conserved modes of recruitment of ATM, ATR and DNA-PKcs to sites of DNA damage. *Nature* **434**, 605-611 (2005).

197 Wu, X. *et al.* ATM phosphorylation of Nijmegen breakage syndrome protein is required in a DNA damage response. *Nature* **405**, 477-482 (2000).

198 You, Z., Chahwan, C., Bailis, J., Hunter, T. & Russell, P. ATM activation and its recruitment to damaged DNA require binding to the C terminus of Nbs1. *Molecular and cellular biology* **25**, 5363-5379 (2005).

199 Andres, S. N. & Williams, R. S. CtIP/Ctp1/Sae2, molecular form fit for function. *DNA repair* **56**, 109-117 (2017).

200 Davies, O. R. *et al.* CtIP tetramer assembly is required for DNA-end resection and repair. *Nature structural & molecular biology* **22**, 150-157 (2015).

201 Andres, S. N. *et al.* Tetrameric Ctp1 coordinates DNA binding and DNA bridging in DNA double-strand-break repair. *Nature structural & molecular biology* **22**, 158-166 (2015).

202 Wilkinson, O. J. *et al.* CtIP forms a tetrameric dumbbell-shaped particle which bridges complex DNA end structures for double-strand break repair. *Elife* **8**, e42129 (2019).

203 Yu, X. & Chen, J. DNA damage-induced cell cycle checkpoint control requires CtIP, a phosphorylation-dependent binding partner of BRCA1 C-terminal domains. *Molecular and cellular biology* **24**, 9478-9486 (2004).

204 Stracker, T. H. & Petrini, J. H. The MRE11 complex: starting from the ends. *Nature reviews Molecular cell biology* **12**, 90-103 (2011).

205 Uchisaka, N. *et al.* Two brothers with ataxia-telangiectasia-like disorder with lung adenocarcinoma. *The Journal of pediatrics* **155**, 435-438 (2009).

206 Waltes, R. *et al.* Human RAD50 deficiency in a Nijmegen breakage syndrome-like disorder. *The American Journal of Human Genetics* **84**, 605-616 (2009).

207 van den Berg, J. *et al.* A limited number of double-strand DNA breaks is sufficient to delay cell cycle progression. *Nucleic acids research* **46**, 10132-10144 (2018).

208 Sandell, L. L. & Zakian, V. A. Loss of a yeast telomere: arrest, recovery, and chromosome loss. *Cell* **75**, 729-739 (1993).

209 Waterman, D. P., Haber, J. E. & Smolka, M. B. Checkpoint responses to DNA double-strand breaks. *Annual review of biochemistry* **89**, 103 (2020).

210 Nakada, D., Matsumoto, K. & Sugimoto, K. ATM-related Tel1 associates with double-strand breaks through an Xrs2-dependent mechanism. *Genes & development* **17**, 1957-1962 (2003).

211 Kim, J. H. *et al.* The Mre11-Nbs1 interface is essential for viability and tumor suppression. *Cell reports* **18**, 496-507 (2017).

212 Zou, L. & Elledge, S. J. Sensing DNA damage through ATRIP recognition of RPA-ssDNA complexes. *Science* **300**, 1542-1548 (2003).

213 Mantiero, D., Clerici, M., Lucchini, G. & Longhese, M. P. Dual role for Saccharomyces cerevisiae Tel1 in the checkpoint response to double-strand breaks. *EMBO reports* **8**, 380-387 (2007).

214 Levy, M. Z., Allsopp, R. C., Futcher, A. B., Greider, C. W. & Harley, C. B. Telomere end-replication problem and cell aging. *Journal of molecular biology* **225**, 951-960 (1992).

215 Lamarche, B. J., Orazio, N. I. & Weitzman, M. D. The MRN complex in double-strand break repair and telomere maintenance. *FEBS letters* **584**, 3682-3695 (2010).

216 Harley, C. B., Futcher, A. B. & Greider, C. W. Telomeres shorten during ageing of human fibroblasts. *Nature* **345**, 458-460 (1990).

217 Marcand, S. How do telomeres and NHEJ coexist? *Molecular & cellular oncology* **1**, e963438 (2014).

218 Wu, P., Takai, H. & de Lange, T. Telomeric 3′ overhangs derive from resection by Exo1 and Apollo and fill-in by POT1b-associated CST. *Cell* **150**, 39-52 (2012).

219 Dimitrova, N. & de Lange, T. Cell cycle-dependent role of MRN at dysfunctional telomeres: ATM signaling-dependent induction of nonhomologous end joining (NHEJ) in G1 and resection-mediated inhibition of NHEJ in G2. *Molecular and cellular biology* **29**, 5552-5563 (2009).

220 Zhu, X.-D., Küster, B., Mann, M., Petrini, J. H. & Lange, T. d. Cell-cycle-regulated association of RAD50/MRE11/NBS1 with TRF2 and human telomeres. *Nature genetics* **25**, 347-352 (2000).

221 Takata, H., Tanaka, Y. & Matsuura, A. Late S phase-specific recruitment of Mre11 complex triggers hierarchical assembly of telomere replication proteins in Saccharomyces cerevisiae. *Molecular cell* **17**, 573-583 (2005).

222 Rai, R. *et al.* NBS1 phosphorylation status dictates repair choice of dysfunctional telomeres. *Molecular cell* **65**, 801-817. e804 (2017).

223 Attwooll, C. L., Akpınar, M. g. & Petrini, J. H. The mre11 complex and the response to dysfunctional telomeres. *Molecular and cellular biology* **29**, 5540-5551 (2009).

224 McGee, J. S. *et al.* Reduced Rif2 and lack of Mec1 target short telomeres for elongation rather than double-strand break repair. *Nature structural & molecular biology* **17**, 1438-1445 (2010).

225 Martina, M. *et al.* A balance between Tel1 and Rif2 activities regulates nucleolytic processing and elongation at telomeres. *Molecular and Cellular Biology* **32**, 1604-1617 (2012).

226 Khayat, F. *et al.* Inhibition of MRN activity by a telomere protein motif. *Nature Communications* **12**, 3856 (2021).

227 Roisné-Hamelin, F. *et al.* Mechanism of MRX inhibition by Rif2 at telomeres. *Nature Communications* **12**, 2763 (2021).

228 Lilley, C. E., Schwartz, R. A. & Weitzman, M. D. Using or abusing: viruses and the cellular DNA damage response. *Trends in microbiology* **15**, 119-126 (2007).

229 Shah, G. A. & O'Shea, C. C. Viral and cellular genomes activate distinct DNA damage responses. *Cell* **162**, 987-1002 (2015).

230 Weiden, M. D. & Ginsberg, H. S. Deletion of the E4 region of the genome produces adenovirus DNA concatemers. *Proceedings of the National Academy of Sciences* **91**, 153-157 (1994).

231 Boyer, J., Rohleder, K. & Ketner, G. Adenovirus E4 34k and E4 11k inhibit double strand break repair and are physically associated with the cellular DNA-dependent protein kinase. *Virology* **263**, 307-312 (1999).

232 Stracker, T. H., Carson, C. T. & Weitzman, M. D. Adenovirus oncoproteins inactivate the Mre11–Rad50–NBS1 DNA repair complex. *Nature* **418**, 348-352 (2002).

233 Rawlins, D. R., Rosenfeld, P. J., Wides, R. J., Challberg, M. D. & Kelly Jr, T. J. Structure and function of the adenovirus origin of replication. *Cell* **37**, 309-319 (1984).

234 Bernstein, J. A., Porter, J. M. & Challberg, M. D. Template requirements for in vivo replication of adenovirus DNA. *Molecular and cellular biology* **6**, 2115-2124 (1986).

235 Kondo, T. *et al.* DNA damage sensor MRE11 recognizes cytosolic double-stranded DNA and induces type I interferon by regulating STING trafficking. *Proceedings of the National Academy of Sciences* **110**, 2969-2974 (2013).

236 Connelly, J. C. & Leach, D. R. The sbcC and sbcD genes of Escherichia coli encode a nuclease involved in palindrome inviability and genetic recombination. *Genes to Cells* **1**, 285-291 (1996).

237 Connelly, J. C., De Leau, E. S. & Leach, D. R. DNA cleavage and degradation by the SbcCD protein complex from Escherichia coli. *Nucleic acids research* **27**, 1039-1046 (1999).

238 Lim, C. T., Lai, P. J., Leach, D. R., Maki, H. & Furukohri, A. A novel mode of nuclease action is revealed by the bacterial Mre11/Rad50 complex. *Nucleic acids research* **43**, 9804-9816 (2015).

239 Cannon, B. *et al.* Visualization of local DNA unwinding by Mre11/Rad50/Nbs1 using single-molecule FRET. *Proceedings of the National Academy of Sciences* **110**, 18868-18873 (2013).

240 Eykelenboom, J. K., Blackwood, J. K., Okely, E. & Leach, D. R. SbcCD causes a double-strand break at a DNA palindrome in the Escherichia coli chromosome. *Molecular cell* **29**, 644-651 (2008).

241 Aedo, S. & Tse-Dinh, Y.-C. SbcCD-mediated processing of covalent gyrase-DNA complex in Escherichia coli. *Antimicrobial agents and chemotherapy* **57**, 5116-5119 (2013).

242 Leach, D. R. Long DNA palindromes, cruciform structures, genetic instability and secondary structure repair. *Bioessays* **16**, 893-900 (1994).

243 Lewis, S. M. & Coté, A. G. Palindromes and genomic stress fractures: bracing and repairing the damage. *DNA repair* **5**, 1146-1160 (2006).

244 Deng, S. K., Yin, Y., Petes, T. D. & Symington, L. S. Mre11-Sae2 and RPA collaborate to prevent palindromic gene amplification. *Molecular cell* **60**, 500-508 (2015).

245 Wendel, B. M., Cole, J. M., Courcelle, C. T. & Courcelle, J. SbcC-SbcD and ExoI process convergent forks to complete chromosome replication. *Proceedings of the National Academy of Sciences* **115**, 349-354 (2018).

246 Park, Y. B., Chae, J., Kim, Y. C. & Cho, Y. Crystal structure of human Mre11: understanding tumorigenic mutations. *Structure* **19**, 1591-1602 (2011).

247 Suter, B., Schnappauf, G. & Thoma, F. Poly (dA· dT) sequences exist as rigid DNA structures in nucleosome-free yeast promoters in vivo. *Nucleic acids research* **28**, 4083-4089 (2000).

248 Gobbini, E., Vertemara, J. & Longhese, M. P. Local unwinding of double-strand DNA ends by the MRX complex promotes Exo1 processing activity. *Molecular & cellular oncology* **5**, e1511208 (2018).

249 Sharma, S. *et al.* MRE11-RAD50-NBS1 complex is sufficient to promote transcription by RNA polymerase II at double-strand breaks by melting DNA ends. *Cell reports* **34**, 108565 (2021).

250 Kissling, V. M. *et al.* Mre11-Rad50 oligomerization promotes DNA double-strand break repair. *Nature Communications* **13**, 2374 (2022).

251 Bazzano, D., Lomonaco, S. & Wilson, T. E. Mapping yeast mitotic 5′ resection at base resolution reveals the sequence and positional dependence of nucleases in vivo. *Nucleic Acids Research* **49**, 12607-12621 (2021).

252 Gnügge, R., Reginato, G., Cejka, P. & Symington, L. S. Sequence and chromatin features guide DNA double-strand break resection initiation. *Molecular Cell* (2023).

253 Cannavo, E., Reginato, G. & Cejka, P. Stepwise 5′ DNA end-specific resection of DNA breaks by the Mre11-Rad50-Xrs2 and Sae2 nuclease ensemble. *Proceedings of the National Academy of Sciences* **116**, 5505-5513 (2019).

254 Gerlitz, G., Darhin, E., Giorgio, G., Franco, B. & Reiner, O. Novel functional features of the Lis-H domain: role in protein dimerization, half-life and cellular localization. *Cell Cycle* **4**, 1632-1640 (2005).

255 Kim, M. H. *et al.* The structure of the N-terminal domain of the product of the lissencephaly gene Lis1 and its functional implications. *Structure* **12**, 987-998 (2004).

256 Alani, E., Padmore, R. & Kleckner, N. Analysis of wild-type and rad50 mutants of yeast suggests an intimate relationship between meiotic chromosome synapsis and recombination. *Cell* **61**, 419-436 (1990).

257 McKee, A. H. & Kleckner, N. A general method for identifying recessive diploid-specific mutations in Saccharomyces cerevisiae, its application to the isolation of mutants blocked at intermediate stages of meiotic prophase and characterization of a new gene SAE2. *Genetics* **146**, 797-816 (1997).

258 Zdravković, A. *et al.* A conserved Ctp1/CtIP C-terminal peptide stimulates Mre11 endonuclease activity. *Proceedings of the National Academy of Sciences* **118**, e2016287118 (2021).

259 Cannavo, E. *et al.* Regulatory control of DNA end resection by Sae2 phosphorylation. *Nature communications* **9**, 4016 (2018).

260 Jumper, J. *et al.* Highly accurate protein structure prediction with AlphaFold. *Nature* **596**, 583-589 (2021).

261 Huertas, P. & Jackson, S. P. Human CtIP mediates cell cycle control of DNA end resection and double strand break repair. *Journal of Biological Chemistry* **284**, 9558-9565 (2009).

262 Wang, H. *et al.* The interaction of CtIP and Nbs1 connects CDK and ATM to regulate HR–mediated double-strand break repair. *PLoS genetics* **9**, e1003277 (2013).

263 Casari, E. *et al.* To Fix or Not to Fix: Maintenance of Chromosome Ends Versus Repair of DNA Double-Strand Breaks. *Cells* **11**, 3224 (2022).

264 Marsella, A. *et al.* Sae2 and Rif2 regulate MRX endonuclease activity at DNA double-strand breaks in opposite manners. *Cell Reports* **34**, 108906 (2021).

265 Okamoto, K. *et al.* A two-step mechanism for TRF2-mediated chromosome-end protection. *Nature* **494**, 502-505 (2013).

266 Khayat, F., Alshmery, M., Pal, M., Oliver, A. W. & Bianchi, A. Binding of the TRF2 iDDR motif to RAD50 highlights a convergent evolutionary strategy to inactivate MRN at telomeres. *bioRxiv*, 2023.2003. 2025.534200 (2023).

267 Myler, L. R. *et al.* DNA-PK and the TRF2 iDDR inhibit MRN-initiated resection at leading-end telomeres. *bioRxiv*, 2023.2003. 2006.531339 (2023).

5 Acknowledgements

First of all, I would like to thank my supervisor Prof. Dr. Karl-Peter Hopfner for the opportunity to work in his lab and for all of his support during the years. I am very grateful for the project I was able to work on and the constant help and advice that I received. Furthermore, I am very thankful for the given freedom and trust, which made it possible to also develop and explore own scientific ideas.

I also want to thank Lisa Käshammer, who introduced me into the *Ec*MR project, the DNA repair subgroup and especially cryo-EM. I am very grateful for the amazing team work throughout the years of collaboration and the constant help, support, and nice discussions.

Moreover, I want to thank Katja Lammens, who was a great support, in and around the lab, and taught me a lot, especially about cryo-EM but also scientific approaches in general. I am very thankful for the nice working atmosphere, the possibility to always ask questions and that I was given so much trust regarding the independent operation of the microscopes.

In addition, I want to thank Anna-Maria Boggusch, who joined the *Ec*MR team at the right time. I am very glad for the good teamwork, the help with the revisions of the second paper and the upcoming joint work on this project.

Additional thanks go to all other members of the MRN subgroup, current ones and alumni, with whom I was able work with during the years: Joseph Bartho, Brigitte Kessler, Matthias Rotheneder, Kristina Stakyte, Erik van de Logt, Marijke Jansma, Yilan Fan, Filiz Kuybu. I really enjoyed working with you.
Special thanks go to Joseph Bartho for teaching me a lot about cryo-EM data collection and processing; Gregor Witte for answering all of my questions, scientific and non-scientific, and for his help with all biophysical and IT-related issues; Brigitte Kessler, Alexandra Schele, Manuela Moldt and Olga Fettscher for the lab organization and being the good souls of the Hopfner lab; Dirk Kostrewa for his help with data processing and management.

I would also like to thank the whole Hopfner lab for the great working atmosphere, as well as the received help, input and support. I had an amazing time with all of you!

Most importantly, I would like to thank my girlfriend Carolin, my parents, family and friends from the bottom of my heart. Thank you so much for your tireless support, patience and encouragement throughout all these years. I am very lucky and glad to have you in my life.